Ilmenau University of Technology

Department of Electrical Engineering and Information Technology

M-sequence based ultra-wideband radar and its application to crack detection in salt mines

Dipl.-Ing. Ralf Herrmann

Dissertation zur Erlangung des akademischen Grades

Doktor-Ingenieur (Dr.-Ing.)

vorgelegt der Fakultät für Eletrotechnik und Informationstechnik der Technischen Universität Ilmenau von Dipl.-Ing. Ralf Herrmann, geb. am 19.09.1978 in Schmalkalden

Gutachter:

1. Prof. Dr.-Ing. habil. Reiner S. Thomä
2. Prof. Dr.-Ing. Motoyuki Sato
3. Prof. Dr.-Ing. Reinhard Knöchel

Acknowledgement

> "Zwei Dinge sollten Kinder von ihren Eltern bekommen:
> Wurzeln und Flügel ... "[1] (J. W. v. Goethe, 1749 - 1832)

Even though times are very different now than they used to be in the 18th century, some wisdom is even more true today. Without contribution of so many people it is unthinkable to follow an academic path and finish a dissertation.

I want to express my deep gratitude to my parents, grandparents, brother, and friends for everlasting support and encouragement on my way.

Besides personal support, good education is invaluable to unfold one's potential. Starting from my teachers at school, the lecturers at the Ilmenau University of Technology during my years of study to my colleagues at the Electronic Measurement Research Lab I like to thank everybody for providing knowledge, scientific stimulation, and motivation.

I want to especially thank my supervisors Prof. Dr.-Ing. Habil. Reiner Thomä and Dr.-Ing. Jürgen Sachs for giving me the chance to work on an interesting research project, continues scientific guidance, and numerous technical discussions and support. Furthermore, I want to thank Prof. Dr. Motoyuki Sato and his colleagues at the Centre for Northeast Asian Studies from the Tohoku University in Sendai (Japan) for accepting me as a guest student and introducing many aspects of radar data processing.

Dipl.-Ing. R.Herrmann Ilmenau, July 6, 2011

---

[1] Translation — Two things children should receive from their parents: roots and wings ...

Contents

List of Figures

List of Tables

List of Abbreviations and Symbols

NDTCE	Non-Destructive Testing in Civil Engineering
RADAR/radar	RAdio Detection And Ranging
GPR	Ground Penetrating Radar
UWB	Ultra-WideBand
MLBS	Maximum Length Binary Sequence, M-Sequence
VNA	Vector Network Analyser
ACU	Automatic Calibration Unit
IRF	Impulse Response Function
FRF	Frequency Response Function
FWHD	Full Width Half Duration
ADC	Analogue to Digital Converter
DAC	Digital to Analogue Converter
ENOB	Effective Number Of Bits
LSB	Least Significant Bit(s)
DSP	Digital Signal Processor
RCS	Radar Cross Section
RMS	Root Mean Square
SFDR	Spurious Free Dynamic Range
SNR	Signal to Noise Ratio
SCR	Signal to Clutter Ratio
DUT	Device Under Test
LTI	Linear Time Invariant
DFT	Discrete Fourier Transform
IDFT	Inverse Discrete Fourier Transform
FEM	Finite Elements Method
SVD	Singular Value Decomposition
OSL	open, short, load
ACF	Auto-Correlation Function
CW	Continuous Wave
FMCW/SFCW	Frequency Modulated/Stepped Frequency CW
HH	Horizontal-Horizontal co-polarisation
VV	Vertical-Vertical co-polarisation
HV	Horizontal-Vertical cross-polarisation
LO	local oscillator
IF	intermediate frequency
MEMS	MicroElectroMechanical Systems
ISM	Industrial, Scientific, and Medical
TIRFM	Total Internal Reflection Fluorescence Microscopy

v_g	group velocity of EM waves
$\bar{c}$	mean propagation velocity for EM waves of different frequencies
$c, c_{\text{air}}, c_{\text{salt}}$	EM wave velocity in dielectric medium (e.g. air/salt rock)
c_0	free space EM wave velocity
ε	permittivity of dielectric medium
ε_r	relative permittivity
μ	permeability of dielectric medium
$x(t), y(t)$	time domain functions/signals
$X(f), Y(f)$	frequency spectra of functions/signals
$\underline{Z}, \underline{Z}_x$	EM wave impedance in dielectric media
T	Transmission amplitude at dielectric boundary
Γ	Reflection coefficient at dielectric boundary
t_p	period duration of periodic time domain signal
$\lambda, \lambda_{\text{air}}, \lambda_{\text{salt}}$	wavelength of EM wave (e.g. air/salt rock)
σ	radar cross section
$\frac{\partial(..)}{\partial t}$	partial derivative with respect to time
d	gap thickness
V	volume of spherical defect
$\mathbf{S}, \mathbf{S}_i$	matrix of complex-valued true S-parameters for a (i^{th}) two-port test object
$\underline{s}_{xy}$	single complex-valued true S-parameter
$\underline{s}_{HH}$	S-parameter representing horizontal co-polarisation
$\underline{s}_{HV}$	S-parameter representing horizontal-vertical cross-polarisation
$\underline{s}_{VV}$	S-parameter representing vertical co-polarisation
$\underline{s}_{VH}$	S-parameter representing vertical-horizontal cross-polarisation
a_{max}, a_{min}	maximum and minimum signal amplitude
P_{max}, P_{min}	maximum and minimum signal power
D	general dynamic range
D_{SG}	ratio between amplitudes of surface- and gap reflection
$SFDR_{td}$	spurious-free dynamic range of time domain impulse responses
B	bandwidth
f_l	lower frequency cut-off
f_u	upper frequency cut-off
b_{rel}	relative bandwidth
B_{-10dB}	UWB bandwidth defined by 10 dB cut-off
$h(t)$	impulse response function of LTI system
$H(f)$	frequency response function (transfer function) of LTI system
$\delta(t)$	Dirac delta function
ψ_{xy}	cross-correlation between signals x and y
ψ_{xx}	auto-correlation of signal x
f_t	FMCW transmit frequency
f_r	FMCW receive frequency
f_d	Doppler frequency

v_{rad}	target velocity, radial component
f_{step}	SFCW frequency step
f_c	master clock frequency
T_0	period duration of master clock
PRF_{MLBS}	pulse repetition frequency of M-Sequence sensor
T_p	period duration of M-Sequence
$f_{s,equiv}$	equivalent time sampling rate
$t_{s,equiv}$	equivalent time sample spacing
f_s	real time sampling rate
T_S	period duration of real sampling rate
$T_x; x = 1..4$	equivalent time sample spacing for interleaved sample sets
$\Delta T_x; x = 1..4$	time sample spacing for equivalent time dense subsampling
$mlbs9(t)$	waveform of ideal 9th order M-Sequence
$uwb(t)$	periodic, idealised up-converted M-Sequence stimulus
ϕ_0	initial phase shift of sine wave
ϕ_s	unknown phase offset of sine wave
t_r	10% to 90% rise time of signal slope
U_{pp}	peak-to-peak amplitude
$\hat{U}$	maximum amplitude
ΔU_{max}	maximum amplitude variation
Δt_{max}	maximum sampling time variation
$\mathrm{e}(t)$	elementary signal of up-converted M-Sequence stimulus
SCR_{samp}	signal-to-clutter ratio caused by sampling time errors
$\mathbf{S}_m$, $\mathbf{S}_{m,i}$	S-parameter matrix of (ith) two-port test object as measured by a sensor
$\mathbf{E}$, $\mathbf{E}_A$, $\mathbf{E}_B$	S-parameter matrices of virtual error network
$\underline{e}_{xy}$	S-parameter representing single error term of virtual error network
$\mathbf{T}$	true T-parameter matrix of a two-port test object
$\mathbf{T}_m$, $\mathbf{T}_{m,i}$	T-parameter matrix of (ith) two-port test object as measured by a sensor
$\mathbf{T}_{err}$, $\mathbf{T}_A$, $\mathbf{T}_B$	T-parameter matrices of virtual error network
$\underline{t}_{err,xy}$, $\underline{t}_{A,xy}$, $\underline{t}_{B,xy}$	T-parameter representing single error term of virtual error network
$\underline{s}_m$, $\underline{s}_{m,i}$	single S-parameter of (ith) one-port test object as measured by a sensor
$\underline{s}$, $\underline{s}_i$	single true S-parameter of (ith) one-port test object
$\mathbf{C}$	calibration matrix containing all data for standards in 3-term correction
$\mathbf{C}_{OSL}$	calibration matrix containing all data for open, short, load standards in 3-term correction
$\underline{s}_{match}$	S-parameter: reflection of a matched standard
$\vec{b}_i; i = 0..3$	directed coaxial EM waves travelling out of a device/network
$\vec{a}_i; i = 0..3$	directed coaxial EM waves travelling into a device/network
$\mathbf{A}$	matrix of T-parameter error coefficients at measurement port A during 8-term correction
$\mathbf{B}$	matrix of T-parameter error coefficients at measurement port B during 8-term correction
$\mathbf{S}_x$	true S-parameter matrix of any two-port test object during 8-term correction
$\mathbf{T}_x$	true T-parameter matrix of any two-port test object

	during 8-term correction
$W(f)$	frequency domain window function
$x_i(t)$	subsequently acquired realisations of measured sensor in time domain
$\bar{x}(t)$	mean sensor data over several realisations
$\text{SCR}_{\text{drift}}$	signal-to-clutter ratio between measured test signal and average amplitude errors caused by drift
$\text{SFDR}_{\text{drift}}$	SFDR relating measured test signal and maximum amplitude error caused by drift
SCR_{rep}	signal-to-clutter ratio between measured test signal and average amplitude errors caused by switch repeatability
SFDR_{rep}	SFDR relating measured test signal and maximum amplitude error caused by switch repeatability
$x_k(t),\, y_k(t),\, z_k(t)$	processed impulse responses in time domain at k$^{\text{th}}$ scanner position in salt mine measurements
ϕ	angle of antenna arm in cylindrical scan (corresponding to counter k)
$xtalk_{\text{ref}}(t)$	reference impulse response of antenna crosstalk/mismatch
$xtalk_{\text{meas}}(t)$	estimate of antenna crosstalk/mismatch obtained from on-site data
$c(\tau)$	cost function for finding optimum delay of reference function
τ_{opt}	optimum delay between reference and estimated crosstalk/mismatch
$surf_k(t)$	estimate of surface reflection waveform at k$^{\text{th}}$ scanner position
α	forgetting factor in exponential filtering
$c_k(\tau, a)$	cost function for finding optimum delay and gain of surface reflection reference for k$^{\text{th}}$ scanner position
$\tau_{\text{opt,k}},\, a_{\text{opt,k}}$	optimum delay and gain of surface reference for k$^{\text{th}}$ scanner position
$tdg(t)$	propagation time dependent gain applied to processed impulse responses for better visualisation
$z_{\text{vis},k}(t)$	fully prepared (for visualisation) impulse responses in time domain at k$^{\text{th}}$ scanner position
t_{surf}	propagation delay of surface reflection in processed impulse responses
$c_{\text{subs}}(\tau, a)$	cost function for finding optimum delay and gain of surface reflection for subsidence analysis
$t_{\text{UWB}}(t)$	UWB test signal used for sampling time optimisation
$c(t)$	processed signal used for determination of cost value in sampling time optimisation
$C_{\text{UWB}}(r_1, r_2, r_3, r_4)$	cost function used for sampling time optimisation
$\mathbf{C}_{\text{full}}(r_2, r_3, r_4)$	matrix of cost function values for discrete variation of three control states
$\mathbf{C}_{2D}(r_i, r_k)$	matrix of cost function value subset for discrete variation of two control states
$\mathcal{F}\{\,\}$	Fourier transform
$\mathcal{F}^{-1}\{\,\}$	inverse Fourier transform
$(\;)^*$	complex conjugate
$[\;]^T$	matrix transpose
$\tilde{r}_i;\, i = 1..4$	discretised phase shifter control states used in modified Nelder-Mead search
$r_{i,\text{init}};\, i = 1..4$	initial control value of i$^{\text{th}}$ phase shifter state

N_{cost}	number of cost function evaluation during optimisation search
m_{init}	initial maximum search margin for variation of phase shifter states
$m_{\text{cur}}, m_{\text{cur,k}}$	current maximum search margin for variation of phase shifter states in k$^{\text{th}}$ iteration
$ld(\ )$	logarithm of base two
$lg(\ )$	logarithm of base 10
$\vec{b}_{i,\mathbf{fw}}; i = 0..3$	directed coaxial EM waves travelling out of a device/network in forward measurement mode
$\vec{a}_{i,\mathbf{fw}}; i = 0..3$	directed coaxial EM waves travelling into a device/network in forward measurement mode
$\vec{b}_{i,\mathbf{bw}}; i = 0..3$	directed coaxial EM waves travelling out of a device/network in backward measurement mode
$\vec{a}_{i,\mathbf{bw}}; i = 0..3$	directed coaxial EM waves travelling into a device/network in backward measurement mode
$\mathbf{E}_i; i = 1..4$	S-parameter sub-matrices of virtual error network (full matrix $\mathbf{E}$)
Z_0	reference EM wave impedance for coaxial calibration (defined by standards, usually $50\ \Omega$)
$\mathbf{T}_i; i = 1..4$	T-parameter sub-matrices of virtual error network (full matrix $\mathbf{T}_{\mathbf{err}}$)
$\underline{t}_i$	T-parameter representing single error term of virtual error network in 16-term formulation
$[\mathbf{0}]$	zero matrix
$\mathbf{T}_{8T}$	sparse T-parameter matrix of virtual error network derived for 8-term correction
$\mathbf{T}_{i,8T}; i = 1..4$	sparse T-parameter sub-matrices of virtual error network derived for 8-term correction

Abstract

This dissertation describes an innovative ultra-wideband (UWB) electromagnetic sensor device based on a pseudo-noise principle developed in the context of non-destructive testing in civil engineering.

Non-destructive testing is becoming a more and more important field for researchers and engineers alike. Besides the vast field of possible applications and testing technologies, a prime and therefore typical topic is the inspection and monitoring of constructions and materials by means of contactless remote sensing techniques.

This work focuses on one example — the assessment of the disaggregation zone in salt rock tunnels. The background and relevance of knowing the state of salt rock layers near a tunnel's surface are explained and simple theoretical considerations for requirements of suitable UWB sensor devices are shown. The most important sensor parameters are a very large measurement bandwidth and a very clean impulse response. The latter parameter translates into the mandatory application of calibration techniques to remove systematic errors of the sensor system itself. This enables detection of weak scattering responses from near-surface disaggregation despite the presence of a strong surface reflection.

According to the mentioned requirements and other side conditions in salt mine environments an UWB sensor principle based on pseudo-noise stimuli — namely M-Sequences — is selected as a starting point for system development. A new transmitter frontend for extending the stimulus bandwidth up to 12 GHz is presented. Furthermore, a technique for increasing the (equivalent) sampling rate while keeping the stable and low-jitter sampling regime of the M-Sequence approach is introduced and its implementation is shown.

Moreover, an automatic calibration unit for full two-port coaxial calibration of the new UWB sensor has been developed. Common calibration techniques from the area of vector network analysers are shortly reviewed and a reasonable algorithm — the 8-term method with an unknown line standard — is selected for the M-Sequence device. The 8-term method is defined in the frequency domain and is adapted for use with time domain devices. Some performance figures and comparison with calibration results from network analysers are discussed to show the effectiveness of the calibration. A spurious-free dynamic range of the time domain impulse responses in excess of 60 dB has been achieved for reflection as well as transmission measurements.

The new UWB sensor was used in various real world measurements in different salt mines throughout Germany. Two measurement examples are described and results from the disaggregation zone of a very old and a freshly cut tunnel will be presented. Measurement setup and data processing are discussed and finally some conclusions for future work on this topic are drawn.

Abstrakt

Die vorliegende Dissertation beschreibt einen innovativen ultra-breitband (UWB) elektro-magnetischen Sensor basierend auf einem Pseudo-Rauschverfahren. Der Sensor wurde für zerstörungsfreies Testen in zivilen Anwendungen entwickelt.

Zerstörungsfreies Testen entwickelt sich zu einem immer wichtiger werdenden Bereich in Forschung und Entwicklung. Neben unzähligen weiteren Anwendungen und Technologien, besteht ein primäres Aufgabenfeld in der Überwachung und Untersuchung von Bauwerken und Baumaterialien durch berührungslose Messung aus der Ferne.

Diese Arbeit konzentriert sich auf das Beispiel der Auflockerungszone im Salzgestein. Der Hintergrund und die Notwendigkeit, den Zustand der oberflächennahen Salzschichten in Salzminen kennen zu müssen, werden beleuchtet und die Messaufgabe anhand einfacher theoretischer Überlegungen beschrieben. Daraus werden die Anforderungen für geeignete UWB Sensoren abgeleitet. Die wichtigsten Eigenschaften sind eine sehr hohe Messbandbreite sowie eine sehr saubere Systemimpulsantwort frei von systematischen Gerätefehlern. Beide Eigenschaften sind notwendig, um die schwachen Rückstreuungen der Auflockerungen trotz der unvermeidlichen starken Oberflächenreflexion detektieren zu können. Da systematische Fehler bei UWB Geräten technisch nicht von vorne herein komplett vermeidbar sind, muss der Sensor eine Gerätekalibrierung erlauben, um solche Fehler möglichst gut zu unterdrücken.

Aufgrund der genannten Anforderungen und den Nebenbedingungen der Messumgebung unter Tage, wurde aus den verschiedenen UWB-Technologien ein Prinzip ausgewählt, welches pseudozufällige Maximalfolgen als Anregungssignal benutzt. Das M-Sequenzkonzept dient als Ausgangpunkt für zahlreiche Weiterentwicklungen. Ein neues Sendemodul erweitert dabei die Messbandbreite auf 12 GHz. Die äquivalente Abtastrate wird um den Faktor vier auf 36 GHz erhöht, ohne den geringen Abtastjitter des ursprünglichen Konzepts zu vergrössern.

Weiterhin wird die Umsetzung eines Zweitormesskopfes zur Erfassung von S-Parametern sowie einer automatische Kalibriereinheit beschrieben. Etablierte Kalibrierverfahren aus dem Bereich der Netzwerkanalyse werden kurz rekapituliert und die Adaption des 8-Term Verfahrens mit unbekanntem Transmissionsnormal für das M-Sequenzsystem beschrieben. Dabei werden Kennwerte vorgeschlagen, die dem Bediener unter Tage einfach erlauben, die Kalibrierqualität einzuschätzen und Hinweise auf mögliche Gerätefehler oder andere

Probleme zu bekommen. Die Kalibriergenauigkeit des neuen Sensors im Labor wird mit der eines Netzwerkanalysators verglichen. Beide Geräte erreichen eine störungsfreie Dynamik von mehr als 60 dB in den Systemimpulsantworten für Reflexion und Transmission.

Der neu entwickelte UWB Sensor wurde in zahlreichen Messungen in Salzminen in Deutschland getestet. Zwei Messbeispiele werden vorgestellt — ein sehr alter, kreisrunder Tunnel sowie ein ovaler Tunnelstumpf, welcher kurz vor den Messungen erst aufgefahren wurde. Messaufbauten und Datenverarbeitung werden beschrieben. Schließlich werden Schlussfolgerungen und Vorschläge für zukünftige Arbeiten mit dem neuen M-Sequenzsensor sowie der Messung von Auflockerungen im Salzgestein diskutiert.

Stichworte:

- Ultra-breitband M-Sequenz Sensor

- Dichte Unterabtastung

- Koaxiale Kalibrierung für Zeitbereichssensoren

- Zerstörungsfreies Testen für zivile Anwendungen

- Auflockerungszone im Salzgestein

1. Introduction to non-destructive testing

Driven by today's amazing speed of technical and scientific developments, researchers and engineers alike have to face new challenges. While the classical task has always been to *answer a question* or *to find any solution for a problem*, now other aspects such as economical feasibility, time to market, and environmental impact are highly involved and must be taken into account. As a consequence, principles such as modularity and flexibility to be adjusted to different specific tasks are found in more and more technical systems. Furthermore, since production technologies and computing power have increased considerably in the last decades, many solutions involve some kind of digital control or regulation mechanism. In fact, modern technologies enable very complex constructions which have not been possible before. A key factor for seamless and safe operation of complex machines or constructions is the ability to monitor components or processes throughout deployment. This could be constant monitoring or assessment at regular and frequent maintenance intervals often implemented using various kinds of modern sensors with computer-aided processing and interpretation of measured data. In this regard, measurement impact on the system's operation and overall monitoring costs are often critical points for sensors and the systems they support. Consequently it is no surprise, that **n**on-**d**estructive **t**esting (NDT) along with the development of new sensor technologies have become vital and fast developing topics in our times. This dissertation contributes to NDT by considering one example application and presenting a new ultra-wideband (UWB) sensor based on the RADAR[1] principle.

This chapter will start with a short introduction to the field of NDT and some of its different applications and sensor solutions. The background of the work presented here — the assessment of the disaggregation zone in salt mine tunnels — will be described. The possibility to use radar sensors for this task will be explained and a short overview of the state of the art in salt mine radar will be given.

In chapter 2, some simple thoughts and simulation calculations will be shown, providing key points for the development of a suitable sensor device.

---

[1] The author has found several pronunciations for this abbreviation in literature. This may be attributed to the versatile usage of the technology. However, the origin of RADAR is military use and the pronunciation should be **RA**dio **D**etection **A**nd **R**anging.

With these goals in mind, chapter 3 will introduce the newly developed UWB sensor. The chapter starts with a summary of current UWB sensor principles and selects the most suitable one — a pseudo-noise principle based on M-Sequences — for the intended task. The basic system is then reviewed and conclusions for necessary enhancements are drawn. In the last part of this chapter, the system design of the new sensor is shown and its different modules are described in more detail.

The following chapters 4 and 5 present the major technical contributions of this dissertation to the state of the art in UWB sensor technology. Chapter 4 gives a detailed description of the software-defined dense equivalent time sampling employed in the device. Starting again from simple theoretical considerations and simulations for the sampling of UWB pseudo-noise signals, an easy implementation and its operation are shown. As the second technical focus, chapter 5 deals with the removal of systematic errors by means of coaxial calibration. The used methods originate in the field of vector network analysers and will be shortly reviewed at the beginning. The adoption to the M-Sequence device is then explained. Implementation issues will be discussed and some possibilities for the assessment and supervision of calibration quality will be presented. The chapter is closed with a performance comparison of calibrated measurements from the M-Sequence device and a vector network analyser.

After the technical parts, chapter 6 leads back to the application of measurements in salt mine tunnels. Real-world measurements will be shown along with a description of measurement setups and the data processing involved. One example deals with the disaggregation zone of a very old salt tunnel in the mine of Bernburg, Germany. The results are discussed and performance is compared to another NDT sensor principle — namely ultra-sound sonar sensors. The second example is of particular interest since it presents measurements from a freshly cut tunnel where the beginning of the formation of a disaggregation zone can be observed.

The final chapter 7 draws some conclusions about the new UWB sensor system and its usefulness for the salt mine application. Further system development and other possible tasks for such a sensor device will also be mentioned. For now let us start with a short description of non-destructive testing in civil engineering as well as the background and motivation for the work presented in this dissertation.

1.1. Non-destructive testing — an emerging research field with many applications

The term non-destructive testing is pretty self-explaining at first glance. NDT summarises testing methodologies and sensors which acquire information without destroying or harm-

ing the object under test. Some realisations employ even non-contact measurements, i.e. the sensor does not have any physical contact to the investigated object. Interestingly, it is not a new field of technology and can be found in many modern systems or devices. NDT is not very present in public media because it often works in the background of a system or process. Examples range from extremely simple proximity sensors controlling on a guiding light at a door step going to very complex systems like impedance spectroscopy sensors used to identify materials or check material properties. Other well-known examples for NDT are the application of ultra-sound measurements in medicine or application of electro-magnetic waves in magnetic resonance tomography (MRT). Recently, the use of harmless microwaves in the context of breast cancer detection is being investigated by different groups [1–3].

A common point of all mentioned applications is that the sensors allow to analyse the inside of the test objects, i.e. providing information about the otherwise hidden inner structure. Imaging of an object's inside is a prime and particular task for NDT sensors. The inner structure of materials is also of major interest in other areas — mechanical engineering and architecture. In this context the term non-destructive testing in civil engineering (NDTCE) is commonly used. For the assessment of constructions like bridges, large houses, or streets integrity of the material is a main concern in order to avoid or predict failures or breakdowns.

In the case of buildings, usually sonar measurements, seismic sensors, or vibration sensors are used. The devices might already be included at the time of creation to enable long-term observation. Given the large number of new constructions nowadays — just to mention new sky scrapers and bridges spanning ever-increasing distances — and taking into account that many older facilities require repeated observation to guarantee their safety, there is an urgent need for cost-effective, fast, and easy-to-apply NDT solutions.

Besides sensors using mechanical waves there exists another important research field which partly employs NDT — ground penetrating radar (GPR)[2]. As the abbreviation indicates, GPR sensors are used to assess structures in the ground for various reasons. Applications are again manifold, starting from the use in humanitarian demining [4–6] for detection of anti-personal plastic mines, over managing ground water pump facilities [7], ranging to archaeological or exploration surveys like in [8,9].

These few applications already show the variety of topics and importance of NDT. Like in the mentioned cases, wave-based sensors are often used. This includes principles with mechanical as well as electromagnetic waves and implies an indirect measurement, i.e. the wanted information must be obtained through analysis of the recorded responses from test objects. This is called solving an inverse problem and emphasises another

---

[2]Some GPR sensors are based on borehole antennas which require drilling of holes. Such systems may not be counted as NDT solutions. However, other GPR devices use antennas moved along or above the ground and are therefore non-destructive.

aspect — data processing is of particular importance for NDT methods and should be considered when talking about developments in this area. Data processing is an integral part of the whole sensor and greatly influences the functionality and performance of NDT systems. Popular examples of solutions to inverse problems are migration algorithms like in [10] or [11] which originated from the field of seismics and are nowadays also applied for radar imaging and GPR [12–14]. Tomography is another well known example of imaging via inverse problems. Depending on the amount of data to be processed, such algorithms demand a lot of memory and computational power which is recently becoming more and more available even in small personal computer devices. It is the author's believe that even though many NDT technologies might have been existing for many years, it is only today that a widespread deployment is being enabled through system integration (smaller and energy-efficient devices), advances in fabrication technology, and digital data processing capabilities.

In this work, the development of one UWB sensor for NDT in the context of GPR will be presented. It makes use of some of the aforementioned advancements in technology and can be seen as a prototype or intermediate step towards a compact, fully integrated NDT sensor solution. Before describing the technical details, the research will be motivated by the example application described in the following section.

1.2. A challenging task — inspection of the disaggregation zone in salt mines

Ground penetrating radar and non-destructive testing in general can not only be applied to constructions above ground. In fact, integrity checking of underground tunnels in any kind of mine is a major security measure. By their nature, such tests aim at looking inside the materials surrounding the tunnels and other facilities. Underground mining activities have been around for hundreds of years and therefore different older methods exist alongside modern concepts such as GPR. Important classical methods include non-destructive and destructive testing as well. An obvious possibility is the constant supervision of construction geometries, e.g. recording changes and the rate of change in tunnel height might indicate an immanent failure. A destructive example involves drilling deep holes in the sides and ceilings of tunnels and using a hook mounted on a long thread to find gaps and cracks in the structures along the borehole [15]. This method can provide punctual information on the creation of near-surface failure cracks and how they grow over time. These simple methods are easy to apply, but demand a lot of practical experience and knowledge of the geological conditions when interpreting the gathered data. Furthermore, the punctual nature of such measurements is a disadvantage because there is no guarantee that all important developments inside the geological formations are observed.

Especially in the case of salt mines there are also other reasons besides security for looking into the salt rock. One task is the investigation of material layers in a larger scale to aid the daily mining activities, i.e. find the best directions in which existing tunnels or mining repositories should be expanded. Another example is not as obvious but becoming more and more important nowadays. Salt mines in Germany [16–18] have been run for many decades now and therefore vast underground networks and large voids exist. It makes sense to think of a second use of these constructions as storage areas [19–22]. A lot of research — see [23, 24] for example — has been put into salt mines in the last decades because salt rock has some properties making it especially attractive for long-term storage of problematic waste, e.g. nuclear or other highly toxic waste. One important aspect when considering salt rock for the storage of such materials is the ability to compact or heal itself over the years after structural damages such as cracks occurred [25]. Reasons for damages could be geological processes of the surroundings of a mine or problems created by mining activities themselves. Self-healing helps to prevent leakage of problematic substances on the long run even though geological stability cannot be exactly predicted or guaranteed for hundreds or even thousands of years. Another advantage of salt mines is the large available storage capacity. Given the amount of nuclear waste already waiting for final disposal in the intermediate storage facilities above ground, finding feasible and safe solutions has been and will be a hot topic for years [26–29].

One current problem is that the studies of long-term stability in salt mines have not yet come to final conclusions [30] [31]. Adding to that, another very important aspect is still undergoing extensive research as well. Not only must the storage areas themselves remain sealed for a very long time, but also the supply tunnels through which the waste is transported must be closed and have to stay leak-free for the same amount of time. Modern materials and complex building principles [32, 33] seem to provide a solution for such sealing constructions, even though there is also no general answer yet. Some critical points are the secure connection of the constructions to the salt rock and the compactness of the surrounding salt rock layers itself. When a tunnel is cut, it is known that the near-surface layers are distorted and form a so-called disaggregation zone [34]. This basically means that the salt rock near the surface looses its compactness through the formation of small cracks and damages which create potential leakage paths for gases or liquids. More details about the properties of this disaggregation zone are given in the following section 1.3. When planning a sealing construction for a storage area with problematic waste, the disaggregation zone must be carefully considered since it may render any sealing effort useless and therefore limit the long-term security of the whole facility. Of course, larger cracks or distortions in the surroundings of such a sealing construction must be avoided, too, but it is particularly challenging to assess the state and extension of the disaggregation zone to find a suitable tunnel section where the rock is still compact enough. The reason for that is simply the very small size of the distortions forming the

disaggregation zone. Current GPR systems used in salt mines do not detect cracks of sub-cm or even sub-mm size. For an overview about current mine radar systems please refer to section 1.4.

Other established testing methods fall short in different aspects. A long-known example are mechanical permeability measurements [35] which can provide integral information about the compactness of the salt rock in a larger section of a tunnel. These measurements usually involve the drilling of boreholes (and are therefore destructive or at least damaging methods). A gas or liquid is then pressed into the holes on one side of the investigated section and corresponding sensors are deployed in the boreholes on the other end. The amount of gas or liquid reaching the sensors indicates the compactness of the salt rock between the boreholes and potential high-leakage paths can be recognised. Permeability measurements are able to indirectly detect the small defects if they lead to an increase of gas/liquid throughput. However, besides needing the boreholes, application of this method to large networks of tunnels is elaborate, expensive, and rather slow.

In general, if structural defects or the disaggregation of near-surface salt rock layers are of concern, techniques causing damage are not desirable. That is why, non-destructive testing methods are investigated and further developed nowadays. Wave-based sensors employing the sonar or radar principle are possible candidates because they are also used for testing material integrity of constructions above ground. This dissertation deals with the latter approach and the design of an ultra-wideband radar sensor for the assessment of the disaggregation zone in salt rock. The next section provides a little more detail about this zone and discusses how NDT sensor technologies could be used.

1.3. Properties of the disaggregation zone in salt rock and NDT sensors

The disaggregation zone can be comprised of different kinds of defects leading to less compact salt rock layers. It may look very different from case to case, but some basic similarities can be identified. First of all, major causes for distortions in the rock's structure are the same. When a tunnel is cut, the surrounding bedrock and other geological layers put pressure on the void. Depending on the mine's depth under ground, the actual shape of the tunnel, and material properties of the surroundings a certain force distribution results. These forces lead to cracks of different sizes. Another source for cracks are vibrations or shocks, which can have many causes in a salt mine. For example, heavy machinery passing through the tunnel will lead to strong vibration and even far-away activities will lead to shock waves when explosives are used to expand the mine.

The disaggregation zone therefore also depends on the usage pattern and consequently develops over life time of the tunnel. A third common aspect is that it usually only expands up to about one metre underneath the surface [36] limiting the necessary range of a possible sensor to short distances. The self-healing tendency of the salt material counteracts the disaggregation and so over time the distorted zone may stabilise [25]. If pressure on a tunnel is very high or the tunnel's shape is very wide, the salt rock may not be able to fully carry the near-surface layers by itself and over time large distortions will appear. Such large cracks are considered a security risk in underground mines and even though they might be part of the disaggregation zone they are not our prime target in this investigation. It is rather the formation of micro cracks in the crystalline structure of salt. These tiny defects can occur everywhere in near-surface layers and might be individual distortions at first. Since force distribution usually doesn't change much on such a small scale, neighbouring defects will have similar directions and might connect over time growing the distortion size in a local scale. Eventually, different types of larger defects will form inside the rock, e.g. thin local gaps or small volume voids. Starting with sub-millimetre sizes, some will become larger to the millimetre range or even beyond (finally leading to security-relevant macroscopic cracks). But even in their millimetre state they create potential leakage paths for gases or liquids and must be detected prior to building sealing constructions. It can be expected that gap-like disaggregation will form along major force paths while volume defects may show up rather randomly distributed over the whole circumference of a tunnel [36].

From a sensor's point of view, not only the expected small size of the defects is a major challenge, but also the fact that a lot of (possibly very long) tunnel sections need to be inspected with a very high resolution. A feasible measurement system consequently needs to be precise, easy to deploy, and also reasonably fast. When starting the research project on non-destructive methods for inspection of the disaggregation zone, discussion with other experts lead to the idea of a two-stage solution. An ultra-wideband sensor based on electromagnetic waves (as described in this dissertation) can be coupled through the air interface and can therefore be used for fast scanning at limited sensitivity. This enables pre-selection of tunnel sections with overall low distortion in the disaggregation zone. In a second stage, an ultra-sound sensor could be used to finally confirm expansion of the zone only in the selected sections. Ultra-sound sensors usually need to be attached to the surface which yields much lower scanning speed but has advantages in terms of sensitivity for very small distortions. The approach using a novel ultra-sound sonar sensor was investigated by fellow researchers from Fraunhofer Institute for Non-Destructive Testing in Dresden (Fraunhofer IZPF Dresden) in a partner project. As it turned out, both sensor principles show specific advantages and disadvantages almost as expected from theory. There will be a short discussion on how the results support each other towards the end of this dissertation in chapter 6.

Using radar in salt mines is not new in general, but due to the special nature and small size of the near-surface defects, there are a number of important features a suitable sensors system must have. Before examining these prime requirements in more detail, let us take a quick look at the state of the art in GPR and salt mine radar systems and how they are used in daily routine.

1.4. Current radar sensors in salt mines and GPR

The first radar devices in salt mines were used back in the early 1970[s] [37] and their deployment has been increasing ever since. In the beginning, a main field of application was the investigation of how the layers of different types of salt and surrounding materials further evolve inside the rock. The knowledge of layer horizons is useful for deciding if and in which direction the mine expansion should proceed, e.g. to avoid instabilities or cutting into liquid repositories which can be dangerous in underground mines. For such a task, usually borehole radar has been used in a rather low frequency range and with limited bandwidth [38]. These systems are feasible, since only larger structures are of interest and the sensor must look from some ten up to a few 100 m into the material to gather the wanted information. The basis of common borehole radars is impulse technology (details of radar technologies are discussed in section 3.1) and a some manufacturers have specialised in the field of GPR. To name only a few, MALA Geoscience Corp. [39], GSSI Inc. [40], PENETRADAR Corp. [41], and Geozondas Ltd. [42] are typical examples. Operating frequencies of borehole sensors usually extend an octave around a carrier frequency in the lower MHz range, e.g. 25 MHz, 100 MHz, or 250 MHz. Besides the need for a hole, these frequencies are infeasible for high-resolution short-range inspection. Over the recent years, researchers have been using network analysers in combination with borehole antennas to extend frequency range beyond 1 GHz and even made polarimetric measurements [38].

When commercial radar technologies with larger bandwidths and surface-coupling antennas became available, smaller distortions or layer boundaries could be recognised and radar measurements have been introduced as an additional tool for security related checks. The correct interpretation of radar images for this task requires a lot of specific experience and geological knowledge that has been gathered over the years. Today, radar inspections have become part of regular security concepts in modern salt mines [43].

During our own research project, several measurement campaigns were carried out in Germany. The first few occasions were used to get familiar with conditions and test selected measurement areas with established mine radar systems. This was done by the respective mining personal and our project partner BoRaTec GmbH [44]. The radar systems came from the above listed manufacturers and provided a good view onto the

state of the art in practical salt mine sensors (apart from borehole systems which were not used during our campaigns).

The MALA ProEx Series [45] of radars can be used as a general example as it features typical frequency ranges including the highest bandwidths currently available for these sensors. Antennas are advertised from as low as 25 MHz for rough terrain and soil up to 2.3 GHz for short-range inspection. The latter option can be regarded as an UWB system with more than 500 MHz bandwidth around the carrier and was also employed by BoRaTec. The ProEx radars as well as the RAMAC/GPR brand (also manufactured by MALA) use the concept of combining antennas and pulse transmitters into modules coupled to an operator unit responsible for triggering and acquisition of data. Data is processed by commercial software like ReflexW [46]. Pulse repetition rates of up to several 10 kHz are achievable enabling very fast scanning speeds (e.g. for scanning while driving along a street or tunnel in a car). Similar offerings can be found from GSSI, who sell systems with air-coupled antennas from below 100 MHz up to 2.6 GHz [47]. Their current GPR data acquisition unit SIR-20 [48] even allows pulse repetitions up to 500 kHz for extremely fast scanning applications. Systems staying below 2 GHz centre frequency from both manufacturers had been used by mining companies during our measurement campaigns.

For applications in research and development requiring even more bandwidth, UWB systems from Geozondas are available with pulse stimulus generators covering a 10 dB cut-off bandwidth up to 18 GHz, e.g. [49]. Repetition rates are up to 1 MHz. Timing uncertainty (jitter) is in the order of 2.5 ps for this extremely wideband transmitter. Sampling units with corresponding input bandwidth and equivalent-time sampling are also available, e.g. [50]. It features an equivalent-time resolution of 2 ps and allows to set a number of averages to improve signal-to-noise ratio at the expense of an increased measurement time. Sampling timing has peak jitter errors in the order of 10 ps and 2.5 ps RMS jitter. These components have been used in a recent study of using GPR to detect people buried under building rubble by their respiratory movement or heart beat during rescue operations [51]. The group used different ultra-wideband devices but did not exceed frequencies of 2.5 GHz due to propagation conditions in the rubble material. The author lists different GPR sensors used for person detection by respiration, but non of the mentioned pulse-based sensors exceeds 2 GHz operational frequency either.

If very high dynamic range and measurement accuracy is of concern, the usual sensors of choice for researchers have been heterodyne vector network analysers [52–54] to date. They can be combined with borehole or air-coupled antennas and are very flexible with regards to frequency band (exceeding 18 GHz if needed). These devices are very bulky, sensitive, and are therefore rarely found outside a laboratory. Recently, less flexible hand held analysers for field use have appeared covering the frequency band up to 6 GHz [55]. Besides the limited ruggedness, low measurement speed is a major downside of network

analysers and consequently they are not established for use in salt mines so far.

The EMR Lab has contributed to the GPR sensor field with systems based on pseudo-noise stimuli originally used for humanitarian demining [4]. The systems provide UWB operation up to 4 GHz in the basic configuration. Some advancements allowed extending the operational band to arbitrary frequencies with bandwidths of 7 GHz and more [56–58]. These sensors were not widely commercially available until recently and have also not been used in salt mines before our disaggregation investigations. More technical details of ultra-wideband sensors — including impulse radars, network analysers, and pseudo-noise sensors — are given in section 3.1.

It was shown in this section, that a certain level of experience and daily routine of using radar sensors and NDT already exists for salt mines. However, not all available GPR options are being used by the companies leaving room for further research and development. Before selecting the best sensor from existing devices or a possible new system design for the investigation of salt rock disaggregation, it is necessary to examine important requirements of the task and provide some design goals for such a sensor. These requirements are analysed in the next chapter.

2. Theoretical analysis and design goals for a new sensor system

There are a number of different aspects to be considered when choosing or designing a sensor for measuring disaggregation in salt rock. It has already been motivated, that non-destructive testing is mandatory in this case and that radar sensors could be used as a potentially time-efficient tool. Additionally, the following aspects should be addressed:

- Propagation conditions within salt rock, e.g. propagation velocity, frequency-dependent attenuation, etc.
- Scattering behaviour of disaggregation in salt rock
  - Preferred frequency range?
  - Measurement bandwidth?
  - Necessary dynamic range?
  - Preferred polarisation?
- Mode of operation, i.e. what kind of interaction between electromagnetic waves and near-surface salt rock could be exploited
- Working conditions in salt mines (e.g. environmental conditions, ruggedness, etc.)

In the following sections, some general conclusions and design goals for these issues will be derived. It should be pointed out, that the presented analysis does not aim at an accurate and complete discussion of the mentioned aspects. Rather, an overall picture of the main requirements shall be developed.

2.1. Propagation conditions for electromagnetic waves within salt rock

When designing a radar sensor, a feasible frequency range for its operation depends on two major factors. On one hand it must be assessed, which frequencies can propagate in the medium anyway and what physical effects need to be considered. On the other hand,

wave attenuation must be investigated to find a frequency band, where damping of the stimulus energy is feasibly low while the waves travels through the disaggregation zone and back to the sensor.

There are usually different minerals in salt mines, of course. Not all of them are considered good hosts for problematic waste [24], so the discussion can be limited to commonly known salt — *NaCl*. In section 1.4 it was mentioned, that some borehole radar systems working in the lower 10 MHz range are employed to look several ten up to a few hundred metres into the rock. This indicates that at least for low frequencies penetration by electromagnetic waves works very well and attenuation is low, too. It is known [59–61] for lower microwave frequencies, that salt does not have much conductivity (if not dissolved in a aqueous solution), its magnetic permeability equals that of free space, and that it behaves isotropic (since wavelengths are much longer than the crystalline structures). This is summarised by the following assumptions.

$$\mu_{\mathrm{NaCl}} = \mu_0 \forall f \tag{2.1}$$

$$\sigma_{\mathrm{NaCl}} = 0 \forall f \tag{2.2}$$

However, a thorough investigation about the propagation properties of salt rock above 3 GHz could not be found in literature. What about microwave frequencies typically used in common radar sensors? This includes the lower GHz range up to X-band (about 8-12 GHz, [62]), the band around 24 GHz [63, 64], and the recently more and more investigated range above 60 GHz [65, 66]. To get an estimate about dielectric permittivity and wave attenuation for these frequencies, a rather big salt block was measured above ground. The block had the dimensions of 1.5 m by 1.5 m by 1 m and was provided by the Fraunhofer Institute IZFP in Dresden. The measurements were done in a cooperation of the EMR Lab and the colleagues from the IZFP. It was possible to collect useful information with this block, but the validity for salt rock in a mine will be somewhat limited because of differences in environmental conditions (most notably increased air humidity above ground). The measurements have been conducted with a ZVK vector network analyser (VNA) from Rohde&Schwarz. This device can cover frequencies from 10 MHz up to 40 GHz. Two different types of UWB horn antennas have been used — double ridged horn antennas working from about 500 MHz to 15 GHz and wave guide K-band horns for the frequency range between 20 GHz and 40 GHz. The analyser was calibrated for transmission measurements at the cable ends connecting to the antennas. Figure 2.1 shows the salt block and explains the different measurement setups. Investigations around 60 GHz could not be done due to the lack of corresponding equipment.

In both cases, the transmitting and receiving antenna were located at opposite sides of the block. Measurements have been conducted with the antennas directly in the centre over the stud hole (i.e. propagation through air and salt) and also with the antennas
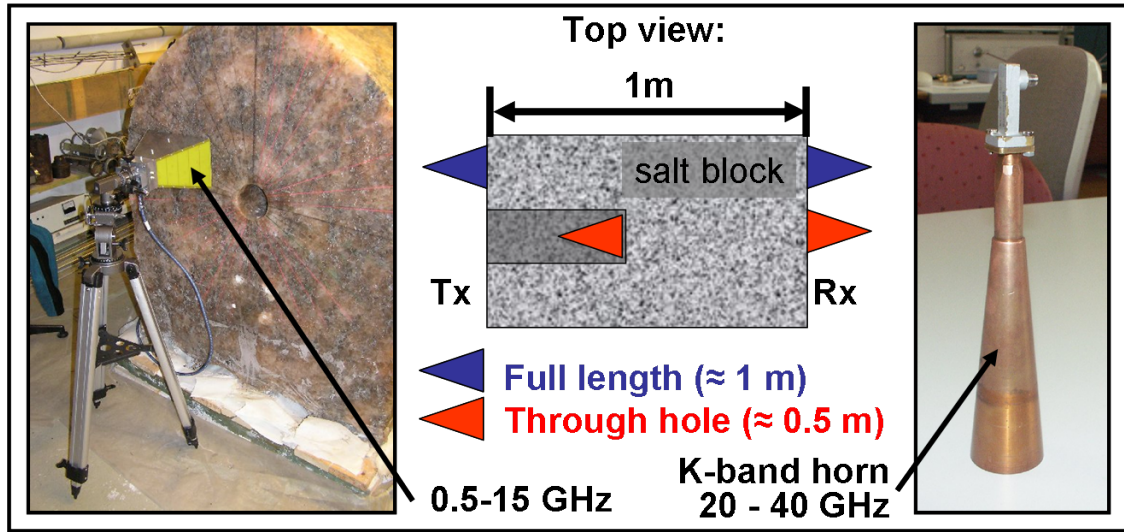
Fig. 2.1.: Salt block and measurement setup for investigation of propagation conditions up to 40 GHz

slightly displaced away from the centre (full transmission through salt). For comparison of wave attenuation, a reference measurement in air with 1 m distance between the antennas has been recorded as well. Processing and analysis of the gathered data was rather simple. Even though everything could be done directly in frequency domain using the measured frequency response function (FRF), some information is easier observed using the time domain impulse response function (IRF). The IRF is given by the inverse Fourier transform of the FRF. One can choose to create an analytic complex-valued IRF by neglecting the negative frequencies or one could reconstruct a real-valued IRF by assuming the negative part of the FRF to be complex conjugate with respect to the measured positive part.

The latter option enables a more intuitive interpretation of the resulting time domain data and was used in this case. In the IRF, transmission through the salt block is indicated by an impulse appearing after the propagation delay. The delay includes not only propagation through the salt block, but also the delay introduced by the antennas themselves (other delays have been removed by calibrating the VNA). If the total delays from salt and the reference measurement in air are compared, the group velocity of the covered frequency range can be calculated, since the length of the salt block is known to be 1 m. The group velocity v_g represents the propagation speed of all the frequency components of the FRF and can be interpreted as an average phase velocity $\bar{c}$ in the covered frequency range. This only provides a good description of propagation conditions, if dispersion is low. Looking at the resulting IRFs depicted in the upper part of figure 2.2, one can conclude that such an assumption is approximately valid. A more detailed analysis of the dispersion in the medium could be done through impedance spectroscopy, but average data is sufficient for a basic analysis of propagation conditions. From the average phase

velocity, the average relative permittivity ε_r of salt rock in the lower GHz range can be calculated according to equation 2.3 and amounts to $\varepsilon_r \approx 6.0$.

$$\overline{c} = \frac{1}{\sqrt{\mu\varepsilon}} = \frac{1}{\sqrt{\mu_0\varepsilon_0\varepsilon_r}} \tag{2.3}$$

It is interesting to note, that comparing the amplitude of transmission results over and besides the stud hole indicates almost no additional attenuation due to propagation in salt rock. This result is important because it means that even frequencies beyond 10 GHz can be used to completely penetrate the disaggregation zone without suffering significant losses other than those of expansion in space.

The measurements with K-band horns were done to test the feasibility of using frequencies beyond 20 GHz. The measured data has been analysed in the same simple manner as described above. As it turned out, average permittivity is somewhat higher than in the previous case: $\varepsilon_r \approx 6.4$. Furthermore, additional attenuation caused by the medium becomes evident. Compared to propagation through air, the K-band IRF amplitude was 20 dB down. The measured spectra through the full and half block are shown in the lower part of figure 2.2. An average attenuation of 20 dB/m is still rather small compared to many other dielectric materials found in GPR applications given the high frequency range of 20 GHz to 40 GHz. If the maximum expansion of the disaggregation zone is assumed to be 1 m, the results indicate that this frequency band could still be used for its investigation. However, the larger attenuation compared to the band below 20 GHz might increase the dynamic range requirements for the sensor system. Even though it could not be measured, the results up to 40 GHz also indicate that the usage of the higher operational band around 60 GHz will suffer even stronger attenuation and might therefore not be very useful in this case. At this point it can be concluded, that the band below 20 GHz can potentially be used by the new sensor. Before formulating a corresponding design goal, the next section tries to analyse what frequencies and bandwidth values are desirable for the intended application.

2.2. Bandwidth and frequency

Important properties of any sensor using electromagnetic waves are frequency range and bandwidth. Besides laboratory devices with a flexible configuration, most equipment is tailored for a specific application. There were no previous practical experiences for measurement of salt rock disaggregation. Therefore, some theoretical analysis was useful to decide the frequency parameters. As described in section 1.3, the nature of disaggregation can be quite different and its exact distribution is usually unknown. That is why the two most common forms shall be considered by means of simplified models.
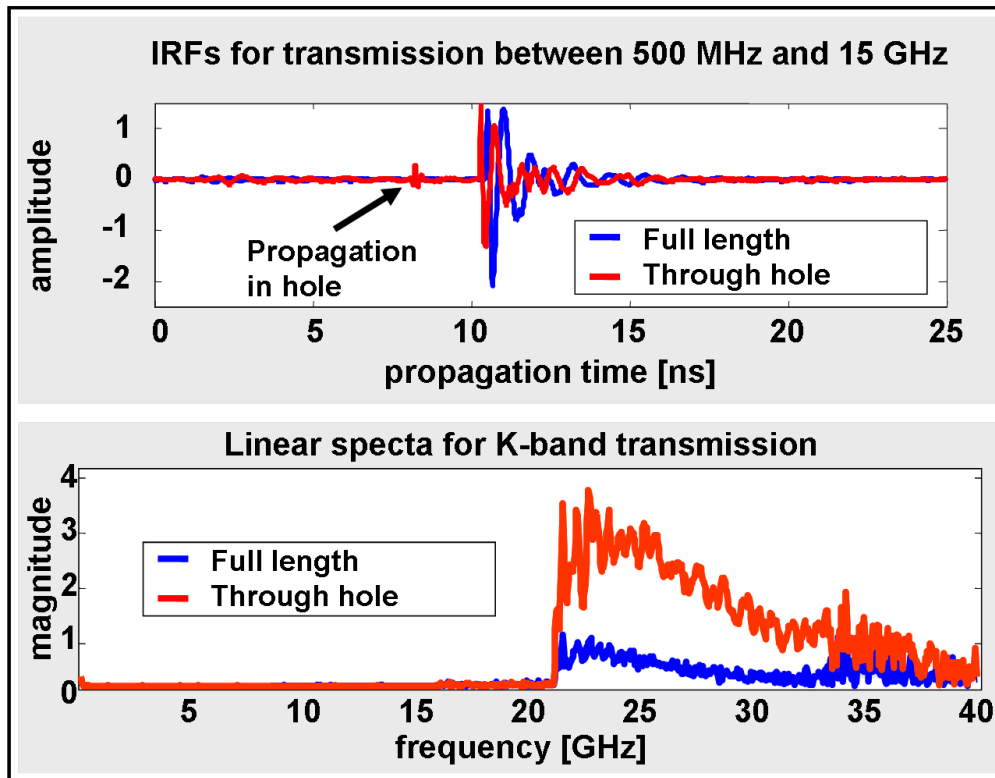
Fig. 2.2.: Measurement results for transmission through salt rock with UWB stimuli from 500 MHz to 40 GHz

2.2.1. Scattering of thin gaps or layers

Detection of larger cracks and gaps is one of the security tasks performed by salt mine radars. In such cases gap thicknesses in the cm- or dm-range are of interest. Smaller and thinner gaps of sub-cm or even sub-mm thickness, which may be part of the disaggregation zone, are usually no security issue, but they could provide a leakage path for liquids and gases. To analyse the wave interaction with thin gaps inside salt rock, the following simplifying assumptions have been made:

- the gap is surrounded by homogeneous salt rock and is unfilled (vacuum)

- the boundaries are plane

- the gap's extension is large compared to the section illuminated by the stimulus [1]

- the stimulus wave is a plane wave (i.e. in the far-field of the transmitting antenna) with perpendicular incidence to the gap

---

[1]This assumption is true for infinitely large gaps, of course. In real measurements, however, one has to keep the area of wave interaction limited, e.g. by using directional antennas. A further discussion can be found in section 2.3.

Let us define the waveform of the stimulus to be the arbitrary function $x(t)$. The backscattered waveform shall be $y(t)$. Please note that location dependencies of both waveforms can be omitted for the following analysis due to the assumptions stated above. The variable t represents propagation time. At each of the gap's sides, dielectric boundaries exist. The stimulus wave is partly reflected at the first boundary, while the remainder travels into the gap. When the 2nd boundary is reached, another reflection occurs and again a part of the wave is transmitted behind the gap. The wave reflected at the first boundary directly becomes part of $y(t)$, while the reflected wave from the other side travels back through the gap and has to face the first boundary again before also becoming part of the backscattered wave. In fact, each interaction of a wave with any of the two boundaries leads to splitting of the total power into a reflected and transmitted component. That is why, multiple reflections occur and a part of the wave inside the gap bounces between the two boundaries. However, each time a fraction of wave energy travels out of the gap either in the direction of the receiver or away further into the salt rock behind the gap. Thus the amplitudes of the multiple reflection components vanish fast and can be neglected for a simple analysis. The described first-order phenomena are illustrated in figure 2.3 showing the discussed signal components. The gap thickness is denoted as d in the picture.
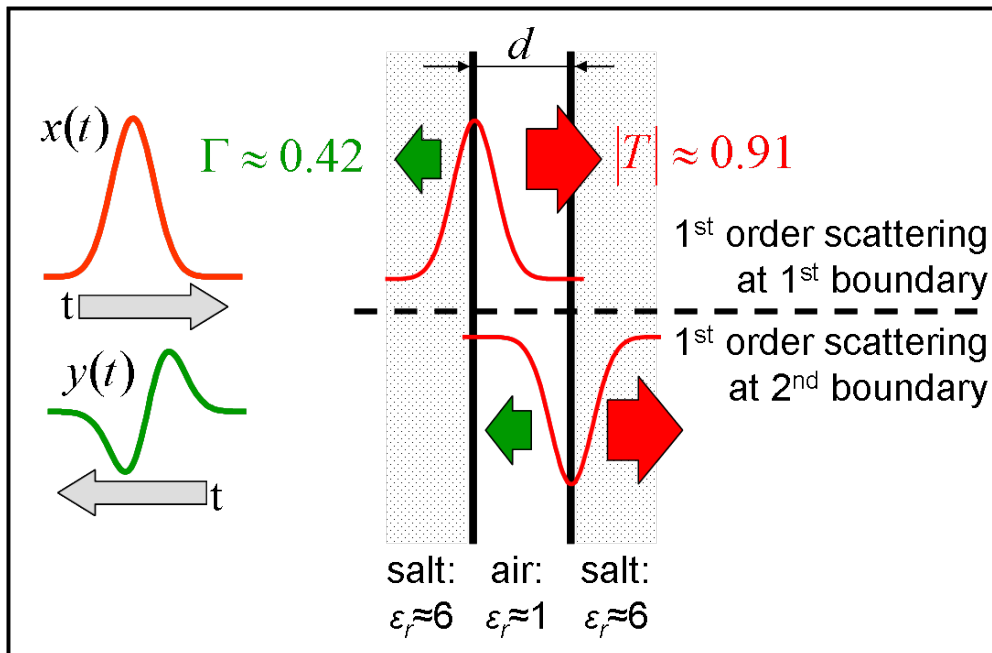
Fig. 2.3.: Scattering model for thin gaps in salt rock

How much of the wave is reflected and how much is transmitted at a boundary, can be derived from Maxwell's equations given the conditions of our simple model. For dielectric materials, Fresnel found a simple expression for reflection and transmission coefficients [67] with plane wavefronts. These coefficients are usually expressed in terms of power

but for our analysis it is better to refer to amplitudes normalised to the respective wave impedances. In the case of perpendicular incidence, they only depend on the material properties, more specifically on the permittivities of the two media defining the complex wave impedance $\underline{Z}_x$ as in equation 2.4. Using the average relative permittivity $\varepsilon_r \approx 6.0$ of salt rock derived in the previous section, reflection and transmission amplitude factors at the salt-air boundary can expressed as follows:

$$\underline{Z} = \sqrt{\frac{\varepsilon}{\mu}} = \sqrt{\frac{\varepsilon_0 \varepsilon_r}{\mu_0}} \tag{2.4}$$

$$\Gamma = \frac{\underline{Z}_{\text{air}} - \underline{Z}_{\text{salt}}}{\underline{Z}_{\text{air}} + \underline{Z}_{\text{salt}}} = \frac{\sqrt{\varepsilon_{r,\text{salt}}} - \sqrt{\varepsilon_{r,\text{air}}}}{\sqrt{\varepsilon_{r,\text{salt}}} + \sqrt{\varepsilon_{r,\text{air}}}} \approx 0.42 \tag{2.5}$$

$$T = \left| \sqrt{1 - |\Gamma|^2} \right| \approx 0.91 \tag{2.6}$$

Herein, Γ represents the reflection factor and T stands for the transmission amplitude factor, respectively. The frequency-dependency is accounted for by using average relative permittivities for the frequency range of interest. The relative permittivity ε_r can be complex, so in general also equations 2.4 through 2.5 could become complex, too. However, in the simple case discussed here, Γ is real-valued and the sign depends on the direction the boundary is crossed. For construction of the backscattered signal $y(t)$, knowledge of the magnitude of T from equation 2.6 is sufficient. $y(t)$ can now be written as in equation 2.7, if only the first-order reflections corresponding to figure 2.3 are included. It is assumed, that the stimulus wave $x(t)$ hits the gap at time $t = t_0$.

$$y(t) = |\Gamma| \, x(t - t_0) - |T| \, |\Gamma| \, |T| \, x\left(t - t_0 - \frac{2d}{c_0}\right) = |\Gamma| \left(x(t - t_0) - |T|^2 \, x(t - t_0 - \Delta t) \right) \tag{2.7}$$

$$y(t) \approx |\Gamma| \, \Delta t \frac{\partial x(t - t_0)}{\partial t} = |\Gamma| \frac{2d}{c_0} \frac{\partial x(t - t_0)}{\partial t} \tag{2.8}$$

The delay Δt is the time of travel within the gap from the first boundary to the second one and back. c_0 represents wave velocity in vacuum. When the second reflection reaches the first boundary, it superimposes with the first reflection. Even though the second reflection has a somewhat lower amplitude compared to the first one, the factor is $|T|^2$ which amounts to about 0.83 and is still very close to one in our case. For $\Delta t \to 0$ the approximation of equation 2.8 results. It becomes clear that backscattering amplitudes decrease with gap thickness[2] d. In other words, the two main reflections almost cancel out, if the delay Δt between them is small enough. Moreover, if the stimulus waveform

---

[2]In fact, if d was 0.0 m (which means there would no gap at all), there would also be no reflection. Of course, this case does not make sense when assuming the existence of boundaries.

$x(t)$ does not change much while travelling through the gap, i.e. its derivative $\partial x(t)/\partial t$ is low, most of the stimulus signal is lost for the received response $y(t)$. Then again, a fast change in $x(t)$ within Δt would be retained in the response as a significant amplitude. Let us take a look at what *small enough, slow change, or fast change* mean here. Table 2.1 shows the delay for small gap thicknesses down to sub-mm range on the left side. The right side shows the periods $t_p = 1/f$ of different microwave frequencies up to 40 GHz (see the previous section for a discussion on possible frequencies).

d [mm]	Δt [ps]	f [GHz]	t_p [ps]	λ_{air} [mm]	λ_{salt} [mm]
1.0	≈ 3.3	0.1	10,000.0	$\approx 3,000.0$	$\approx 1,200.0$
0.1	≈ 0.3	1.0	1,000.0	≈ 300.0	≈ 120.0
0.01	≈ 0.03	10.0	100.0	≈ 30.0	≈ 12.0
		40.0	25.0	≈ 7.5	≈ 3.0

Tab. 2.1.: Gap thickness and delay time Δt compared to frequency and wavelength

The comparison shows clearly, that gaps in the mm and sub-mm range produce delays one or more orders of magnitude lower than the periods of usable microwave frequencies. Thus, really only local signal behaviour of $x(t)$ influences the amplitude of $y(t)$ meaning that steep slopes produce higher amplitudes in the response than flat intervals. The picture does not change when looking at wideband or even UWB signals as opposed to single frequencies in the discussed frequency range. A 10 GHz bandwidth Gaussian-shaped impulse has a 10 % to 90 % rise time of about 35 ps according to the approximation in [68]. This is still long compared to the delays within thin gaps. The gap literally acts as some kind of high-pass preferring higher frequencies (or steep slopes) over lower ones (or flat signal intervals). The thinner the gap gets, the steeper signal edges must be present in $x(t)$ to produce detectable response amplitudes (given a fixed receiver sensitivity).

Just as common sense would expect, the scattering of thin gaps in salt rock favours high frequencies in reflections. More specifically, it turns out that the use of signals with steep slopes leads to higher reflection amplitudes and is mandatory for detection of very thin gaps with sub-mm thickness. This basically translates into the requirement of providing a measurement bandwidth as large as possible. Considering the simplifications used in this analysis, the results will qualitatively still hold in reality, but additional requirements arise. To compensate for the limited expansion of real gaps (as opposed to the assumption of infinite flat boundaries), directional applicators could be used to concentrate the wave energy around smaller gaps to get maximum response amplitudes, i.e. keeping the overall interaction volume as small as possible.

2.2.2. Scattering of small volume defects

Another major kind of salt rock disaggregation could be defects or small cracks limited to a local volume and not spanning a larger area as the gaps discussed above. Due to forces inside the salt, such defects might occur everywhere at grain boundaries in the crystalline structure and will usually have no connection at first. Eventually they become the basis for continuous gaps as the disaggregation zone develops over the years. The size of such defects is expected to be in the mm and sub-mm range in every dimension. From table 2.1 it becomes again evident, that the considered defects are very small with respect to the wavelengths in the prospected microwave band. Such defects can therefore be considered and modelled as point scatterers (spherical voids within the salt).

If a point or spherical scatterer is assumed, the backscattered power in the case of narrowband waves can be judged by using the radar cross section (RCS) σ of the scatterer [67][3]. It represents an equivalent reflection area under far field conditions, i.e. assuming a plane wave over the target. The larger the RCS, the more power is reflected back to the receiver. For spherical scatterers, Mie [69] developed a relationship between sphere diameter, RCS, and wavelength. Again, Maxwell's equations form the basis but some simplifications and approximations of the closed-form solution exist for special cases. Before using these results for further analysis, it should be noted that Mie treated the case of an ideal spherical reflector rather than an object with dielectric contrast as in the case of disaggregation in salt. This basically means, the absolute RCS value will be lower than predicted by Mie for voids in salt rock, but the dependencies we are interested in will still be correct. A common way of showing the narrowband RCS after Mie is depicted in figure 2.4. The X-axis refers to the wave number k, i.e. the wavelength λ of the stimulus normalised to the sphere's circumference: $k = 2\pi r/\lambda$. Herein, r is the radius of the scatterer. The Y-axis shows the corresponding RCS normalised to the sphere's projected area in a logarithmic scale.

As indicated in the figure, commonly three cases are distinguished. In the last case called optical region, the sphere is much larger than the wavelength of the electromagnetic stimulus. Under such conditions, its whole area is effective and specular reflection occurs. The middle region also known as Mie region shows special behaviour. Since the wavelength and the sphere's circumference are almost equal, resonance effects occur leading to an RCS sometimes even greater than the object's area. For our example of volume defects, the last case must be considered. When the wavelength is much larger than the sphere, the Rayleigh region shows the corresponding RCS. Actually, Mie's full solution is still a rather complicated expression, but Rayleigh developed a simple ap-

---

[3]Please note that the overall received power depends on other factors such as the distance to the target or antenna gain, too. A complete description for the narrowband case is given by the full radar equation. The interested reader is encouraged to consult [67]. Since only the RCS is dependent on the reflector itself, analysis can be limited to this variable in our case.
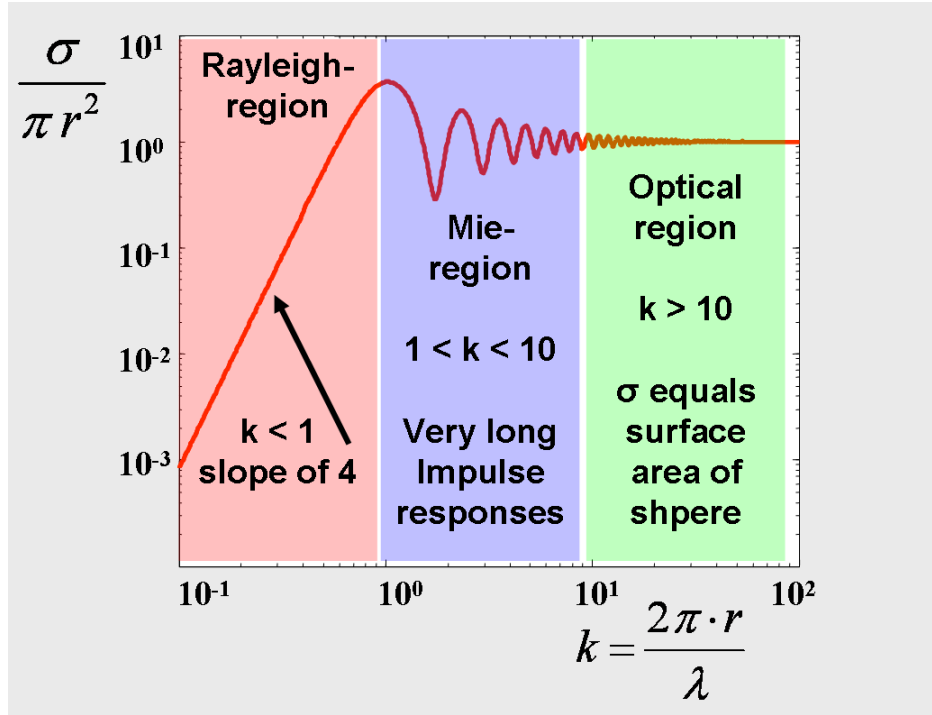
Fig. 2.4.: Radar cross section of spherical scatterers in the far field

proximation [70] given in equation 2.9 for $k \ll 1$. The terminus Rayleigh scattering is commonly used to describe such cases. It is often found in optics covering the interaction of dust particles or molecules with visible light [71].

$$\sigma = a\pi r^2 k^4 = \frac{a16\pi^5 r^6}{\lambda^4} = \frac{a\pi^3 V^2}{9\lambda^4} = \frac{a\pi^3 V^2 f^4}{9c^4} \tag{2.9}$$

$$y(t) \propto V \frac{\partial^2 x(t)}{\partial t^2} \tag{2.10}$$

Herein, a is a constant, V the volume of the scatterer and c wave velocity in the medium surrounding the defect. This expression shows two important things. Firstly, the backscattering is strongly dependent on the wavelength (or frequency), because it appears in 4th power in equation 2.9. In fact, the Rayleigh region in figure 2.4 shows a slope of four indicating this relationship. The result is a highly selective high-pass character favouring higher frequencies (short wave lengths) over lower ones. Since the RCS refers to power, amplitude relations can be obtained by the square root of σ. Finally, for an UWB signal $x(t)$, the backscattered signal $y(t)$ is proportional to the volume of the scatterer and the second derivative of the stimulus as expressed in equation 2.10. This can be easily shown by constructing the UWB signal as a superposition of sine waves with different frequencies, considering the RCS relationship in equation 2.9 as a filter, and using rules of inverse

Fourier transform. A more detailed discussion can be found in [72]. Thus, the situation is similar to the scattering of small gaps discussed above, but this time the advantage for higher frequencies is even stronger. So far, the conclusions drawn in subsection 2.2.1 regarding the frequency and bandwidth requirements for a new radar sensor are consistent with the findings here and are even emphasised in the case of small volume defects.

The second aspect of equation 2.9 is the strong 2nd order dependency on the actual volume V of the defect (dependency on its radius r is a 6th order relationship). It is clear that if the volume becomes smaller, keeping the backscattered amplitude at an detectable level by using higher frequencies will soon become infeasible. If you recall the prospected frequency range from section 2.1, variations of f are quite limited to only about 1.5 orders of magnitude. That means if one was able to detect a volume defect of a certain size, a drop in volume by a factor of 10 (drop in radius of about two) could not even be compensated in the frequency range available. It can be predicted that sensitivity for volume defects will be much lower than for gaps. Consequently, the minimum detectable gaps thickness is likely to be much smaller than the minimum radius of a volume defect which is registered as an individual target. However, if there are many volume defects in a certain part of the disaggregation zone, their backscattering might still have influence on the statistical properties of received signals and their presence could be recognised.

In conclusion, the dynamic range or sensitivity of the new sensor is another major factor for the development. This topic will be discussed in section 2.4, but since dynamic range requirements not only depend on the targets to be detected but also on how the sensor applies the stimulus, let us first talk about the mode of interaction between electromagnetic waves and the disaggregation zone.

2.3. Mode of operation — electromagnetic wave interaction with salt rock

Radar sensors work in general by exciting the test object with an electromagnetic wave stimulus and recording its reaction. Common effects involved are reflection of the wave, refraction, and penetration into the test object. Usually, more than one of these phenomena occur in real measurements and influence the received sensor signal. There are different possibilities to provoke an interaction of the sensor stimulus with the disaggregation zone in salt rock through an applicator. In this section, the pre-selection of a feasible applicator is discussed.

2.3.1. Electro-magnetic surface waves

Since the properties of near-surface salt rock layers are of interest in this investigation, using some kind of surface wave could be a solution. There are two main types of surface waves involving dielectric materials without a significant conductivity — Goubau waves [73] (sometimes the more general term Sommerfeld waves [74] is used) or evanescent waves. Unfortunately, it turns out that neither of these are feasible for the intended task. Let us have a quick look at the reasons.

Goubau waves   Goubau waves are electromagnetic waves travelling along a single conductor coated with some dielectric material (usually called Goubau-line or short G-line). This could be a modified coaxial cable without an outer conductor. The mode of propagation is the so-called TM-mode, i.e. the magnetic field is perpendicular to the propagation direction while the electric field is not. The phase velocity (and thus also group velocity) depends on the properties of the dielectric material and most of the energy is concentrated a few wavelengths around the conductor.

All these aspects make Goubau waves a prime candidate to assess near-surface variations of material properties, e.g. due to disaggregation in salt rock. However, the application in salt mines would have several problems. First of all, the Goubau waves assume a conductor surrounded by the dielectric material, but since we are seeking a non-destructive sensor, the only option would be to attach a conductor to the surface. This makes the description of wave propagation more complicated, because on one side the dielectric would be air, while on the other side it would be salt rock. Apart from that, G-lines are usually fed by a conical wave guide launcher and also the transmitted wave is received by such a device. Since these launchers have a size in the order of supported wavelengths, they cannot be placed as close to the surface as the conductor itself. That is why further discontinuities at both ends would result, making a simple description of the propagation even more difficult. Finally, the fact that a conductor would have to be attached to the salt rock surface is a serious drawback for two reasons. Obviously, this would mean a slow measurement procedure, because the applicator would have to be attached and detached by an operator all the time. A further problem would be, that the surface roughness of tunnels can be quite different — depending, for example, on the way it was created. As the surface is usually not smooth, a close and reproducible attachment of the conductor would be very difficult.

Evanescent waves   This form of wave appears at dielectric boundaries in the case of total inner reflection. When a wave approaching the boundary from the side of lower velocity is inclined beyond a critical angle (Brewster angle), no transmission into the second medium takes place and the wave is completely reflected at the boundary [75]. Since the electric

and magnetic fields need to be continuous at the boundary, there still exists a wave field penetrating into the other medium. It decays exponentially with distance from the boundary and therefore vanishes fast, hence the name evanescent wave. This type of wave is sometimes used in optics to characterise test objects near the boundary, e.g. in total internal reflection fluorescence microscopy (TIRFM) [76]. In the case of light, penetration depth is only a few 100 nm, but if used with microwave frequencies feasible penetration could result.

Total internal reflection, however, only occurs when a wave hits the boundary from within the medium with slower velocity. In the pair salt rock and air this would clearly be salt rock, so an evanescent wave would only appear for an incident wave from within the disaggregation zone and it would be established on the outside in air. This situation is not useful for inspection of the disaggregation zone.

2.3.2. Radar sensor using antennas

In a classical sense, radar systems use antennas to transmit the stimulus to the test objects and record the responses. There are two common antenna configurations — either monostatic or bistatic radar. Monostatic systems use the same antenna as transmitter and receiver[4] and are usually used to record reflections. In the bistatic case different antennas are employed to transmit the stimulus and receive the responses. Since antenna separation is a degree of freedom, bistatic setups can also record reflections or could be used to record transmission through a test object.

Besides the antenna configuration, the coupling of the antennas to the test objects must be decided. There are again two common choices, if one is interested to look inside the test object (in this case the near-surface salt rock). The first option would be to directly apply the antennas to the salt rock surface. There are a number of advantages and disadvantages to this approach. On one hand, the electromagnetic wave would be directly transmitted into the salt rock and at least for the ideal case there would be no surface reflection. On the other hand, this usually limits antennas to flat structures[5] (e.g. patch antennas) which may not provide all desirable properties. A more serious problem is the surface roughness of the salt rock. There are many ways of creating tunnels and there are many different shapes as well leading to different surface conditions. In fact, the surface roughness can be rather high up to RMS values of a few millimetres up to centimetres [34]. All these aspects make it very hard to get reproducible and high-quality direct coupling. Even common sense dictates that if micro-cracks or small defects of

---

[4]Sometimes, separate antennas are used but their separation is small compared to the distance to the test object. Such a configuration behaves much like a monostatic setup and is therefore called quasi-monostatic radar

[5]Other more complex antenna types, e.g. horn antennas, could also be used when coupling to the surface. However, the antennas would need a dielectric filling material with similar properties like salt rock.

mm- or sub-mm size inside the test object are to be detected, a surface-coupled antenna should be closer to the surface than a millimetre to ensure reproducible results. Another disadvantage would be a slow and complicated scanning as the antennas would need to be guided exactly along the surface. The scanning effort is a major factor for practical deployment of the sensor and contact to the surface is not a favourable solution.

There is the second common option of coupling the waves through the air interface. This means the antennas transmit into free space in the direction of the test object and the responses are again received from free space. Pros and cons are quite opposite to surface-coupled antennas. Scanning is much easier realised and potentially much faster because there is no mechanical contact to the salt rock. However, in this coupling mode a significant amount of energy is reflected at the dielectric boundary formed by the salt surface and air. Any reflection from inside the disaggregation zone must pass the boundary, too. The amount of energy lost for penetration depends on the dielectric contrast between air and salt rock. As can be derived from the results of sections 2.1 and 2.2.1, about 17% of the power is reflected for perpendicular incidence at an air/salt boundary. This seems to be acceptable at first glance, but has influence on the necessary dynamic range as will be discussed in section 2.4. Further losses are due to the spreading of the stimulus wave in free space before the surface. This problem can also be seen in a different way. If we assume a similar antenna pattern (i.e. same directivity), the illuminated area (interaction volume) within the disaggregation zone is smaller in the case of surface-coupling than in the case of coupling through air. As stated in section 1.2, the distribution of defects is usually not known and responses from all cracks in the interaction volume superimpose for each antenna position. They might cancel out, so it is desirable to have the illuminated area as small as possible.

Overall, it seems difficult to choose one solution over the other without in-depth consideration of the wave propagation mechanisms involved, antenna properties, and perhaps a series of propagation simulations. Since such analysis was not in the focus of the overall investigation and is also not the focus of this thesis, let us end the theoretical discussion here. Instead, practical aspects such as the aim to develop a sensor for fast scanning as well as test measurements have been used to find a suitable antenna configuration. Finally, the much easier way of scanning an air-coupled antenna along a surface limited the choices to this option. To find a way to cope with the disadvantages mentioned above and find rules for antenna placement/scanning, several measurements in real salt mines have been conducted. Different antenna types and how they should be placed with respect to the salt rock surface have been tested. For the sake of compactness, main conclusions shall be given in chapter 6. For further theoretical considerations, let us simply assume the use of air-coupled antennas. The next subsection deals with the question of polarisation.

2.3.3. Antenna polarisation

Some antennas radiate and receive in a preferred wave polarisation. Polarisation refers to the alignment of the electric field vector with respect to a reference coordinate system [77]. There are linear polarisations — horizontal and vertical polarisation — where the alignment stays fixed in the corresponding direction. Another well-known polarisation mode is circular (or more general elliptical) polarisation, where the alignment rotates along the propagation path. Despite the different modes, in most dielectric media (with linear and isotropic properties) every case can be composed as a superposition of the two linear modes.

This is why in many radar applications where polarisation is of concern, only four linear polarisation combinations are considered — horizontal and vertical co-polarisation denoted as HH and VV, respectively, as well as linear cross-polarisations denoted as VH and HV. The first polarisation refers to the transmitted stimulus, while the second mode refers to reception. In most cases, the test objects are passive (i.e. do not generate electromagnetic waves themselves) and reciprocal. For such objects, the direction of measurement can be switched, e.g. transmitting and receiving antenna can be interchanged, without giving different results [77]. Therefore, VH and HV are often redundant and only three of the combinations are linearly independent. In technical terms, it must be decided by appropriate antenna choice and alignment, which of the combinations should be measured. In some cases, more than one combination is measured to gather additional information about the test object, up to fully polarimetric measurements acquiring all linear combinations.

When designing a sensor for the disaggregation zone in salt rock, the question should be answered, if polarisation matters. It is known from other applications of radar sensors, that some test objects with very unequal geometrical dimensions or complex geometries are very sensitive to wave polarisation. One example from [78] deals with remote sensing for environmental monitoring. It was shown, that the scattering from tree trunks is dominant in vertical co-polarisation, while scattering from the tree crown shows strong cross-polarisation scattering due to the rather random distribution of leaves. Further investigation at microwave frequencies described in [79] indicates, that flat or smooth surfaces in environmental monitoring prefer both co-polarisations while vegetation covered regions have stronger cross-polarisation components in the scattered waves. When comparing magnitudes of the polarisation components it was observed, that co-polarisation is usually much stronger than cross-polarisation.

Even though these examples are quite different from the salt mine situation, some indications can be derived. First of all, it can be expected that the surface reflection from the salt rock will be strongest in co-polarised measurements. One possibility of lowering this problem of using air-coupled antennas would be the use of the cross-polarised

mode. On the other hand, defects such as discrete cracks could come as thin, flat distortions. Depending on the direction of the incident wave, either a plane boundary is hit, or the thin edges of the crack could be the major source of backscattering. In both cases, co-polarised scattering dominates and important information could be missed in systems only relying on cross-polarised measurements. Furthermore, as described in section 1.3, the alignment of discrete cracks, gaps, other defects is usually not known a-priori. It can be concluded, a versatile sensor system able to do fully polarimetric measurements would be valuable for the investigation.

The easiest way to realise such a system is to provide two measurement ports and to measure the full two port scattering parameter (S-parameter) matrix S given in equation (2.11). This matrix summarises the S-parameters existing between the two ports. They represent complex wave ratios, which are defined in the frequency domain [67]. The diagonal elements $\underline{s}_{11}$ and $\underline{s}_{22}$ represent reflection measurements at the respective ports while the other two parameters $\underline{s}_{12}$ and $\underline{s}_{21}$ describe the transmission between them.

$$\mathbf{S} \equiv \begin{pmatrix} \underline{s}_{11} & \underline{s}_{12} \\ \underline{s}_{21} & \underline{s}_{22} \end{pmatrix} \tag{2.11}$$

If the two ports are connected to two antennas with opposite linear polarisations, i.e. port one is connected to a vertical polarised antenna and port two to a horizontal polarised antenna, fully polarimetric datasets can be acquired with the mapping indicated by equation (2.12). Please note, that in such a setup the co-polarisations are measured in a monostatic fashion as reflections at either antenna and the cross-polarisations are acquired in a bistatic mode as transmission between the antennas. In order to provide two measurement ports, the new sensor should have multiple receivers. If S-parameters are to be measured, not only the received waves need to be acquired, but also the transmitted stimulus should be recorded or must be known.

$$\begin{pmatrix} \underline{s}_{11} & \underline{s}_{12} \\ \underline{s}_{21} & \underline{s}_{22} \end{pmatrix} = \begin{pmatrix} \underline{s}_{VV} & \underline{s}_{VH} \\ \underline{s}_{HV} & \underline{s}_{HH} \end{pmatrix} \tag{2.12}$$

So far, a few desirable features and configurations for measuring the disaggregation zone in salt rock have been derived. Given these conditions, the next section finally tries to estimate the dynamic range requirements for an UWB sensor system with air-coupled antennas.

2.4. Dynamic range requirements

Some important system parameters design goals have been derived so far. The last obvious aspect is the required sensitivity or dynamic range of the sensor. It can be assessed by analysis and simulation of a typical measurement situation. Before doing so it is worthwhile to talk a little bit about a suitable definition of dynamic range for UWB time domain measurements.

2.4.1. Dynamic range for UWB time domain signals

Dynamic range is a concept commonly used when describing sensors and their sensitivity. The basic idea of a dynamic range is given by equation 2.13 and simply refers to the ratio of a largest to a smallest value of some kind. It is usually given in a logarithmic scale of base 10 and can be expressed in terms of amplitude a (often a voltage), in terms of power P, or as intensities.

$$D[dB] \equiv 20lg\left(\frac{a_{max}}{a_{min}}\right) \equiv 10lg\left(\frac{P_{max}}{P_{min}}\right) \tag{2.13}$$

According to what kind of property should be expressed, different specific definitions are used in science and engineering [80]. As for transceivers, raw performance is often given as the ratio of the largest signal the electronic can handle to the lowest detectable quantity which is often limited by the noise floor. Such values are not generally useful since the upper boundary is often specified under undesirable conditions such as severe receiver saturation and therefore non-linear behaviour. Even more so, effective receiver noise can be lowered by multiple measurements and coherent averaging of the results. This, of course, increases measurement time and may not be feasible with all applications. Raw performance figures for receivers are therefore merely best-case values with little practical relevance.

For the purpose of analysing our specific task and to find a design goal, the spurious-free dynamic range (SFDR) is a better suited figure of merit. It is often used to characterise amplifiers, analogue-to-digital converters, or complete receivers. Most of the time SFDR refers to a case where the device is stimulated by a single or double frequency signal at full scale level. The received (or amplified) signal is judged in the frequency domain and the SFDR is given as the ratio of the wanted components (i.e. amplitudes at the stimulus frequencies) to the strongest unwanted component. In the case of non-linear device behaviour, unwanted parts could be higher order harmonics or intermodulation frequencies. If a receiver was used in its linear working range, the noise floor would be the strongest unwanted component.

For wideband or UWB signals and devices, an analysis in frequency domain is rather complicated because there are many frequency components and all of them could produce harmonics or intermodulation, etc. But the idea of SFDR can be transferred to a time domain analysis as well. If one is able to measure an impulse response function (IRF) of the device to be characterised, it becomes possible to judge the ability to detect small events (such as reflections from disaggregation) in the presence of a strong event (e.g. the surface reflection at the air-salt interface). The system-IRF of a wideband sensor itself usually consists of the measured stimulus impulse and different kinds of unwanted events caused by the device. This includes multiples of the stimulus pulse, signal distortions due to linear and non-linear behaviour, and noise. All these effects are summarised by the term *device clutter*. The situation is illustrated by figure 2.5. The time domain SFDR can then be defined as the ratio of the registered stimulus impulse amplitude to the amplitude of the strongest clutter impulse as denoted by equation 2.14. It is a good measure for a wideband receiver's real-world sensitivity because usually one cannot reliably detect weak events in a measurement signal, if their amplitudes are smaller than or equal to the strongest spurious clutter produced by the device itself. If non-linear distortions are reduced to negligible levels by proper sensor design, the remaining linear device clutter often scales with the amplitudes of main events in an IRF, i.e. multiple reflections will have a fixed amplitude ratio compared to the original pulse it originated from.

$$SFDR_{td}[dB] \equiv 20lg \left(\frac{max(|IRF|)}{max(|clutter|)} \right) \tag{2.14}$$
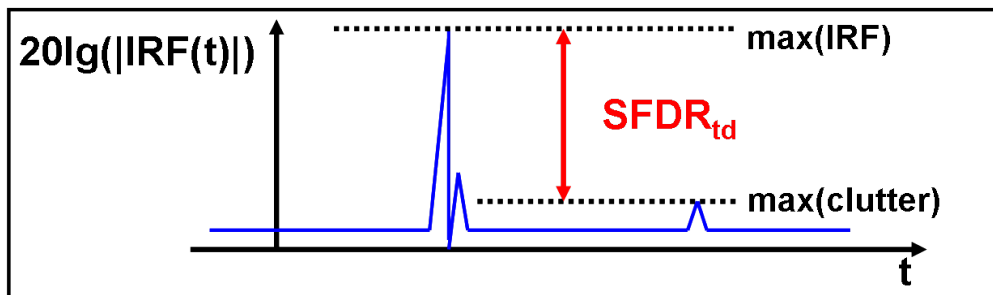
Fig. 2.5.: Illustration of $SFDR_{td}$

We will be using $SFDR_{td}$ later in chapter 5 when describing ways to reduce device clutter. For now it is interesting to find out, what $SFDR_{td}$ is at least required for the new UWB sensor when investigating the disaggregation zone in salt rock.

2.4.2. Setup for a typical measurement situation

Again, a simple model of a typical measurement situation under idealised conditions can provide reasonable answers. In section 2.2 above, the scattering behaviour of two different types of distortions has been studied. It seems that thin gaps or layers are the easier target because they are not as frequency-selective as small volume defects. Furthermore, layered defects are a more critical disaggregation regarding leakage paths through the salt. That is why we'll consider thin gaps in the following simulation for a typical measurement situation.

There are two different ways of interpreting a dynamic range requirement for the sensor. Even though not our main interest here, the first aspect to be discussed is indeed raw system performance (or more specific SNR at full scale reception) which leads to some practical conditions for the measurements. As described in section 2.3, the stimulus will be applied through the air interface using UWB antennas. It is clear that even in the case of directional antennas the transmitted energy spreads in free space and that even for moderate distances to a gap the path loss will considerably attenuate the received signal with respect to transmit power. The detection of responses from far-away targets is usually limited by receiver noise (or available measurement time used to improve effective SNR). Since responses from small gaps are expected to be overall very low it is not wise to increase SNR requirements by placing the antennas far from the surface and the disaggregation zone. Putting them near the surface also keeps the interaction volume small. Details about antenna placement will be explained in chapter 6. For the simulation we can conclude that the salt rock surface and parts of the disaggregation zone should be in the near field of the antennas and that path loss must be accounted for in the calculations. To be able to use the derived scattering model for thin gaps here, the gap can still be placed further away from the antennas to better respect the far-field assumption of the model. Finally, receiver noise will not be included in the simulation. It is rather assumed that the SNR is high enough such that noise has negligible influence on the amplitudes of deterministic signal components.

The second (and more involved) interpretation of a dynamic range requirement is related to the introduced definition of $SFDR_{td}$. In a real measurement, the surface reflection will be the strongest component of the receive signal possibly creating multiples caused by device clutter. These clutter components superimpose with the responses from the gap or other distortions. Thus, the question to be answered is: How strong is the gap response with respect to the surface reflection, i.e. what is their amplitude ratio? This information can be used to get an overview how well the sensor must suppress device clutter to be able to detect the gap with confidence.

In order to keep things simple, transmit antennas are assumed to be point sources with an omnidirectional radiation pattern. The gain of more complex antennas is not consid-

ered here since it depends on antenna type and is highly frequency-dependent. Using directional antennas will only improve SNR performance over omnidirectional radiators, so assuming point sources will lead to a worst-case estimate for backscattered amplitudes. Considering the prospected frequencies in the lower microwave range, physical size of UWB antennas will be in the order of a few cm to one dm. Placing the antennas $r_1 = 10 \; cm$ away from the salt rock seems a technically feasible condition while scanning along the surface. Another parameter of simulation would be the distance between salt rock surface and the thin gap. Since the average extension of the disaggregation zone is known to be roughly half a metre (see also section 1.3), let us place the air-filled gap $r_2 = 50 \; cm$ away from the surface as a worst case situation. This also puts it in the far-field of the antennas. As in section 2.2.1, an infinitely large extending gap is assumed. Moreover, we are simulating a monostatic reflection measurement here, i.e. the transmitting and receiving antenna are identical. The described measurement situation is summarised in figure 2.6. It also shows the main reflection events to be included in the simulation calculations.
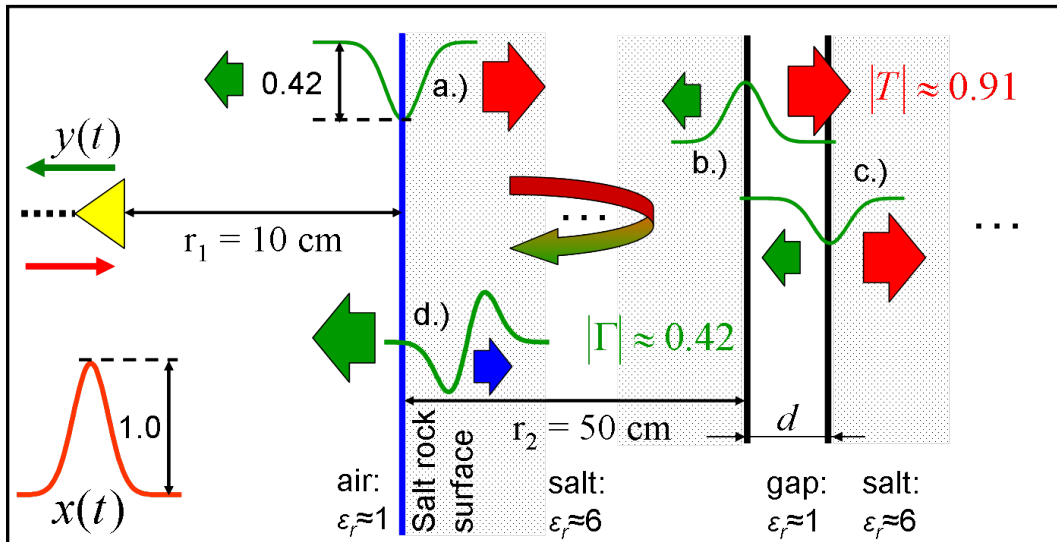
Fig. 2.6.: Simplified typical measurement case for thin gaps in the disaggregation zone

2.4.3. Simplified model for dynamic range simulation

As can be seen from figure 2.6, the stimulus travels towards the surface, first. Being transmitted by a point source, spherical waves emerge from the antenna and part of it is reflected in a mirror-like fashion at the air-salt boundary (the event is marked *a.)*) in the figure. Due to spreading of the energy in space and considering the flat boundary, path loss up to the receiver has a $1/2r$ dependency. The amount of reflection can be approximated by the reflection coefficient Γ from subsection 2.2.1. The remainder of the

stimulus penetrates into the salt rock until it reaches the gap. Due to further spreading of the total energy in space, path loss increases. Even though the wave front will no longer be exactly spherical after passing the surface boundary, an $1/r$ relationship can still be used as a simple approximation because the dielectric properties of salt and air are not too different. The resulting backscattered wave from the gap (comprised of events *b.)* and *c.)*) travels towards the antenna again, but it has to pass the surface boundary before being registered by the receiver (see mark *d.)* in the figure). This leads to a further weakening of the target amplitudes. Again, only the most important first order scattering events are included in the model. For example, the small portion of the gap's response that cannot leave the salt rock and is reflected back towards the gap is neglected in the calculation. All parameters but the measurement bandwidth B, waveform of the stimulus $x(t)$, and gap thickness d have been fixed so far. They shall be used as parameters of the simulation. In summary, the received signal $y(t)$ can be calculated according to equation 2.15. It originates from equation 2.8 but takes into account the additional boundary of the salt rock surface as well as additional path loss due to near-field conditions. Here, c_{air} and c_{salt} are the propagation velocities in air and salt, respectively. The constant b is used for normalisation, i.e. to set the maximum amplitude of the surface reflection to one. It does not influence the $SFDR_{td}$ requirement coming out of the simulation but it has influence on the receiver parameters full scale level and achievable SNR which are not in the focus of this simulation.

$$y(t) \approx b \left[|\Gamma| \frac{1}{2r_1} x\left(t - \frac{2r_1}{c_{\text{air}}}\right) - |\Gamma| \, |T| \frac{1}{2(r_1 + r_2)} \left(\frac{2d}{c_{\text{air}}} \frac{\partial x\left(t - \frac{2r_1}{c_{\text{air}}} - \frac{2r_2}{c_{\text{salt}}}\right)}{\partial t} \right) \right] \qquad (2.15)$$

The calculation can be done for different stimulus bandwidths and different gap thicknesses. The stimulus bandwidth defines how sharp the time domain impulse $x(t)$ becomes. For the sake of simplicity let us assume a flat stimulus spectrum $X(f)$ with zero phase for all frequencies in the selected range and retrieve $x(t)$ via direct inverse Fourier transform of such a spectrum. It is better to use slightly smoothed edges in the spectrum to avoid the strong time-domain side lobes of the rectangular spectrum. The topic of using smooth window functions when switching between time- and frequency-domain is thoroughly discussed in [81] and will influence the basic detectability of weak scatterers right behind the surface as we will see soon. Please also note, when constructing the stimulus impulse $x(t)$ this way, it represents an acausal signal, i.e. it has side lobes in the direction of positive and negative times. This is caused by the zero-phase condition in the spectrum but does not limit the generality of the investigation[6]. To choose example bandwidths for the calculations, state-of-the-art GPR technology will be considered as well as

---

[6]In fact, such signals cannot be generated as transients by real devices. Causality dictates that side lobes must appear after the event. On the other hand, if the devices are based on repeated (e.g. periodic) signals, causality is always maintained by their cyclic nature if a steady state is reached.

devices with extended bandwidth. The lower cut-off frequency is always assumed to be 1 GHz given the high-pass character of the gap's backscattering and that antennas for even lower frequencies would be large compared to the surface distance r_1. Commercial GPR sensors will be represented by a bandwidth of 1 GHz, experimental GPR-systems by a bandwidth of 5 GHz [82], and prospective GPR systems with 10 GHz up to 20 GHz fully spanning the feasible frequency range discussed in section 2.1. Figure 2.7 shows the spectra $X(f)$ and time domain impulse responses $x(t)$ for the four different stimulus cases. Please note that since the stimulus signal has been synthesised for this simulation, its shape is exactly known and consequently it could be replaced by Dirac delta pulses for the simulation showing only propagation delay and amplitude. However, in real measurements the precise shape of the scattered signal cannot be known due to surface properties or antenna effects. When processing real measurement data, the presence of pulse side lobes caused by finite measurement bandwidth cannot be avoided completely (please refer to section 6.2 for a detailed discussion) and thus the simulation results retain these effects to emphasise the challenges associated with the task.

2.4.4. Results of dynamic range simulation for thin gaps

The last variable to be chosen is gap thickness d before equation 2.15 can be applied. For each of the different stimuli, three different values are investigated: $d = 1.0\ mm$, $d = 0.1\ mm$, and $d = 0.01\ mm$. The results are shown in figures 2.8 through 2.10 sorted by ascending stimulus bandwidth. Figure 2.8 is in a linear scale showing relative amplitudes. Please note that due to the low bandwidth a gap thickness of $d = 10.0\ mm$ has been included as well. The responses for 10 mm and 1 mm gaps can be recognised, but the backscattering from thinner gaps cannot be seen in this view. In order to be able to see the backscattering from all gaps, it was necessary to show the time domain data in a logarithmic scale for the other figures. It is preferable to plot $20lg(|y(t)|)$ since this allows to directly read the dynamic range contained in the idealised receive signals from the graphs. In our case, the amplitude ratio D_{SG} of the surface reflection to the gap's reflection event hints on the required $SFDR_{td}$ of the sensor. Table 2.2 summarises the simulation results for bandwidths beyond 1 GHz. It also includes results for the full feasible bandwidth of 20 GHz not shown in the figures.

The calculations support the expected behaviour. For a fixed stimulus bandwidth, the backscattered event becomes weaker when d decreases. The necessary dynamic range to detect the gap despite the surface reflection becomes higher. The situation can be relaxed by using higher bandwidth stimuli, something that was also expected from the findings in section 2.2. However, the values of D_{SG} in table 2.2 are overall very high for sub-mm gaps. A bandwidth beyond 10 GHz seems at least necessary to be able to realistically detect them at all. However, building ideal electronic components able to
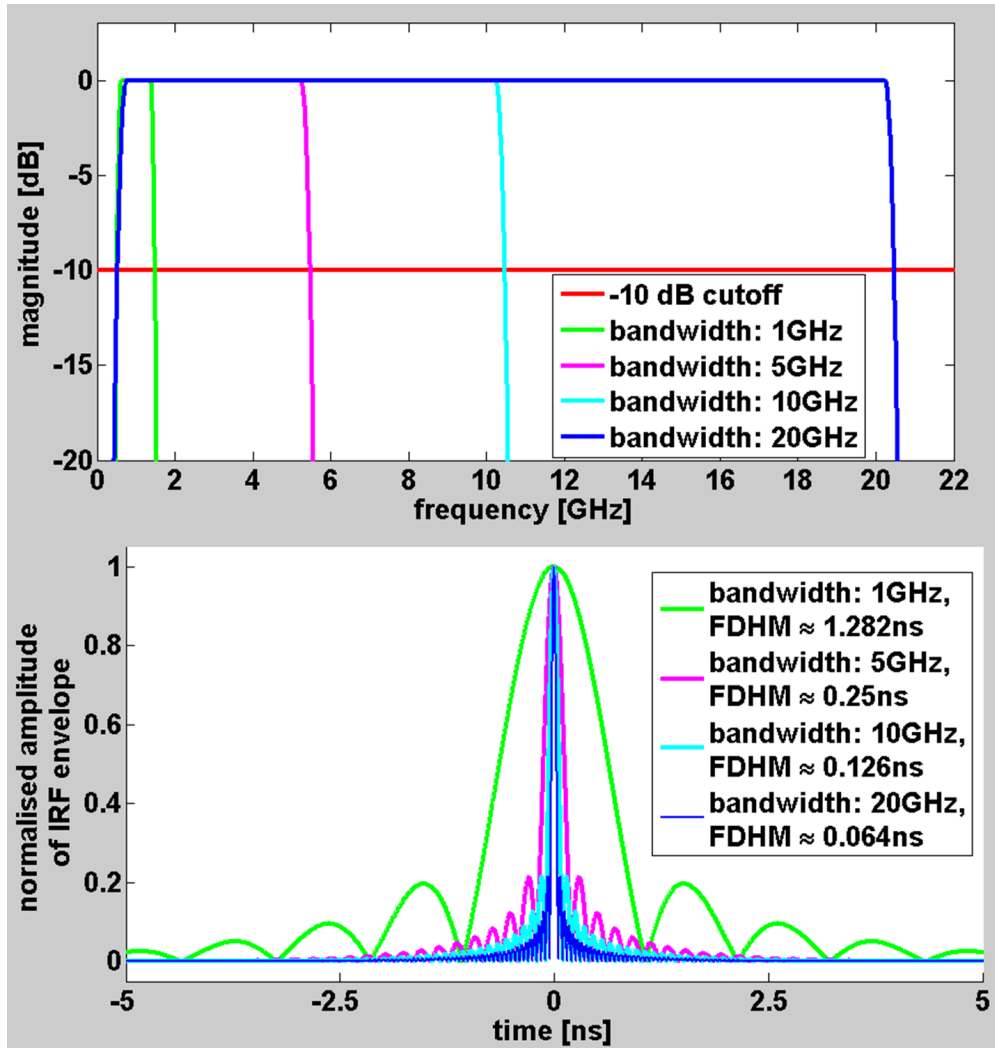
Fig. 2.7.: Stimuli spectra $X(f)$ and time domain IRFs $x(t)$ for simulation

handle such high frequencies and cover large bandwidths is a difficult task. Unwanted device clutter increases with bandwidth. For example, a 10 GHz bandwidth amplifier will certainly not have a completely flat frequency response thus producing signal distortions. The matching of wave impedance of such an amplifier (or even of a simple coaxial RF cable for that matter) is usually far from ideal as well — it is often only about 20 dB over the whole bandwidth [83]. This can cause multiple reflections when the stimulus wave passes a device or cable junction. Such device clutter effectively limits the $SFDR_{td}$ of the sensor. Thus, the uncorrected performance of UWB sensors is not likely to satisfy the requirements of table 2.2 — regardless of the bandwidth used. Device calibration is a way to improve system accuracy over a large bandwidth by removing reproducible device imperfections such as the mentioned mismatch at cable junctions or the frequency response of an amplifier. Calibration is regularly used in laboratory measurements with vector network analysers and many techniques [84] have been developed to date. However, such

B [GHz]	d [mm]	D_{SG} [dB]
5.0	1.0	33.9
5.0	0.1	54.0
5.0	0.01	71.7
10.0	1.0	29.2
10.0	0.1	49.2
10.0	0.01	68.7
20.0	1.0	24.0
20.0	0.1	43.9
20.0	0.01	63.8

Tab. 2.2.: Simulated signal dynamic D_{SG} for different stimuli bandwidths and gap thicknesses

methods are unusual (and for the most part unnecessary) for current GPR systems. For a new UWB sensor with several GHz of bandwidth it can be concluded, that the application of correction techniques is mandatory to achieve a satisfactory clutter-free dynamic range. Thus, calibration can be formulated as another design goal and the new system should combine a bandwidth of 10 GHz or more with an $SFDR_{td}$ in excess of 50 dB. Otherwise, responses from sub-mm gaps or other disaggregation cannot be distinguished from device clutter with enough confidence.

Another important point becomes evident when looking at the figures 2.8 through 2.10. Despite the large bandwidth used, the side lobes of the surface reflection are strong compared to the responses from thin gaps. If the gap was near the salt rock surface, its response would be a bit stronger due reduced path loss. Nevertheless, it could hardly be noticed at all because it would superimpose with the large side lobes of the surface reflection. This problem cannot be completely circumvented in any way because signals of limited bandwidth always spread infinitely[7] in time domain [85]. However, there are a few things that can be done to suppress the influence on the detection of weak events.

As mentioned before, the shape of the stimulus impulse can be changed by a frequency domain filter or window. Since the surface reflection in equation 2.15 is a scaled copy of the stimulus impulse $x(t)$, it could be tailored to exhibit more desirable shapes, e.g. with smaller side lobes right next to the main pulse. As described in [81], there is always a compromise between the sharpness of the main impulse and the side lobe level. For example, the smoother the transition of the frequency domain window, the lower side lobes can become but the wider the main impulse will be.

Furthermore, if the shape of the surface reflection would be exactly known, it could also be subtracted from the received signal leaving only the reflections from disaggregation. This is the basic idea of so-called super-resolution techniques [86]. The problem of sur-

---

[7]In the case of periodic signals, bandlimited signals occupy the whole period.
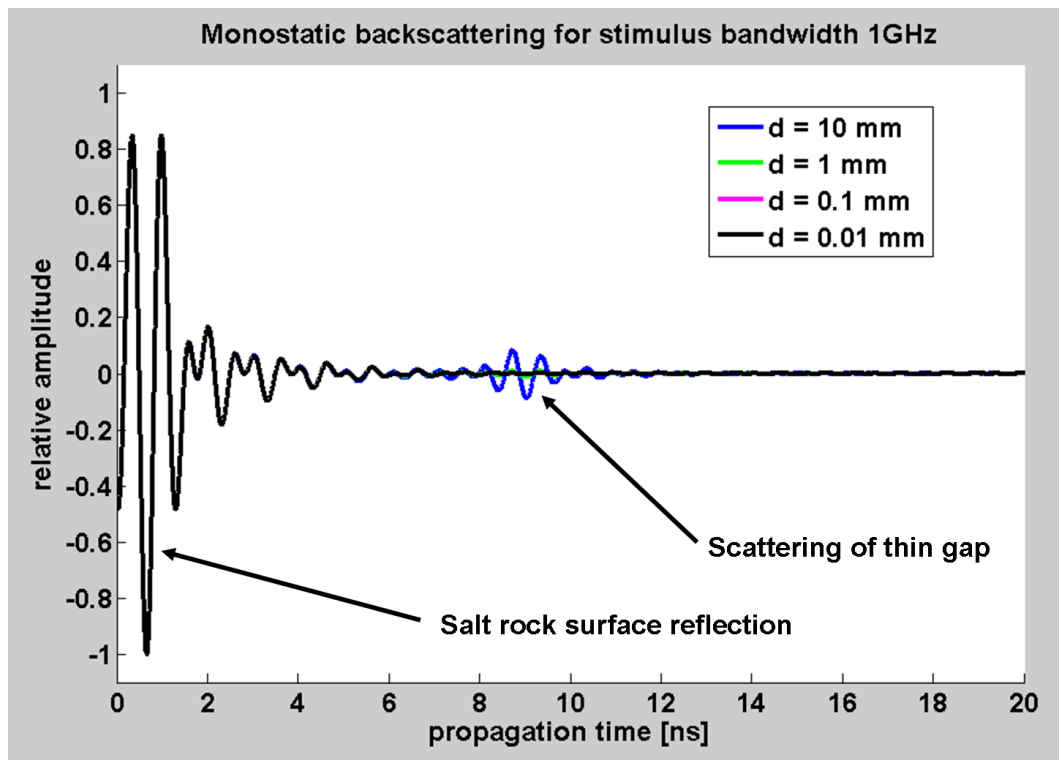
Fig. 2.8.: Simulated receive signals $y(t)$, stimulus bandwidth 1 GHz
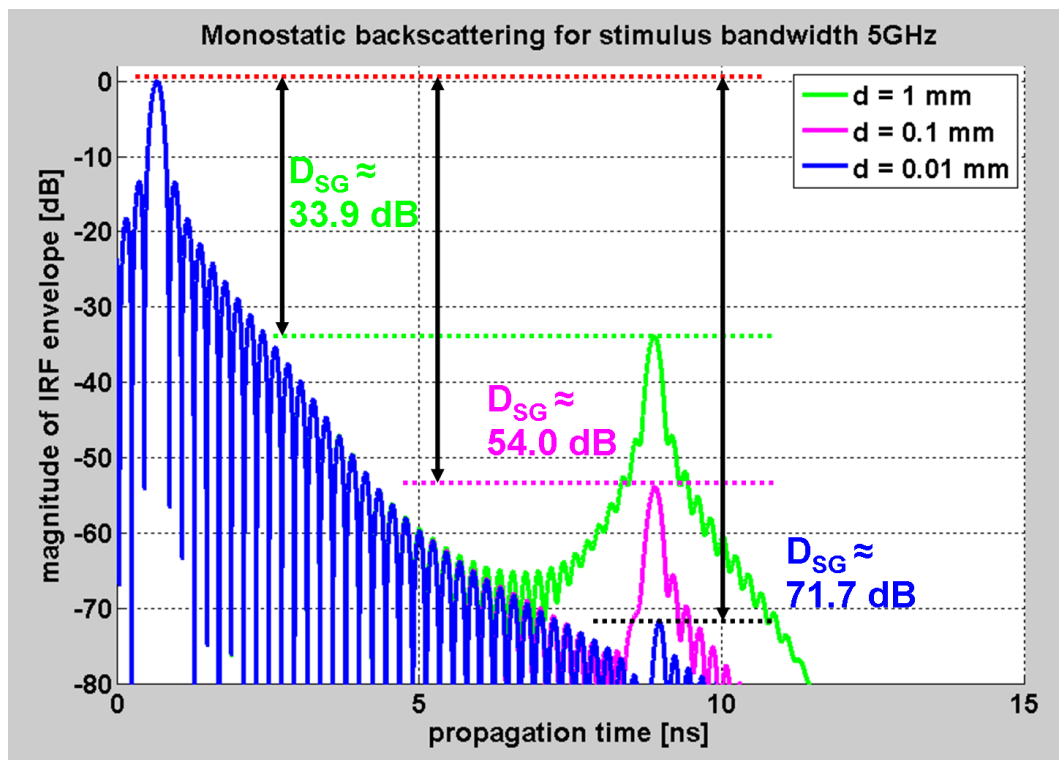
Fig. 2.9.: Simulated receive signals $20lg(|y(t)|)$, stimulus bandwidth 5 GHz
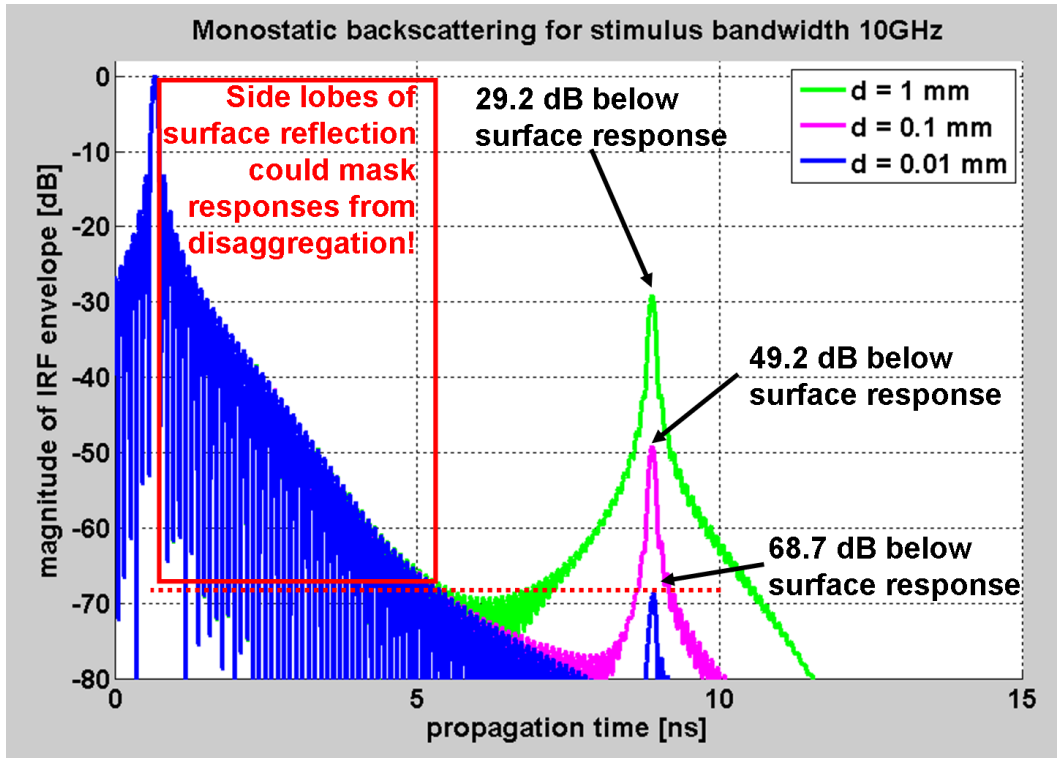
Fig. 2.10.: Simulated receive signals $20lg(|y(t)|)$, stimulus bandwidth 10 GHz

face reflection removal must be taken into account when designing data processing. For such an approach to work, the sensor must be extremely stable to obtain reproducible waveforms for the surface reflection. Recent investigation [87] has shown, that the time jitter of an UWB sensor is a crucial factor determining the ability to detect small targets hidden behind a reflecting surface. Even with a perfect device, the shape of surface reflections usually depends on surface roughness which is likely to change along a scan path. Good prediction of the exact time shape becomes difficult in such a case and it can be expected that the success of surface reflection removal will be limited. According to the author's experience a suppression in the order of 20 to 30 dB would already mean a good result. It can be concluded that detection accuracy for disaggregation very near (e.g. up to 10 cm or 1.6 ns propagation delay) the surface depends on resolution (measurement bandwidth), dynamic range, and success of surface response removal in data processing. For defects further away from the surface, device clutter suppression by calibration and noise performance of the sensor are the major limiting factors.

2.5. Summary of design goals for the new UWB sensor

In the preceding sections of this chapter, different aspects of disaggregation measurements in salt mines have been considered and some design goals for system architecture and parameters have been defined. Before presenting the newly developed UWB sensor device let us make a quick summary of these requirements.

The first question regarded a feasible frequency range for the radar sensor. The electromagnetic waves should be able to penetrate salt rock deep enough to cover the whole disaggregation zone (up to about 1m inside the salt rock) with moderate attenuation. Experiments have shown, that salt has good propagation properties for microwave frequencies below 20 GHz due to low attenuation. Even the range from 20 GHz to 40GHz shows moderate attenuation of about 20 dB/m and could be used. However, after analysing the dynamic range requirement of the measurement task the usage of frequencies below 20 GHz was preferred as a design goal due to low attenuation and easier handling of RF components.

For microwave frequencies the relative permittivity of salt rock is rather constant (low dispersion) and only changes between $\varepsilon_r \approx 6.0 \ldots 6.4$. The material shows no conductivity and has the permeability of free space. Therefore, the Fresnel transmission and reflection coefficients for perpendicular wave incidence on an air-salt boundary are $T \approx 0.91$ and $\Gamma \approx 0.42$ giving a moderate dielectric contrast between the materials forming the disaggregation zone.

With such a wide possible range of frequencies, the questions of operational frequency band and measurement bandwidth have been investigated. Two simple scattering models — one for thin gaps and one for small volume defects — merely provided the same conclusion. Both models show a high-pass character favouring the high frequencies or steep flanks over lower ones. Especially in the case of volume defects the reflection amplitude increases strongly with frequency. Steep flanks not only come along with high frequencies but also a very high bandwidth. Therefore, the goal was to build an UWB sensor covering a large part of the microwave spectrum below 20 GHz. Rather low frequencies, e.g. below 1 GHz, could be left out because they are not likely to contribute much to the backscattering from disaggregation yet would lead to large antenna sizes.

Even though there are different possibilities to realise interaction between electromagnetic waves and the disaggregation zone, only the use of air-coupled antennas proved reasonable and are the next design goal. Different types of surface waves could not be used because of physical reasons (evanescent waves exist only when looking from salt into air) or of technical reasons (Goubau lines need to be applied close to the medium and must usually be surrounded by it). The technical difficulties of scanning in different tunnel shapes and providing reproducible and close contact to the salt rock surface for

different surface roughnesses lead to the exclusion of surface-coupled antennas. Since occurrence, distribution, and alignment of defects or gaps in salt rock can generally not be predicted, it is desirable to do polarimetric measurements, i.e. acquire fully polarimetric datasets containing information on the two linear co-polarisations VV and HH as well as the cross-polarisation VH. For the measurement system this means to provide two ports, each connected to an antenna of different polarisation.

After the mode of operation has been fixed, the last aspect to be considered was the necessary dynamic range. In the case of ultra-wideband systems it makes sense to transfer the concept of spurious-free dynamic range (SFDR) into time domain by judging impulse response functions. System imperfections, which are essentially unavoidable for UWB devices, cause unwanted components in the received signal — the so-called device clutter. The nature of the device clutter can be very different so the time domain SFDR ($SFDR_{td}$) should be defined as the amplitude ratio of the wanted impulse to the largest clutter amplitude produced by system imperfections. To get an idea, how much $SFDR_{td}$ the new sensor must provide, the scattering model of thin gaps has been used in simple simulation calculations considering a system with air-coupled antennas and one gap in the disaggregation zone. The calculations have been done for different gap thicknesses and measurement bandwidths. The ratio of the surface reflection to the backscattering from the gap hints on the minimum $SFDR_{td}$ a system must have to be able to safely detect the gap. As it turned out, especially for sub-mm gaps **10 GHz and more bandwidth** are necessary to get achievable dynamic range requirements. Even with such a large measurement bandwidth, the $SFDR_{td}$ **should be in excess of 50 dB**. This is only possible with the appropriate calibration techniques not commonly used for GPR systems to date. The last design goal is therefore the ability to use system calibration for reaching an $SFDR_{td}$ of more than 50 dB for all measurement ports (full two-port calibration).

One design goal has not yet been mentioned throughout this chapter. The new UWB sensor must be able to work under the environmental conditions in salt mines, of course (most notably influence of salt dust in the air and the ambient temperatures). Furthermore, even the prototype must be rugged enough to survive handling in the mines even though specialised and trained personnel can be assumed during research experiments. The final longer-term goal (not in the focus of this work) is, of course, the seamless operation of the sensor by mining stuff and integration into the routine measurement activities. The following chapter now introduces the system concept of the new UWB sensor according to the design goals just defined.

3. UWB system design for detection of sub-mm disaggregation in salt

This chapter introduces the newly developed UWB sensor and explains its main components and features. Before doing so, a short review about available radar technologies will be given in order to motivate the choice of a particular design. The design goals derived in the previous chapter will be used to judge the feasibility of different technologies. The basic concept of the chosen technology will be introduced in more detail and the remaining part of this chapter describes the resulting new design and its functional units.

3.1. Overview of available UWB electromagnetic sensor technologies

Sensors using electromagnetic waves can come in many different flavours. It is not always obvious that the basic principle behind the different device types is the same. The sensor excites the test object with an electromagnetic stimulus and observes the reaction. The vast majority of test objects and scenarios (DUT — device under test) investigated falls in the category of linear time invariant (LTI) systems [88]. In this regard, linear means the object's reaction does not depend on the amount of excitation power and superposition of different responses holds. Time invariance of an object can be assumed, if the object remains in a steady state while the sensor acquires its response. This is also related to sampling theory and further explanation shall be postponed until section 4.1 of the next chapter. The behaviour of any LTI system can be fully described by its impulse response function (IRF) [88] $h(t)$[1] and the aim of any UWB sensor is to acquire a precise estimate of this function. Figure 3.1 shows the principal approach.

The relationship between stimulus, object response, and impulse response function is given in equation 3.1 [85]. The symbol $*$ denotes convolution. Obviously, if $x(t) = \delta(t)$ then $h(t)$ can be directly obtained. Most UWB devices use this approach. Generating a Dirac delta function is impossible in reality, but if the stimulus has a pulse-like shape and its duration is much shorter than the smallest time constant of the test object, $y(t) \approx h(t)$

---

[1]For the sake of simplicity, dependence from spacial dimensions is not mentioned here.
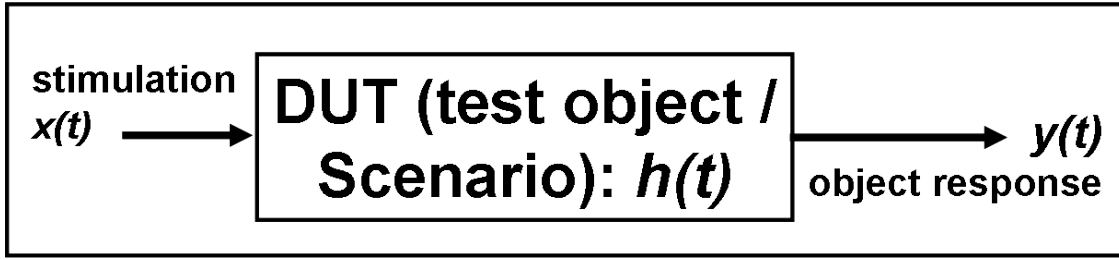
Fig. 3.1.: Principle for characterisation of an LTI system by UWB sensors

results. However, there are different equivalent solutions which result in other device conceptions. Equation 3.2 is easily derived from 3.1 by simple Fourier transform (equivalence of the equations requires linearity of the test object and sensor). The spectral counterpart of the impulse response is the frequency response function (FRF) $H(f)$. It can also be derived directly, if $X(f) = 1; \forall f$. This would mean a stimulus with infinite bandwidth, which cannot be generated in reality. The measured approximation $Y(f)$ will be a good estimate of $H(f)$, if the stimulus bandwidth extends beyond the frequencies relevant for the test object. Measurement devices may cover the desired bandwidth by using continuously or stepwise swept sine waves.

$$y(t) = h(t) * x(t) \tag{3.1}$$

$$Y(f) = H(f) \cdot X(f) \tag{3.2}$$

$$\psi_{xy}(t) = y(t) * x(-t) = h(t) * x(t) * x(-t) = h(t) * \psi_{xx}(t) \tag{3.3}$$

So far, devices either need to use pulses (very wide instantaneous spectrum) or sine waves (very narrow instantaneous spectrum) to acquire the IRF/FRF of the test object. The most flexible approach arises from equation 3.3. It is again derived from the initial solution 3.1 by correlation with the stimulus waveform at both sides. ψ_{xy} denotes cross-correlation and ψ_{xx} auto-correlation, respectively. The IRF $h(t)$ can be measured, if $\psi_{xx}(t) \approx \delta(t)$, i.e. the auto-correlation of the stimulus needs to be pulse-like. This requirement is fulfilled for every signal covering a large bandwidth regardless of its actual time domain shape $x(t)$. Devices can use specialised stimuli with desirable features such as low maximum amplitude, for example. The devices briefly discussed in the following subsections use either one of the above given equations.

To choose an appropriate basis for the development of a new salt mine radar it makes sense to list the main properties of common existing technologies and check them against the design goals. Electromagnetic sensors first appeared in the form of long-range radar for military purposes [89]. Since then, applications have become manifold and technology evolved quite a bit. The following technologies belong to the state-of-the-art:

- CW/FMCW principle: continuous wave/frequency modulated CW sensors, usually narrow- to wideband operation (compare equation 3.2)

- VNA principle: vector network analysers, stepped frequency CW sensors, narrowband to UWB operation (compare equation 3.2)

- Impulse principle: uses short and high impulses, usually wideband to UWB operation (compare equation 3.1)

- Correlation principle: uses noise or pseudo-noise signals, usually wideband to UWB operation (compare equation 3.3)

Good sources for technical descriptions and functional details summarised in the following subsections can be found in [90] and [91], for example.

3.1.1. CW/FMCW principle

As the name 'continuous wave´ indicates, CW and FMCW sensors use continuous signals for their measurements, more specifically sinusoidal waveforms. The most simple form of a CW-system are so-called Doppler sensors transmitting a sine wave with a fixed single frequency f_t. When the stimulus wave hits a reflector, a sinusoidal wave with frequency f_r is scattered back. If the reflector is not moving, then $f_t = f_r$. Otherwise, there exists a frequency shift proportional to the radial component of the target's velocity v_{rad}: $|f_d| = |f_r - f_t| \propto |v_{rad}|$. This is called Doppler Effect and the receiver is able to calculate the target speed by measuring the Doppler frequency f_d. Even though these sensors are quite sensitive and can have a very good resolution with respect to velocity, they do not have range resolution — i.e. they cannot say where a target is, only how fast it moves. Obviously, Doppler sensors are not useful for our application.

An extension to Doppler sensors are FMCW systems [92]. They use a tunable oscillator to produce a chirp signal. The frequency of the transmitted sine wave is continuously changed from a lower boundary f_l to an upper boundary f_u. After f_u is reached, the frequency is driven back to f_l and so on. This can be achieved by applying a repeated up and down ramp (or sawtooth) signal to the control input of the oscillator. The bandwidth covered by the device is given as $B_{FMCW} = f_u - f_l$. It is therefore possible to detect stationary targets as well. The stimulus wave leaves the transmitter with frequency f_t and takes some time to reach the reflector and get back to the receiver. Meanwhile, the stimulus frequency in the device has changed a little bit and is fed into the receiver as f_r. The receiver again measures the difference $\Delta f = f_t - f_r$. If the frequency is changed linearly over time (e.g. using an ideal linear ramp to control an ideal oscillator), the frequency difference Δf is proportional to the target's range. The situation is more complicated if the target moves. In this case, the frequency difference depends on target

range and Doppler shift simultaneously. This ambiguity is often resolved by doing an up- and down-chirp, i.e. controlling the oscillator with a triangular signal rather than a sawtooth.

The RF part of FMCW devices is not too complicated to build and highly integrated modules are commercially available at very low cost. For example, in the 24 GHz ISM band FMCW frontends covering up to 250 MHz of bandwidth are available for less than 20 Eur, e.g. from [63]. They are usually applied as motion or proximity sensors in automation and surveillance. Another well-known variety are automotive sensors working in the 76 GHz range [66]. A common property of these systems is the overall low relative bandwidth which is usually between the possible minimum of one and an upper value of two. Equation 3.4 shows the definition of relative bandwidth b_{rel}.

$$b_{rel} = \frac{f_u}{f_l} \qquad (3.4)$$

For the 24 GHz ISM band this would be $b_{rel} = 24.25\ GHz/24.00\ GHz \approx 1.01$. The main reason for a usually rather low b_{rel} that is the technical difficulty to build tunable oscillators spanning frequencies too far away from the centre frequency of the device. In most cases, not more than one frequency octave is technically feasible [90]. For the aim to cover as much of the band from 20 GHz down to 1 GHz as possible, at least a decade must be spanned, i.e. $b_{rel} \geq 10$. To use a single oscillator seems infeasible at the moment. A common option would be to build a cascade of sources splitting the whole operational band into octave sections. Synchronisation of the different stages would be a major problem. Another approach is using an oscillator for much higher frequencies, say 20 GHz to 30 GHz ($b_{rel} = 1.5$), and to mix this band down, e.g., to 5 GHz through 15 GHz. That would require RF mixers with extremely wide intermediate frequency output (IF output) range. Even though these solutions are possible, such systems would loose the simplicity of the FMCW approach.

Another critical point with these systems is calibration. To be able to apply correction methods for systematic errors, the complete information must be measured, i.e. not only the amplitude but also the phase must be acquired for every Δf. This could be done by I/Q-downmixing [93], using two versions of the local oscillator frequency f_r which must be exactly 90° apart. Since the transmitted frequency (and thus f_r) changes continuously, it is very difficult to assure the 90° phase shift for the I/Q-mixing in the receiver. Furthermore, reproducibility of the system would be severely affected by the stability of the oscillators involved, i.e. their phase noise over the whole range of frequencies. There exist other CW principles tailored for spanning larger relative bandwidths with well-established calibration techniques. These devices circumvent the mentioned problems by changing the frequency in discrete steps rather than in a continuous manner. All oscillators and the I/Q-stages involved are given enough time to stabilise into a controllable steady state.

Such systems are called network analysers and will be described in the next subsection. For now it can be concluded, that FMCW is not a promising approach for inspection of the disaggregation zone with a large bandwidth in the lower GHz range.

3.1.2. Vector network analysers

Network analysers are very flexible devices usually found in a laboratory environment. As the name indicates, they are used to characterise electrical networks. As an interface to the networks, one or more coaxial measurement ports are provided and in most cases reflection at each port and the transmission between any two of the ports can be acquired. The measured networks can be of very different nature, e.g. coaxial devices such as filters or amplifiers, a waferprobe environment for characterising circuits on a wafer or substrate, or radar measurements involving antennas at the test ports. The measurement principle is also based on continuous wave stimulation by single frequency sine waves. The frequency is changed throughout a measurement cycle, but in contrast to FMCW it is swept in discrete steps. At each frequency between the lower limit f_l and the upper limit f_u, the analyser waits until the stimulus source, the test object and the receive filter have settled. Usually the amplitudes of the stimulus sine wave and the returned signal are acquired and their ratio is measured. In the case of vector network analysers (VNA), not only the amplitudes but also the phase shift between the transmitted and received sine wave are analysed. This task is especially challenging, since perfect I/Q-demodulation is necessary for precise measurements. Appropriate settling time and regulation of the I- and Q-part of the receiver's reference oscillator must be provided. Measurements are done directly in frequency domain and a VNA basically acquires the FRF of the tested network. The time domain equivalent IRF can be calculated by the inverse Fourier transform, if the frequency step f_{step} is kept constant over the whole bandwidth and f_l as well as f_u are compatible with the step size. The duration of the IRF t_p is then the inverse of f_{step}. The bandwidth spanned is simply $B_{VNA} = f_u - f_l$.

Since the major task of network analysers is the precise characterisation of unknown networks in a laboratory, these devices are build very complex to ensure good performance and flexibility. For example, modern devices span the whole frequency range from as low as 10 MHz to as high as 67 GHz with up to a few thousand frequency samples [94] all in one device. The operator can chose the operational band almost completely arbitrary. Furthermore, an extensive amount of research has been put into calibration techniques in the last decades. Examples can be found in, e.g., [84], [95], or [96]. These techniques and their accuracy boundaries are well understood and established. Some methods demand more complex procedures than others, but recently automatic calibration units containing all needed calibration standards have been developed and can be easily deployed. The raw performance (or raw dynamic range) of leading-edge equip-

ment is specified up to about 150 dB by the manufacturers [94]. The achievable accuracy and $SFDR_{td}$ after calibration depends on the system stability, the calibration standards used (more precisely on how accurate their real behaviour is known), and the specific calibration method. To date it is accepted that VNAs provide among the most accurate measurements of all sensors.

So far, many of the design goals defined for our salt mine task could be accomplished by VNAs: UWB operation below 20 GHz (and even beyond), multi-port configuration, and the ability for high-quality calibration. However, all the advantages of network analysers come with some downsides. These devices are most of the time very bulky, sensible to environmental and mechanical conditions, consume a lot of power, and are very expensive. Recently, hand-held VNAs appeared and are applied for outdoor tasks in GPR like in [55] and [97]. Current compact devices are still expensive and feature only a limited frequency range (e.g. up to 6 GHz in the mentioned examples). Another important downside is measurement speed. Since the frequency samples are taken sequentially, it usually takes longer to complete a frequency sweep than to measure a time-domain IRF by other systems. The main reason is the mentioned settling time of the narrowband receive filters at the intermediate frequency and the regulation of reference oscillator phases. Modern devices as in [98] use some kind of sweep time optimisation by replacing stepped with continuous sweeps but this introduces problems for test objects with long electrical delay and finally the settling time of receive filters remains as limiting factor of measurement speed.

All in all, VNAs seem a possible solution for the intended task. If some of the flexibility of these devices would be sacrificed, smaller and less expensive designs could result. Slow measurement speed could be tolerated for the prototype stage of the investigation but would be a problem for later productive systems. However, current VNAs summarise decades of experience collected by the manufacturers and researchers alike, so it would not be feasible to make a specialised system without this expertise. Even if VNAs are not ideal for salt mine deployment, it certainly is wise to learn from their system architecture and the vast calibration possibilities. Their are also a prime candidate for verification of calibration accuracy of other systems.

3.1.3. Impulse radar

Contrary to the principles discussed so far, impulse radar works in time domain. The classical tasks of radar — detection and ranging — are easily accomplished by looking at the impulse responses of the observed scenery. Impulse radar directly measures the IRF (limited, of course, to the respective working frequency band) by using short pulses as stimulus. The more bandwidth the system covers, the shorter the impulses become.

Modern UWB pulse radars [99] can typically cover a few GHz resulting in full-width half-duration (FWHD) of the pulse in the order of a few ten ps. The pulse is issued by means of a repeated trigger signal also synchronising the data acquisition. Repetition rate and therefore stimulus period can be setup by the operator. An UWB stimulus spans a large bandwidth and consequently real time sampling is often not feasible (limited accuracy of very fast analogue to digital converters (ADCs), handling of the large digital data stream, etc.). That is why many systems use sub-sampling, also known as stroboscopic sampling or equivalent-time sampling. The capturing of one complete waveform is distributed over subsequent impulse periods, i.e. per generated impulse only one or few samples are taken. Typical real sampling rates are in the kHz to MHz range enabling the use of high-resolution ADCs. The triggering unit has to ensure a different (and known) offset between the sample time and the impulse event in each period. Sub-sampling lowers the overall receiver efficiency, because a large amount of transmitted power goes unnoted and it takes longer to acquire an IRF. Data acquisition speed is nevertheless a strong point of impulse radars, especially when comparing them to network analysers.

There are some other implications in the way these sensors work. On one hand, pulse repetition rates of these radars often start from 10 MHz minimum enabling a period duration of up to 100 ns for short-range applications. On the other hand, to cover an ultra-wide bandwidth, sub-ns pulses are needed. Therefore, the transmitter is not active most of the time. This is expressed as the so-called duty cycle, giving the fraction of the repetition period in which energy is actually generated. Typical duty cycles are 1% or even below in contrast to CW techniques which reach up to 100%. The basic signal-to-noise ratio (SNR) of the measurement is influenced by the total submitted energy and the energy of the wideband noise in the received signal. That means, in order to achieve good SNR values, a lot of stimulus energy must be put into only a small portion of the whole signal period. Since the transmitted waveform are short pulses, their peak power and consequently their maximum voltage must be very high. Tens of volts are not uncommon [49]. This fact is a major downside of impulse systems. The high voltages impose a lot of stress to the electronics decreasing the repeatability of the exact stimulus waveform and requiring difficult on-chip shielding of the pulse generator. To circumvent internal crosstalk problems the pulse generator is often a separated device connected only to the triggering unit. In classical applications of ranging, the targets are in the far field of the antennas, i.e. the stimulus has to travel a certain minimum delay time before any useful reflection can reach the receive antenna. In order to avoid detecting the large stimulus amplitudes, the receivers can be muted for a short time right after the pulse has been sent and antenna crosstalk has settled. This is called range gating. In such an operation mode, impressive raw system dynamic ranges can be realised because receiver sensitivity can be high even though the transmitter submits very high power levels. However, for our application in salt mines far-field measurements can not be assumed and are even rather unlikely.

Gating out the transmitter pulse and antenna crosstalk will not be working here and for good calibration results the stimulus waveform must be acquired anyway (more on that topic in chapter 5).

The lack of a stable stimulus waveform or the ability to acquire it without burdening the receiver electronics is one reason why calibration is hard to apply for these devices. Another one is related to the timing of sampling. As mentioned above, trigger pulses are used to start the generation of the stimulus. At the same time, the trigger has to pass a variable delay before it causes the ADC to take a new sample. The delay must be varied in constant steps over the whole stimulus period in order to allow the acquisition of a complete waveform (again, this is a requirement of common calibration techniques). The stability of this delay and the equality of its steps determine the accuracy of the time base lying under the acquired impulse responses. Unfortunately impulse radars often suffer from large jitter (random variation in the delay step) additionally decreasing repeatability of the whole system. The main reason for the rather unstable delay steps is that many systems use slow ramp signals and a variable threshold detector to realise the delay [90]. The ramp must span the whole stimulus period (e.g. up to 100 ns) and its low slope together with unavoidable amplitude noise translates into these unwanted variations. Another source of system jitter is the pulse generator producing a slightly different delay after each trigger. State-of-the-art UWB systems are specified with RMS jitter values of a few ps [50], clearly limiting the ability to sample UWB signals with frequency components beyond 10 GHz or with steep flanks of rise times in the order of a few ten ps.

Summing it all up, impulse radars have some pros and cons just like the principles discussed before. They are widely commercially available (though models with more than 10 GHz bandwidth are not common), use a well-established technology, and are quite flexible in terms of data acquisition setup (e.g. repetition rate, equivalent sampling rate, etc.). However, stability problems of the pulse generators and the inaccuracies of the sampling time base caused by jitter and other effects put doubt into successful application of calibration methods. Moreover, range gating to protect the receivers from the high peak powers of the pulse generator is not feasible with our application. The impulse radar principle is therefore not a prime candidate for measuring the disaggregation zone in salt.

3.1.4. Noise and pseudo-noise principles

The last sensor principle to be considered here are noise-based radars. The idea of these devices is to use a random (or pseudo-random) stimulus signal covering an ultra-wide bandwidth. The noise is amplified and transmitted into the test object and its response is captured. To get the IRF of the test object, correlation of the measured data with the stimulus signal needs to be calculated. From a signal theory point of view this works

because the auto-correlation function (ACF) of wideband noise is very short resembling some sort of impulse. If real noise is used as a stimulus, the transmitted signal is not periodic and must be sampled for correlation, The use of sub-sampling is not very straight forward in this case and that is a major issue for UWB operation. Classical solutions like in [100] used analogue correlators instead of digital calculations. While this seems like a good idea to ease the requirements on the sampling unit, it has some serious drawbacks. First of all, one has to construct steerable delay lines for the correlator spanning the whole duration of one IRF period. To reach short ranges of a few metres like needed in our application, the periods must be several ten ns. This causes rather bulky delay lines which are difficult and expensive to build. Another disadvantage is the fact, that the IRF must be sampled directly just like in the case of impulse radars. In principle the same issues would apply.

Another class of noise-based UWB sensors are not really using random noise as stimulus. Pseudo-random signals are employed instead. Such signals can also cover large bandwidths, but sub-sampling can easily be applied due to their periodic nature. The IRF of the test object is again calculated by cross-correlation. In fact, each signal with a short auto-correlation function (i.e. impulse-shaped ACF) is feasible. The main difference to impulse radars is the distribution of the stimulus energy over the whole period, i.e. the duty cycle reaches up to 100%. This means for the same SNR, the overall voltage levels can be much lower than for the pulse case. That relaxes requirements on the generator and the receiver electronics quite a bit, enabling a more reproducible and stable behaviour.

For pseudo-noise sensors the stimulus does not need to be acquired, because a stored digital representation of the known signal can be used for correlation calculation. The correlation is another difference to impulse radars, which do not need such processing. Even though the acquisition by sub-sampling can be used, range gating to protect the receiver cannot be applied because the whole signal is needed for correlation. It is therefore mandatory to choose signals with low maximum levels. Otherwise receiver sensitivity would have to be sacrificed, i.e. they would need to cope with large voltages just like unprotected pulse radar receivers. The timing unit must assure the sampling of different time instants within the stimulus period. The same conditions and issues noted for impulse systems in subsection 3.1.3 apply here as well. However, because of the overall relaxed requirements to handle peak voltages, a tight integration of stimulus generator, timing unit, and sampling unit is possible and lower jitter can be achieved.

An interesting example of a family of pseudo-noise sensors has been developed by the group of Sachs et.al. [82] at the EMR Lab. The stimulus used is a special kind of pseudo-random binary code — a so-called maximum length binary sequence (M-Sequence, MLBS). It has many desirable features — a short ACF, an even distribution of energy over the whole stimulus period (thus avoiding high peak voltages), and very good reproducibility due to its binary nature. The period duration of the M-Sequence system is defined by

the system clock f_c pushing the MLBS generator and the order of the MLBS. Most of its spectral energy is concentrated in the baseband from DC to $f_c/2$ which is considered the most useful frequency range of these sensors. Another big advantage is the fact, that not only the stimulus, but also the sampling timing can be derived from the same single clock in a very stable manner without the need for slow ramps. It is based on another digital circuit — a binary divider. This should help to keep the jitter as low as possible and the accuracy of the time base very high. Older publications like [101] estimate jitter values in the order of 100 fs. Recent investigation [102] has stated similar performance with even more confidence in the results. The basic system concept realises an equivalent sampling rate of $f_{s,equiv} = f_c$. The stimulus is band-limited to $f_c/2$ without wasting too much of the total signal energy. Acquisition speed is comparable to other time-domain systems such as impulse radars.

The M-Sequence sensor does have some issues as well. Besides the inability of range gating, the baseband system concept is less flexible than VNAs or impulse sensors in terms of acquisition setup, e.g. stimulus duration and sampling rate cannot be freely chosen. For example, any change in f_c must be reflected in the band-limiting filters. As described in chapter 2, baseband operation is not preferred and a bandwidth of more than 10 GHz is desired. The basic M-Sequence principle has been published with up to 4 GHz bandwidth and an ambiguity range of about 9 m in air so far. However, modifications using up- and down-mixing of the stimulus to shift and enhance the operational frequency band have been introduced in [82]. This is done without introducing another clock domain such that the whole system still only depends on a single stable clock.

Since the unambiguous range of the existing system is large enough for the disaggregation zone, multi-GHz bandwidth examples exist, and M-Sequence sensors work very stable and reproducible, the lack of flexibility can be tolerated. However, some aspects would have to be developed while trying to keep the advantages: even larger bandwidth, higher equivalent sampling rate, and calibration procedures suitable for the M-Sequence systems.

Especially the last point — calibration — is very interesting to investigate and to compare with results from network analysers. If good performance after calibration could be achieved, an alternative for the expensive and bulky lab-VNAs would arise for field applications. Another strong feature of the M-Sequence concept is its high integration potential. Current devices are already very compact and efforts for further reductions in size and power consumption are being made [103].

Considering all discussed sensors principles, only the M-Sequence concept or network analysers remain as promising solutions. The other principles have disadvantages making their adoption to the needs of salt mine measurements infeasible — especially the missing calibration capability would be hard to overcome. Given the rough environmen-

tal conditions in salt mines not suitable for most VNAs and the high integration potential of M-Sequence devices, it is worth the effort of extending the basic concept as stated above. The M-Sequence principle was consequently chosen as a starting point. Before discussing the extensions in more detail, the basic system is described more elaborately in the next section.

3.2. The starting point — review of the M-Sequence UWB sensor principle

Even though the M-Sequence principle has already been described in many publications like [104], [82], or [103], it makes sense to repeat some details here to facilitate the understanding of the enhancements introduced throughout the rest of this chapter. Figure 3.2 shows the block schematic of the basic M-Sequence system working in the baseband. It can be divided into two main groups of components — the RF chipset containing high frequency circuitry and the high speed digital backend responsible for digitising, preprocessing, and data transfer to a computer. Their respective roles will be reviewed in the following subsections.
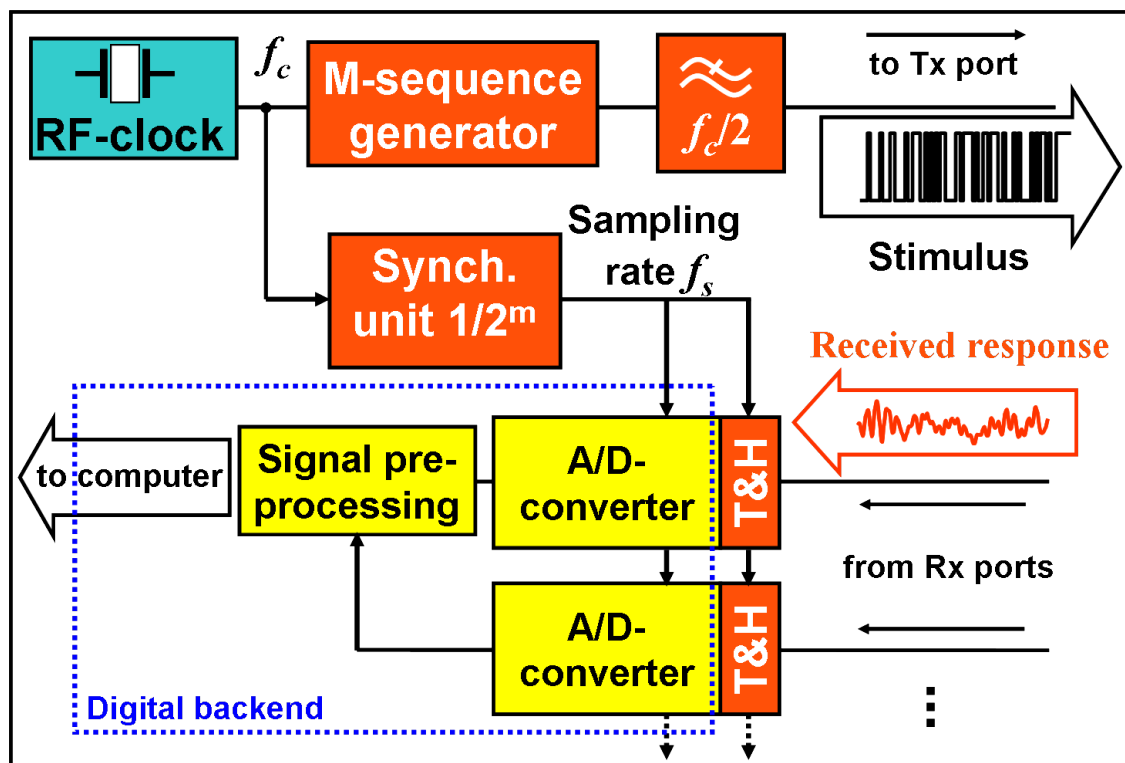
Fig. 3.2.: Block schematic of a baseband M-Sequence sensor

3.2.1. RF chipset of basic M-Sequence devices

There are three main components forming the basic chipset for an M-Sequence sensor. One integrated circuit (IC) is responsible for stimulus generation, the [nd] is a synchronisation unit, and 3rd a track&hold circuit with ultra-wide input bandwidth aids the digitising by slower ADCs.

Besides these custom-designed ICs, the master clock source belongs to the RF part as well. It could be a specially crafted circuit or a commercially available oscillator. In the latter case, stable devices with very low phase noise are available, e.g. [105].

M-Sequence generator   An M-Sequence is a binary signal easily generated by a digital shift register with appropriate internal feedback. The number of flipflops n in the register defines the order of the pseudo-random code. They are pushed by the master clock rate f_c and in each clock cycle, an elementary rectangular pulse is put out. The randomness lies in the polarity of the pulse, i.e. whether it represents a logical 0 or 1 (or -1 and 1, respectively). The amplitude of the elementary pulses is much lower than in the impulse radar case — it depends on the logic voltage levels of the semiconductor technology used to realise the generator. Current devices are fabricated in a special SiGe:C bipolar process [103] using symmetrical signals with swings of about 400 mVpp. The crest factor of an ideal M-Sequence is 1.0 — the lowest possible value. Figure 3.3 shows the time shape, frequency spectrum, and ACF of an ideal M-Sequence of order 3. Equations 3.5 through 3.7 express the basic relations.

$$N = 2^n - 1 \tag{3.5}$$

$$T_0 = 1/f_c \tag{3.6}$$

$$T_p = NT_0 = 1/PRF_{\text{MLBS}} \tag{3.7}$$

Herein, N is the total number of elementary pulses (also called 'chips') per period, T_0 is their duration, and T_p the duration of a complete period (or the inverse of the equivalent pulse repetition frequency PRF_{MLBS}). As can be seen in figure 3.3, the ACF really is short resembling a pulse with a FWHD of T_0. Due to the rectangular nature of the elementary pulses, the power spectrum of an M-Sequence has the typical $sinc^2(f)$ envelope. As stated in subsection 3.1.4, it makes sense to use the band up to $f_c/2$, since its spectrum is rather flat and contains about 80% of the total signal energy. Moreover, in real systems the steep flanks of the ideal signal cannot be generated, i.e. the rise time is limited by the abilities of the semiconductor technology, load conditions, etc.

Signal period
$$T_p = N T_0$$

relative amplitude

A

0

$T_0 = 1/f_c$ … single state of M-sequence ('chip')

time

Auto-correlation function

A^2

$$-\frac{A^2}{N}$$

$$T_p = N T_0$$

$2T_0$

0

time lag τ

spectral power

$f_c/2$

$\approx$ **80% of total signal energy up to $f_c/2$**

Sinc²(f) envelope

$1/T_p$

0   f_c $2f_c$ frequency
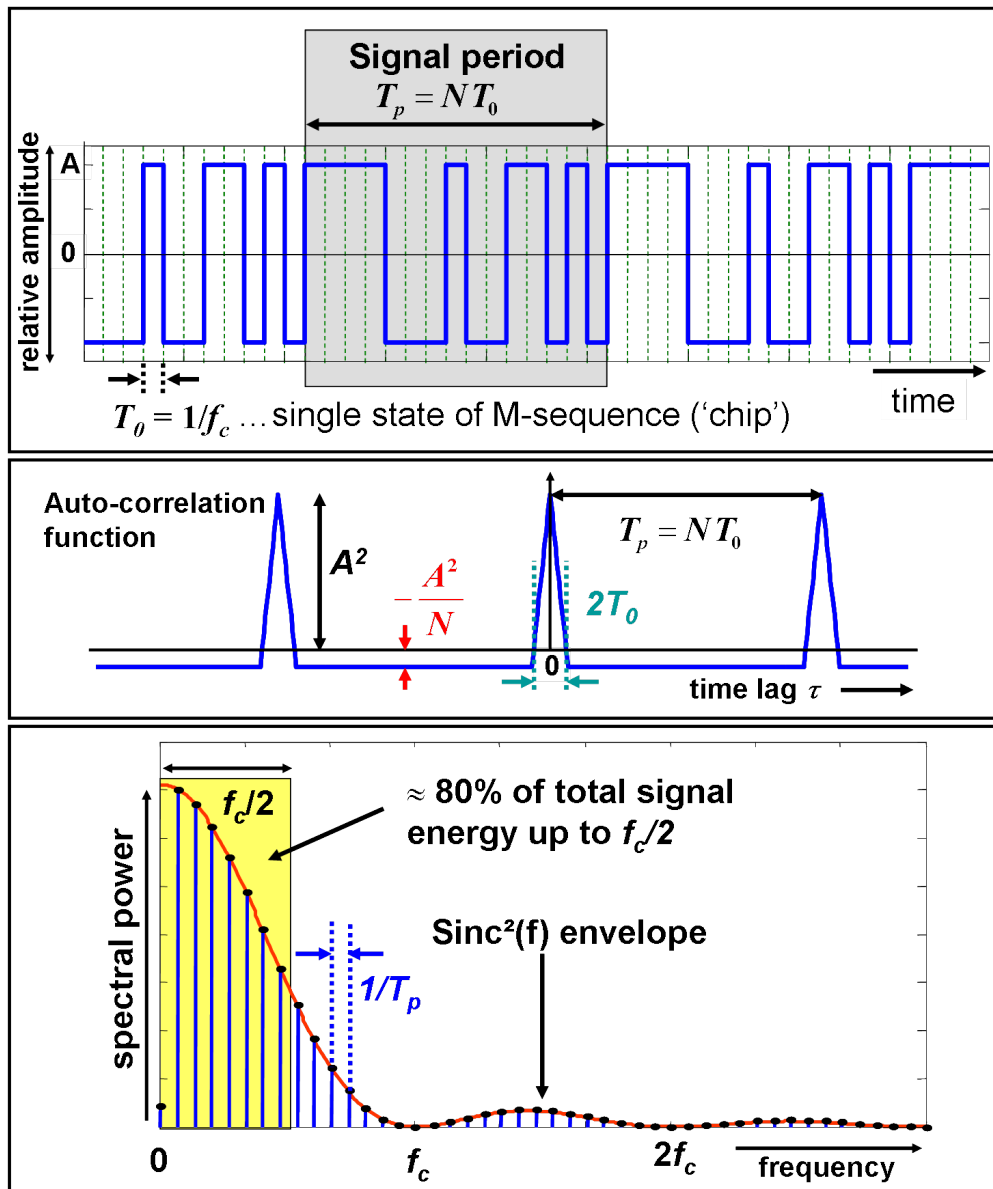
Fig. 3.3.: Ideal M-Sequence of order 3

Common realisations of baseband sensors use a 9th order stimulus at clock rates of 9 GHz. The circuits are easily able to cover frequencies up to 4.5 GHz, since the 3 dB-bandwidth of the output amplifiers has been measured to be well beyond 10 GHz [103] in 50 Ω environments. Figure 3.4 shows a section of a 9th order M-Sequence (without the lowpass filter) as generated by a realised M-Sequence generator.
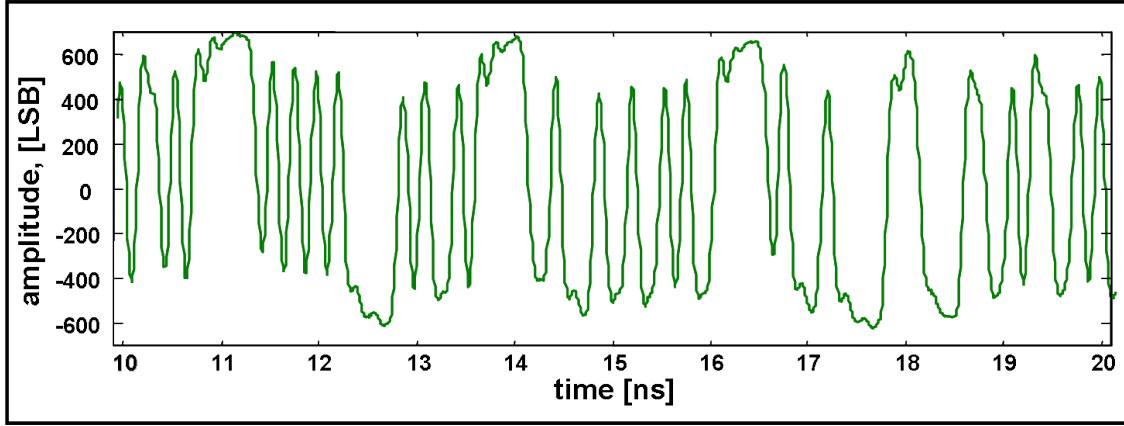
Fig. 3.4.: Section of a 9th order M-Sequence recorded by an oscilloscope

Synchronisation unit   Main purpose of the synchronisation unit is the generation of the real sampling rate f_s by a digital pre-scaler. Besides that, it translates the master clock signal, which comes in as a sine wave, into a rectangular clock signal with rate f_c. This signal is used to trigger the generator with very steep flanks. It is also used to drive the internal pre-scaler. The scaler itself is once again a simple digital circuit — a binary counter with m flipflops dividing the master clock according to equation 3.8. It should be noted that the divided output of the synchronisation unit also features very steep flanks to drive the track&hold stages despite the fact that f_s is usually in the MHz-range while f_c is worth several GHz.

$$f_s = f_c/2^m \tag{3.8}$$

$$T_s = 1/f_s = T_p + T_0|_{m=n} \tag{3.9}$$

Theoretically, any power of two would do as pre-scale factor [104], but the most obvious choice is $m = n$. In such a case the divider can be constructed almost the same as the generator — it simply lacks the internal feedback. In order to understand the sub-sampling mechanism let us compare the sampling frequency f_s to the repetition frequency PRF_{MLBS} of the M-Sequence. Both are derived from f_c, but in the case of f_s the scaling factor is 2^n compared to $2^n - 1$ for PRF_{MLBS}. This slight mismatch ensures, that every time

a sample is taken it is not taken at the same point within the stimulus period. As stated in equation 3.9, the sampling period is exactly one clock cycle longer than the M-Sequence period. This means that subsequent sampling points belong to subsequent elementary pulses of the stimulus and are therefore one clock period T_0 apart. The resulting equivalent sampling rate is consequently equal to the master clock rate: $f_{s,\text{equiv}} = f_c$. The situation is illustrated in figure 3.5 for a 2nd order M-Sequence.
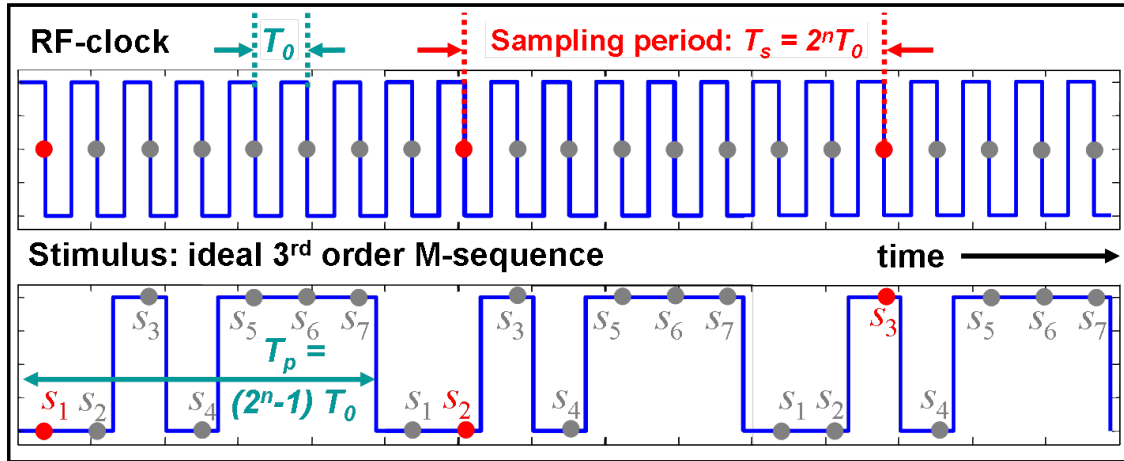
Fig. 3.5.: Illustration of sub-sampling timing in M-Sequence devices

There are two aspects standing out when comparing the synchronisation unit to other sub-sampling circuits in time domain UWB sensors. The first advantage is the easy digital implementation. It not only ensures proper repeatability of the timing, it is also based on a single clock frequency, i.e. a single time base. The second aspect is the fact, that everything is triggered by very steep flanks. The stimulus generator is driven by a rectangular clock rather than a sine-shaped signal. The same flank steepness is used to drive the sampling circuits. The only slower rising signal is the master clock at the input of the synchronisation unit. However, the actual rise time within the switching threshold of the input buffer (which is in the order of a few 100 mV) can be lowered by using high output power oscillators if needed. There are no slow ramps involved and the slew rate of the pre-scaled output clock is well above that of a sine signal with the same low frequency in the MHz range. In [106] it has been shown that typical 10%–90% rise times of synchronisation signals are about 20 ps. All these aspects help to stabilise the time base of an M-Sequence sensor resulting in the already mentioned low jitter values.

Track&hold circuit The last custom IC of the RF part is the track&hold circuit which is used to aid the capturing of the receive signals at the sensor inputs. During half the sampling clock period T_s, it simply passes the received signal to its output (track phase). At the falling edge of the sampling clock it enters the hold phase in which the momentary

value of the input (at the time of clock transition) is stored and provided at the output as a constant voltage level. Thus it translates the fast-changing UWB signals at the input into a series of snapshots changing with the slow regime of the sampling clock. During the hold phase, analogue to digital conversion can take place.

Due to its function, this IC is not a digital circuit like the others discussed before. It is by far the most complex component and has a large influence on the noise performance and saturation level of the sensor, e.g. it heavily influences the raw dynamic range. Characterisation of an older generation of ICs in [106] has shown the very wide input bandwidth of the receivers. A 3 dB bandwidth of about 12 GHz was obtained and it can be expected that newer generations work well beyond this limit. The wide bandwidth can be judged from different points of view. For baseband operation with a band-limited 4.5 GHz stimulus it is disadvantageous, since a lot of noise power is collected in the unused frequencies. On the other hand, for our goal of spanning more than 10 GHz bandwidth with the new UWB sensor it opens up interesting options for system design — more on this topic in section 3.3.2 and chapter 4. Besides the basic functionality, the track&hold circuit also features a sampling clock recovery stage. It can be used for easy chaining of multiple receive channels all using the same sampling clock. This is an important factor for building sensors with multiple measurement ports as needed for the salt mine sensor. However, the clock chain could provide a path for unwanted receiver crosstalk as well.

3.2.2. Digital backend of basic M-Sequence devices

The tasks of the digital backend are threefold. It contains the actual ADCs, manages data acquisition and optionally a certain degree of pre-processing, and provides an interface to a measurement computer (most of the time a common PC). Due to the use of sub-sampling, the circuits do not need to work in the GHz range and standard ICs and common interface solutions can be employed. Nevertheless, the amount of data to be handled should not be underestimated. In the standard implementation, the M-Sequence sensors work with a 9th order stimulus and a 9 GHz master clock rate. The pre-scale factor for the sampling clock is 512, leading to a sampling rate f_s of approximately 17 MHz according to equation 3.8. Typical resolutions of modern megasample ADCs are around 12 bit. Assuming such conditions, the resulting raw data stream would be more than 25 MByte/s per receive channel and would contain more than 34.000 IRFs/s.

While modern storage solutions and peripheral bus systems such as USB2.0 are certainly able to handle one or two receivers in such a raw mode, in most applications this is neither necessary nor feasible. Using the periodic nature of the sensor principle, averaging of subsequently measured periods is one way to reduce the amount of data to be transferred to the PC and processed later. Another advantage would be lowering of

the noise level in the resulting averaged data as long as coherency (or stationarity) of the measured objects holds during averaging time. Further pre-processing steps could be the calculation of the actual IRFs by implementing the correlation with the known M-Sequence stimulus in some kind of embedded signal processor. Such operations can be realised very efficiently with specialised hardware thus reducing the demands on processing power in the (non-specialised) PC. If the backend was designed as a complete embedded computer system, it could cover the whole data processing needed by an application and simply show the results to the operator without the need for a PC at all.

It should also be noted that the digital backend has major influence on the raw system dynamic range. On the lower end, the noise level is influenced by the averaging capabilities and the quatisation noise produced by the ADCs. The upper signal levels are finally limited by saturation of buffer amplifiers and the linearity of the converters. Another issue could arise when implementing multiple receive channels in one design — ADC channel crosstalk should be minimised in this case.

As a basis for development of a new sensor for salt mine measurements, a commercially developed custom backend has been used. The design with part number "MLC40V2.1" was obtained from MEODAT GmbH — a partner company in M-Sequence system development. They kindly provided details about the component and its firmware for further enhancements. The MLC40 backend features two buffered ADC channels with 12 bit resolution each. The data is captured and transferred into a software-configured digital hardware circuit (field programmable gate array — FPGA). The design also includes an embedded digital signal processor (DSP) and a 100BaseTx Ethernet interface for communication with a PC. An optional single digital-to-analogue converter (DAC) was available as well. Since the main components of an M-Sequence sensor system have been introduced so far, we can now start to discuss the extensions realised for the new system.

3.3. New 12 GHz bandwidth M-Sequence UWB sensor

Using the basic M-Sequence principle, a number of extensions have been developed to meet the goals derived in chapter 2. An important paradigm for the new system was to keep as much of the stability and reproducibility as possible in order to facilitate calibration. Since calibration methods are well-known for network analysers and these devices are easily able to acquire fully polarimetric datasets (using two measurement ports) in S-parameter configuration, VNAs have been used as an archetype for some aspects of system design. For example, two-port VNAs exist in different setups using three or four receivers. The latter case is better suited for modern calibration methods [84] and has therefore been adapted for the new M-Sequence sensor. In particular, three main steps

have been taken from the basic to the new system:

- Increased stimulus bandwidth to cover more than 10 GHz

- A four channel receiver able to handle the new stimulus

- Frontend for measuring the complete S-parameter set of two ports incl. calibration

The following subsections will describe these steps. To provide a first overview, a rough system outline is shown in figure 3.6.
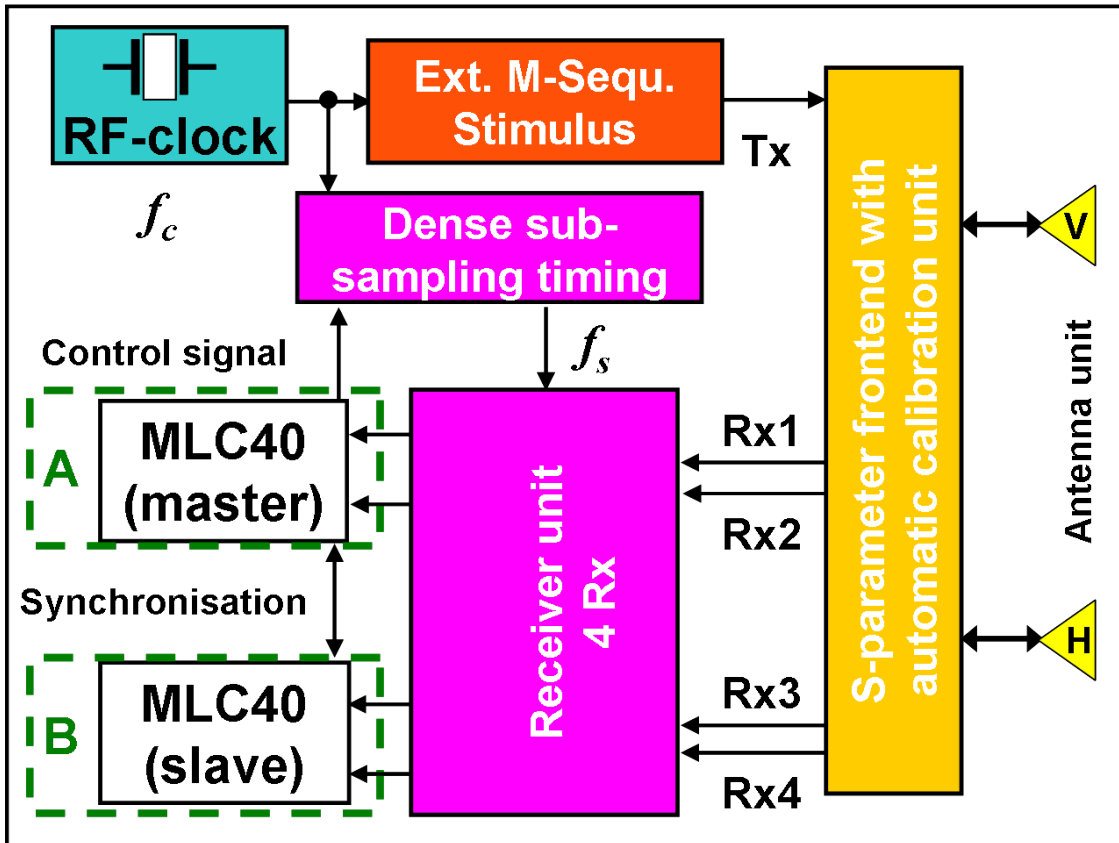
Fig. 3.6.: System outline of 12 GHz bandwidth M-Sequence sensor

3.3.1. Extended M-Sequence stimulus

Extending the bandwidth of an M-Sequence system is straightforward, if higher master clock rates f_c can be used. At the time the development of the salt mine system began, common clock rates were 7 GHz and 9 GHz providing about 3 GHz or 4 GHz bandwidth in the baseband, respectively. Measurements have shown [106] that clock rates above 10 GHz could be used with the available RF chipset but functioning was not expected beyond 15 GHz. Resulting bandwidths would have still been too low so this simple approach was not used.

Other examples of extending bandwidth have been realised as well. In [82] a system is described, which uses commercial wideband mixers to shift and extend the operational band at the transmitter and to fold it back into the baseband at the receivers. This system used a master clock of 7 GHz also applied as the local oscillator signal to all mixers. This way, the resulting stimulus covered the band from about 3.5 GHz to 10.5 GHz while keeping everything synchronised to only one single clock source and using the same stable sub-sampling scheme. It should be noted that the resulting stimulus is not a simple M-Sequence any more. It still has the pseudo-random nature, but the crest factor of the signal is somewhat degraded. Capturing of the actual transmitted signal as a reference is therefore recommended to aid the digital correlation needed to obtain the IRF from measured data.

Using the same approach with a master clock rate of 9 GHz would consequently result in spanning the band from 4.5 GHz to 13.5 GHz — a promising perspective even though the lower frequency cut-off would be too high. An obvious way to fill the low frequency band again would be to add the baseband stimulus and its up-converted counterpart by means of a passive power divider or an active power combiner. Figure 3.7 illustrates this idea also showing the resulting power spectra from simulation calculations assuming ideal components and signals. Please note that the band-limiting filters at the output of the M-Sequence generator have been removed compared to figure 3.2. Their stop-band transition is from 4 GHz to 4.5 GHz which would lead to an unwanted gap between 4 GHz and 5 GHz in the extended stimulus spectrum.
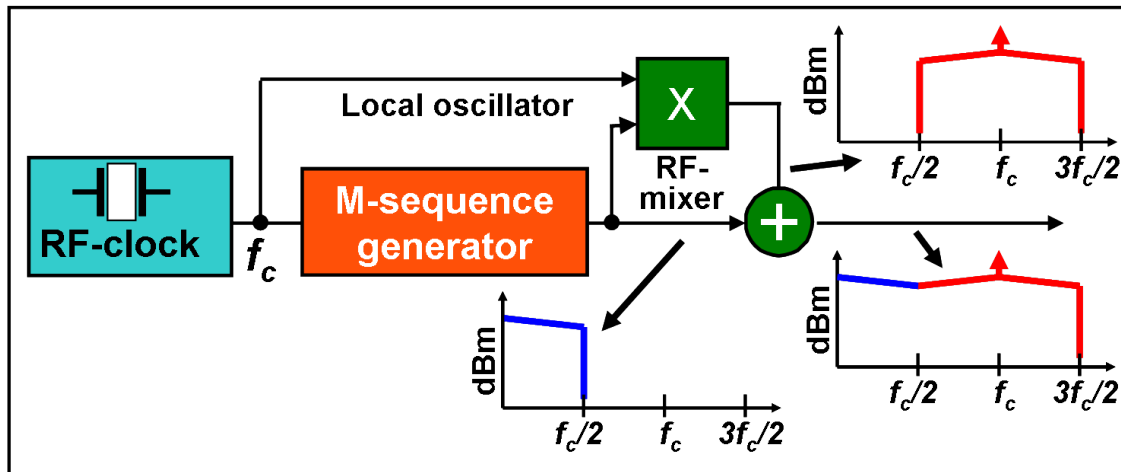
Fig. 3.7.: Principle and power spectra of extending an M-Sequence stimulus

The feasibility of this idea has been demonstrated for a 7 GHz system in [56] using a power divider to combine the baseband and up-converted band. However, the investigation showed that an implementation with discrete components has some drawbacks regarding the flatness of the resulting spectrum. These are due to interference patterns

in overlapping frequency regions when adding the baseband and up-converted signals. For some frequencies, constructive interference occurs leading to higher spectral power levels, but for others superposition is destructive resulting in spectral power gaps. The pattern can be influenced by controlling the relative delay between the baseband and up-converted component as well as the phase of the local oscillator. However, the solution in [56] still has a significant amount of stimulus energy below 1 GHz (which is not considered useful for our case) and the spectral gaps appeared in the middle of the covered frequency band. That is why a modified solution has been developed.

In practical implementations there are a few effects not present when simulating ideal circuits and signals. Most notably the behaviour of real wideband mixers is much more complicated than a simple multiplication of the signal provided at the IF input with the local-oscillator (LO) sine wave. Most notably the feedthrough of the IF signal to the RF port of the mixer seems to have severe impact on the RF outcome. Even if the baseband feedthrough was not present, slightly different RF spectra have been observed due to the relative phase between the M-Sequence and the local oscillator. Analysing the properties of real mixers in detail is clearly beyond the scope of this thesis, but important properties have been obtained by real-world testing. For that purpose, a 9 GHz baseband M-Sequence generator was coupled with a commercial wideband mixer similar to the one used in [56] and according to the setup depicted in figure 3.8. The resulting stimulus was analysed with a Rohde & Schwarz FSEM spectrum analyser. In a first approach, the addition of the M-Sequence baseband was omitted and the relative delay between IF and LO input was accomplished by means of a mechanical phase shifter in the LO path.
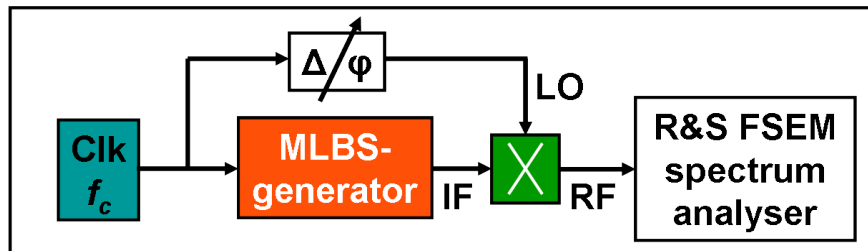
Fig. 3.8.: Testing setup for the extended M-Sequence stimulus

During the measurements it was observed, that at least for the actual mixer device, feedthrough from IF input to RF output was heavily dependent on the relative delay between the IF input and the LO input. The feedthrough was always strongly attenuated below 1 GHz, but between 1 GHz and 5 GHz the spectral power at the RF output was sensitive to changes of the LO phase shifter. In some cases, almost complete coverage of the lower band was achieved. For this reason, the addition of the baseband signal to the RF output of the mixer could be avoided at all, i.e. the RF signal coming out of the mixer was solely used as stimulus in the new UWB sensor. The employed mixer works ef-

ficiently up to about 13 GHz, higher frequency components do not have significant power levels at the RF output and will consequently not be used due to bad SNR conditions. In addition to figure 3.8, a low-order low pass filter with 3 dB cut-off at 12.6 GHz has been added to further reduce power at higher frequencies. This filter helps to avoid aliasing when sampling the stimulus. Figure 3.9 shows the relative power spectrum of the realised transmitter module measured with a Rohde & Schwarz FSEM spectrum analyser.
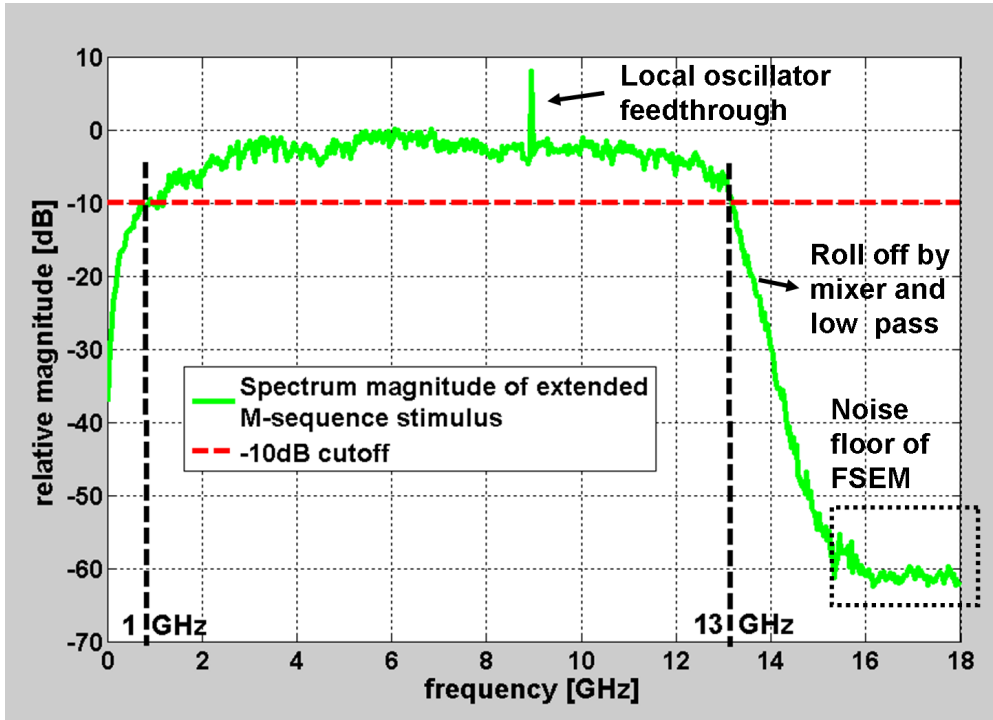
Fig. 3.9.: Spectrum magnitude of the realised extended M-Sequence stimulus

As is evident from the figure, the resulting spectrum is not really very flat. Furthermore, the local oscillator feedthrough at 9 GHz is very strong. This is another property of every real mixer device and cannot be avoided in most cases. If this single frequency component is not considered, the 10 dB cut-off[2] bandwidth B_{-10dB} is 12 GHz spanning from $f_l = 1\,GHz$ to $f_u = 13\,GHz$. Please note that the stimulus period T_p does not change in comparison to the baseband M-Sequence. Besides the mentioned issues, this solution has enough advantages to justify its application:

- No severe spectral gaps within the covered band

- Frequency coverage matches design goals very well, i.e. $B_{-10dB} > 10\,GHz$ and $f_l \geq 1\,GHz$

- Low count of additional RF components: mixer, LO delay by RF cable, lowpass filter, optional IF driver amplifier

---

[2]In the case of UWB stimuli, 10 dB cut-off is more common than a 3 dB cut-off when defining the bandwidth.

- Everything is still derived from and synchronised to a single master clock f_c

The next subsection describes, how the receivers have been adapted to be able to acquire the modified UWB stimulus.

3.3.2. Software-defined dense equivalent time sampling with four receivers

Because of the extended stimulus bandwidth, the sub-sampling scheme needs to be changed as well. It should be noted that the actual sampling rate f_s does not need to be changed for the new stimulus since it is still a periodic signal (a short discussion on sub-sampling will follow in chapter 4). However, the equivalent sampling rate of the original scheme equals $f_{s,equiv} = f_c = 9\ GHz$ and is therefore too low to directly capture the new signals. The first idea would be to check, if changing the pre-scaling factor of the synchronisation unit (see subsection 3.2.1) could help. Unfortunately this is not the case. Both the M-Sequence period and the period of any 2^m pre-scaled clock derived from f_c will always be apart an integer multiple of the clock cycle T_0. In the basic implementation the difference is exactly one T_0 — the lowest possible offset. It can be concluded that by changing the pre-scaling factor no equivalent sampling rate greater than f_c can be achieved.

An alternative solution has been realised for the 7 GHz I/Q system in [56]. The idea was to keep the original and stable sub-sampling scheme while avoiding direct sampling of the up-converted stimulus. In order to acquire the signals with the equivalent sampling rate of 7 GHz, I/Q down-mixing was implemented at the receivers. A major challenge was to achieve a very good I/Q balance — a problem also mentioned when discussing UWB FMCW radars in subsection 3.1.1. The same receive channel was used for I and Q reception to keep conditions as equal as possible and only the local oscillator signal driving the down-mixer was switched between 0° an 90° phase shift by means of tuned delay lines. Although successfully implemented, the realisation of this approach was not preferred for the new system. First of all it has been shown by measurements, that perfect I/Q-balance could not be reached despite the careful system design. There are possibilities to calibrate this balance, but other aspects had to be taken into account as well. In the mentioned system, the stimulus is strictly limited to the frequency band from $f_c/2$ of $3f_c/2$, i.e 3.5 GHz to 10.5 GHz. After down-mixing, the resulting spectra fit in the baseband width of the basic M-Sequence approach. In the new system, however, the region below $f_c/2$ is also occupied by the stimulus making simple I/Q downconversion infeasible.

Splitting the received signals into different frequency bands is not favourable anyway, since this could introduce problems when trying to calibrate the sensor. Moreover, current

the track&hold circuits of the RF-chipset are specified with a 3 dB input bandwidth of up to 15 GHz [103]. Both factors lead to the conclusion, that direct sampling of the complete bandwidth occupied by the stimulus is desirable and feasible. In order to do so, the equivalent sampling rate needs to be increased. The stimulus decays to the noise level around 14 GHz (compare figure 3.9), so an $f_{s,equiv}$ greater than 28 GHz is necessary. To accomplish this, the sub-sampling time offset within the stimulus period needs to be changed in finer steps than the original value of T_0, i.e. changes in fractions of the master clock cycle T_0 must be realised. Because the original stable sampling scheme takes care of covering the complete stimulus period T_p in coarse steps, the task reduces to the introduction of additional fine steps always smaller than T_0. Regardless of the implementation, this is an important fact for avoiding jitter problems caused by slow-ramp based longer delays often used for impulse radars [90].

There are different technical solutions to the problem. Since the relative delay between the transmitted stimulus and the real sampling clock edges defines sub-sampling steps, three possible intercept points can be identified in the clocking scheme. One could alter the delay of the M-Sequence generator clock, the delay of the pre-scaler clock, or the delay of the real sampling clock after the pre-scaler. The latter option is not favourable since the real sampling clock is a wideband signal itself, featuring steep edges responsible for the overall low jitter of M-Sequence sensors. The other two clocks are only narrowband signals and can be easily delayed by delay lines or phase shifters. Figure 3.10 shows the chosen solution. A steerable phase shifter controlled by analogue voltage has been introduced in front of the sampling clock pre-scaler.
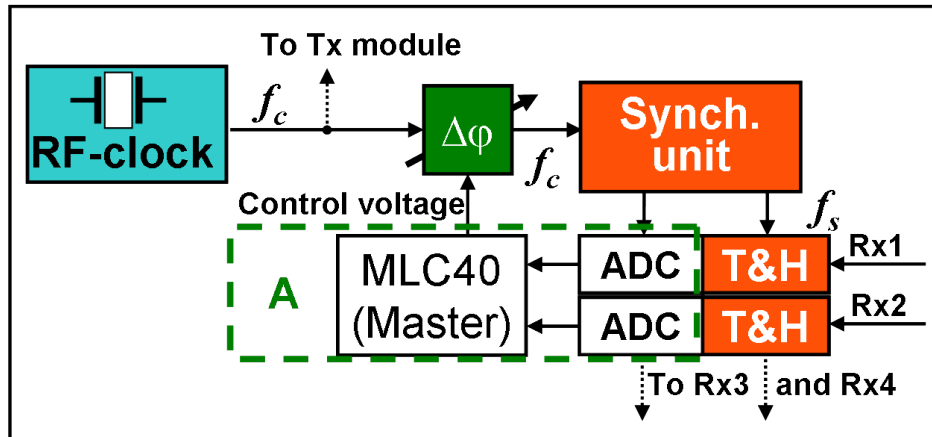
Fig. 3.10.: Modified receiver structure of the new M-Sequence UWB sensor

The resulting sub-sampling scheme is very similar to the original one. The phase shift is fixed by applying a constant and stable control voltage to the shifter. Once a steady state has been reached, the original sub-sampling including optional averages takes place, i.e. $2^n - 1$ samples are taken as many times as desired. The spacing within this set of

samples is exactly T_0 just like in the baseband system. After finishing the acquisition, the control voltage of the phase shifter is changed resulting in a slight shift of sampling times. This shift is worth a fraction of T_0. Next, another set of (probably averaged) $2^n - 1$ samples is taken. The whole process is repeated $r = 4$ times, each time with a different phase shift. The resulting samples are interleaved to reconstruct their correct position within the stimulus period. This way, the equivalent sampling rate can finally be increased by a factor of four, e.g. in the case of a 9 GHz master clock the new system achieves $f_{s,equiv} = 36\ GHz$ and $t_{s,equiv} \approx 27.8\ ps$. Of course, the number of samples per signal period also increases by a factor of r. Using a 9th order M-Sequence and $r = 4$ it is 2044 for the new system. Figure 3.11 illustrates the algorithm just described using a 3rd order M-Sequence (sub-sampling is not shown in the figure for compactness reasons).
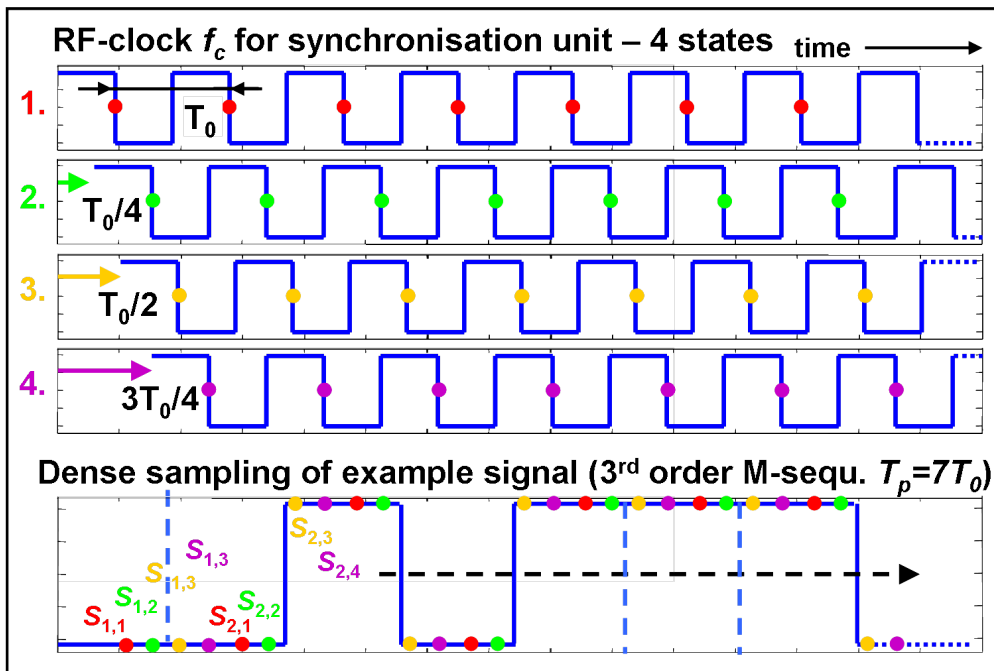
Fig. 3.11.: Illustration of new dense sub-sampling scheme

Using the normal sub-sampling of the baseband concept ensures equidistant (or uniform) sampling within each set acquired with a fixed phase shift. But the offset between samples of different phase shifter states is not automatically equidistant. As will be explained in chapter 5, Fourier transform of all measured data is needed for calibration. Thus, overall uniform sampling must be ensured. The goal of the phase shifter control is to change the clock phase in such a way, that the resulting delay offset is an equal fraction of the master clock period according to equation 3.10. The realisation of the phase shifter control is quite involved and will be described in great detail in chapter 4.

$$\Delta t_i = \frac{iT_0}{r}, i = 0..(r-1) \tag{3.10}$$

The new sub-sampling scheme has some pros and cons which should be mentioned here. One of the strong aspects is certainly that the stable mechanism of the basic M-Sequence approach is widely kept. Another interesting aspect is that the equivalent sampling rate can be defined by software in the phase shifter control. Any multiple of the master clock rate can theoretically be reached by taking an appropriate number of sampling sets. However, ensuring uniformity of the sampling becomes more complicated with increasing r. On the negative side there is the potential introduction of additional sampling jitter caused by unwanted variations of the phase shift. This can be partly circumvented by carefully stabilising the control voltage of the shifter but cannot be completely avoided. As mentioned before, measurement data is only acquired when the phase shifter reached a steady state. Its settling time increases the total time needed to acquire a complete data vector. Settling occurs r times per signal period and generally takes longer, the more stable the control voltage should become. As will be shown later in chapter 4, the impact can be mitigated by changing the phase shift only when really needed, e.g. after the time consuming averaging process.

In order to realise a system with four receivers without the need for multiple phase shifters and synchronisation units, the clock recovery feature of the track&hold circuits was exploited and a chain of four ICs was realised in one compact module. The multi-channel receiver module was build as part of a diploma thesis and is described in [107]. Special care has been taken to minimise crosstalk between the individual receivers, which could propagate along the clock path. As shown in figure 3.11, two MLC40 digital backends have been attached to digitise the four channels. One of the modules acts as a master and has been modified to control the phase shifter via its digital-to-analogue converter. It also synchronises all activities with the second module being the slave backend. The firmware of the modules was altered to account for phase shifter control, the increased number of samples per signal period, and correct interleaving.

3.3.3. Frontend for measuring full two-port S-parameters and calibration

As already mentioned in subsection 2.3.3, acquiring a fully polarimetric dataset can be achieved by providing two measurement ports each connected to a linear polarised antenna with different orientation. The sensor needs to acquire the full S-parameter set, i.e. the reflections at both ports ($\underline{s}_{11}$, $\underline{s}_{22}$) and the transmissions between them ($\underline{s}_{21}$, $\underline{s}_{12}$). In order to measure S-parameters, the respective stimulating wave (port number as second index of the parameter name) and resulting response wave (port number as first index) need to be captured. This can be done by means of directional couplers separating the signals leaving and entering the port. To avoid ambiguities, only one of the ports should be stimulated at a time. If port one is active, $\underline{s}_{11}$ and $\underline{s}_{21}$ can be measured. The other

two parameters are gathered subsequently when port two is driven. For that purpose, an S-parameter frontend according to figure 3.12 has been implemented. It consists of a solid state RF crossbar switch for directing the stimulus to either port and four directional wideband couplers — two for each port. While the frontend pretty much resembles a conventional S-parameter test set found in VNAs, there are some aspects one has to keep in mind. Since the measurements are done in time domain, the wideband couplers need to cover the whole frequency band of interest and cannot be optimised for parts of the spectrum. This generally leads to a low directivity — a major source of unwanted internal device clutter. Another aspect is the use of the port crossbar switch. It finally limits the port isolation, i.e. how much energy leaks from the active to the inactive port and vice versa. The switch must also cover the whole bandwidth at once. Even though a component with good isolation (about 60 dB over the whole bandwidth, see [108]) was found for the current system, future implementations with even more bandwidth could suffer from the fact that it is technically difficult to ensure high isolation, the wider the operational band becomes. An alternative solution could be to implement two separate transmit modules and mute the one of the inactive port. However, this increases component count and system complexity. Though it was not considered for the current sensor, using two transmitters could become feasible when further system integration evolves in the future.
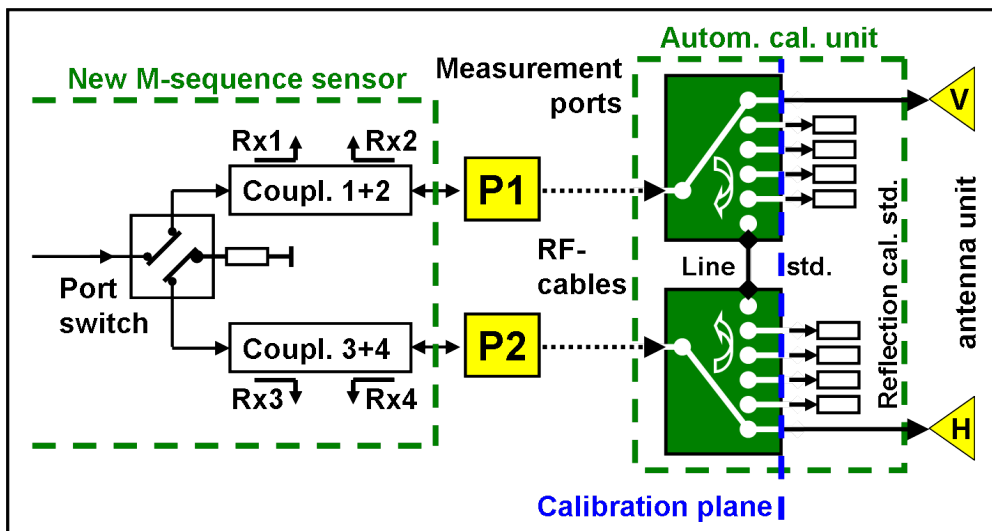
Fig. 3.12.: Frontend for S-parameter measurements and automatic calibration unit

Besides the S-parameter frontend, figure 3.12 also shows the automatic calibration unit, which is connected to the measurement port during normal measurements in salt mines. It would be possible to connect the antennas directly to the ports, but this would mean the sensor operator had to do the calibration process manually. Doing so in the harsh operating environment below ground didn't seem appropriate — especially since trained personnel would be required to achieve good calibration quality. Details of the

process are described in chapter 5. For now it should be noted, that the calibration unit is able to connect either of the two ports independently to one of six different RF paths. One path attaches the antennas, of course, while the other five paths connect different kinds of calibration standards. This is achieved through one-to-six (SP6T) mechanical RF switches. They are specified with very low impedance mismatch, high path isolation, and low insertion loss up to 18 GHz [109]. A common problem with mechanical switches is their limited useful lifetime due to the wear of movable internal connectors. This makes the technology not the best choice for the port crossbar switch which is operating all the time during measurements. On the other hand, calibration takes place only once in a while and causes a small number of reconnections. The good RF properties of mechanical switches benefit the overall achievable accuracy despite the ageing issues. Both the port switch and the automatic calibration unit are controlled by the master digital backend. The actual connected signal path can be chosen by the computer controlling the MLC40 master, but the crossbar switch is always internally operated to ensure subsequent stimulation of both ports.

3.4. Summary of system design for a 12 GHz bandwidth M-Sequence sensor

The new UWB sensor to be used in salt mine inspections has been based on a correlation principle using pseudo-noise stimuli, namely M-Sequences. The basic system concept has been extended to improve various measurement properties. The resulting device has four main components — a transmitter module for generating the stimulus, a four channel receiver module, a two-port S-parameter frontend, and an automatic calibration unit.

The transmitter module extends the bandwidth of the original M-Sequence by mixing the generator's output with the master clock of 9 GHz. Due to the properties of the employed wideband mixer, the resulting stimulus now covers the frequency band from 1 GHz to 13 GHz while keeping the period duration of the M-Sequence.

Track&hold ICs of the M-Sequence chipset have proven a very large input bandwidth and thus direct sampling of the sensor signals was possible. The stable sub-sampling mechanism of the M-Sequence concept was almost completely kept. A necessary increase of equivalent sampling rate has been realised by means of denser sampling through a steerable phase shifter responsible for controlled small-scale clock delays between the transmitter and receivers. An equivalent sampling rate of 36 GHz was realised that way. The phase shifter is an addition to the synchronisation unit which then drives a chain of four track&hold circuits capturing the RF responses. Two commercial digital backends with two ADC channels each are used to digitise the signals. The modules are

coupled and one of them is used for various control purposes like setting the phase delay and controlling the other frontend components.

The four receivers are connected to an S-parameter frontend providing two measurement ports. It uses a crossbar port switch to excite either of the ports at a time. The waves travelling out of and into each port are separated by dedicated wideband couplers feeding the receivers. By subsequent stimulation of the two ports, the full S-parameter set can be acquired. The antennas of the sensor are not directly connected to the frontend, but to the automatic calibration unit. It attaches the sensor ports to the antennas or alternatively to a number of calibration standards.

Figure 3.13 is a more detailed version of the outline from figure 3.6 before. All in all, the realised sensor can be seen as a new kind of two-port time-domain VNA. Of course, it does not feature the flexibility of classic VNAs, but it fulfils the design goals defined for inspection of the disaggregation zone in salt rock and could be used for almost any measurement task in the covered frequency range. However, calibration capabilities have not yet been discussed and it can be expected that the raw performance in terms of device clutter is somewhat lower than that of modern VNAs. Main reason for this are the UWB couplers and other components spanning the whole bandwidth which cannot be manufactured with optimal RF properties. In the next two chapters, the topics of uniform equivalent-time sampling and system calibration are treated.

Fig. 3.13.: Detailed block diagram of 12 GHz bandwidth M-Sequence sensor

4. Uniform dense equivalent time sampling

Modern sensors almost always transfer their data into the digital domain at some point, because this way it can easily be processed or stored for a long time without degradation or ageing. In the case of UWB electromagnetic sensors digitising is also mandatory since the wanted information is seldom directly visible in the measured signals — it rather has to be extracted by means of more or less complex inverse problems hardly solvable by analogue circuitry. Unfortunately, there is always a compromise between acquisition rate, resolution, and most notably accuracy of ADCs. Modern ADC devices are highly integrated and surely provide higher sampling rates for the same accuracy than ICs from the past, but multi-GHz real time samplers are even nowadays limited to an effective number of bits (ENOB) less than eight. Not only analogue-to-digital conversion is a challenge here, one also needs to handle the digital data stream of ultra-fast ADCs. Consequently, such ADCs are only found in specialised and again very complex laboratory devices — like real time oscilloscopes, e.g. [110] and [111].

For that reason, UWB sensors employ sub-sampling with ADCs in the megasamples range providing higher resolutions and accuracy. There are different philosophies regarding the equivalent sampling interval — non-uniform and uniform sampling. The first case does not consider equidistant sampling points as long as the time instants of sampling are known. However, the latter case producing equally spaced sampling points is preferred for its easier interpretation and processing in the digital domain. The same is true for the basic M-Sequence concept as described in section 3.2. The timing mechanism is realised in such a way, that equidistant sampling of the RF signal is assured. The new UWB sensor is a mixture of both approaches. For each fixed value of the clock phase shifter, a dataset of $2^n - 1$ samples is uniformly acquired (where n is the M-Sequence order). Nevertheless, when the phase shifter is changed to a new value, the amount of change in sampling time instant is not automatically an integer fraction of the master clock cycle T_0 as would be needed for overall uniformity. In the new system, $r = 4$ such sets of samples are interleaved to build the final data vector. Without any further effort, subsequent samples in the resulting vector might not have a constant distance, but every 4th sample will fulfil this condition, no matter at which sample number you start within the data vectors. This special case is known in literature as periodic non-uniform sampling,

e.g. see [112–114], and has some consequences when interpreting the gathered data in digital domain. The task of phase shifter control is to find a way of setting correct phase values such that uniform sampling occurs in the end. For easier understanding, let us recall the sub-sampling scheme of the new sensor in figure 4.1.
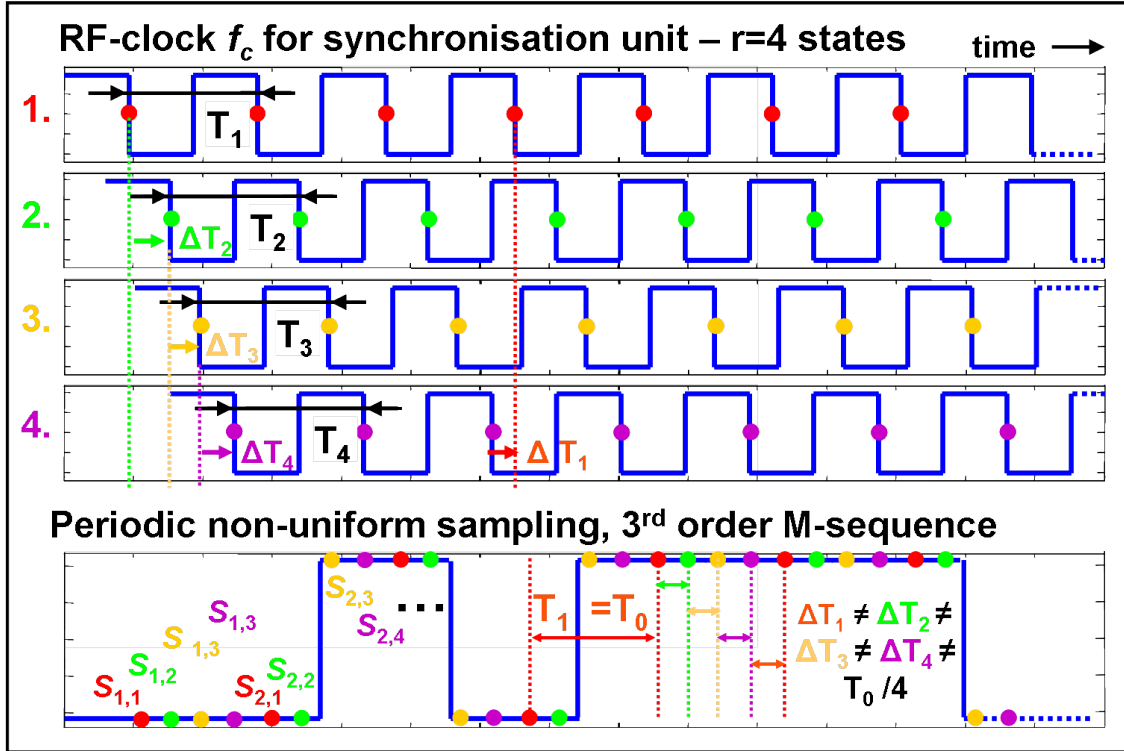
Fig. 4.1.: Sub-sampling scheme of new M-Sequence sensor

The sample spacing of snapshots taken for a fixed phase shifter state all have the same value according to equation 4.1. The additional small offsets introduced by subsequent changing of the phase shifter in front of the synchronisation unit are intended to be equal fractions of T_0 but are generally not uniform in the first place as expressed by equation 4.2. The goal is to make ΔT_x equal to T_0/r which means the whole data vector would be uniformly sampled with the equivalent rate of $f_{s,equiv} = r \cdot f_c$. Before introducing a way to achieve this condition in section 4.3, it is a good idea to first recall some aspects of sub-sampling in general which is done in the next section 4.1. Furthermore, it can be expected that an exact adjustment of phase shifter values is at least limited by noise of its control voltage. It's therefore important to investigate the question how accurate ΔT_x must be tuned to achieve sufficiently uniform sampling. Such analysis is presented in section 4.2.

$$T_1 = T_2 = T_3 = T_4 = T_0 \tag{4.1}$$

$$\Delta T_1 \neq \Delta T_2 \neq \Delta T_3 \neq \Delta T_4 \neq \frac{T_0}{r} \tag{4.2}$$

4.1. General aspects of sampling for UWB sensors

When asked about sampling rate, what often comes to mind is the simplest form of the sampling theorem: the rate needs to be at least twice as high as the highest significant frequency component of the signal to be captured. While doing this leads to correct digital signal representations, options to reduce the effort for some kinds of signals are disregarded. Direct sampling of UWB signals spanning several GHz is technically not easy as stated before. Fortunately, if one is interested to retain the complete information as it was present in the continuous-time UWB signal, the theoretically necessary lowest sampling rate would be higher than twice the frequency bandwidth occupied by the signal [85] which can be much lower than the highest frequency component.

This leads to an interesting observation. If perfectly periodic signals are assumed, the sampling rate becomes independent of the frequency components of the signal. Periodic signals have a discrete spectrum, i.e. Dirac delta functions at the locations of harmonic frequencies. The width of these delta functions is zero per definition and thus the accumulated bandwidth of the whole signal is zero, too. Coming back to the sampling theorem this would mean the actual sampling rate could become almost zero as well. While this does not seem intuitive at first glance it still makes sense. Since the signal is periodic, it never changes its shape. If one wants to sample such a signal, it is irrelevant how long one waits in between taking snapshots, as long as sampling takes place at all and different points within the period are observed. However, if complete reproduction of the signal's shape is of concern, spacing of distinct samples within the period need to fulfil the statement given at the beginning of this section and it is this point where the actual frequency content of the signal comes into play. The effective time distance between neighbouring samples defines the so called equivalent sampling rate, which must be high enough to account for all significant frequency components.

Please also note, that taking a snapshot might not be as easy as it sounds. The sampling theorem only tells about the time instants where values are to be taken, but it does not talk about how they are to be measured. Theoretically, the instantaneous value of the signal is of interest, i.e. the sampling process should not consume any time. This is technically not possible but an approximation to the current signal value can be captured. To achieve this, the responsible track&hold or sample&hold circuit (sometimes also called a *sampling gate*) needs to have an appropriate input bandwidth or equivalently a

short-enough time window in which the signal's amplitude is extracted. To ensure good reproduction of an UWB signal, the circuit's acquisition time needs to be much shorter than the period duration of the highest frequency of interest. For example, the input bandwidth of the latest series of M-Sequence track&hold circuits from our group is specified to be about 15 GHz (period duration 67 ps). Therefore, the transition time between track and hold state must be in the low ps or even sub-ps range.

Any sub-sampling scheme makes use of the aspects just discussed. It only works, if periodic signals are used (thus the periodic stimulus of all UWB sensors using sub-sampling) and the slow analogue-to-digital conversion is aided by a suitable fast sampling gate. However, in reality truly periodic signals cannot be assumed. One obvious reason is the inevitable noise contained in any kind of real-world signal. Another reason is that sensor circuits are prone to drift effects or ageing induced by, e.g., temperature changes of the environment. Even if these effects are slow they introduce a change in behaviour and therefore influence the shape of transmitted and received signals. Despite the technical reasons, the issue becomes even more evident when considering the way an UWB sensor works. Even if a completely stable stimulus and device were provided, it would be used to measure the IRF of external test objects. In most cases, a test object changes over time and consequently the captured responses are changing, too. Changing test objects are by far the most significant cause of breaking the periodicity assumption of the sub-sampling scheme. The other way round, a system is usually only considered suitable for a specific task, if device-internal changes are much slower than the changes in the test object itself while the device measurement speed is much faster. This includes the requirement, that the time used to capture a complete IRF (including any form of averaging for noise reduction) is short enough compared to changes of the measured target. Under such conditions, a temporary steady state of the device and the test object can be assumed and all signals involved can be treated as approximately periodic during acquisition and in processing.

For all sensors capturing impulse responses (or the equivalent frequency responses) of some object, data capturing can also be described in another way: sampling effectively takes place twice. The first kind regards the capturing of actual stimulus and response signals by the device. For UWB sensors this is done by sub-sampling and is often called the fast-time domain, range-direction, or propagation time in radar jargon. The second sampling takes place by observing the behaviour of the test object as represented by its complete IRF/FRF. Taking one IRF delivers a snapshot of the current state and changes of the object are acquired during subsequent IRFs. This is called slow-time domain or in radar terms cross-range direction, respectively. In both domains, the sampling theorem needs to be adhered when aliasing errors must be avoided. The slow-time "sampling rate", i.e. the rate of IRFs per second, is given by the real sampling rate f_s and the number of samples measured per IRF (again including any form of averages for SNR

improvement). Consequently, the intended sensor application finally puts a lower limit on f_s and an upper limit on the number of averages. If the measurement task involves fast-changing targets, the sensor must capture the IRFs at a high enough rate to get a correct snapshot.

All this should be kept in mind when reading the following sections. To ease the discussion on how uniform sampling can be achieved in the newly designed UWB sensor, a temporary steady state of the device and the measured test object are assumed during the process of finding the optimal phase shifter values. After phase control calibration when using the device to scan the disaggregation zone in salt mines — which basically implies a changing test object — the maximum scanning speed is limited by the real sampling rate. For a prototype system, slower scanning can be tolerated than for a production system. That is why the question of acquisition speed with regards to changes in the test object is not further discussed throughout this thesis. An obvious way to increase the possible scanning speed is to increase the actual sampling rate f_s of the sensor and/or to improve its noise performance (lowering the number of necessary averages). This is a matter of ongoing technical development rather than a principal issue and will not be of concern here. The next section tries to provide some reasoning on how accurate the uniformity of fast-time sampling in the new sensor should be.

4.2. Analysis of accuracy requirements for uniform dense sampling

If uniform sampling of periodic signals is correctly applied, the digitised data vector matches (disregarding quantisation errors) the information of the original analogue signal in time domain. After applying discrete Fourier transform (DFT), the resulting coefficients also match the spectrum of the signal at the corresponding harmonic frequencies. In the case of periodic non-uniform sampling, time domain data might actually not look very different from its uniformly sampled counterpart. At least if the latter cannot be known — as is generally the case with measurement data — slight deviations from uniformity of sampling are hard to identify in the individual time domain sample. On the other hand, every coefficient in frequency domain contains part of the information of every sample of the data vector. This might lead to noticeable deviations from the expected spectrum — at least for coefficients of frequencies originally not containing much energy. To get a better understanding of the impact of periodic non-uniform sampling, simple simulations shall be used to show the effects and how severe the resulting errors can be. The next two subsections use idealised signals to ease this analysis.

4.2.1. Periodic non-uniform sampling with sine signals

Initially it is the easiest way to use a single tone signal for analysis, i.e. a sine wave. Without affecting generality, let us use the master clock signal of the sensor with a frequency of 9 GHz. The ideally sampled signal is calculated in MatLab [115] by using the `sin(x)` function. Per period of the sine wave, $r = 8$ samples with uniform spacing of about 13.8 ps are calculated resulting in an equivalent sampling rate of $f_{s,\text{equiv}} = 72$ GHz. To achieve the same frequency resolution of the real sensor (which is about 17.5 MHz) 511 sine periods are simulated. Besides the correctly sampled signal, 1000 additional signals sampled in a periodic non-uniform manner are calculated as well. For that purpose, the eight samples of each period are taken at slightly displaced time instants (but using the same offsets for each of the 511 periods as the sensor would do). The displacement was chosen randomly for each of the eight samples but the maximum deviation has been limited to 1% of the uniform sample spacing, i.e. maximum displacement was ± 0.138 ps. Figure 4.2 illustrates the simulated sampling by exemplifying the sampling of the first two periods. Please note that sampling time deviation in the picture was allowed to be larger than 1% to facilitate readability.
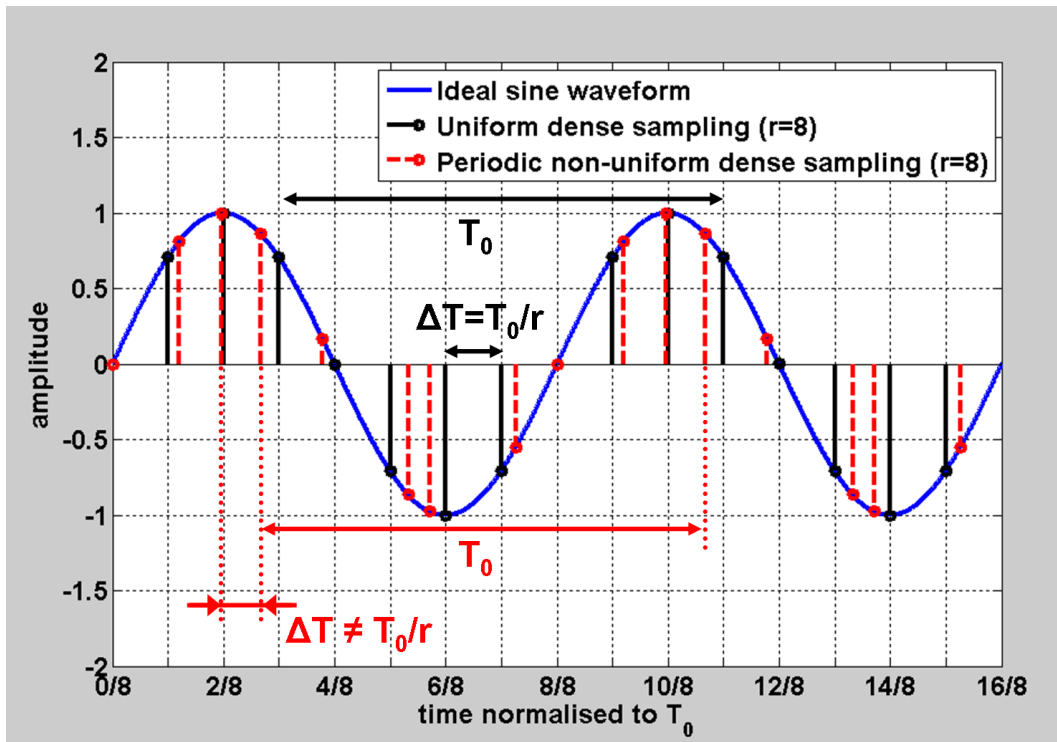
Fig. 4.2.: Dense sampling of ideal sine signal for the uniform and periodic non-uniform case

Figure 4.3 shows two periods of the ideally sampled sine (green curve) alongside one of the 1000 falsely sampled examples (red curve). The plot also contains the difference between both signals (black). At first glance, there is not much difference evident, i.e. it is

hard to identify any errors at all. After simulating the time domain signals, a DFT has been applied to get the corresponding spectra. The spectrum magnitude of the uniformly and periodic non-uniformly sampled signal are shown in a logarithmic scale in figure 4.4 for further comparison. Only the positive half of the spectrum is plotted, since the other coefficients are redundant for real-valued signals. Moreover, it should be noted that showing values spanning more than 300 dB is far from any real technical meaning, but it emphasises the synthetic nature of this test.

There are a number of things to observe. The only noise to be considered here is the quatisation noise of the data type used for simulation — which is double precision floating point representation. The spectral components marked in the lower part of the figure can be accounted to quantisation noise, the residual errors of calculating the actual sine value at the sampling time instants, and finally errors while calculating the DFT in digital domain. Obviously, the implementation in MatLab shows high precision and consistency. Another obvious thing is that the correctly sampled signal and the falsely sampled signal show significantly different spectra despite the fact that the maximum deviation from uniform sampling time instants was only 1%. The original sine spectrum only contains a single discrete frequency at 9 GHz. The other plotted spectrum additionally has components at DC and all harmonics of 9 GHz which fall into the covered frequency band (up to 36 GHz). The magnitudes of these spectral components vary between the 1000 simulated signals with different sampling time offsets, but on average they are only approximately 50 dB below the wanted spectral line at 9 GHz as shown in the picture. The largest power of any harmonic frequency during the whole simulation process is also marked — it is just a bit more than 40 dB down. Even though not visible in figure 4.4, also the magnitude at 9 GHz differs between the correctly and incorrectly sampled cases. The difference is very small, though, and amounts to about 0.003 dB on average of all simulations.

For the case of a sine signal the observed behaviour can be explained in a rather simple manner. In each of the 511 simulated sine periods the same sample time errors have been used. Therefore, discussion can be limited to one period and this also explains, why no other frequency components apart from 9 GHz harmonics appear. Looking at one sine period, the deviations in sampling time lead to small differences in the gathered amplitudes compared to the correctly sampled signal. After the sampling data vector is generated, it is interpreted as if it was sampled in a uniform manner (e.g. by DFT processing). Consequently, the signal represents a slightly deformed sine wave. This finally leads to a different signal with the same period duration as the 9 GHz sine and additional harmonic components of that frequency. The explanation is illustrated in figure 4.5 again using larger sampling time deviations for clarity. The upper part shows once more, how the samples were originally obtained. The lower part of the figure depicts how they are implicitly interpreted when assuming uniform sampling during subsequent digital data processing.
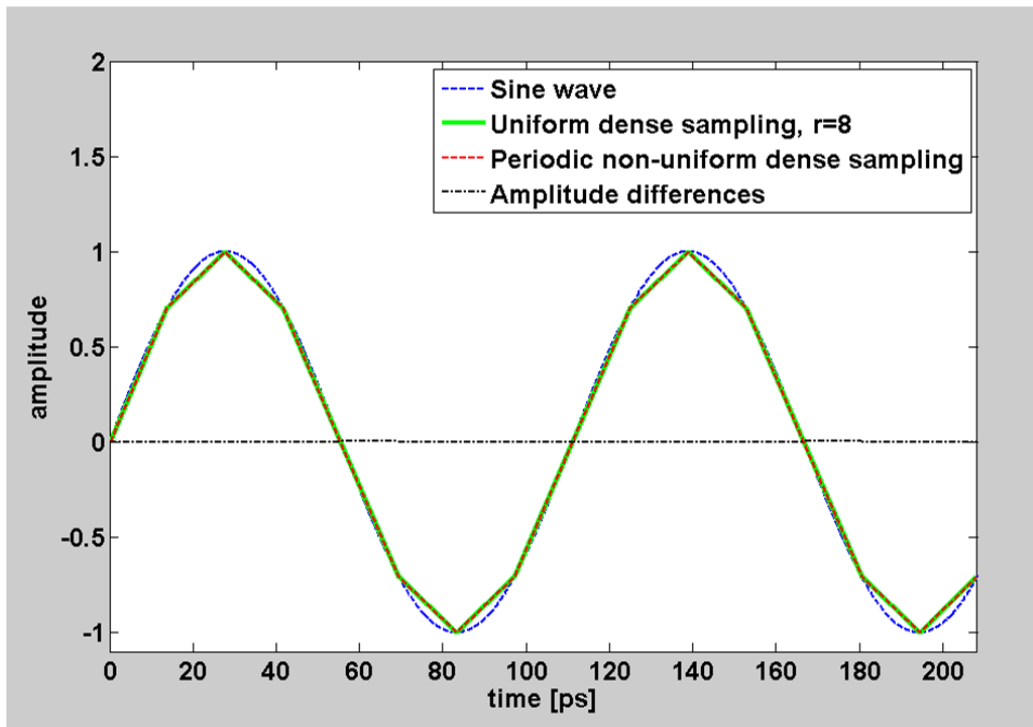
Fig. 4.3.: Time domain comparison of a uniform and periodic non-uniformly sampled ideal 9 GHz sine
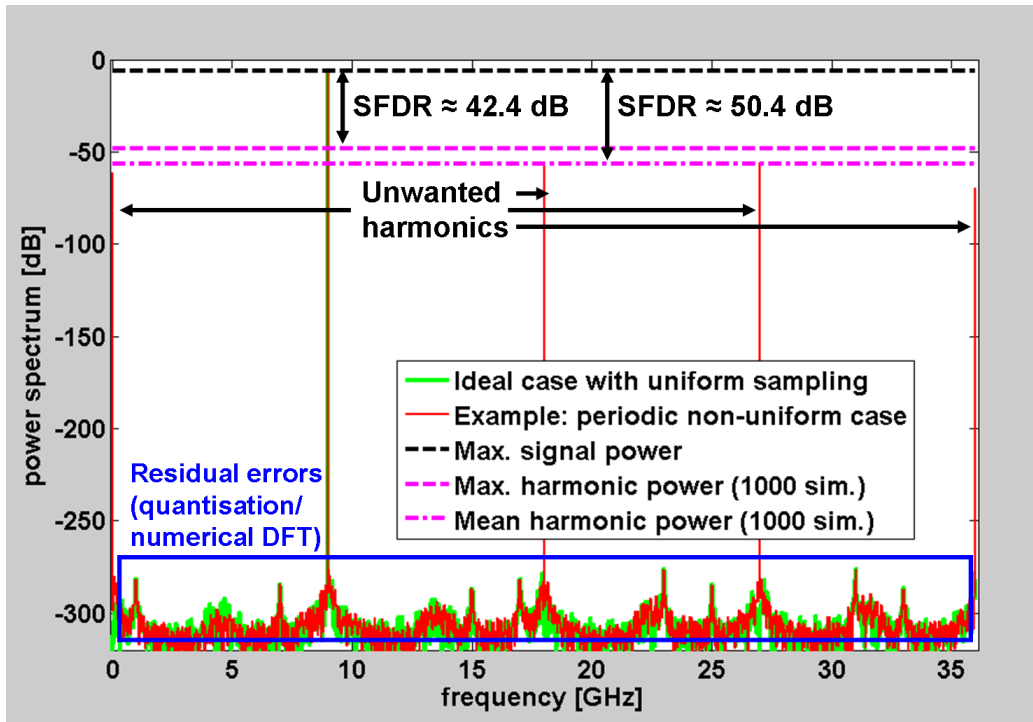
Fig. 4.4.: Comparison of power spectra from a uniformly and a periodic non-uniformly sampled ideal 9 GHz sine
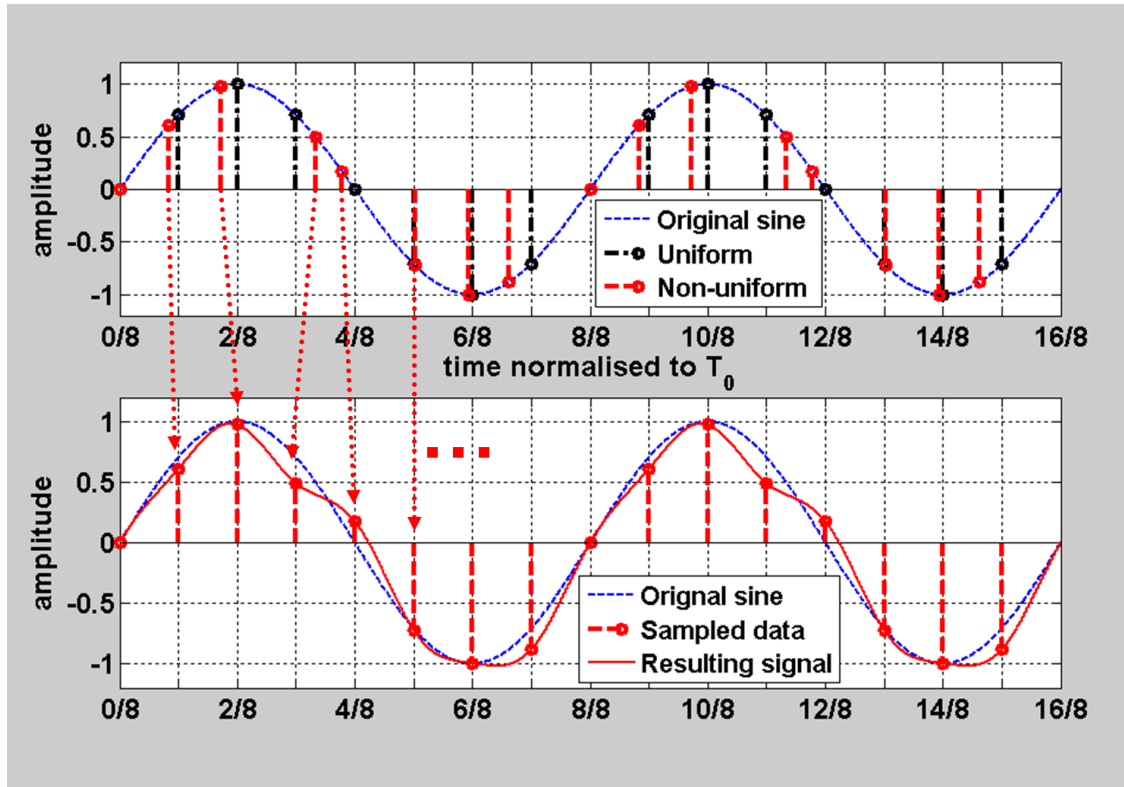
Fig. 4.5.: Explanation of interpreting a periodic non-uniformly sampled ideal 9 GHz sine

Coming back to the quantitative results, it seems surprising that even small sampling time errors of less than 1% could have such a pronounced effect. Judging from the spectrum, the SFDR of the falsely sampled signal was less than 50 dB and it can be expected that this error will spoil the accuracy that can be reached by sensor calibration. Of course, the simulation using a sine signal is not representative for the case of UWB signals used by the new sensor. But what can be learned from this simple example is that even small sampling time errors could cause significant problems or misinterpretations of the gathered data. The amplitude differences between correctly and falsely sampled sines are higher at signal edges (e.g. around zero crossings of the sine) than in flat regions, of course. This means that further analysis of amplitude errors could concentrate on steep signal regions. Another point is that an upper bound for the error can be derived from the steepest signal slopes. Such a largest possible error can be used in the sense of a special $SFDR_{td}$ (see equation 2.14 in section 2.4) relating it, e.g. to the maximum signal value. One goal of the phase shifter control could be to ensure that clutter due to non-uniform sampling stays well below the overall required $SFDR_{td}$ of 50 dB. A more realistic UWB signal is considered in the following subsection to derive accuracy requirements for phase shifter control.

4.2.2. Periodic non-uniform sampling with an UWB stimulus

Since the amplitude errors introduced by wrong sampling times are signal-dependent, the analysis should be focused on stimuli similar to the one used in the real sensor in order to provide a realistic insight. The ideal transmit signal $uwb(t)$ considered in the following calculations is easily derived by multiplying the ideal 9th order M-Sequence $mlbs9(t)$ with a sine using the clock rate f_c as in equation 4.3. In this context, the ideal M-Sequence is normalised, i.e. the signal changes between plus and minus one. The construction of the test signal $uwb(t)$ resembles the idealised behaviour of the realised extended M-Sequence stimulus generator module (compare section 3.3.1). An excerpt of the signal is shown in figure 4.6.

$$uwb(t) = mlbs9(t) \cdot sin(2\pi f_c t + \phi_0) \tag{4.3}$$
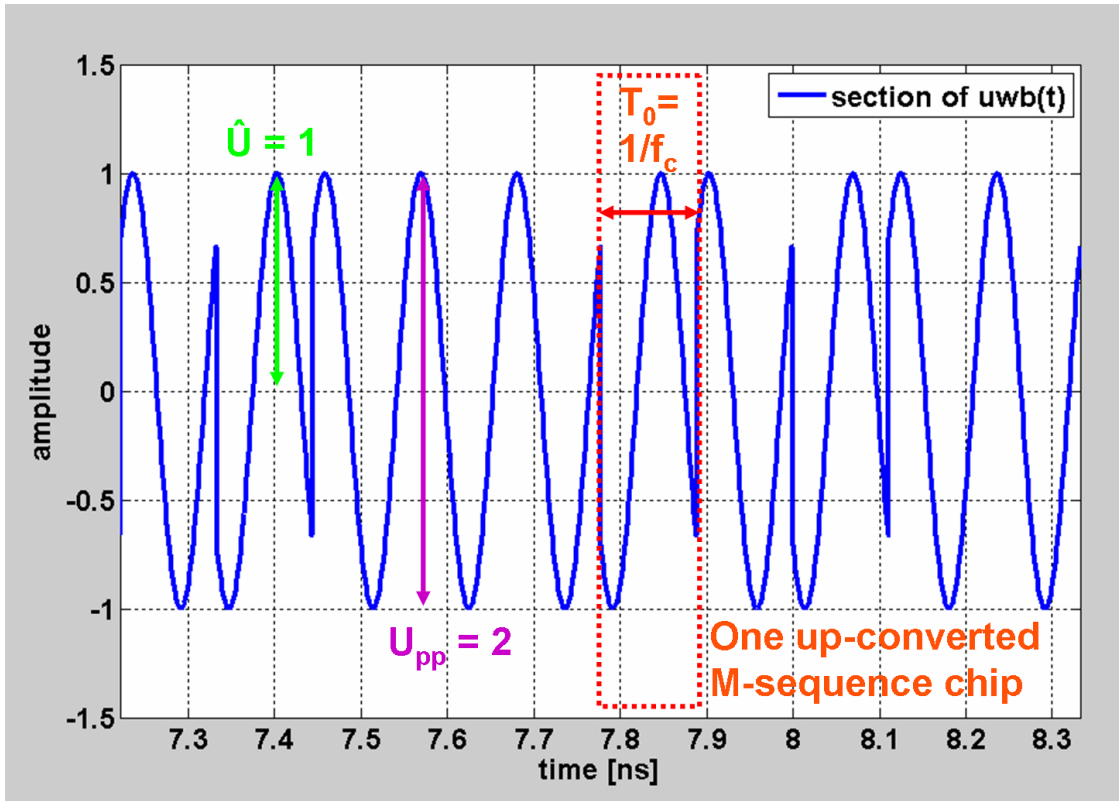
Fig. 4.6.: Section of idealised extended M-Sequence stimulus with $f_c = 9\ GHz$ and $\phi_0 = 45°$

Two properties are of interest this time: the maximum amplitude error and the power of the error signal when all deviations of one stimulus period are considered. The first value can be used in the sense of defining a $SFDR_{td}$ and the latter one can be translated into a signal-to-clutter ratio (SCR).

Maximum amplitude error   The maximum possible error due to misplaced sampling occurs at the steepest signal edges[1]. Using the approximate relationship [85] between the bandwidth B_{UWB} of an UWB signal and the signal's 10% to 90% rise time t_r at edges according to equation 4.4, the maximum error is easily derived. For 12 GHz bandwidth t_r amounts to about 30 ps. With a linear approximation at the steepest point and the peak to peak amplitude $U_{pp} = 2$, the maximum slope $dU/dt|_{\mathrm{max}}$ can be calculated as in equation 4.5. If an $SFDR_{td}$ of 50 dB was aimed at, the maximum allowed amplitude error ΔU_{max} would be 0.0031 according to equation 4.6. To ensure that maximum error, deviation from correct sampling times must be lower than $\Delta t_{\mathrm{max}} \approx 0.059$ ps as obtained by equation 4.7. Compared to the sampling period of the new UWB sensor $t_{s,\mathrm{equiv}} \approx 27.8$ ps this is only 0.21%. The same calculation can be repeated for other $SFDR_{td}$ values. Some examples are listed in table 4.1. The relative accuracy in the third column again relates to $t_{s,\mathrm{equiv}}$.

$$t_r = \frac{0.35}{B_{\mathrm{UWB}}} \approx 30 \ \mathsf{ps} \tag{4.4}$$

$$\frac{dU}{dt}|_{\mathrm{max}} = \frac{(90\% - 10\%)U_{pp}}{t_r} \approx 53.3\mathrm{e}9 \ \frac{1}{s} \tag{4.5}$$

$$\Delta U_{\mathrm{max}} = \frac{\hat{U}}{10^{SFDR_{td}/20}} \tag{4.6}$$

$$\Delta t_{\mathrm{max}} = \frac{\Delta U_{\mathrm{max}}}{dU/dt|_{\mathrm{max}}} \tag{4.7}$$

$SFDR_{td}$ [dB]	ΔU_{max} [% of $\hat{U}$]	Δt_{max} [ps]	Δt_{max} [% of T_0/r]
40	1.00%	0.188	0.68%
50	0.31%	0.059	0.21%
60	0.10%	0.019	0.07%
70	0.03%	0.006	0.02%
80	0.01%	0.002	0.007%

Tab. 4.1.: Simulated sample timing accuracy for different $SFDR_{td}$ values

Even though the results have been derived using some simplifications and approximations, the accuracy requirements in table 4.1 are quite high. Despite a rather mediocre $SFDR_{td}$ target of 50 dB, the timing of sampling points must still be correct to within the low sub-ps range. For errors less than 60 dB below the signal amplitude, maximum deviation must not exceed a few fs! This would indicate a tremendous effort for the phase shifter control. The presented calculation obtained an upper bound for the amplitude error by

---

[1]In the real system it is not guaranteed, that an actual sample is taken exactly at the steepest flank, However, assuming such a situation leads to an upper bound for the amplitude error.

considering false sampling at the steepest signal slopes. Another way to judge accuracy requirements is to analyse the average amplitude error instead.

Average amplitude error   Not all samples of the UWB stimulus are taken at steep edges. Therefore, the average amplitude error should be lower than the maximum one. The impact can be judged by treating deviations at each sample point as a device clutter signal and relating its power to the total power of the idealised stimulus (after sampling, of course). This leads to an SCR value which can be challenged against the overall wanted dynamic range. The phase shifter control must at least ensure a low-enough SCR to enable successful device calibration. A problem for calculating the SCR value is the fact, that the actual offset of sampling points with respect to the clock period T_0 cannot be known, i.e. there are different possible combinations of signal slopes around individual samples within T_0. Another degree of freedom seems to arise from the relative phase ϕ_0 of the local oscillator used to produce the stimulus (compare equation 4.3). However, this variable can be absorbed into the uncertainty of overall sample time alignment as we will see soon.

The idealised stimulus $uwb(t)$ is not really a complicated signal when recalling, how the new sampling scheme works. The M-Sequence basically consists of rectangular pulses with the same duration as the local oscillator period. In each of its 511 elementary pulses, it simply switches the polarity of the corresponding sine's period, i.e. except for the sign each elementary pulse looks the same even for the modified stimulus. This can be confirmed when looking at figure 4.6. Since the non-uniformity of sampling also only occurs within T_0 and power calculation does not account for polarity, analysis can be limited to sampling one sine period with $r = 4$ points. This is the reason, why ϕ_0 and the unknown offset ϕ_s of the sampling points within T_0 can be summarised into ϕ_s for this discussion. So far, it turned out that allowed deviations from ideal sampling times must be very small anyway. When calculating amplitude errors, using linear approximations with the signal's slope at the sampling points will therefore be sufficient — further Taylor series expansion will not be necessary. The situation is illustrated in figure 4.7 using an example M-Sequence chip (any of them would do).

Equation 4.8 expresses the representative elementary stimulus interval $e(t)$. For each of the r samples taken, the slope at the ith point is given by equation 4.9. The additional angle ϕ_s covers the unknown alignment. The SCR is finally given by equation 4.11. Everything is fixed except the unknown ϕ_s and the unknown (but small) sample time errors Δt_i defined by equation 4.10 (also compare 4.1). In reality, these values cannot always be influenced and in the default case, all Δt_i will be different.
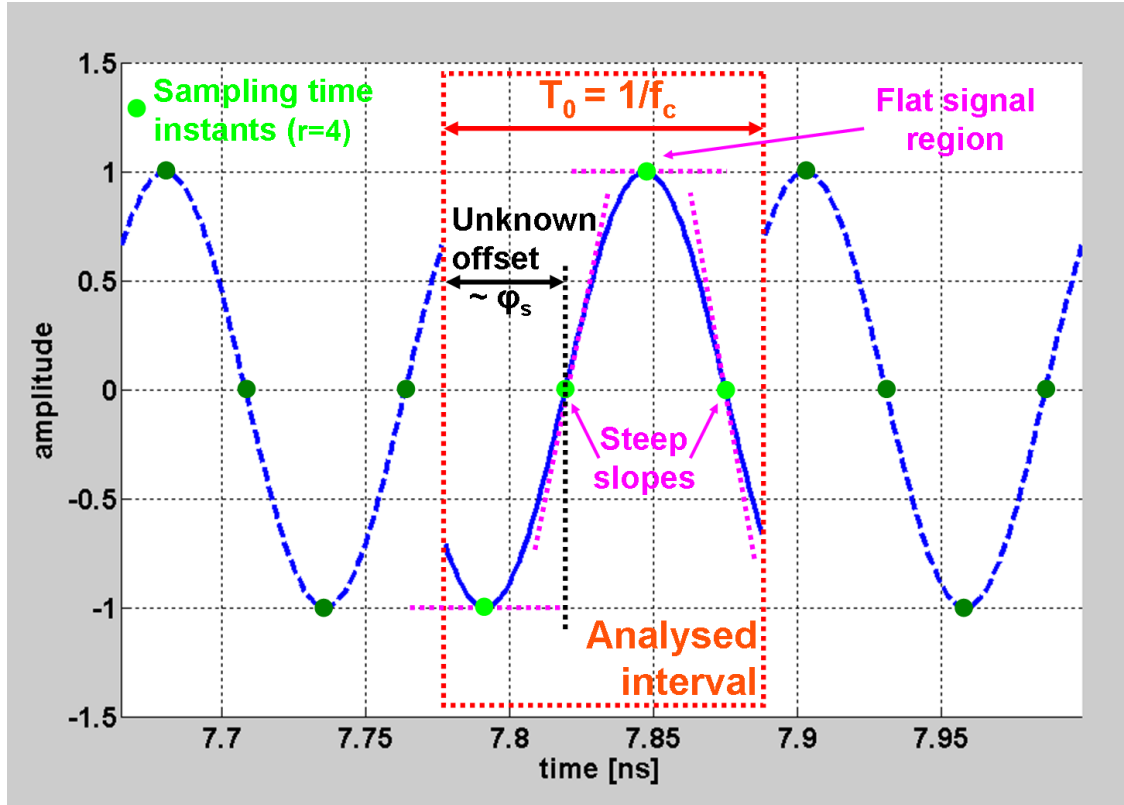
Fig. 4.7.: Illustration of analysed interval for non-uniform sampling of the UWB stimulus

$$e(t) = sin\left(\frac{2\pi t}{T_0}\right); 0 \le t \le T_0 \qquad (4.8)$$

$$\frac{de_i}{dt} = \frac{2\pi}{T_0}cos\left(\frac{2\pi i}{r} + \phi_s\right); i = 0..(r-1) \qquad (4.9)$$

$$\Delta T_i = \frac{T_0}{r} + \Delta t_i; i = 0..(r-1) \qquad (4.10)$$

$$SCR_{samp} = 10\lg\left(\frac{\sum_{i=0}^{r-1} e^2\left(\frac{iT_0}{r}\right)}{\sum_{i=0}^{r-1}\left(\Delta t_i \frac{de_i}{dt}\right)^2}\right) = 10\lg\left(\frac{\sum_{i=0}^{r-1} sin^2\left(\frac{2\pi i}{r}\right)}{\sum_{i=0}^{r-1}\left(\frac{2\pi\Delta t_i}{T_0}\right)^2 cos^2\left(\frac{2\pi i}{r} + \phi_s\right)}\right) \qquad (4.11)$$

However, to get an idea how these variables work, an example assuming equal errors with a value for $SFDR_{td} = 40$ dB from table 4.1 might be useful: $\Delta t_i = \Delta t_{40dB} = 0.188$ ps; $\forall i$. In that case, equation 4.11 can be simplified to look like equation 4.12. It might not be obvious, but in this case the sums in both numerator and denominator simply express the energy of one complete sine period, if the sampling theorem has been respected (i.e. $r > 2$). This energy must be independent from phase, of course, and consequently ϕ_s does not have any influence here. Basically only Δt_{40dB} defines the SCR_{samp} which in this case amounts to about 40 dB, too.

$$SCR_{samp} = 10 \lg \left(\frac{\sum_{i=0}^{r-1} sin^2 \left(\frac{2\pi i}{r} \right)}{\left(\frac{2\pi \Delta t_{40dB}}{T_0} \right)^2 \sum_{i=0}^{r-1} cos^2 \left(\frac{2\pi i}{r} + \phi_s \right)} \right) = -20 \lg \left(\frac{2\pi \Delta t_{40dB}}{T_0} \right) \qquad (4.12)$$

When any of the Δt_i was smaller than the assumed maximum deviation of Δt_{40dB}, the SCR_{samp} could only improve over equation 4.12. If all Δt_i approach zero, the SCR_{samp} will go to infinity as one would expect. One example of equation 4.11 with randomly chosen deviations subject to $\Delta t_i \leq \Delta t_{40dB}; \forall i$ is shown in figure 4.8. As can be seen from the figure, the SCR is generally higher than 40 dB and that the unknown ϕ_s causes a limited oscillation of the value. The explanation for this result is quite easy. The largest Δt_i values generally lead to large errors if sampling takes place at edges. On the other hand, they do not have much contribution to the error signal power in flat regions. Variation of the alignment phase within 360° simply shifts all the sample times through a complete cycle of high and low derivatives.
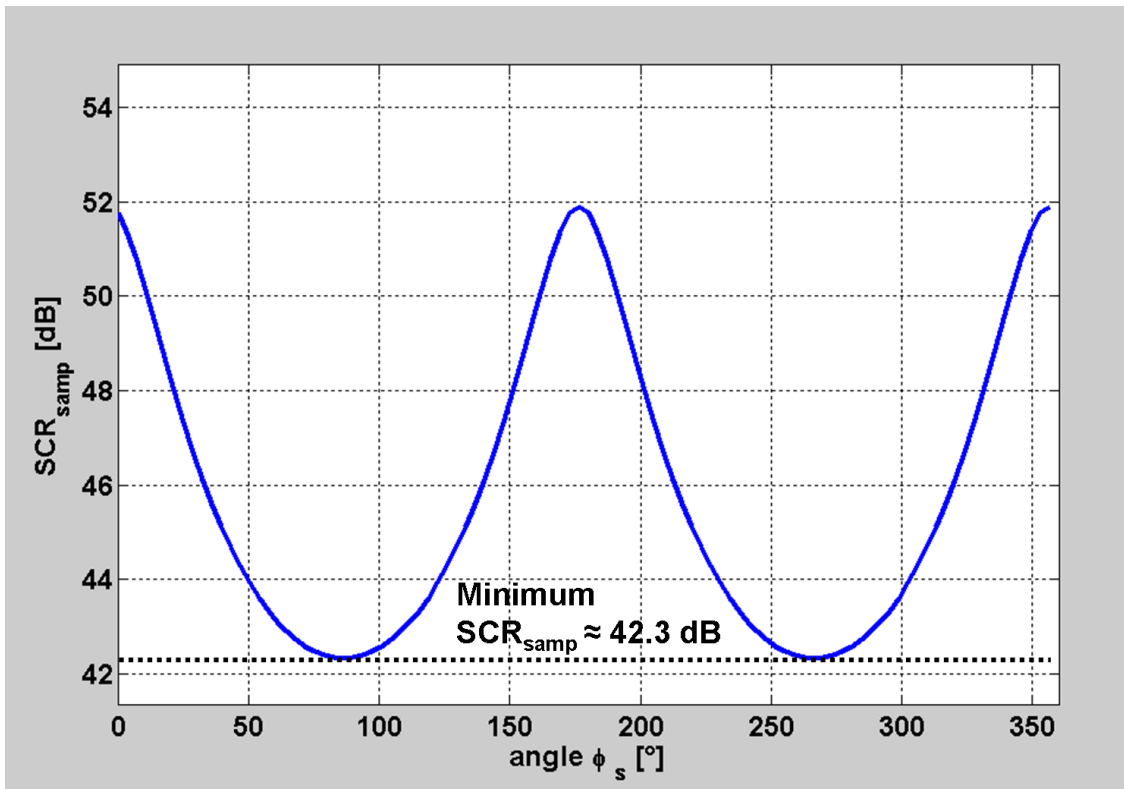
Fig. 4.8.: SCR_{samp} for different alignment phases ϕ_s with random sampling time errors Δt_i

In conclusion of the described analysis, the sampling time accuracy requirements noted in table 4.1 seem to be realistic values that must be reached for a certain maximum sampling error. It should be pointed out again that the margins are quite tight and special

care must be taken to achieve very accurate sample time spacing under any working condition of the sensor system. When comparing the real stimulus with the ideal one used in this section, the real case should lead to a little bit relaxed requirements. The reason for that is the fact, that the idealised stimulus has frequency components up to infinity in its spectrum and the real one does not. Even though the energy of frequencies beyond 18 GHz is small compared to the main spectral part, there are unsteady points in the ideal signal $uwb(t)$ at the boundaries of each elementary pulse, i.e. every T_0. Such points do not exist in the real stimulus which does not contain energy beyond 14 GHz (the power spectrum decays to the noise floor at this point). The overall lower frequency coverage of the real transmitter module translates into a smoother time domain signal with generally slightly less steep edges than the maximum slopes assumed for table 4.1. However, the potential differences in steepness between real and idealised stimulus are small so the given accuracy requirements provide a realistic picture of the problem. The next section describes the implementation of phase shifter control and how correct values for uniform equivalent time sampling are obtained.

4.3. Calibration of phase states for uniform dense sampling

For a sensor system that will be used outside the laboratory it cannot be assumed, that the environmental conditions are constant and known all the time. Finding a correct set of phase shifter control values through experimentation and relying on them in the field is not an option. For example, different ambient temperatures will change the behaviour of every component in the sensor. Even if those changes were small, it is unlikely that they were small enough to not violate the accuracy margins derived before. The phase shifter component alone has a specified temperature dependence of actual phase shift that could spoil a good sampling control as found in the lab. Therefore, a mechanism to calibrate the control values on site when the device has reached a steady state in the given working environment is mandatory. Before describing how this is done, a little more detail of the involved hardware and control regime is given in the following subsection.

4.3.1. Phase shifter control hardware and timing

As explained in section 3.3.2, the phase shifter controls the relative delay between the transmitted signal and the sampling times of all four receivers because it is inserted before the synchronisation unit and the receivers are arranged in a sampling clock chain. Figure 4.9 shows an overview of the hardware involved in controlling the phase shift of the master clock. The phase shifter itself is a Hittite HMC-C010 [116] specified for operating in the frequency range from 6 GHz to about 15 GHz. It guarantees far more than the necessary

360° phase shift at 9 GHz and is controlled by a positive analogue control voltage up to 5 V. The relationship between control voltage and phase shift is not linear but at least monotonically increasing. Insertion loss is also generally slightly non-linear with respect to phase shift. Both properties finally influence the synchronisation unit since it has to make a threshold decision at its input. However, the actual phase shift is by far the main factor to be taken into account. The control voltage is generated by a DAC which is an optional component of the master MLC40 digital backend. The DAC was given by the design of the backend and could not be chosen freely. It offers 14 bits of resolution with update rates in the megasamples range and is optimised for fast settling times. Therefore, the outputs of the DAC are quasi-symmetric current sources and could not directly be used to drive the phase shifter. A transimpedance buffer, which was also part of the MLC40 design, was used to translate the currents into single-ended control voltages. Due to the bipolar mode of operation in the design, only the positive half of the DAC's full scale range could be used reducing the available resolution to 13 bits. The full-scale voltage of the buffer amplifier was limited to about 3 V which is enough to provide a 360° shift of a 9 GHz sine with the HMC-C010. The connection between the buffer and the phase shifter was carefully shielded in order to avoid coupling of external clutter signals and a low pass filter was placed just before the shifter to limit the noise bandwidth.
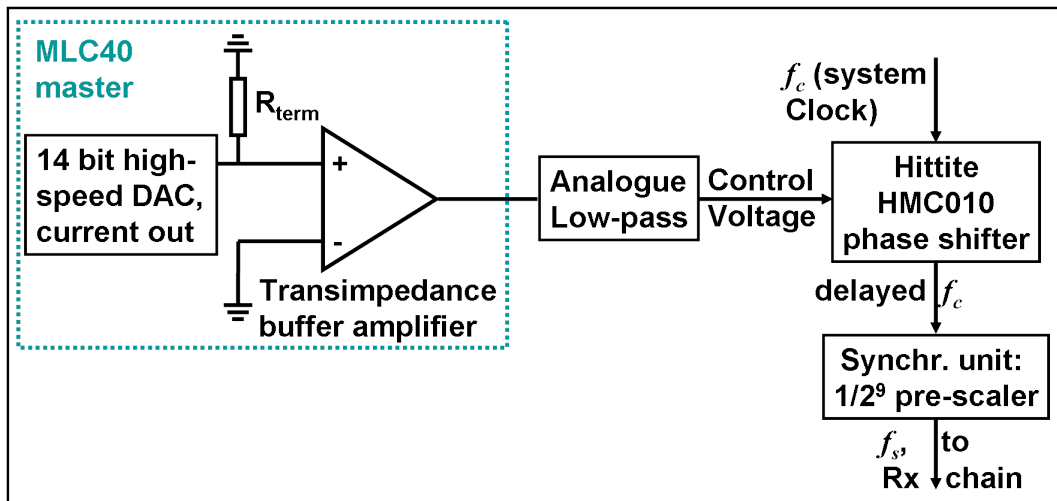
Fig. 4.9.: Phase shifter control hardware

Assuming the ideal case of a linear relationship between control voltage and phase shift, a noise-free operation, and fast-enough settling times, a first limit on accuracy can be approximated. In such a case, 13 bits of resolution are available to span the whole 360°. With $r = 4$ the resolution for accurately steering each single phase shift drops to 11 bits or 2048 discrete steps. The relative quantisation related to the wanted 90° (or equivalently T_0/r) amounts to 0.0488%. Comparing this value to the last column of table 4.1 it becomes clear that the $SFDR_{td}$ due to sampling time errors will be a bit better

than 60 dB at best. Considering the real case with the presence of noise in the control signal and the slightly non-linear relation of control voltage to the phase shift, accuracy expectations must be somewhat lowered.

At least the noise could be lowered by using even higher-resolution DACs and further limiting of the bandwidth of the control signal. However, there are feasibility issues in a real world implementation with these approaches. Just because a DAC has a higher resolution, that does not automatically increase its accuracy. The more resolution is to be exploited, the more effort has to be put into circuit design — e.g. the reference voltage and power supply must be stabilised to the same accuracy which is an elaborate task in a high-speed digital backend for resolutions beyond 14 bits. Also band-limiting the control voltage cannot be done without bound because lowering the frequency cut-off of the low pass also increases transition and settling time whenever the control voltage is to be changed. If settling time becomes too long, the receiver efficiency is severely degraded and results in low overall capturing speed. For those reasons the provided hardware of the MLC40 was considered sufficient for the task and the $SFDR_{td}$ of 60 dB was excepted as the best case result for this setup. Filter and control timing have therefore been optimised for the available circuits and acquisition procedure.

If the acquisition timing would provide a fixed maximum allowable settling time for the phase shifter control voltage, the low pass filter could be matched to achieve maximum noise suppression while ensuring fast enough transitions. There are two main options for integrating the change of control voltage into the existing acquisition cycle. In the most obvious case, a complete data vector is captured directly, i.e. after each set of 511 equally spaced samples the phase shift takes place and another set is acquired until the $r = 4$ cycles are completed. Due to the high actual sampling rate of $f_s \approx 17.5$ MHz (compare sections 3.2.1 and 3.3.2) one such cycle takes only about $30\,\mu s$. Consequently, more than 30,000 cycles happen per second in the basic as well as the new M-Sequence sensor. The time overhead of introducing a phase shift change in between each of them would be significant.

Since the operation at maximum IRFs/second is infeasible and also unnecessary for most of the sensor's tasks, synchronous averaging is used as in other M-Sequence systems to improve the SNR and lower the effective data rate. The timing scheme of phase shifter control can be realised accordingly. For each phase shifter value, the averaging process of the current cycle takes place, before the control moves on to another phase state. In the default configuration, $p = 64$ averages are completed for each fixed phase value. While the MLC40 copies the averaged results to a transfer buffer, the phase shifter control voltage is adjusted to the next state. The duration of the copy operation is one complete cycle, i.e. the phase shifter has about $30\,\mu s$ to settle the new value before the next valid samples are taken. Changing the control values only happens 525 times per second (or only every 65th cycle). This timing is a good compromise between receiver

efficiency, measurement speed, and limitation of the noise bandwidth in the control signal. However, during capturing a complete stimulus period which consists of four different phase shifter states, the measurement object is assumed to be in a steady state. This assumption must be made for all systems using sub-sampling as pointed out in section 4.1. The resulting measurement rate of the new UWB sensor is up to 131 IRF/s which is close to the rate achieved by the basic M-Sequence sensor (133 IRF/s) with the same 9 GHz master clock rate.

4.3.2. Phase shifter control calibration

The control values for all four phase states can be setup with an initial guess at the laboratory. Once approximate values for uniform sampling are found, a detailed adjustment can be done by some calibration procedure at the actual site of sensor operation. As pointed out before, this only makes sense once the environment and the device have reached a steady state, e.g. after time to warm up the electronics to a stable temperature. Out of the r phase states, only $r - 1$ need to be adjusted with the other one being the reference phase. Since the accuracy requirements are very high, calibration must be implemented in a careful way. There are two basic approaches of finding appropriate control values. If one knows the *exact* shape of a signal to be captured, corrections to wrong sampling times are straight forward. Even under very high SNR conditions it is difficult to ensure correct reproduction of a signal under all external conditions — for example output amplifier behaviour may change with environmental parameters. If an exact shape cannot be guaranteed, a model for the principal behaviour of a test signal could be build and exploited. The latter option was used to implement phase state calibration for the new UWB sensor.

Choice of test signals   The question now arises, what kind of test signal can be used and what expectations of its model can be realised with high confidence. From a practical point of view, it is beneficial to require that generation of the test signal should not use too many additional components or disregard the completely synchronous operation of the sensor system. It is also clear that simple test signals would be preferable because it is easier to model them reliably. When looking at the transmitter module of the new sensor, two possible test signals could easily be generated. If the M-Sequence generator was disabled, only the local oscillator feedthrough of the master clock f_c would come out of the mixer producing a very clean sine waveform. Even though the actual amplitude is not exactly known, the fact that it is a sine wave with high harmonics suppression could be used. As shown in section 4.2.1, the sampled signal would show significant power in the harmonics when sampling times are not correct. This could be used for calibration. Unfortunately, the MLC40 digital backends do not allow exact sampling of the master clock

frequency due to technical reasons. The actual sampling rate f_s is derived from f_c by a fixed pre-scaling factor and f_c appears as a DC component after the track&hold circuits. The backend is not capable of precise DC measurements but for future implementations a different solution could enable the use of the master clock sine wave as a test signal.

The other available test signal is the full sensor stimulus, of course. To derive a valid model for this signal is not an easy task. For example, the idealised form of equation 4.3 is too far from the real stimulus to be useful. On the other hand, observations made in 4.2.1 indicate that periodic non-uniform sampling can lead to frequency components in the sampled data that are not present in the actual analogue signal. This fact can be exploited for calibration of phase control values. In [107] the effect of periodic non-uniform sampling on the spectrum of UWB signals — namely the typical band-limited stimulus of the basic M-Sequence system concept covering DC up to about 4 GHz — has been investigated. Based on the theoretical treatment in [112] it has been shown, that the periodic nature of the sampling time errors leads to special spectral effects. In a nutshell, with the overall equivalent sampling rate $f_{s,\text{equiv}}$ and the periodicity of non-uniformity r, the original spectrum of the analogue signal is copied to all harmonics of the fractional sampling rate $f_{s,\text{equiv}}/r = f_c$ with different weights depending on the amount of sampling time deviation. In our case, the stimulus spectrum would appear around DC, 9 GHz, and 18 GHz. All these copies will have unknown weights and superimpose to form the spectral content of the sampled data vector. After calibration and if uniform sampling is achieved, only the correct spectrum around DC will remain and the other invalid images will vanish. The effect is shown in figure 4.10 using the example of a band-limited M-Sequence. The blue curve shows the power spectrum of a data vector gathered with incorrect sample times. The images of the real spectrum are evident around 9 GHz and 18 GHz as predicted. The green curve shows the power spectrum of the same signal but this time sampled in an almost uniform manner. Even though the reduction of false spectral images is evident, the result is not perfect. Maximum clutter level is only 56 dB below the correct signal, but mean clutter power is an acceptable 72 dB down.

Using the stimulus of the new sensor produces a little more complicated result. Due to the very large bandwidth, the spectral images alias into each other making a distinction of true and false spectral parts difficult. However, from the characterisation measurements of the transmitter module it is known that the signal has almost no power above 14 GHz (the power level is vanishing in the noise floor). When the initial guess of the phase shifter control values is not too bad, the weights of the false images will be low compared to the real spectrum. Some of the unwanted energy will still be present between 14 GHz and 18 GHz in the sampled data. This fact can be used to calibrate the control values. Aim of the calibration would be to adjust control values in such a way, that the residual spectral footprint of the original signal above 14 GHz is minimised. The assumption of an empty spectral range in the upper frequencies is the model developed for this test
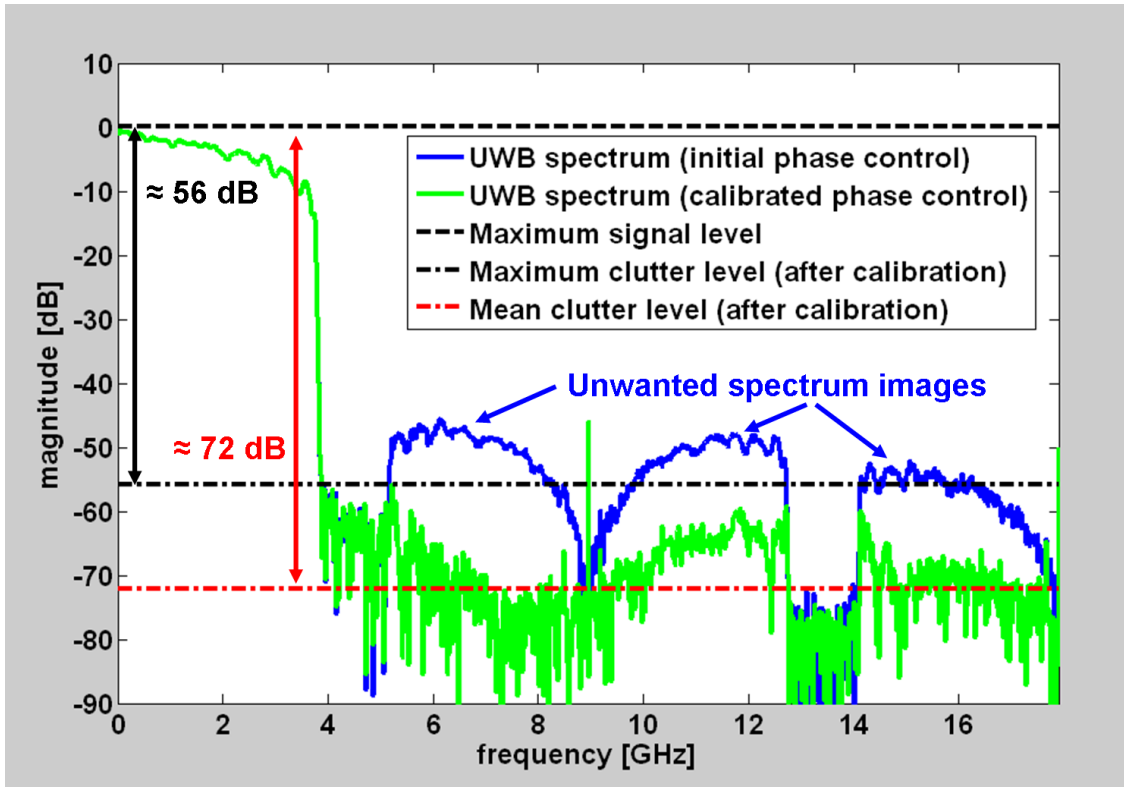
Fig. 4.10.: Comparison of a correctly and periodic non-uniformly sampled UWB power spectrum

signal. In trying to minimise the image energy in that region, the calibration process can be seen as a model-fitting approach. Obviously, the information obtained from this simple model is very limited. For example, it does not allow to derive a direction for adjusting each individual phase shift to achieve improvements. It simply provides a measure, if a given combination of control values means an improvement over a previous one. For that reason, the model can be transformed into a cost function to be used in an optimisation process.

Cost functions for optimisation When phase control calibration is formulated as an optimisation problem, the nature of the cost function usually determines what kind of search algorithms is applicable and should be discussed first. The cost function will have the phase shifter control values as an input and is based on the spectral content of the corresponding acquired data vector in the range between 14 GHz and 18 GHz. The less of the stimulus signal was present in that frequency interval, the closer the acquisition scheme must be to uniform sampling. A little experimentation showed, that the behaviour just mentioned is only valid in the vicinity of correct phase control values, i.e. the initial guess must be reasonably well to avoid travelling in the wrong direction during optimisation. This observation was true for different cost functions tested. The reason behind

this is the simplicity of the test signal's model. It only copes with spectral content that shouldn't be there, but it does not account for the errors below 14 GHz which arise due to aliasing of the correct spectrum with parts of the invalid images. Since non-uniform sampling of a complex UWB signal is quite difficult to predict, there might exist control value combinations where the power in the upper frequencies is well suppressed while still having strong distortions in the actual stimulus frequency range. However, in practical tests it has also been proven that the default control values setup at the laboratory are a satisfactory initial guess and do not lead to such situations.

An important aspect of cost functions is whether a closed-form representation can be found or not. This decides about the applicability of most gradient-based search algorithms. Unfortunately, a closed form is generally not available in our optimisation problem. The reason is simply that the inputs of the function are rather abstract numbers (control values) that translate into a phase shift and finally into a complex sampled signal. As can be seen from figure 4.9, even the way from the digital values to the actual inserted phase shift contains a number of components, whose behaviour is dependent on the a-priory unknown environmental conditions. Furthermore, the response curve of the HMC-C010 phase shifter is not exactly known either and also changes with temperature. The large number of factors that influence the actual achieved phase shift for a particular control value and the fact that the shape of the sampled stimulus signal is not exactly known make a closed formulation of a cost function infeasible. The cost value can only be obtained implicitly by measuring the test signal with the given control value combination under current environmental conditions.

The specific implementation of a cost function has some degree of freedom. As long as it delivers higher cost values the more stimulus energy is found above 14 GHz, every analysis approach is usable. There are some considerations limiting the number of acceptable cost functions. If the sampling would almost be uniform, the remaining traces of the stimulus will be very low and not far from the noise floor. Fortunately, it is possible to incorporate the similarity between the unwanted images and the idealised test signal $uwb(t)$ of equation 4.3 to improve SNR significantly. The time domain representation of the spectral image can be cross-correlated with $uwb(t)$ to form a kind of impulse response for the current sampling time error. The final implementation and specific form of the cost function is described and motivated in appendix A to allow a compact description of the calibration process in this section.

In order to investigate convergence behaviour, some experimentation has been done in the laboratory. Starting from the initial guess, test signals have been measured for all possible permutations of the three control values r_2, r_3, and r_4 (r_1 represents the reference phase shift and is always fixed). Each control value was allowed to be changed within a margin of 256 LSBs, i.e. they were varied in $r_{i,\text{init}} - 256 \leq r_i \leq r_{i,\text{init}} + 256; i = 2..4$. The control values were changed in steps of two LSBs and the cost function has

been calculated for the more than 16,000,000 combinations in this brute-force test. This resulted in a cost value matrix $\mathbf{C}_{\text{full}}$ of size 257 x 257 x 257, which is difficult to visualise in order to judge behaviour of the function. To get a compact view, the number of dimensions of the cost function needed to be reduced. This was done by finding the minimum value along the first dimension according to equation 4.13 and finally plotting the remaining two-dimensional matrix $\mathbf{C}_{2D}$ in figure 4.11.

$$\mathbf{C}_{2D}(r_3, r_4) = \min_{r_2} \mathbf{C}_{\text{full}}(r_2, r_3, r_4) \tag{4.13}$$
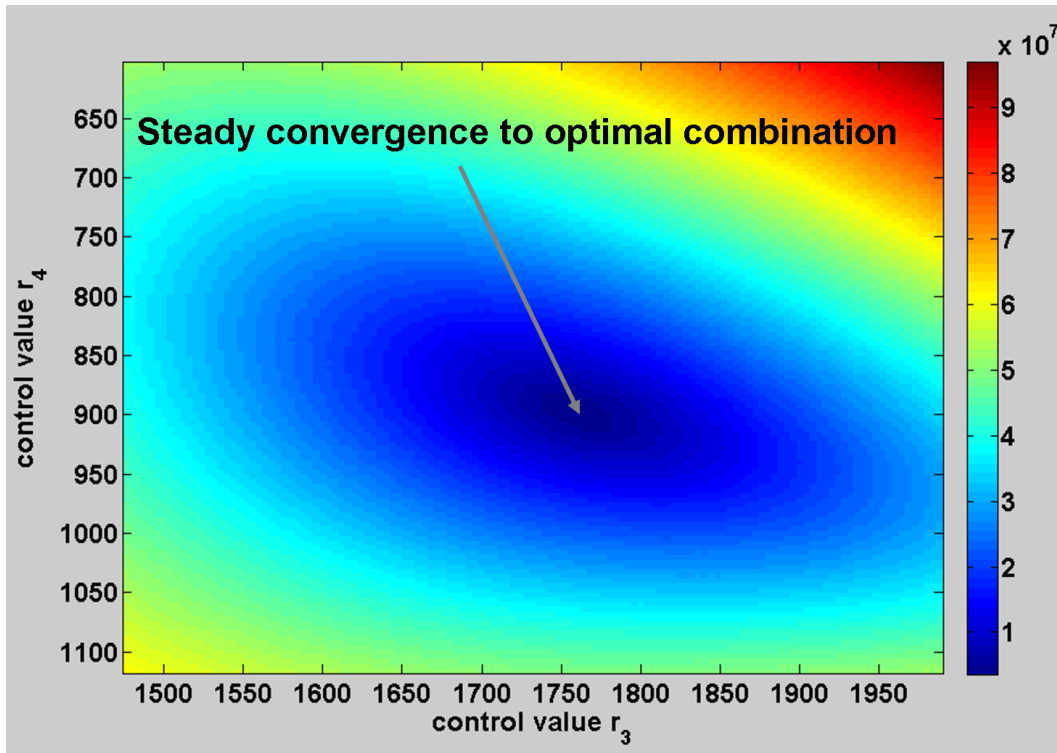
Fig. 4.11.: Cost function values $\mathbf{C}_{2D}$ for variation of phase shifter control values r_3 and r_4

Figure 4.11 alone does not show the full cost function behaviour. A similar view can be obtained by minimising $\mathbf{C}_{\text{full}}$ for r_3 (along 2nd dimension) and looking at $\mathbf{C}_{2D}(r_2, r_4)$. $\mathbf{C}_{2D}(r_2, r_3)$ can be extracted in a similar way by minimising the full dataset along the 3rd dimension. The resulting graphs look similar to figure 4.11 and are therefore not shown here. Well-behaved convergence of the cost function in the vicinity around the optimal control value combination is evident in all $\mathbf{C}_{2D}$. It can be concluded, that a unique optimal control value combination can be found by a search algorithm within a certain margin around the initial guess. Please note that the actual optimum will depend on environmental conditions at the test site.

Choice of search algorithm Gradient-based search algorithms are difficult to apply for this optimisation task, since the only way to get the gradient is to measure the costs for many combinations of control values around the current one or to predict and approximate it. However, the number of measurements for the calibration process needs to be restricted in order to limit the amount of time taken to complete the process. Making matters even worse, the measured data vectors need to have a very good SNR — much better than 60 dB to ensure meaningful and stable cost function results. Consequently, enough averaging must be provided for each single measurement which can lead to long search durations when a large number of combinations is to be tested. Form a practical point of view, the calibration of sampling timing should finish after a few minutes at most. With a sufficient SNR, each measurement will take about 2 s in the current implementation of the new M-Sequence sensor. Up to 150 such measurements are possible within 5 min, for example. It is clear that a brute-force test as presented before is not feasible. Testing of the new sensor device under different environmental conditions, such as in the laboratory and in different salt mines, showed that the minimum search margin around the initial guess values should be at least $r_{i,\mathrm{init}} - 32 \leq r_i \leq r_{i,\mathrm{init}} + 32; i = 2..4$ in order to always find the optimal combination — more than 270,000 tests would result. Therefore, smarter search algorithms have been investigated. Two methods turned out to produce good results.

The first procedure was based on the Nelder-Mead simplex search algorithm introduced in [117]. This approach has many advantages — it can easily handle many-dimensional optimisation problems, it does not need gradients or a closed expression of the cost function, and it is known to converge well even for complicated and partly unsteady cost functions [118, 119]. There are some downsides, of course. The number of cost function evaluations, which equals the number of test signal measurements for our problem, cannot be known a-priori. However, it is possible to set a limit on the number of function calls and use this as one stopping criterion for the search (optimal control values cannot be guaranteed in such a case). The second issue is the fact that the original Nelder-Mead method is defined only on a continuous and unbound parameter space. This means that the parameters of the cost function would need to be real values rather than integers. The algorithm has been modified to account for the discrete definition of optimisation parameters r_i and also for the maximum search margin (e.g. ± 32). Besides the limitation of cost function calls, a second abort criterion for the search was defined. The algorithm keeps track of a number of control value combinations it challenges against each other. When the process approaches the optimal values, all combinations will become equal or will only differ at most by one in any control values. If such a state has been reached, the search is finished and the actual combination with best cost function value is chosen as the optimum result. A more detailed description of the modified Nelder-Mead search is given in the appendix in section A.2.

Testing with different initial values in the lab proved that the search will usually converge to a good result and that it will take between 80 and 140 cost function calls to do so. This rather predictable behaviour can be accounted to the fact, that the cost function is well behaved as exemplified by figure 4.11. It should be pointed out, however, that due to the modifications of the original algorithm and also the limitation of allowed function calls, convergence to an optimum may not always be ensured if the cost function would become more complicated or the initial guess was too far off the optimum. A thorough theoretical treatment of the convergence properties of the implemented modified algorithm was postponed for future research because an alternative search method has been developed and tested as well.

The second search algorithm considered is also described in the appendix (section A.3). It was designed to work with a discrete parameter space in the first place and to overcome some of the downsides of the Nelder-Mead approach — most notably the unknown number of cost function calls. It is based on the assumption that the optimal control values are all near the initial guess and that the cost function has only one minimum at these optimal values, i.e. there are no nearby local minima for other control value combinations[2]. The proposed new algorithm basically checks combinations of control values using the outer limits at the current margin around the initial values. This results in an information about the direction the search should continue. In this sense, a generalised gradient (not defined locally around the current combination) is analysed. The combination with the best cost function value is then used as a new initial guess and the same process is repeated with a narrower margin. Iterations are done until the margin becomes one. Then the search is finished and the currently best combination of phase shifter control values is used as the optimisation result. In short, the optimum is found by means of successive approximation. Given a maximum margin at the beginning of the process and the number of iteration steps S to narrow the margin subsequently, the total number of cost function calls N_{cost} can be determined from equation 4.14. A flow chart of the whole optimisation process can be found in figure 4.12.

$$N_{cost} = S \cdot \left(3^{r-1} - 1\right) + 1 \tag{4.14}$$

Figure 4.13 finally shows another comparison of power spectra for the UWB test signal. Absolute scale of the power is arbitrarily chosen. The blue curve was obtained from the initial guess phase shifter control and the green one was measured after optimisation with the algorithm just described. The reduction in spectral power above 14 GHz is evident in the presented data. The residual mean spectral power in the upper frequency range is

---

[2]As mentioned before, such behaviour has been observed for the implemented sensor system. These assumptions might not necessarily hold if other hardware, test signals, or cost functions were used. For cost functions with local minima near the global optimum, the new algorithm could run into a non-optimal result. The Nelder-Mead simplex method is more robust regarding such cases.
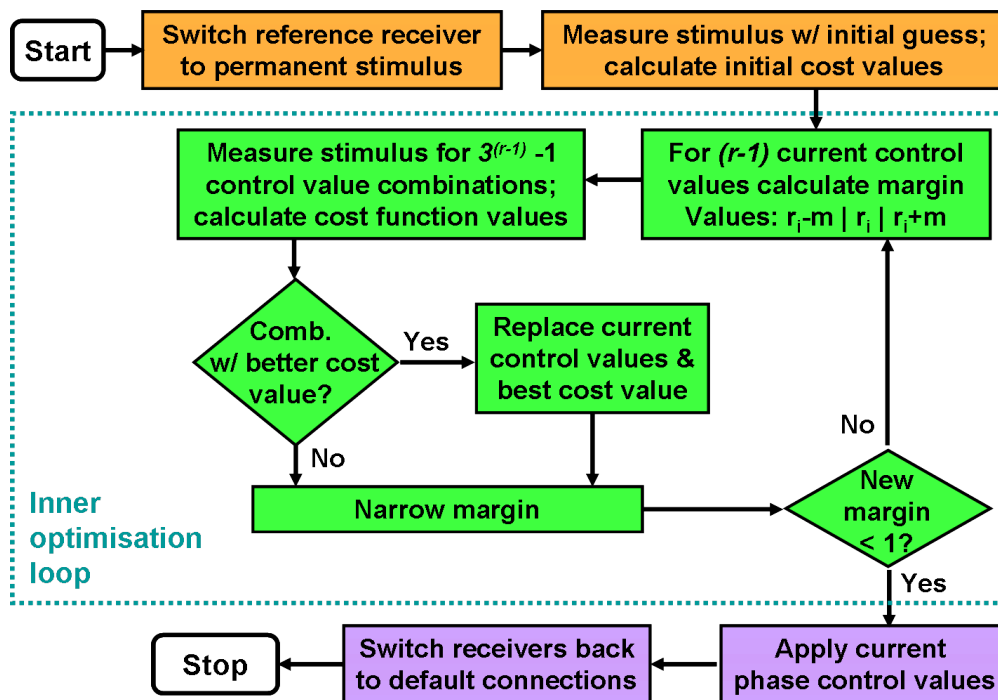
Fig. 4.12.: Flow chart of phase shifter control optimisation in the new sensor
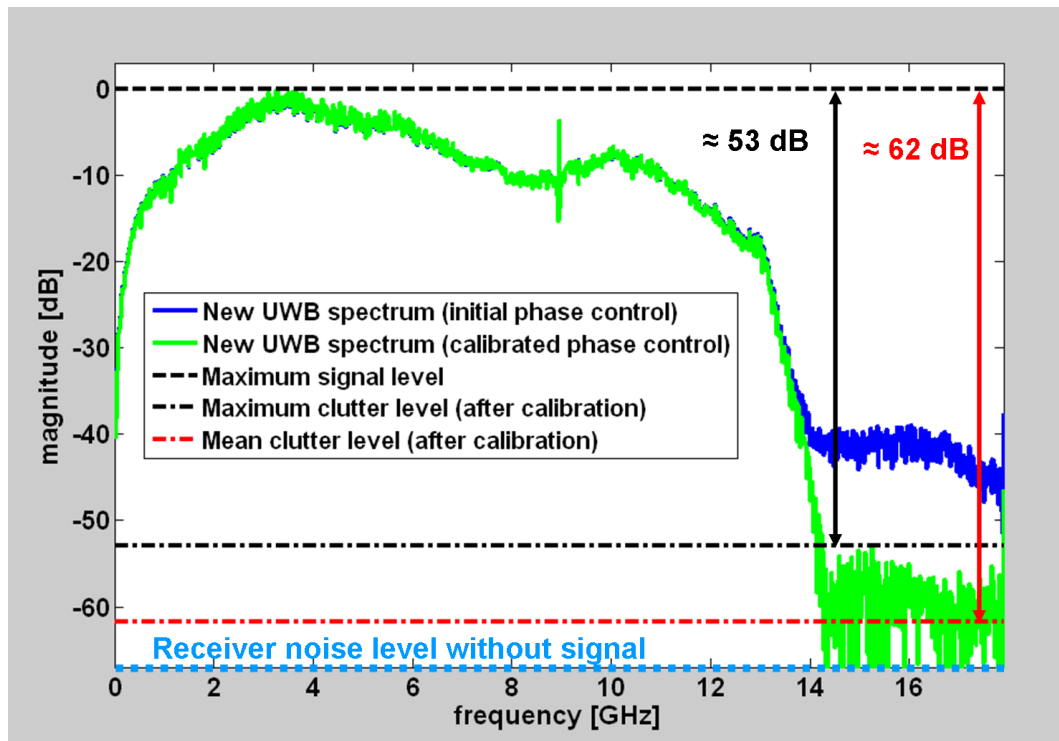
Fig. 4.13.: Comparison of initial and optimised UWB power spectrum of the new sensor

more than 60 dB below the useful signal. This coincides well with the predictions of accuracy analyses in subsections 4.2.2 and 4.3.1. However, maximum clutter level (already influenced by noise, of course) is only about 53 dB down. The noise level of the receiver without any signal would be around -70 dB as indicated in the figure. When comparing this to the optimisation result it becomes clear, that there remains some unwanted energy above 14 GHz in the sampled data. Besides residual errors of inaccurate sampling times, this can also be attributed to the limited linearity of the T&H circuits, buffers, and ADCs on the MLC40 backend. Results of similar quality like figure 4.13 have always been obtained throughout the operation of the sensor in the laboratory as well as in different salt mines with quite different environmental conditions. The performance of sampling timing calibration for the new M-Sequence system has therefore proven to be practical and satisfactory.

4.4. Summary of phase shifter control calibration for uniform dense equivalent time sampling

Like most other UWB sensors out there, the new M-Sequence device uses sub-sampling to acquire the received signals. This is done to enable high-resolution and high-accuracy ADCs and to be able to cope with the resulting digital data stream in an affordable way. The inherently extremely stable sampling scheme of the original M-Sequence approach benefits the new system as well. Without modification it only allows to realise equivalent sample time spacings of multiples of the master clock periods T_0. The scheme has been extended in the new system by a phase shifter for realising sample time spacings in fractions of T_0 in order to increase the equivalent sampling rate according to the needs of the stimulus employed in the new sensor. This time, the phase shifter delays the master clock of the synchronisation unit in $r = 4$ fractions of T_0. Since uniform sampling is beneficial for most processing algorithms and is even more so demanded in many cases, a calibration process has been developed to ensure that the phase shifts are multiples of T_0/r (corresponding to $360°/r$). A closer look at the overall timing of sampling revealed, that this implementation is a realisation of so-called periodic non-uniform sampling.

Theoretical analysis for single-tone as well as an UWB signal have shown, that the maximum allowed deviations from uniformly distributed sampling times are extremely small when the amplitude errors should not exceed a reasonable amount. For example, if the maximum amplitude error (or the average power of the errors alike) for the idealised UWB stimulus of the new sensor should be 40 dB down, sampling time must be accurate to within 0.7% of the sample spacing. For 60 dB accuracy time errors must already be below 0.1% (see table 4.1). The investigation also showed — in accordance to literature about periodic non-uniform sampling — that false sampling times will lead to spectral

components in the sampled data that are actually not present in the original analogue signal.

To be able to achieve such highly accurate delays, the control circuit for the phase shifter was carefully implemented using the available high-resolution DAC of the digital backend plus corresponding signal conditioning. To avoid noise and parasitic external coupling in the control voltage, it is routed in a shielded environment and terminated with a low pass filter just before the shifter device. The filter frequency cut-off was chosen as low as possible to limit the noise bandwidth while still allowing sufficiently fast settling of the signal. To not increase the overall time it takes to acquire a complete data vector (including all synchronous averages) too much, the timing of changing the phase shift was implemented in a smart way. For each fixed phase shift, all samples including the averages are acquired before transitioning to the next phase value. In this way, the maximum measurement rate of the new sensor was kept close to a basic M-Sequence sensor with the same master clock rate (131 vs. 133 IRF/s). On the other hand, the control signal still has a rather long time window of about $30\,\mu s$ for settling. Under these conditions and with the implemented hardware, it could be expected that the relative accuracy of sampling times will not be better than approximately 0.05% and consequently the maximum amplitude error due to false sampling times will be around 60 dB down at best.

The idea of phase shifter control calibration is based on the measurement of some kind of test signal which is accurately known or at least adheres precisely to some signal model. Due to easy generation with the existing transmitter module, two types of test signals have been considered. One would be the sine wave of the master clock source where harmonics suppression by simple filters is easily possible. Such a simple signal would allow straight-forward correction of sampling times since the principal shape of the sine wave is known. Unfortunately, the solution could not be used due to issues with the digital backend. The second test signal is the actual sensor stimulus itself. Since the exact shape of this signal is not known and also depends on environmental conditions such as ambient temperature, only a very simple signal model could be exploited. It is known that the transmitter does not output significant power at frequencies above 14 GHz. If sampled data vectors contain spectral power in the range between 14 GHz and 18 GHz, the effect can largely be blamed on non-ideal phase shifter values leading to periodic non-uniform sampling. This way, a measure for the quality of current phase shifter control could be provided. However, this simple model does not directly provide information in which direction the control values must be changed to improve the situation.

Therefore, an $r-1$ dimensional optimisation problem was formulated using the spectral content above 14 GHz for the definition of a cost function. Intelligent search algorithms needed to be used since the cost function involves measurements of the test signal with the actual control values taking considerable time due to high SNR requirements. For a maximum duration of the calibration process of 5 min, the number of measurements with

sufficient SNR must be limited to 150. Another issue in choosing or designing search algorithms was the lack of a closed-form representation of the cost function because of the complexity and number of influencing factors. The first method investigated was the Nelder-Mead simplex search, which does not use gradients of the cost function and can also handle a limited amount of unsteadiness. Some modifications to the original algorithm were necessary, e.g. limitation to a discrete parameter space and introduction of a maximum margin around the initial guess control values within which the search must take place. The latter modification was attributed to the observation, that a good and generally applicable initial guess could be found in the laboratory and that the cost functions tested were all well-behaved around the optimal control values. Therefore, search efficiency was increased by limiting the search around the starting values and the a-priori unknown number of cost function calls turned out to be low enough. In some tests using different starting values close to the optimal ones it was indeed observed, that the number of search steps was not too different between the runs and that finding the correct control values was achieved in a robust manner. However, not knowing the exact number of necessary test measurements with the Nelder-Mead method and the fact that the employed cost function is not too complicated around its optimum, lead to the design of a second algorithm. It is based on testing permutations of control values at the edges of a margin around the current best guess and calculating some kind of large-scale gradient. This information is used to change the current combination and the search margin is then decreased. The whole cycle is repeated until the margin vanishes around the optimum control value combination.

Throughout operation of the sensor device in different environments, satisfactory phase shift calibration results have always been achieved. The prospected SCR of about 60 dB could almost be reached when judging from the spectral content of the test signal with optimised phase shifter control. Details of the cost functions used and the implementation of the two mentioned search algorithms can be found in appendix A. When the timing of sampling is setup correctly, the sensor can be used for real measurements just like any other UWB device. It is already been motivated that for a system with such a large bandwidth calibration for removal of other systematic errors is mandatory to reach the necessary system performance. This matter is discussed in the following chapter.

5. Device clutter removal by full 2-port calibration

It has been pointed out before, that especially for UWB sensors it is difficult to build even the simplest components with very good properties, i.e. they behave different from their expected ideal functioning. For example, manufacturing RF cables with exact matching of the wave impedance (usually $50\ \Omega$) over several GHz of bandwidth in the lower microwave range is not achievable. The same statement is true for other parts as well — like amplifiers, filters, mixers, and switches, etc. Apart from the inevitable measurement noise, such imperfections influence acquired data and obscure the information about the actual test object. In fact, any sensor or measurement device also causes systematic errors in the resulting data. These deviations should not be confused with noise. While the latter one is random in its nature, systematic errors always occur in the same manner provided constant measurement conditions. Such errors are also called *device clutter* and can usually be corrected or at least suppressed. This is done by means of calibration. Calibration describes a process of determining the systematic errors of a device and then using this knowledge to correct measurement data afterwards. It often involves measurements with objects whose behaviour is exactly known — the so called *calibration standards*.

Calibration can be defined at different levels and for different purposes. For example, correction of sampling timing described in the previous chapter 4 is one step. However, it does not correct any of the other imperfections apart from sampling time errors. Another possible level for correction could be the coaxial measurement ports of the sensor. Up to the port connectors, all RF signals can be described as one-dimensional waves (at least for the considered frequency range) travelling within all sensor components. Finally, since the applicators of the sensor in a salt mine will be antennas, they form another possible calibration interface. Removing device clutter at the antenna level would provide a complete coverage of the sensor but it would also mean to deal with three-dimensional waves in free space. Finding suitable standards with exactly known scattering behaviour and a consistent description is not an easy task. Such methods incorporating the antennas are topics of ongoing research at the EMR Lab but could not be covered in this thesis. Some other researchers are also investigating antenna calibration, e.g. as in [120–122]. Consequently, calibration of the new sensor at the coaxial measurement ports was chosen as an intermediate step to full system correction and will be introduced in this chapter.

Starting with a short review of the basic methods in the following section, the implemented calibration is thoroughly described in section 5.2. The last section of this chapter deals with an accuracy analysis including a performance comparison of the new M-Sequence device with a typical VNA.

5.1. Recapitulation of basic coaxial calibration methods

Since any device component can produce quite different types of systematic errors, it would be difficult to describe them according to their physical cause. Another problem with such an approach is that the description of a system would need to be adopted every time a component or the design was changed. This can happen quite often, e.g. if an RF cable is exchanged with a longer one for a special measurement setup etc. In order to make a correction feasible under real-life conditions, one usually needs to find a consistent and complete way to describe the device clutter under all circumstances the sensor will be used. Fortunately, there is a generalised way of describing all these errors suitable for many sensors. Most of the time, linearity of device components — especially the receivers — is ensured by design and furthermore coaxial test objects as well as standards also behave in a linear fashion. Under these circumstances, the signal components caused by any individual source of device clutter can be described by a number of impulse response or frequency response functions, which simply superimpose in the measured data. Due to linearity, all error components can be summarised into an equivalent error network. The real sensor device is therefore treated as a black box and decomposed into in ideal device (with no systematic errors) and the virtual error network responsible for modelling all deviation from ideal behaviour. This model using a virtual error network can express device clutter regardless of its physical cause.

This basic idea is not a new one — a large number of corresponding examples for calibration methods at a coaxial or wave guide interface can be found, e.g. [84], [95], or [96]. Despite the fact that the original development was usually made for vector network analysers, the calibration implemented for the new M-Sequence sensor was inspired by these common methods. Apart from being advantageous for the salt mine application, the two-port S-parameter frontend introduced in section 3.3.3 was designed to enable the adoption of algorithms originally developed for VNAs. Even though the numerous methods might seem very different or use different kinds of standards, decomposition of the device is always used. Figure 5.1 illustrates the common concept for a sensor with p measurement ports. The error network connects the theoretical ideal sensor to all test objects and consequently must be a $2p$-port. The wave quantities travelling out of or into the ports and the test object are mentioned in figure 5.1, too. The measured S-parameters in $\mathbf{S}_m$ are the outcome of the idealised sensor and contain the information

about the test object[1]. However, usually $\mathbf{S}_m \neq \mathbf{S}$ holds because the waves have to pass the error network, which is described by its $2p$ x $2p$ S-parameter matrix $\mathbf{E}$.
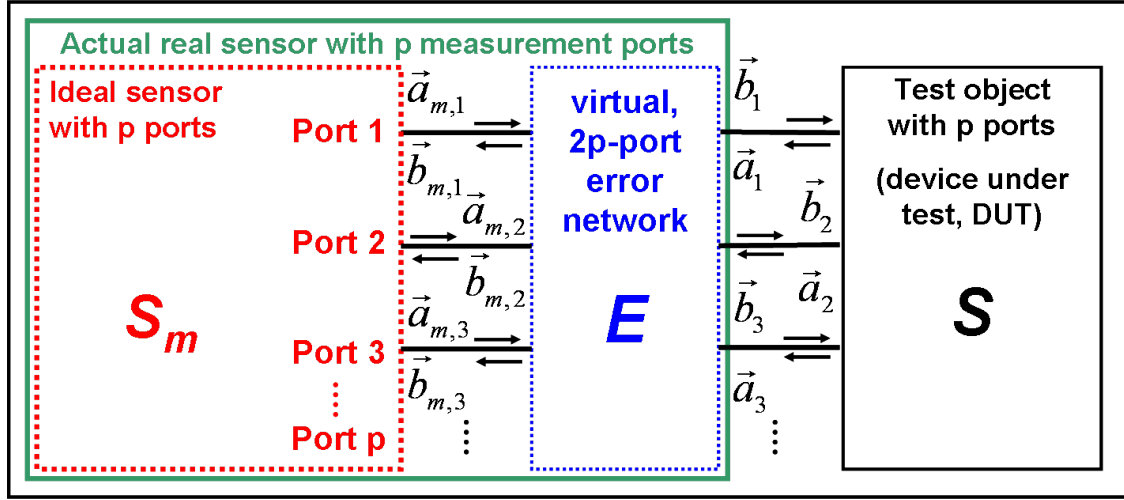
Fig. 5.1.: Decomposition of a measurement device for calibration

Two additional aspects of the decomposition need to be mentioned here. In many cases linearity of the power amplifiers at the stimulus generator inside the device might not be guaranteed. A saturated power source alone does not break the concept's linearity assumption as long as the actual transmitted waveform is exactly known. Most of the time it simply needs to be measured by a reference receiver as realised in the S-parameter frontend of the new M-Sequence sensor. However, all receivers must be working in their linear range — compression or other non-linear distortions will severely degrade calibration success of common methods or make it even impossible to apply the abstraction shown in figure 5.1. With linear receivers, the error network can be interpreted as being source-free, i.e. all stimulus power is assumed to come from the ideal measurement device (or the test objects). The network is therefore passive, reciprocal, and can be fully described by its $4p^2$ frequency dependent scattering parameters. Due to reciprocity, only $4p^2 - 1$ of them are linearly independent. The general process of calibration can now be summarised as follows:

1. Connect k standards to the measurement ports of the device and acquire their S-parameter matrices $\mathbf{S}_{m,i}; i = 1 \ldots k$

2. Use the known real behaviour of the standards, i.e. $\mathbf{S}_i; i = 1 \ldots k$, to calculate the $4p^2 - 1$ independent coefficients of the error network $\mathbf{E}$

3. Use the error coefficients to correct subsequently measured data, i.e. get the real $\mathbf{S}$ of the measured test objects from their $\mathbf{S}_m$

---

[1]Since it is a common RF description, S-parameters are used here as an example. Equivalent formulations using other types of parameters are also possible as long as the description is complete.

Actual calibration algorithms might prefer to use other representations than S-parameters and might also assume to know at least some of the error coefficients a-priori making the second step less elaborate. The algorithms also differ in the number k and type of standards employed. However, the standards must be selected in such a way, that enough linearly independent observations of the error network are ensured.

There are other important common aspects to keep in mind. An implicit assumption is that the device does not change its properties during and after the calibration process (steps 2. and 3.) — the knowledge about the device clutter must stay valid all the time. Especially drift effects or changes in the environment might breach this assumption which means calibration should be repeated from time to time or when conditions change. Also system instabilities or sampling time jitter will have negative influence on calibration performance because repeatability of signals and device clutter will be impaired. Even during the calibration process itself it can be difficult to maintain a steady state, e.g. mounting of the necessary standards or bending cables might already slightly change the sensor. It is therefore important to understand that calibration must be done with extreme care to achieve maximum correction performance. All these issues must be accounted for by proper design of the measurement system.

As an example for coaxial calibration methods using a virtual error network, let us take a quick look at the simple case of the 3-term correction which is often applied for single-port sensors. It is also reused for the two-port algorithm described later in section 5.2.

5.1.1. Example: 3-term calibration

Since the original formulation of the presented method was done for VNAs [84], the following equations are all defined in frequency domain and each step needs to be applied for every single frequency of interest separately (this is another reason for the linearity requirement on the receivers and test objects). In the one-port case, only reflections are measured and the error network is a two-port with only three independent coefficients as shown in figure 5.2. It concretises the decomposition of the real device into an ideal one and the error network. At least three different standards must be measured to obtain all coefficients, hence the name 3-term calibration.

The virtual error network $\mathbf{E}$ is described as S-parameters in the figure. However, in literature they are usually named $\underline{e}_{xy}$ to denote the fact that they represent errors. While a two-port network has four S-parameters, the transmission coefficients $\underline{e}_{21}$ and $\underline{e}_{12}$ are not independent and can only be observed together, i.e. the actual unknown error coefficient is their product $\underline{e}_{21} \cdot \underline{e}_{12}$. Without restricting generality it is common to assign the product to one of the error matrix elements and to set the other element to 1.0 as expressed in equation 5.1.
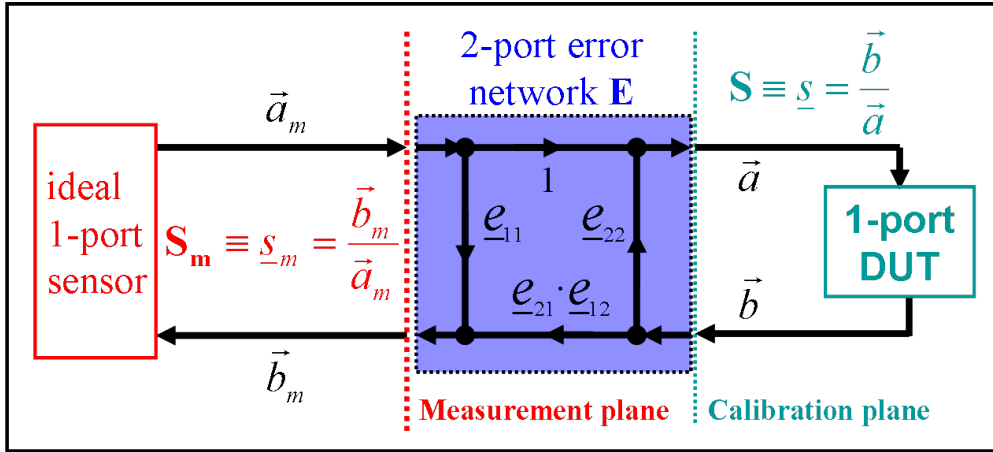
Fig. 5.2.: Error model for 3-term correction

$$\mathbf{E} = \begin{pmatrix} \underline{e}_{11} & \underline{e}_{21} \cdot \underline{e}_{12} \\ 1.0 & \underline{e}_{22} \end{pmatrix} \tag{5.1}$$

For the formulation of the calibration problem it is easier to use transfer parameters (also called T-parameters, or cascading parameters) for the coefficients instead. Equation 5.2 shows the relationship between both representations for a two-port. Putting equation 5.1 into 5.2 yields the expression 5.3.

$$\mathbf{T} = \begin{pmatrix} \underline{t}_{11} & \underline{t}_{12} \\ \underline{t}_{21} & \underline{t}_{22} \end{pmatrix} = \frac{1}{\underline{s}_{21}} \begin{pmatrix} -\det \mathbf{S} & \underline{s}_{11} \\ -\underline{s}_{22} & 1 \end{pmatrix} \tag{5.2}$$

$$\mathbf{T}_{err} = \begin{pmatrix} \underline{t}_{err,11} & \underline{t}_{err,12} \\ \underline{t}_{err,21} & 1.0 \end{pmatrix} = \begin{pmatrix} -\det \mathbf{E} & \underline{e}_{11} \\ -\underline{e}_{22} & 1.0 \end{pmatrix} \tag{5.3}$$

At least $k = 3$ standards need to be measured to determine $\mathbf{T}_{err}$. The standards must be different one-port objects having known reflection coefficients $\underline{s}_i; i = 1 \ldots 3$. For each connected standard, measurement data $\underline{s}_{m,i}; i = 1 \ldots 3$ needs to be collected. The relationship between the real and measured reflection coefficients is given by equation 5.4. While the equation is non-linear with respect to the reflection coefficients, it is linear in the three error T-parameters. Each measurement yields such a relationship and all of them can be summarised as the linear system of equations represented in 5.5. The three error terms can now be calculated by inverting the calibration matrix $\mathbf{C}$. If exactly three standards have been measured, direct inversion can be performed. For the case of $k > 3$, a pseudo inverse could be calculated finding the best solution for $\mathbf{T}_{err}$ in a least squares' sense. Once the error terms are calculated, any further measurement data $\underline{s}_m$ can be corrected to get the real reflection coefficient of the test object $\underline{s}$ using equation

5.6. Please note that expanding 5.6 leads to a similar expression as 5.4.

$$\underline{s}_{m,i} = \underline{t}_{err,11}\underline{s}_i + \underline{t}_{err,12} - \underline{t}_{err,21}\underline{s}_{m,i}\underline{s}_i \forall i \tag{5.4}$$

$$\begin{pmatrix} \underline{s}_{m,1} \\ \underline{s}_{m,2} \\ \vdots \\ \underline{s}_{m,k} \end{pmatrix} = \begin{pmatrix} \underline{s}_1 & 1.0 & -\underline{s}_1 \cdot \underline{s}_{m,1} \\ \underline{s}_2 & 1.0 & -\underline{s}_2 \cdot \underline{s}_{m,2} \\ & \vdots & \\ \underline{s}_k & 1.0 & -\underline{s}_k \cdot \underline{s}_{m,k} \end{pmatrix} \begin{pmatrix} \underline{t}_{err,11} \\ \underline{t}_{err,12} \\ \underline{t}_{err,21} \end{pmatrix} = \mathbf{C} \begin{pmatrix} \underline{t}_{err,11} \\ \underline{t}_{err,12} \\ \underline{t}_{err,21} \end{pmatrix} \tag{5.5}$$

$$\underline{s} = \frac{\underline{t}_{err,12} - \underline{s}_m}{\underline{s}_m\underline{t}_{err,21} - \underline{t}_{err,11}} \tag{5.6}$$

Looking at equation 5.5 it becomes clear, why the standards must be as different as possible in terms of their reflection behaviour. If similar objects were used, the rank of $\mathbf{C}$ would drop and it could become singular making an unambiguous inversion impossible. Besides caring for numerical stability when calculating the matrix inverse, measurement noise must be taken into account. The acquired quantities $\underline{s}_{m,i}$ will have an uncertainty posing a limit on the accuracy of $\mathbf{T}_{err}$. The closer reflection coefficients of the standards are, the more influence noisy data will have on the result or even lead to singularities again. Another important limit on the accuracy arises from the standards. Their real behaviour is assumed to be known without error — something that can normally not be guaranteed in reality. For practical reasons, in the lower GHz range usual OSL standards are used — an open circuit (O), a short circuit (S), and a matched $50 \ \Omega$ load (L, sometimes simply called load). For example, precise manufacturing of the latter object is quite challenging. During calibration, one still assumes $\underline{s}_{load} \equiv 0$ introducing some amount of additional uncertainty. That is why for improved accuracy, variants of 3-term correction using a sliding load instead of a fixed one exist [84, 95]. If high-quality OSL standards are not available, it is still possible to determine their real reflection coefficients through circuit simulations or with the help of a calibration laboratory.

It is interesting to note that equations 5.4 through 5.5 are special cases of a generalised formulation for the calibration of a device with p ports as introduced in [95]. For $p = 1$, the error terms $\underline{t}_{err,xy}$, the measured data $\underline{s}_m$, and the known coefficients $\underline{s}$ are simply complex scalars. If they are replaced by matrices of size p by p and the error sub-matrix $\mathbf{T}_{err,22}$ is introduced appropriately, a multi-port formulation results. The whole error network description $\mathbf{T}_{err}$ then consists of $4p^2$ coefficients, one of which can be used for normalisation. With the development of multi-port sensors ($p > 2$), a modern calibration method using an unknown line as one of the standards has been expanded in a similar way [123]. It is based on 3-term correction of each individual port and much more practical for multi-port devices than many of the other approaches. Fortunately, it can also be used for two-port sensors such as the new M-Sequence device and will be discussed in the following section.

5.2. Full two-port calibration of M-Sequence UWB-sensors with 8-term method

The new M-Sequence sensor is well prepared for coaxial calibration by its design. It is build to be very stable, reproducible, and it has a full featured two-port S-parameter frontend with two reference receivers. On the other hand there are some principal differences to classical devices found in a laboratory environment. First of all, the M-Sequence system acquires data in time domain rather than frequency domain like, e.g., VNAs. Since most correction algorithms are usually defined in terms of frequencies, some modifications needed to be made. Another issue is the prospected working environment of the device. The conditions in a salt mine can be very different from a laboratory and are usually rather harsh. Salt dust is constantly present in the air and the operators may have to wear special protective clothes. All in all, it seems infeasible to aim at manual calibration where the standards need to be attached by hand in a carefully controlled way. This would also imply specially trained personnel. The best solution to avoid such disadvantages is a completely automatic calibration including all standards in a sealed system. This was the reason to implement the automatic calibration unit introduced in section 3.3.3. The port switches in the unit connect the measurement ports of the sensor to a number of standards if needed. Up to five two-port test objects can be applied besides the default connection to the system's antennas. Theoretically, this enables the use of many two-port calibration methods including the full 16-term method outlined in appendix B.

Besides the available standards another aspect is important for automatic calibration. It would be an advantage if the chosen algorithm would also provide some kind of performance figure. This would enable the operator to decide if calibration was successful and if the device is working properly. Rough handling of equipment in a mine can not always be avoided and such a tool enables the detection of even small damages degrading measurement accuracy. Some methods have the potential to provide performance figures without much extra effort. These considerations lead to a suitable choice.

5.2.1. Choice of calibration method

The two-port case is already more complex than the one-port calibration introduced in section 5.1.1 since test objects can also allow transmission between ports. The error network now is a four-port and has up to 16 unknown coefficients of which 15 are linearly independent. For two-port correction quite a number of methods exist and depending on the measurement device not all of the 15 error terms need to be determined. For convenience of the reader, the most general case of 16-term correction has been outlined in appendix B also providing a general mathematical formulation. The downside of the

full method is the need for at least five [96] fully specified two-port standards (i.e. their complete set of S-parameters including transmission coefficients must be known). Knowing the transmission behaviour of a standard with high confidence is very difficult when the device must work under different environmental conditions (e.g. the length and consequently transmission delay may significantly change with temperature). If the number of unknown error terms is decreased, the requirements on the standards can be relaxed. Well-known derivations are the 12-term method and different flavours of the 8-term calibration which are very common today. A good overview can be found in [84].

The 12-term case has been developed for special VNA designs using only three receivers instead of four (with only one reference channel). It was therefore not considered for the M-Sequence sensor. In order to apply one of the popular 8-term methods, however, special requirements exist for sensor design. It is interesting to note that half of the 16 error coefficients relate to crosstalk between the two measurement ports mainly caused inside the device. If the sensor design enables a very high port isolation, these terms do not need to be obtained during calibration and can be set to zero instead. As pointed out in [123], observation of these weak crosstalk terms is very difficult and if they can be measured, it is only under very bad SNR conditions (assuming a feasible, e.g. not too long, measurement time). Incorporating error coefficients with high uncertainty when correcting measurement data might lead to larger residual errors than neglecting these terms in the first place. This is the idea behind all 8-term methods. When the crosstalk coefficients are set to zero, a sparse error matrix $\mathbf{T}_{err}$ with only eight non-zero coefficients results. The general derivation of the 8-term model is given in the appendix in section B.3. One of the remaining terms is used for normalisation (also compare 3-term correction in section 5.1.1). Finally, seven coefficients remain which need to be determined during calibration. That is why these methods are so desirable since the number of necessary standards is reduced.

At this point the question arises, if the new M-Sequence sensor qualifies for these algorithms. The main condition to be fulfilled is either having very high port isolation or to be able to measure and remove port crosstalk in a consistent manner outside the actual calibration process. In figure 5.3 the overall system block diagram from chapter 3 is repeated. The major paths for crosstalk between the two measurement ports are highlighted with marks $\mathbf{X}_1$ and $\mathbf{X}_2$, respectively. $\mathbf{X}_1$ relates to the port switch used to stimulate either of the channels. Its internal path isolation obviously limits port separation. The employed solid state switch is specified to provide isolation better than 60 dB in the frequency range of the sensor. Moreover, the effect of switch errors such as leakage or mismatch can be suppressed by using a special technique for determining the measured S-parameters in $\mathbf{S}_m$. It uses a generalised way for S-parameter calculation from gathered wave quantities requiring a system like the new M-Sequence sensor with four independent receivers working all the time. For compactness reasons, description of the technique was

also moved to appendix B. In conclusion, crosstalk at $\mathbf{X}_1$ is not considered to be a major problem.
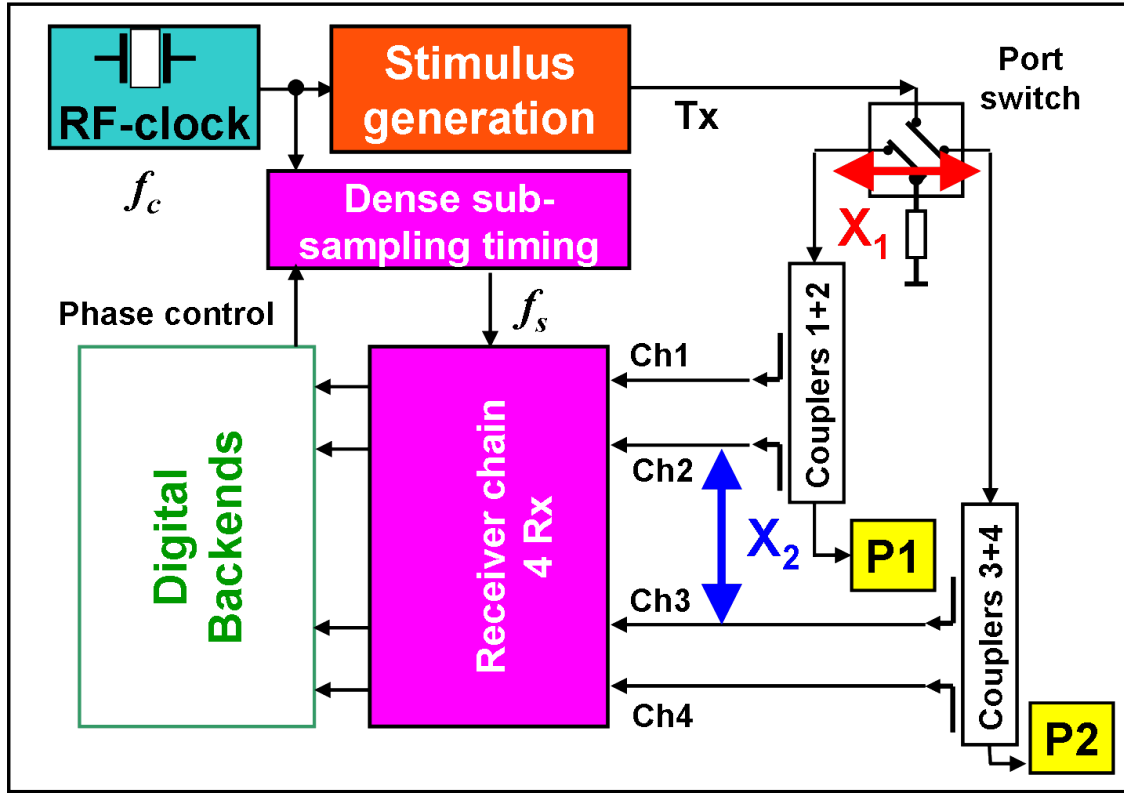
Fig. 5.3.: Main paths of port crosstalk in the new M-Sequence sensor

The second possible leakage path $\mathbf{X}_2$ exists in the four channel receiver module. The module has several track & hold circuits organised in a clock chain. It has been characterised in the laboratory. Channel isolation of neighbouring receivers was measured to be usually better than 70 dB across the occupied bandwidth except for the band from 10 GHz to 12 GHz where it sometimes drops to 57 dB. Leakage can be neglected for farther separated channels. This result is not too bad but it can be expected that if 8-term correction was applied, accuracy in the mentioned critical frequency band would be reduced. However, the effect of receive channel crosstalk can be distributed to influence different error terms and even some of it can be corrected by clever assignment of the receivers. The idea is demonstrated in figure 5.4.

Receivers one and two capture the incoming ($\vec{b}_0$) and outgoing ($\vec{a}_0$) waves belonging to the first measurement port. The crosstalk between them can be corrected by 8-term calibration because it has a similar effect as the limited directivity of the directional couplers used to extract these waves (also indicated in the figure). In fact, directivity of the couplers is only between 15 and 20 dB across the bandwidth, so the small receiver leakage is an insignificant additional contribution. The receivers three and four do the same job for the
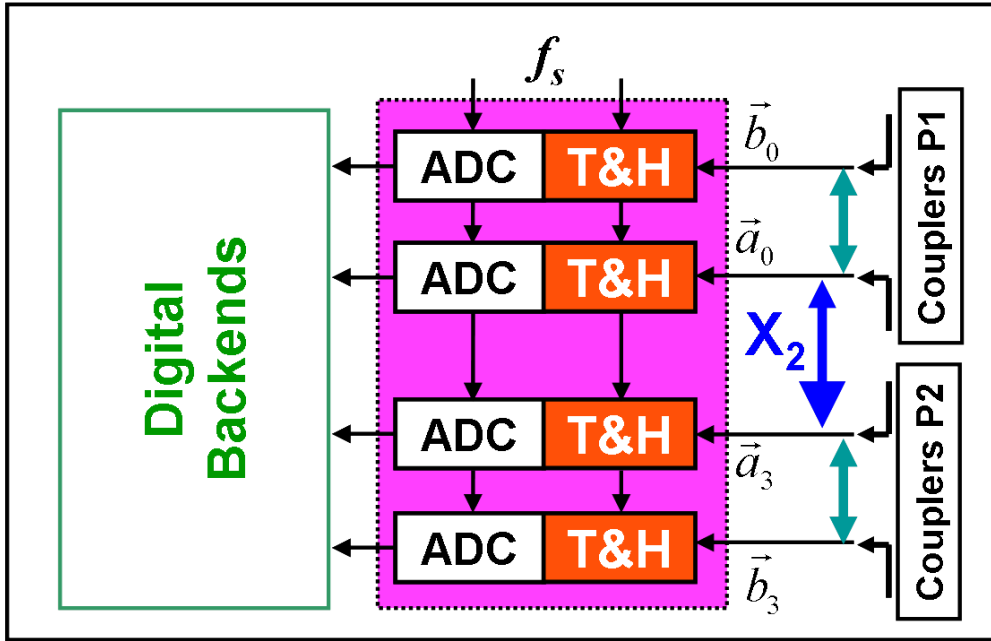
Fig. 5.4.: Receiver assignment of the new M-Sequence sensor

second port capturing waves $\vec{a}_3$ and $\vec{b}_3$, respectively. Again, leakage can be accounted for in the directivity error and will be corrected by calibration. The only critical crosstalk path is between receivers two and three. Both capture reference signals (outgoing waves) so only one of them will usually have a strong signal. At first sight, it seems like this leakage path could be counted into the port switch (and thus corrected by the switch error removal prior to calibration). This is, however, not completely true. Leaking stimulus energy in the port switch would excite the inactive port and consequently send a little energy to the test object as well. This is not the case for receiver crosstalk, it merely exists in the measured data only. In the full 15-term error model, there would be two different coefficients representing this kind of leakage, but they are assumed to be zero in the 8-term case. It is the only spot-on place where the assumption of high port isolation seems breached. On the other hand, the isolation is still not too bad with more than 60 dB for almost the whole stimulus bandwidth. Finally it was decided, that 8-term correction is applicable for the new M-Sequence sensor, but crosstalk $\mathbf{X}_2$ must be kept in mind as a possible accuracy limitation.

The different variants of 8-term calibration use different kinds of standards and pose more or less complicated expectations on their behaviour. According to [96] it is necessary to have at least one standard allowing transmission between the ports for any kind of two-port calibration. Manufacturing and characterisation of a transmission standard with high precision for all four S-parameters is quite difficult. Some of the 8-term variants, however, do not require complete knowledge of the transmission standard. In fact, there exists a method using an unknown through or line standard [84, 123]. The only requirements

on the transmission standard is reciprocity, i.e. $\det \mathbf{T} = 1$ where $\mathbf{T}$ is the T-parameter matrix of the standard (compare equation 5.2). If a line is used instead of a through, the approximate transmission travel time (more precisely the phase shift for each frequency of interest) should be known or must be gained during calibration. These requirements are easy to guarantee with high confidence even under very different environmental conditions. This makes the algorithm ideal for working a salt mines when combined with an automatic calibration unit. The 8-term correction using an unknown line was finally selected for calibration of the new M-Sequence system. Some implementation details will be presented in the next subsection.

5.2.2. Formulation and implementation of 8-term correction

Calibration methods are usually defined in frequency domain which is a natural choice if they are used for VNAs. The new M-Sequence sensor acquires data in time domain so extra steps have to be added.

Acquisition and preparation of measured S-parameters   To measure the full S-parameter matrix of a test object, two subsequent cycles need to be completed. The four receivers measure wave quantities according to the directional coupler they are connected to (compare figure 5.4). In the first cycle, port one is stimulated and receivers are collecting data in the so-called forward mode. The second cycle stimulates port two and is called backward mode. Again, all four receivers are storing data. In total eight wave quantities are acquired as raw digital data. Obviously, these vectors need to be transferred into frequency domain by discrete Fourier transform (DFT). From this point on, all further calculation can be done for every frequency component of the spectrum separately. The next preparation step involves removal of switch errors (like switch leakage, etc.) by using a generalised formulation for S-parameter measurements. The corresponding equations are derived in appendix B.1. As the result of this preparation, the measured S-matrix of the current test object given in equation 5.7 is obtained. Please keep in mind that these steps need to be done for all measurements — for the calibration standards as well as any further test object, i.e the disaggregation zone in a salt mine.

$$\mathbf{S}_m = \begin{pmatrix} \underline{s}_{m,11} & \underline{s}_{m,12} \\ \underline{s}_{m,21} & \underline{s}_{m,22} \end{pmatrix} \tag{5.7}$$

Core implementation of 8-term calibration with unknown line   Since the 8-term correction assumes high port isolation, most of the remaining error coefficients relate to a single port rather than the whole device. The error model for a single port has already

been discussed in section 5.1.1 and can be found in figure 5.2. It needs to be applied for both measurement ports covering a total of six error terms. Only one error coefficient is left and represents transmission tracking between the ports. The general system model and device decomposition is shown in figure 5.5. Please note that it has been derived from the common calibration error model of figure 5.1. The virtual four-port error network $\mathbf{T}_{err}$ can be split into two separate error two-ports $\mathbf{T}_A$ and $\mathbf{T}_B$ each of which belongs to a single measurement port (this reduction results from setting the port crosstalk terms in the full 16-term model to zero).
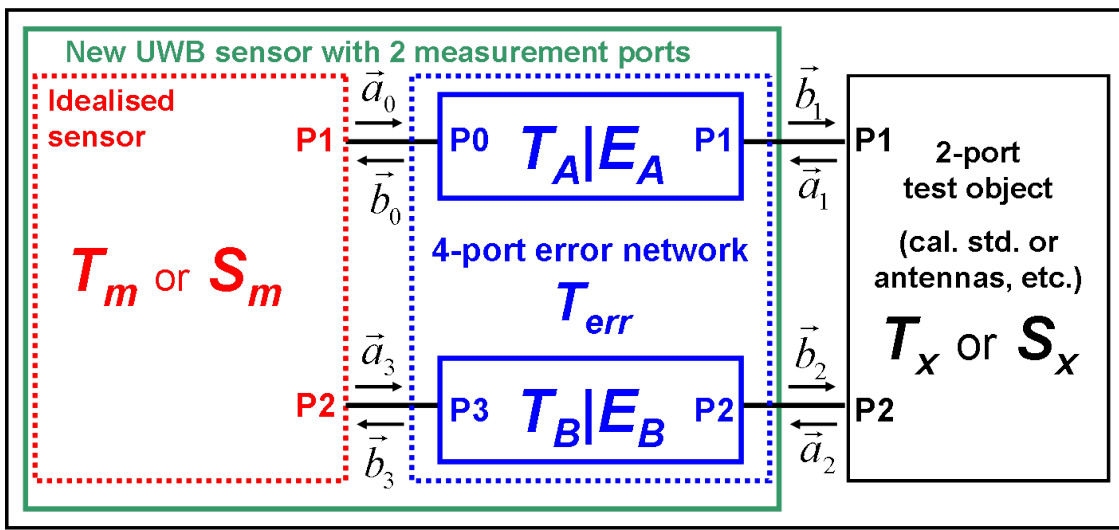
Fig. 5.5.: Error model for 8-term correction

The test objects are two-ports as well, represented by their T-parameters in $\mathbf{T}_x$. The wave quantities $\vec{a}_0$, $\vec{b}_0$, $\vec{a}_3$, and $\vec{b}_3$ denote the waves travelling in and out of the respective device port and represent what the device actually measures. The behaviour of the test object $\mathbf{T}_x$ is the wanted information and defined by the wave quantities $\vec{a}_1$, $\vec{b}_1$, $\vec{a}_2$, and $\vec{b}_2$. The relationships between measured and actual T-matrices ($\mathbf{T}_m$ and $\mathbf{T}_x$), measured and actual S-matrices ($\mathbf{S}_m$ and $\mathbf{S}_x$), the two error network parts $\mathbf{T}_A$ and $\mathbf{T}_B$, and the wave quantities is given by equations 5.8 through 5.13. The notation of the equations and figure 5.5 is similar to [84]. An advantage of using T-parameters is the easy way of expressing chains as, e.g., in equation 5.12. Please note, that the number of unknown error coefficients in equation 5.12 is only seven. One of the eight terms in $\mathbf{T}_A$ and $\mathbf{T}_B$ is used for normalisation. This can be either $\underline{t}_{A,22}$ or $\underline{t}_{B,22}$, since only their product finally appears in the calculation.

$$\begin{pmatrix} \vec{b}_0 \\ \vec{a}_0 \end{pmatrix} = \mathbf{T}_m \begin{pmatrix} \vec{b}_3 \\ \vec{a}_3 \end{pmatrix} = \begin{pmatrix} \underline{t}_{m,11} & \underline{t}_{m,12} \\ \underline{t}_{m,21} & \underline{t}_{m,22} \end{pmatrix} \begin{pmatrix} \vec{b}_3 \\ \vec{a}_3 \end{pmatrix}$$
$$= \frac{1}{\underline{s}_{m,21}} \begin{pmatrix} -\det \mathbf{S}_m & \underline{s}_{m,11} \\ -\underline{s}_{m,22} & 1 \end{pmatrix} \begin{pmatrix} \vec{b}_3 \\ \vec{a}_3 \end{pmatrix} \tag{5.8}$$

$$\begin{pmatrix} \vec{b}_1 \\ \vec{a}_1 \end{pmatrix} = \mathbf{T}_x \begin{pmatrix} \vec{b}_2 \\ \vec{a}_2 \end{pmatrix} = \begin{pmatrix} \underline{t}_{x,11} & \underline{t}_{x,12} \\ \underline{t}_{x,21} & \underline{t}_{x,22} \end{pmatrix} \begin{pmatrix} \vec{b}_2 \\ \vec{a}_2 \end{pmatrix}$$
$$= \frac{1}{\underline{s}_{x,21}} \begin{pmatrix} -\det \mathbf{S}_x & \underline{s}_{x,11} \\ -\underline{s}_{x,22} & 1 \end{pmatrix} \begin{pmatrix} \vec{b}_2 \\ \vec{a}_2 \end{pmatrix} \tag{5.9}$$

$$\begin{pmatrix} \vec{b}_0 \\ \vec{a}_0 \end{pmatrix} = \mathbf{T}_A \begin{pmatrix} \vec{b}_1 \\ \vec{a}_1 \end{pmatrix} = \begin{pmatrix} \underline{t}_{A,11} & \underline{t}_{A,12} \\ \underline{t}_{A,21} & \underline{t}_{A,22} \end{pmatrix} \begin{pmatrix} \vec{b}_1 \\ \vec{a}_1 \end{pmatrix}$$
$$= \frac{1}{\underline{e}_{10}} \begin{pmatrix} -\det \mathbf{E}_A & \underline{e}_{00} \\ -\underline{e}_{11} & 1 \end{pmatrix} \begin{pmatrix} \vec{b}_1 \\ \vec{a}_1 \end{pmatrix} \tag{5.10}$$

$$\begin{pmatrix} \vec{b}_2 \\ \vec{a}_2 \end{pmatrix} = \mathbf{T}_B \begin{pmatrix} \vec{b}_3 \\ \vec{a}_3 \end{pmatrix} = \begin{pmatrix} \underline{t}_{B,11} & \underline{t}_{B,12} \\ \underline{t}_{B,21} & \underline{t}_{B,22} \end{pmatrix} \begin{pmatrix} \vec{b}_3 \\ \vec{a}_3 \end{pmatrix}$$
$$= \frac{1}{\underline{e}_{32}} \begin{pmatrix} -\det \mathbf{E}_B & \underline{e}_{22} \\ -\underline{e}_{33} & 1 \end{pmatrix} \begin{pmatrix} \vec{b}_3 \\ \vec{a}_3 \end{pmatrix} \tag{5.11}$$

$$\mathbf{T}_m = \mathbf{T}_A \mathbf{T}_x \mathbf{T}_B = \frac{1}{\underline{e}_{10}\underline{e}_{32}} \begin{pmatrix} -\det \mathbf{E}_A & \underline{e}_{00} \\ -\underline{e}_{11} & 1 \end{pmatrix} \mathbf{T}_x \begin{pmatrix} -\det \mathbf{E}_B & \underline{e}_{22} \\ -\underline{e}_{33} & 1 \end{pmatrix}$$
$$= \frac{1}{\underline{e}_{10}\underline{e}_{32}} \qquad\qquad \mathbf{A}\mathbf{T}_x \qquad\qquad\qquad \mathbf{B} \tag{5.12}$$

$$\mathbf{T}_x = \mathbf{T}_A^{-1} \mathbf{T}_m \mathbf{T}_B^{-1} \tag{5.13}$$

The error terms in $\mathbf{T}_A$ and $\mathbf{T}_B$ need to be determined during calibration. A closer look at equation 5.12 shows the already mentioned separation. The terms $-\det \mathbf{E}_A$, $\underline{e}_{00}$, and $-\underline{e}_{11}$ of $\mathbf{A}$ form a 3-term correction for measurement port one (compare section 5.1.1). A similar group can be found in $\mathbf{B}$ for a second 3-term correction of port two. The last error coefficient $\underline{e}_{10}\underline{e}_{32}$ relates to transmission tracking between ports. It does not depend on the other six coefficients.

This promotes a separate determination in three steps:

1. Do a 3-term correction on port one to determine $\mathbf{A}$

2. Do a 3-term correction on port two to determine $\mathbf{B}$

3. Use the calculated coefficients, measurement data of the line standard $\mathbf{T}_{m,line}$, and equation 5.12 to solve for the tracking coefficient $(\underline{e}_{10}\underline{e}_{32})$

The first two steps are done with reflective standards at the respective ports, i.e. OSL standards. The last step deserves a little more explanation. It uses the measured data $\mathbf{T}_{m,line}$ of the line standard, i.e. a standard with finite transmission. Since the algorithm does not utilise any S-parameter (or T-parameter for that matter) of the line, equation 5.12 cannot be applied directly. But since the line standard is known to be reciprocal, the determinant of its real T-matrix $\det \mathbf{T}_{x,line}$ must be one. This leads to the following equation 5.14 which is quadratic in the wanted error term. Magnitude is easily calculated, but a sign decision has to be made.

$$\det\left[(\underline{e}_{10}\underline{e}_{32})\mathbf{T}_{m,line}\right] = (\underline{e}_{10}\underline{e}_{32})^2 \det \mathbf{T}_{m,line}$$
$$= \det \mathbf{A} \det \mathbf{T}_{x,line} \det \mathbf{B} = \det \mathbf{A} \det \mathbf{B} \tag{5.14}$$

At this point approximate knowledge about the delay or phase shift for the current frequency caused by the line standard comes in handy. Both root solutions can be put into equation 5.13 to get candidate values for $\mathbf{T}_{x,line}$. The T-parameters are then changed into their S-parameter equivalent (see equation 5.15) and the resulting phase of $\underline{s}_{21,line}$ is finally compared to the known approximation of the real phase shift. This enables the choice of the correct root solution. In-lab measurement of the frequency dependent phase shift for the line can be done, e.g. by a calibrated VNA. Even though the environmental conditions in a mine can be very different from the lab, the line should have approximately the same behaviour and the previously acquired phase shift will be valid to within a few degrees — fair enough for a sign decision. Other approaches exist without the need for any characterisation of the transmission standard, but the described solution is rather easy and has proven to be practical. At the end of the whole process, all error coefficients are known and equation 5.13 can be used to correct any further measurement data $\mathbf{S}_m$.

Post processing and correction of further data   Before correction of further measurement data can take place, the measured S-matrix $\mathbf{S}_m$ needs to be transformed into its T-parameter representation $\mathbf{T}_m$. Correction then takes place by direct application of equation 5.13. The result are calibrated T-parameters in $\mathbf{T}_x$, which are transformed back into corrected S-parameters $\mathbf{S}_x$ as shown by equation 5.15.

$$\left(\begin{array}{c} \vec{a}_1 \\ \vec{a}_2 \end{array} \right) = \mathbf{S}_x \left(\begin{array}{c} \vec{b}_1 \\ \vec{b}_2 \end{array} \right) = \frac{1}{\underline{t}_{x,21}} \left(\begin{array}{cc} -\det \mathbf{T}_x & \underline{t}_{x,11} \\ -\underline{t}_{x,22} & 1 \end{array} \right) \left(\begin{array}{c} \vec{b}_1 \\ \vec{b}_2 \end{array} \right) \qquad (5.15)$$

Even though device clutter removal is entirely done in frequency domain, the radar application in salt mines usually requires the equivalent time domain impulse responses of S-parameters. That is why, the spectra are transformed back into time domain using the inverse discrete Fourier transform (IDFT). This step has some implications which need to be discussed. Unlike network analysers, the stimulus of the new M-Sequence sensor does not uniformly occupy the received frequency band from DC up to 18 GHz (according to the equivalent sampling rate of 36 GHz). Especially below 1 GHz and above 13 GHz there is only few — if any — power transmitted by the device. Consequently the S-parameters in $\mathbf{S}_m$ are dominated by noise in these bands. This is true for the measurements of calibration standards and also for any other test object. It basically leads to an ill-conditioned calibration problem and the error terms in $\mathbf{T}_A$ and $\mathbf{T}_B$ cannot be obtained with high confidence or are completely random. The problem is demonstrated in figure 5.6. The graph shows the power spectrum of the reflection from an open port at the calibration plane after correction. Ideally, magnitude of $\underline{s}_{11}$ would be close to 0 dB over the whole frequency range. Distortions in the lower and upper spectral parts are evident from the picture. If such data was fed into IDFT without caring for these noisy frequencies, unusable time domain vectors would result.
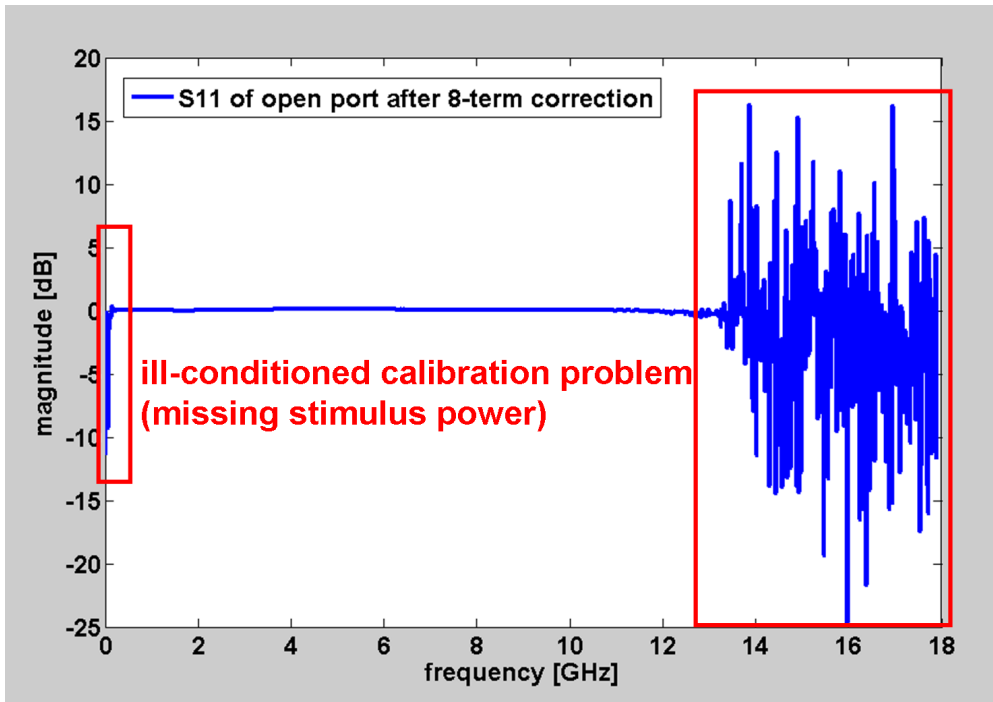
Fig. 5.6.: Power spectrum of a calibrated open port

The usual solution to this issue is the application of frequency domain filters or window functions to attenuate frequencies with low SNR before doing the IDFT. In this case, the IRF of the filter or frequency domain window influences the shape of the resulting time domain data [81]. This topic has already been mentioned and discussed in section 2.4. The tradeoff between sharpness of time domain impulses and the decay of the unavoidable side lobes must be decided. As pointed out in [124, 125], choosing the window function is a degree of freedom as long as the ill-conditioned frequency ranges are sufficiently removed. Using a very smooth window function could result in loss of reflections from disaggregation because it would also limit the effective measurement bandwidth. In section 2.4 it was shown, that this lowers the response amplitudes from very small or thin scatterers. On the other hand using a simple rectangular window would lead to strong side lobes occupying the whole period duration of the IRFs. For the following sections of this chapter and also for the final data processing of measurements from salt mines, the window function plotted in figure 5.7 has been used. The upper part of the figure shows the window in frequency domain. Smooth transitions between passband (where $W(f) \equiv 1.0$) and stopbands ($W(f) \equiv 0.0$) happen between 1 GHz and 3 GHz for the lower frequencies and between 11 GHz and 13 GHz for the upper limit.

Even though the bandwidth covered by the sensor is almost completely retained, side lobe decay is feasible as can be seen in the lower part of figure 5.7. It shows the time domain impulse response of the window in a logarithmic scale. Occupation duration is indicated for different decay levels — 40 dB, 60 dB, and 80 dB. It is clear that despite the very short FWHD of the window (approximately 40 ps), weak responses could be masked out several ns near a strong scatterer like the salt rock surface. This makes the immediate identification of disaggregation responses right behind this boundary very difficult. As will be shown later in chapter 6, this issue will be resolved by using a surface suppression algorithm inspired by super-resolution techniques.

However, for the analysis of calibration accuracy in section 5.3 below the chosen window function was deemed sufficient. Please also note that by using a simple frequency domain window rather than a real filter, acausal IRFs will result. This is also evident from figure 5.7, since side lobes appear before the actual event. However, for the intended application this window property does not cause any problems and is therefore acceptable.

5.2.3. Performance figures of 8-term correction

Main application environment of the new M-Sequence sensor is not the laboratory. It was purposely developed for use in harsh and changing environments. It is therefore a good idea to provide an easy way of on-site checking, if calibration could be applied successfully. An often employed technique is to measure extra standards and compare
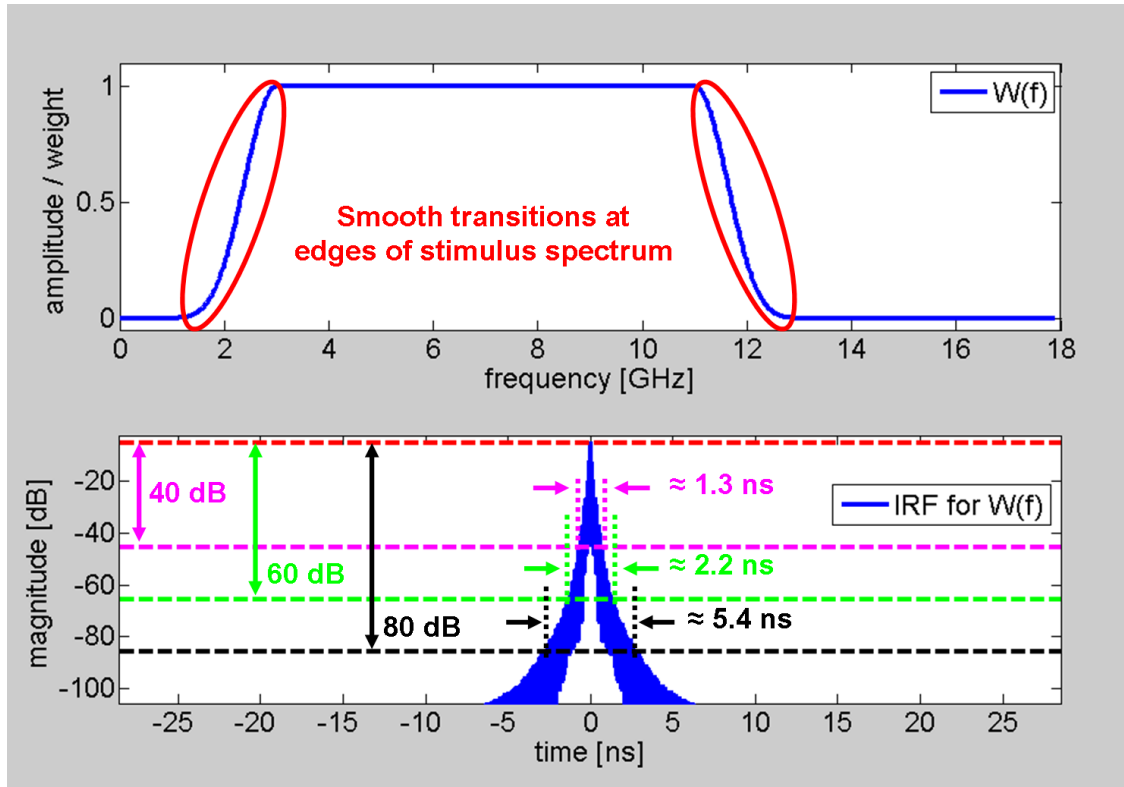
Fig. 5.7.: Frequency domain window function used to suppress ill-conditioned frequencies

the corrected results to their known behaviour. This obvious performance check is also possible with the implemented automatic calibration unit (see section 3.3.3). It features six possible connections for each measurement port. One connection is the default path to the antennas. Four connections are used during calibration - three for 3-term correction and the fourth one connects to the line standard for transmission calibration. The remaining connection holds separate reflective standards, e.g. a short or an open. On one hand, these extra standards can be used to check at least the quality of reflection measurements at the ports, e.g. to judge calibration of $\underline{s}_{x,11}$ and $\underline{s}_{x,22}$. The downside of this kind of check is that certain device errors might not show up. For example, a common problem in mines could be broken RF connectors or bad RF cables. For microwave frequencies, thin gaps in the conductors usually lead to problems near DC while higher frequencies might still travel through the damaged conductor without much notice. As shown before, the frequencies below 1 GHz are not used after calibration, so basically such a problem might not directly show up in test measurements.

On the other hand, the calibration process itself provides some information about the stability of reflection as well as transmission correction for the whole frequency band. This information is likely to reflect any problem that might occur. There are two kinds of performance figures which come at almost no cost during 8-term correction. Even though

they may not be useful to directly point at the culprit of a problem due to their abstract nature, these values provide another quality measure applicable outside the laboratory.

Assessment of reflection calibration   In order to calculate the error coefficients for 3-term correction, the calibration matrix $\mathbf{C}$ needs to be inverted (see equation 5.5 in section 5.1). When three different standards have been measured, $\mathbf{C}$ is a 3-by-3 matrix and direct inversion is possible. It was already explained that the standards should behave as differently as possible to ensure full rank for inversion. Mathematically, the condition of a square matrix tells about the linear independency of its rows and columns. Since each row of $\mathbf{C}$ corresponds to data from one standard, the matrix condition can be used to judge how well separated the observations have been during the three measurements. In the optimal case, a condition of 1.0 would indicate three linear independent rows and columns (the matrix would represent an orthogonal three-dimensional basis). When the usual OSL standards are employed, the ideal condition is not achieved even when the measurement device would be perfect (i.e. with no device clutter). Theoretically, an open end reflects with $\underline{s}_{o,11} = 1.0$, a short circuit with $\underline{s}_{s,11} = -1.0$, and a perfect load would not reflect anything with $\underline{s}_{m,11} = 0.0$. Under the assumption of an ideal measurement device and ideal standards, measured ($\underline{s}_{m,x}$) and theoretical data ($\underline{s}_x$) would coincide and $\mathbf{C}$ would look like equation 5.16.

$$\mathbf{C}_{OSL} = \begin{pmatrix} \underline{s}_o & 1.0 & -\underline{s}_o \cdot \underline{s}_{m,o} \\ \underline{s}_s & 1.0 & -\underline{s}_s \cdot \underline{s}_{m,s} \\ \underline{s}_l & 1.0 & -\underline{s}_l \cdot \underline{s}_{m,l} \end{pmatrix} = \begin{pmatrix} 1.0 & 1.0 & -1.0 \\ -1.0 & 1.0 & -1.0 \\ 0.0 & 1.0 & 0.0 \end{pmatrix} \tag{5.16}$$

The condition of $\mathbf{C}_{OSL}$ is about 3.21. In a real measurement system, especially for higher frequencies the standards themselves will have lower reflection coefficients, i.e. $\left|\underline{s}_{o/s}\right| < 1.0$. Furthermore, device clutter and measurement noise can increase similarity of the rows thus also increasing the condition. In low SNR cases, condition values will also vary strongly between frequencies. This behaviour can be exploited to supervise the calibration process. Figure 5.8 shows the conditions of calibration matrices over the whole frequency range for the in-lab case. The blue graph belongs to port one, the green curve was derived for port two. In the frequency range from 1 GHz to 13 GHz, which is occupied by the stimulus, conditions are not too far from the theoretical value of 3.21. In the other frequency regions conditions increase steadily (below 1 GHz) or become randomly high (e.g. above 14 GHz). These results can be used as a reference for comparison with the actual conditions calculated on-site. Should the current conditions be much higher than the reference, the operator should check the equipment, repeat calibration of sampling timing (compare chapter 4), or repeat the coaxial calibration process. In one occasion during early salt mine measurement campaigns, the RF switches in the automatic cali-

bration unit did not correctly contact some reflection standards at port 1. Just like in the case of a broken conductor in a cable, especially very low frequencies below 1 GHz were severely influenced and it clearly showed in the condition trace of the particular port that can be seen in figure 5.9. The performance of port 2 can be regarded as normal (though hardware was slightly different compared to the setup used for figure 5.8). Since 3-term corrections are performed for each port independently, deviations in the condition graphs can even give a rough clue on the location of the problem.

To be a useful performance measure, interpretation guidelines for condition graphs should be provided to the sensor operator. This is not an easy task since there are many factors influencing the matrix conditions. As already discussed, under low SNR conditions randomness of the values for neighbouring frequencies increases. For overall low stimulus power, large device clutter errors, or reflective standards with $\left| \underline{s}_{x,11} \right| << 1.0$ the condition itself will increase. For example, if the measured reflections from the open and short standard have very low amplitudes (caused by improper system design), the last column of $\mathbf{C}$ scales to a low norm. This increases the condition about inversely proportional to the reflection's magnitude. The same effect can be observed, when standards of weak reflection are used in the first place. However, even under such undesirable circumstances calibration will still work properly when the SNR is high enough to ensure independent observations.

Device problems can usually be identified if the condition gets too high. Then again, environmental differences between lab and actual site are likely to change device clutter and could increase the condition as well. However, it can be expected that these changes are minor compared to the effects of hardware errors and consequently similar performance figures like in the lab should be seen on-site. Empirical comparisons between 8-term data collected at different measurement sites have shown that deviations of matrix conditions up to about **10%** can occur without impacting quality of calibration. Furthermore, if the conditions would increase by more than **50%** over reference values, the operator should check the device for possible damages. Since the calibration matrices are related to 3-term corrections at the respective port only, they do not directly provide information on the stability of transmission calibration. Even though the correction of transmission parameters also involves using the other error coefficients in $\mathbf{T}_A$ and $\mathbf{T}_B$, it would be nice to have a performance measure directly depending on transmission correction. The 8-term algorithm fortunately also provides a value for that purpose.

Assessment of transmission calibration   Determination of the last error coefficient in the 8-term method involves calculating $\underline{s}_{21}$ of the line standard. As described in subsection 5.2.2 above, the phase of this S-parameter is used to make the root decision for the transmission error term. The phase determined from actual calibration measurements using all other error coefficients and the one derived in the laboratory are compared and
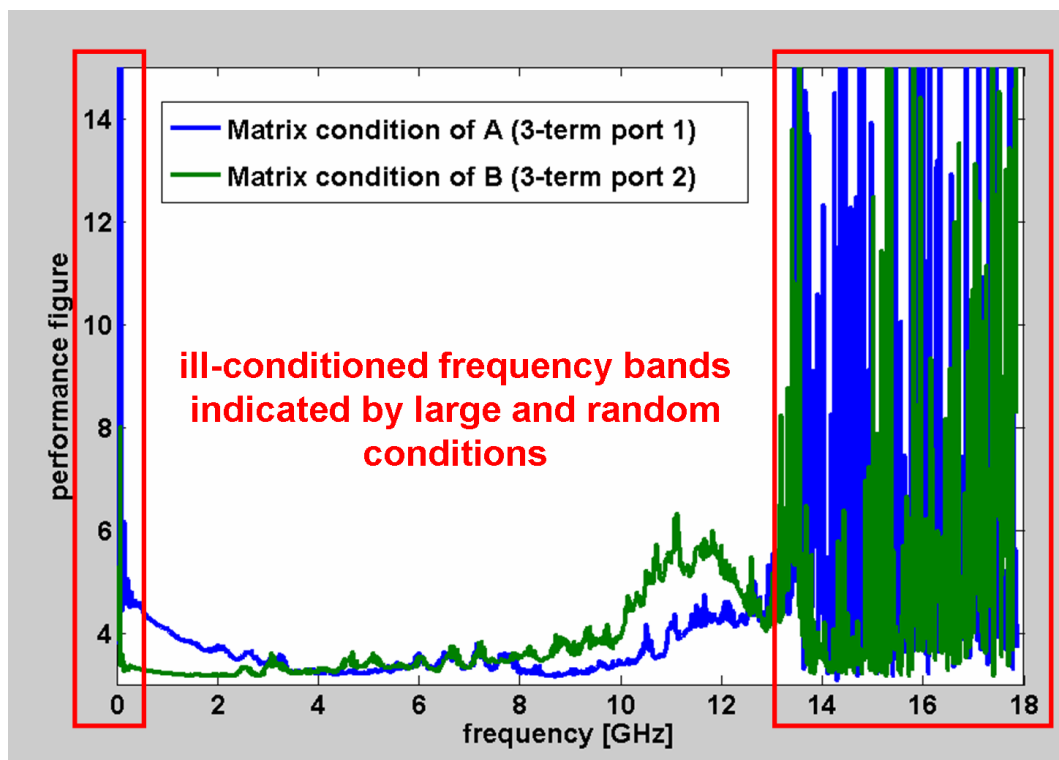
Fig. 5.8.: Calibration matrix condition graphs for the two device ports
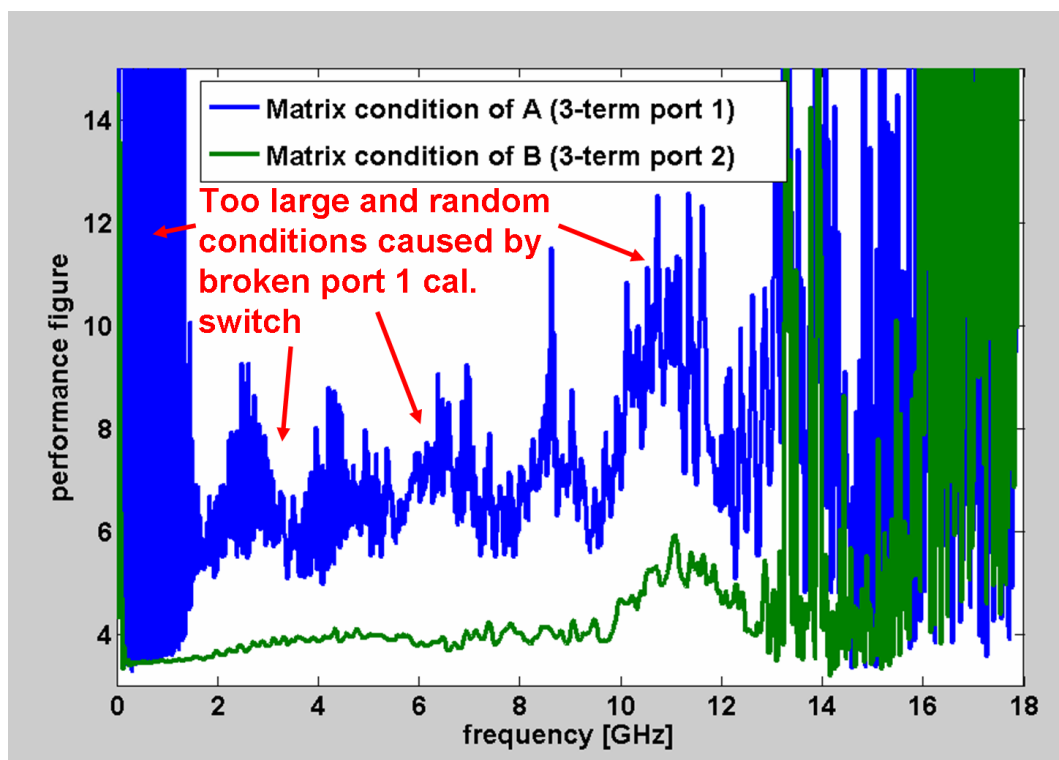
Fig. 5.9.: Calibration matrix condition graphs with a defective RF switch

the closest result is selected to have the correct sign. Under normal circumstances, the phase shift of the line standard does not deviate too much between laboratory and on-site environments. Temperature differences may lead to slight changes in mechanical and electrical length, but the standard is only a few cm long leading to minor changes in the micrometre range at most. Phase shift should be reproducible to within a few degrees throughout the covered frequency range and this expectation has been confirmed in real usage situations of the sensor. Just as in the case of matrix conditions, low SNR conditions lead to increased randomness in phase determination. An example from a calibration done outside the lab is given in figure 5.10. It can be seen that despite the low stimulus power below 1 GHz, phase deviation and randomness do not increase too much until there exists almost no power in the stimulus (below 200 MHz). The reason is simply that for lower frequencies larger absolute errors in terms of length or delay are necessary to produce significant phase differences. High randomness again appears above 13 GHz just like for the 3-term matrix conditions.
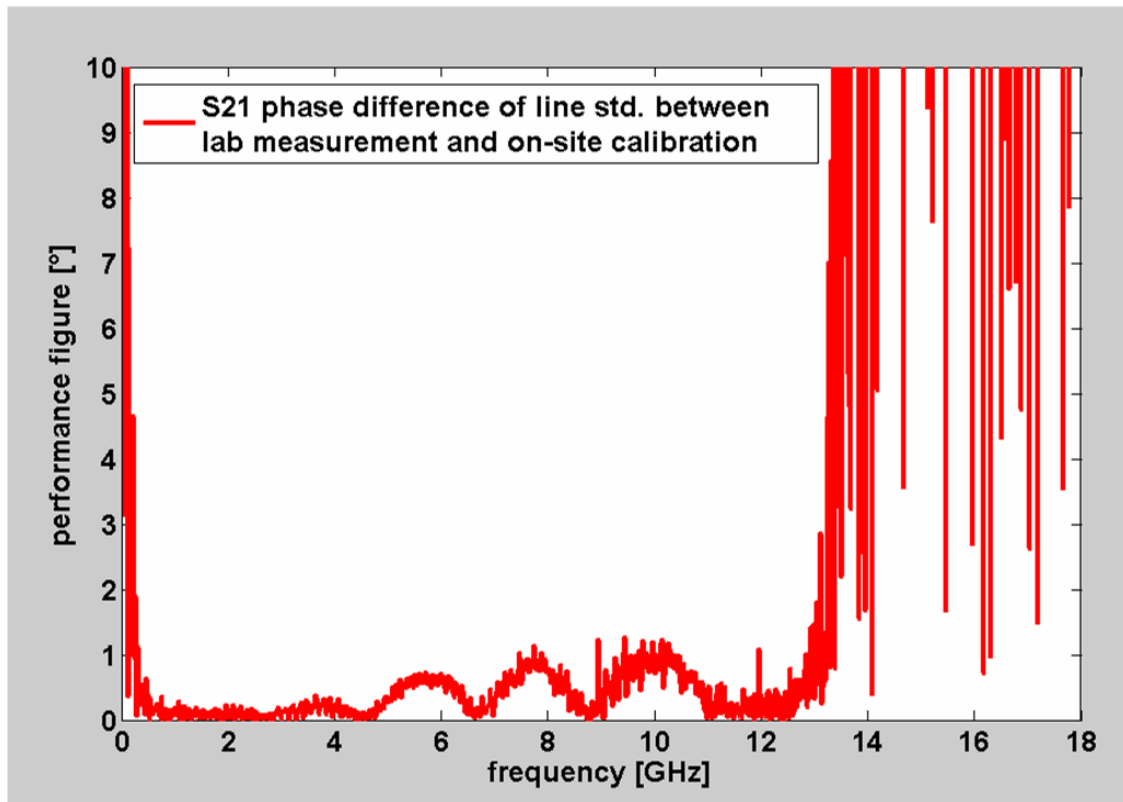
Fig. 5.10.: Phase deviation graphs for the line standard after calibration

Should the device be damaged, e.g. by a broken RF cable or RF switch in the calibration unit, the transmission phase will exhibit stronger differences to the lab measurements. Again, interpretation of this performance figure is not unique and it may not unveil the cause for a possible problem with calibration accuracy. However, should the phase

differences become too high, i.e. larger than 5 degrees in the main frequency band from 1 GHz to 13 GHz, the operator should be alerted to check the setup.

In the overall attempt to provide sensitive performance figures for evaluation of calibration success, the presented approaches are only a beginning. The values have proven to be indicative of device problems during salt mine measurements but a quantitative analysis providing a means for an automatic alert has not been done yet. This is part of future developments regarding coaxial calibration with M-Sequence UWB sensors. In the next section, some thoughts on the best-case performance of the described 8-term process with the new M-Sequence system are presented.

5.3. Accuracy analysis of calibrated MLBS system

Along with the development of calibration methods, some effort was put into a measure on how accurate calibrated measurements can become. In some cases, e.g. in [126], the analysis involves certain types of single physical errors like coupler directivity and how well they will be suppressed after correction. The downside of such approaches is the loss of abstraction and the fact that the presented calculations relate to specific calibration methods and sensor designs only. In [127] another approach is presented, where typical shortcomings of the calibration process (e.g. reconnecting standards) are modelled in a more abstract way and are incorporated as statistical error terms. However, this method requires to measure extra standards which should be avoided in our case.

To assess accuracy after calibration, an empirical approach tailored to the needs of the measurement task in salt mines has been developed. The idea involves measuring other coaxial objects with known behaviour and to judge their time domain impulse responses. These test objects are not used as standards with exactly known S-parameters but rather some simple model of their properties is assumed. This model is then compared to calibration results and a $SFDR_{td}$ for reflection and transmission measurements is derived.There are two general types of inaccuracies which have been investigated — long-term validity of a calibration and residual device clutter.

5.3.1. Calibration repeatability and long-term effects

In most calibration scenarios, important sources for limiting accuracy are drifting of device characteristics over time and reconnection uncertainty of standards during measurements. Drifting can be minimised by proper device design, but even the very stable M-Sequence principle will slightly drift when environmental conditions change. Another often overlooked source for drift effects is an unstable power supply. Especially in salt

mines, power supply has many spurious distortions, but even in a lab the mains quality may vary. That is why the new M-Sequence sensor is usually connected to a high-quality uninterruptible power supply unit. However, it should be investigated how long a calibration stays valid to provide a feasible repetition interval for the sensor operator. The second issue of test object reconnection basically adds uncertainty to the knowledge of their real behaviour $\mathbf{S}_x$. In the new M-Sequence system, the RF switches in the automatic calibration unit have the biggest influence of reconnection repeatability.

Both aspects — drift and switch repeatability — can be analysed in the same simple way. Looking at our main application of salt mine measurements, it is clear that reproducibility of strong reflection events in measured data is very important. More specifically, surface reflection and antenna crosstalk are expected to be dominant signal components. In order to successfully suppress them, their time shape must stay stable when repeatedly measured. It is therefore best to measure a known test object many times over a certain duration and compare the impulse responses.
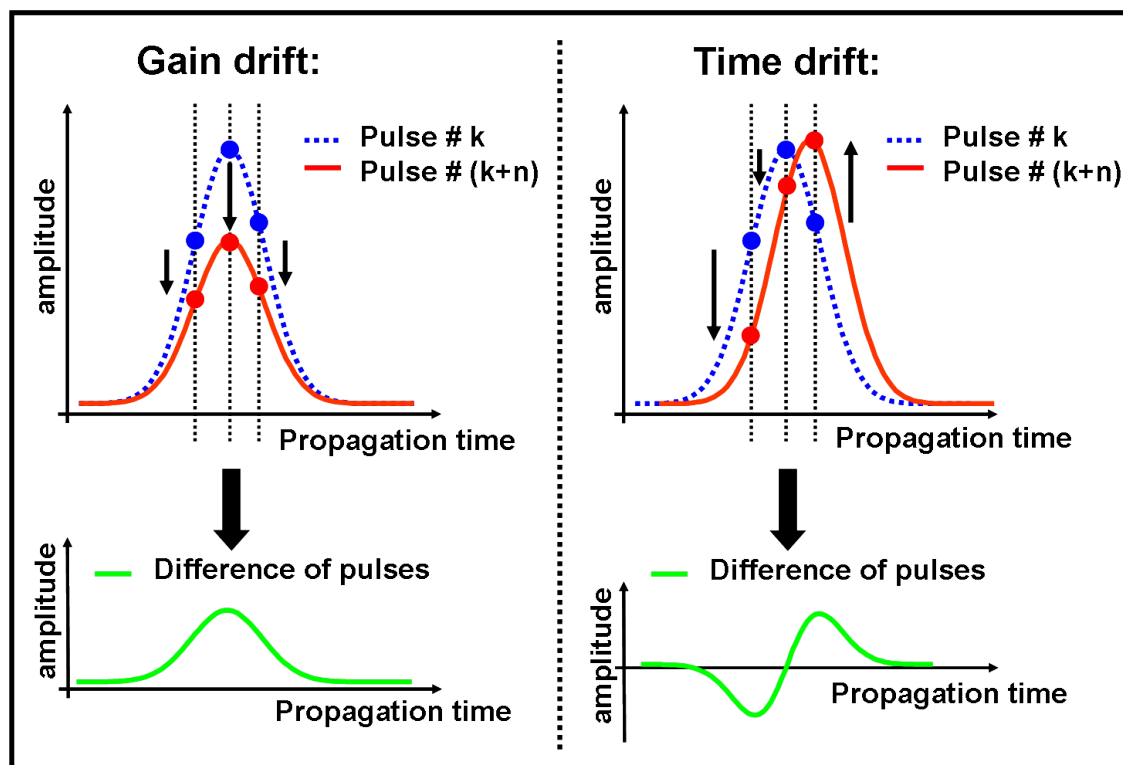
Fig. 5.11.: Illustration of different drift effects on impulse responses

Long-term drift of the new sensor   Slow-time variations of an UWB sensor can have different sources like changes in power supply, ambient temperature, or drifting of the system clock rate. Two main problems often appearing together are gain drift (e.g. changes

in an amplifier) and time drift (e.g. changes in the time base of the system or delay variations due to varying cable lengths, etc.). They are often mitigated by the use of reference channels to acquire the actual transmitted signal. This is also true for the new M-Sequence sensor. However, even with a signal reference, drift effects cannot be suppressed completely.

Figure 5.11 explains, how gain and time drift influence impulse responses acquired at different times k and $k + n$. If drift was negligible, the difference between two measurements of the same test object would only contain noise. When gain drift is present, residual impulses appear in the difference signal. The largest errors arise at the maximum amplitudes of the original pulse. Time drift also leads to deterministic residuals in the difference, but this time maximum error amplitudes are observed at the edges of the pulse. If the amount of time drift is small compared to the duration of the impulse, the residual difference is approximately proportional to the first derivative of the waveform. In conclusion, gain drift is evident around maximum amplitudes and time drift shows up at steep slopes. Investigation of drift can be done with uncorrected measurements, e.g. by comparing the time domain shape of subsequently measured S_m. It is straight forward to define two figures of merit which relate the residual amplitudes in differences to the signal's power. When N impulse responses $x_i(t); i = 1..N$ of the same test object have been acquired, equation 5.17 defines the wanted useful signal $\bar{x}(t)$. Equations 5.18 and 5.19 express an average and maximum residual error along propagation time, respectively. Finally, equations 5.20 and 5.21 define the corresponding quality measures used to judge overall drift. There are different options for calculating the norm. For this investigation, the maximum value has been used, i.e. $p \to \infty$. Please note that the different types of drift do not need to be treated separately here because $\mathrm{SCR_{drift}}$ and $\mathrm{SFDR_{drift}}$ cover all of them in a general manner. Figure 5.12 shows an example dataset obtained for an open standard as test object and illustrates how analysis is done.

$$\bar{x}(t) = \frac{1}{N} \sum_{N}^{i=1} x_i(t) \tag{5.17}$$

$$x_{\mathrm{SCR}}(t) = \sqrt{\frac{1}{N} \sum_{N}^{i=1} (x_i(t) - \bar{x}(t))^2} \tag{5.18}$$

$$x_{\mathrm{SFDR}}(t) = \max_i |x_i(t) - \bar{x}(t)| \; ; i = 1..N \tag{5.19}$$

$$\mathrm{SCR_{drift}} = 20 \lg \left(\frac{|\bar{x}(t)|_p}{|x_{\mathrm{SCR}}(t)|_p} \right) \tag{5.20}$$

$$\mathrm{SFDR_{drift}} = 20 \lg \left(\frac{|\bar{x}(t)|_p}{|x_{\mathrm{SFDR}}(t)|_p} \right) \tag{5.21}$$
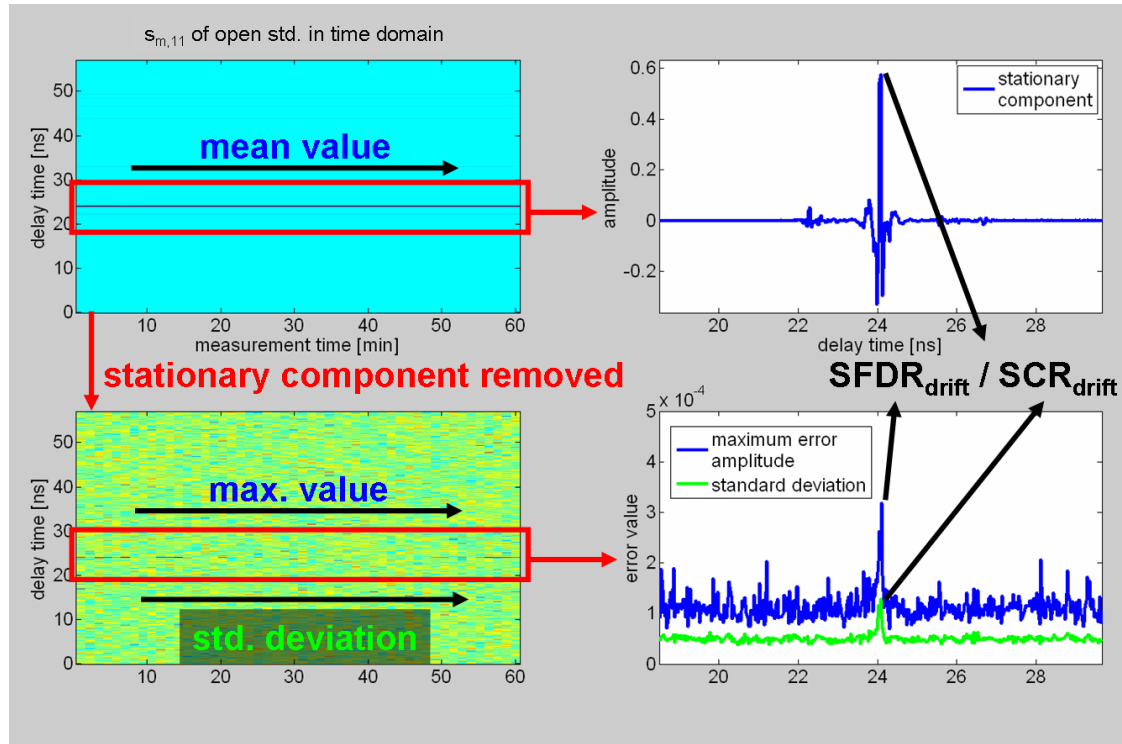
Fig. 5.12.: Acquired data and processing for long-term drift of an open standard in time domain

Assessment of S-parameter drifting was done through repeated acquisition of the same test objects without reconnecting the calibration switches in between. For each of the six possible port connections, 50 realisations have been collected with a high number of averages to assure good overall SNR conditions. Duration was about one hour per test object. In the drifting test, gradual changes rather than random variations are expected in the data. Environmental conditions in the lab can be assumed stable for the duration. After removal of the stationary signal, indeed almost only noise is evident in figure 5.12. However, some drifting still occurred. The $\mathrm{SFDR_{drift}}$ (worst case error) in the example is about 65 dB and the $\mathrm{SCR_{drift}}$ (average amplitude error due to drift) amounts to 73 dB. Results for different test objects are given in table 5.1. Though drift effects certainly do exist, the results are satisfactory. Worst case errors stay below 60 dB and the average error is even below 70 dB for most of the test objects. It is interesting to note that the transmission stability seems a bit worse than reflection stability. A possible explanation could be that the line test object is longer than the very short reflective test objects and consequently more sensitive to temperature changes . However, major temperature changes did not occur during the measurements and the stability differences are not that large to be significant anyway. It can be concluded, that the equipment shows very low drift in a controlled environment. Calibration does not need to be repeated too often, i.e. once per hour (or when environmental conditions have changed significantly) will be sufficient to limit drift errors to more than 60 dB below full scale.

Switch path# (test object)	$\mathrm{SFDR_{drift}}$ [dB]	$\mathrm{SCR_{drift}}$ [dB]
1 (SMA line, $\underline{s}_{m,21}$)	62	71
2 (open, $\underline{s}_{m,11}$)	65	73
3 (short, $\underline{s}_{m,11}$)	65	73
4 (line, $\underline{s}_{m,21}$)	61	68
5 (reflect, $\underline{s}_{m,11}$)	66	74

Tab. 5.1.: Quality values of drift effects for different test objects

Calibration switch repeatability   To asses RF switch influence, a similar approach to drift assessment can be used. This time, repeated measurements of the connected coaxial test objects have been performed with a reconnection of the switch between subsequent realisations. The same switch cycle of six reconnections exactly as it occurs during automatic calibration was repeated 100 times. Data corresponding to the same switch path (and test object) has been analysed according to equations 5.17 through 5.21 and figure 5.12. At first it turned out, that the results indicated rather bad performance. Closer inspection of the dataset showed, that reconnection uncertainties overlapped with drift effects. Since each individual measurement was given time to reach a sufficient SNR, total duration of the experiment was about four hours. Furthermore, ambient temperature changed by about 3 K throughout the measurement. Therefore, the observed drift was in line with expectations.

During normal operation, reconnections necessary for calibration are done within a short time window. That is why drift effects are not expected to have influence. Consequently, they needed to be removed from the dataset in order to get an idea about switch repeatability. It can be expected that gradual changes caused by drift occurred alongside more random variations due to subsequent switch reconnections. To isolate switch influence, the trend in gain and pulse delay variation over measurement time has been removed prior to SCR/SFDR calculation. The gain is judged from the amplitude of the main peak in the time domain representation of the respective S-parameter. Delay is similarly defined as its position within the data vector. Please note that the sampling of the measured data is rather sparse, i.e. the equivalent sampling rate is near the Nyquist sampling rate. In order to get valid gain and delay values, heavy interpolation by Fourier transform method was used. This is a rather simple approach, but it works just like other methods for gain and delay extraction (e.g. using a centre of mass measure, etc.).

Figure 5.13 shows the obtained gain and delay values as blue graphs for data from the open standard. The curves show the expected behaviour. There is a very slow variation which can be accounted to drift effects. It is superimposed by small and more random changes still stronger than noise level. The trend in both gain and delay has been
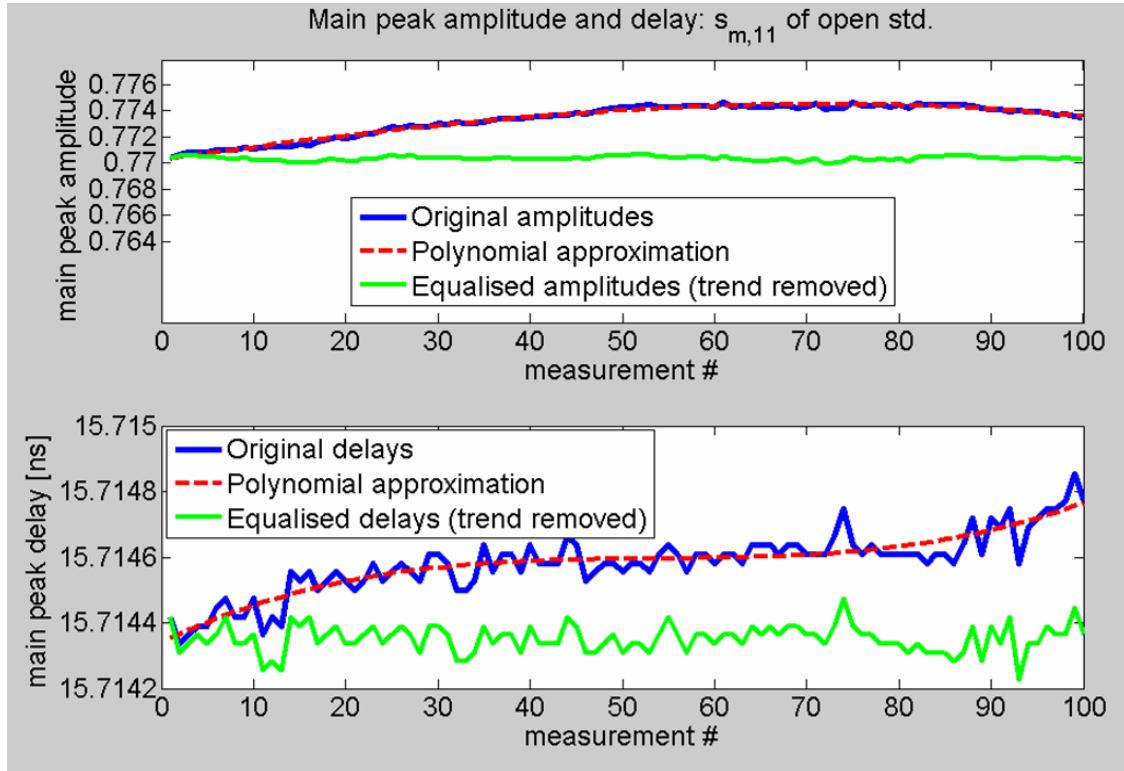
Fig. 5.13.: Gain and delay variation of main peak from open standard

approximated by fitting a third-order polynomial in a least squares' sense. The resulting trend is given as the red traces in figure 5.13. Before calculating the SCR and SFDR values for switch repeatability, the data vectors have been equalised in terms of gain and delay using the trend polynomials. The green curves finally show gain and delay of the main peak after equalisation.

As it turned out, the uncertainty of different switch paths is quite comparable. Table 5.2 lists SCR and SFDR for different paths provided by the RF switches. The values are worse than those obtained for pure drift assessment (compare table 5.1). Another obvious thing is the fact, that SFDR results representing maximum error and SCR results giving average error are very different. This observation deserves some explanation. In figure 5.14, residual amplitudes near the main peak after removal of stationary components are magnified. Looking at the individual deviations as indicated by the colour of corresponding samples, there appear interesting differences throughout the experiment. There were times where data did not change very much from reconnection to reconnection. An example interval is marked with **A** in the figure. On the contrary, spurious large errors can be found for some realisations (an example is marked with **B**). For mechanical RF switches it seems that there exists the possibility of a connection to be less precise than usual while subsequent reconnections show much more repeatable behaviour.
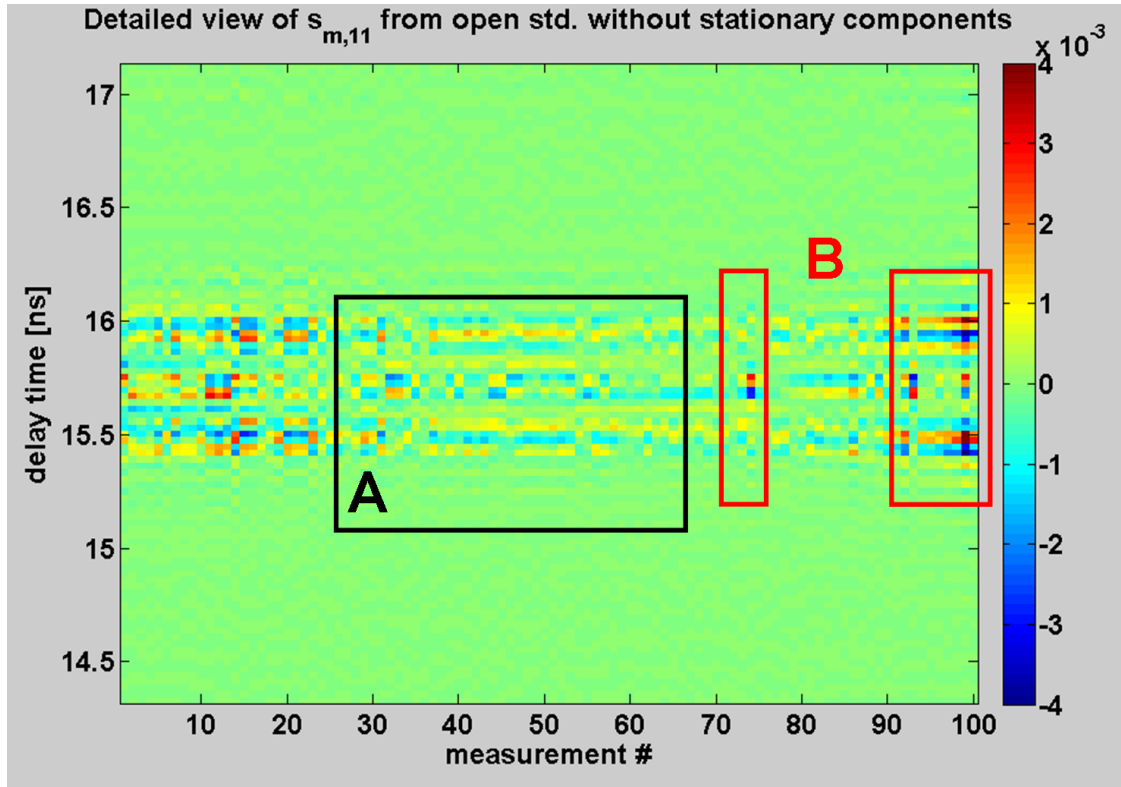
Fig. 5.14.: Residual amplitudes from switch repeatability measurement of open standard

The errors observed here are still rather small in magnitude. The switches have been put under significant stress during the experiment so it can be expected that repeatability indicated by table 5.2 is an upper error bound and that usual errors will be smaller. Furthermore, mechanical switches age with the number of reconnections and may loose some precision over time. Fortunately, calibration does not need to be repeated very often so ageing should not be a serious issue when new switches are employed. An alternative could be solid state switches, which do not age but are usually more temperature dependent than their mechanical counterparts.

All in all, stability of the new system can be regarded as being sufficient enough for longer operation. Switch repeatability errors are in the same order as other possible sources of calibration error (e.g. port crosstalk or residual sampling time errors). If maximum accuracy is needed, the sensor operator should repeat calibration in an hourly schedule or every time environmental conditions change. Practical usability is not limited by such a recommendation because calibration is fully automatic and takes only about two minutes.

The effects described in this subsection can potentially also limit calibration performance of other sensors because they are not a property of the M-Sequence principle. It is therefore interesting to compare calibration results with established laboratory sensors

to see how well the implemented correction works when drift can be neglected. This topic is investigated in the following subsection.

Switch path# (test object)	SFDR_{rep} [dB]	SCR_{rep} [dB]
1 (SMA line, $\underline{s}_{m,21}$)	47	55
2 (open, $\underline{s}_{m,11}$)	43	55
3 (short, $\underline{s}_{m,11}$)	41	51
4 (line, $\underline{s}_{m,21}$)	46	54
5 (reflect, $\underline{s}_{m,11}$)	46	55

Tab. 5.2.: Repeatability performance for different paths of the automatic calibration unit

5.3.2. Comparison of calibration performance

To assess 8-term correction with the new M-Sequence sensor just after the process is finished, it was compared to an established laboratory device — namely a Rohde & Schwarz ZVK network analyser. This VNA is — despite its age — known for precision and can be setup quite flexible. For example, it can be setup to measure any wave quantity ratio to allow different methods for S-parameter calculation. Since both devices allow flexible data acquisition, the simple and generalised way of measuring the S-parameters in $\mathbf{S}_m$ as outlined in appendix B.1 will be compared. All measurements of standards and further test objects have been done within a short time window to avoid drift influence. Besides comparing the two sensor devices themselves, the influence of RF switches in the automatic calibration unit was considered again by using different calibration kits:

- Manual calibration without any switches using a Rohde & Schwarz ZV-Z34 kit which came with the ZVK

- Automatic calibration using the unit of the new M-Sequence sensor (mechanical RF switches)

- Automatic calibration with the commercial kit Rohde & Schwarz ZV-Z59 (solid state RF switches)

Among many possible approaches to judge device accuracy, it seems best to chose an abstract method because regardless of some similarities, the sensors are technically still different. As explained before, the reliable detection of weak scatterers in impulse responses with the presence of strong reflectors is a major concern for the salt mine task. Such weak events could be masked out or obscured by residual device clutter that is not suppressed by calibration. Furthermore, exact reproduction of frequency-dependent reflection coefficients (like it is mandatory for, e.g., impedance spectroscopy) is not very

important here as long as the sensor delivers reproducible responses. The concept of $SFDR_{td}$ which has been introduced before seems therefore a good measure of accuracy and it shall be used for comparing calibration performance. Corrected S-parameters $\mathbf{S}_x$ of simple coaxial test objects producing strong reflections or transmission between the device ports will be used. Their time domain impulse responses are analysed with respect to the strongest residual device clutter events.

To ensure a fair comparison of the technically different hardware, calibration results were produced using the same implementation of the 8-term method from subsection 5.2.2 for all investigated cases, i.e. the sensors were only used to measure raw wave quantities or wave ratios. Of course, the firmware of the ZVK offers a full two-port calibration (e.g. using the ZV-Z34 manual calibration kit), but details about the VNA's internal calibration routines are not exactly known. Furthermore, the ZVK does not natively support the calibration unit of the new sensor. Since time domain impulse responses were needed to obtain an $SFDR_{td}$, the frequency domain window function $W(f)$ shown in figure 5.7 of subsection 5.2.2 has been applied after data correction and prior to inverse Fourier transform despite the fact that the ZVK is able to occupy the whole spectral band up to 18 GHz.

The VNA was setup to measure the same frequencies contained in the M-Sequence data (1022 frequency points from about 17.5 MHz to 18 GHz). Measurement time was chosen to be very high to ensure good SNR. IF bandwidth was set to 300 Hz leading to a (single) sweep time of about **25 s** as recommended by the ZVK. Depending on how S-parameters are calculated, the VNA needed two to four frequency sweeps. The M-Sequence sensor delivers the necessary data for both cases in two subsequent measurement cycles of about **10 s** each. This makes the M-Sequence device over five times faster than the VNA.

Besides the standards needed for 8-term calibration, two kinds of additional simple test objects have been measured. As a reflective object, an open port was used to judge performance of reflection measurements. The expected behaviour was a single strong reflection at the calibration plane. Verification of the reflection performance was done using another strong reflective standard — a short. Results turned out to be comparable to the open port test cases. A 0.5 m long RF cable was used to assess transmission calibration performance. Such a cable should show a single transmitted pulse delayed according to cable length. All results will be plotted in a logarithmic scale to be able to show residual device clutter.

Figure 5.15 shows a reflection dataset of the open port obtained with the new M-Sequence sensor using its automatic calibration unit. The plot contains the uncorrected, raw data $\underline{s}_{m,11}$ as the green curve alongside the calibrated result $\underline{s}_{11}$ in the blue curve. This is to show that calibration really significantly improves measurement accuracy. Raw $SFDR_{td}$

of the sensor is only about 22 dB. Amplitude and delay of the open standard's reflection are not correct and there are multiple unwanted clutter events in the plot. Please note that the main error arises from the limited directivity of the UWB directional couplers which is in the order of 20 dB. The calibrated impulse response on the contrary looks clean and nice as one would expect from the test object. Side lobes of the main reflection make it hard to identify residual errors near the pulse, but after a few ns the IRF decayed by more than 70 dB to a rather steady clutter floor. The terminus noise floor should not be used here as will be explained below. There are still some single pulses standing out from the clutter floor. These residuals finally limit the reachable $SFDR_{td}$ which becomes a bit more than 65 dB in this example.

Now let us do the comparison with the ZVK and among the different versions of S-parameter calculation. Figure 5.16 repeats the calibrated result of the M-Sequence system in the upper part. The blue curve shows the impulse response with simple calculation of S-parameters while the green curve presents the second case using generalised S-parameter calculation. Below, similar results obtained with the ZVK are given. The blue curve used simple ratios for measured S-parameters and the green plot shows generalised S-parameters. There is barely a difference between the two ways $\mathbf{S}_m$ has been derived. This is not very surprising since the dataset contains a reflection at port one only. The reflective test objects did not allow energy to travel between the device ports. Switch error removal by generalised S-parameters mostly effects measurements having some transmission between ports and does not help here. However, the quality of reflection measurements degrades when using simple S-parameters, if the test object allows transmission.

There is another thing to point out in this comparison — it is clear, that the clutter floor of the ZVK is lower than in the M-Sequence sensor data. That means the $SFDR_{td}$ could potentially become better for the VNA. However, looking at the peak residual device clutter, performance is actually similar to the 65 dB reached by our system. Let us move on to an example showing transmission measurements instead of reflections.

A figure for showing raw versus corrected impulse responses of transmission are omitted because the results are similar to figure 5.15. Raw performance of the M-Sequence sensor is again limited by coupler directivity to an $SFDR_{td}$ of about 22 dB. Corrected data is presented in figure 5.17. The M-Sequence results are once more plotted in the upper part, while the results from the VNA are shown below.

This time, significant differences between simple and generalised S-parameter variants are evident. The errors of the respective port switches (leakage and more importantly impedance mismatch) are clearly observed for both devices. The $SFDR_{td}$ for the simple calculation is only 51 dB for the new M-Sequence sensor and an even worse 44 dB for the ZVK. Using generalised S-parameters really improved the results a lot and is there-
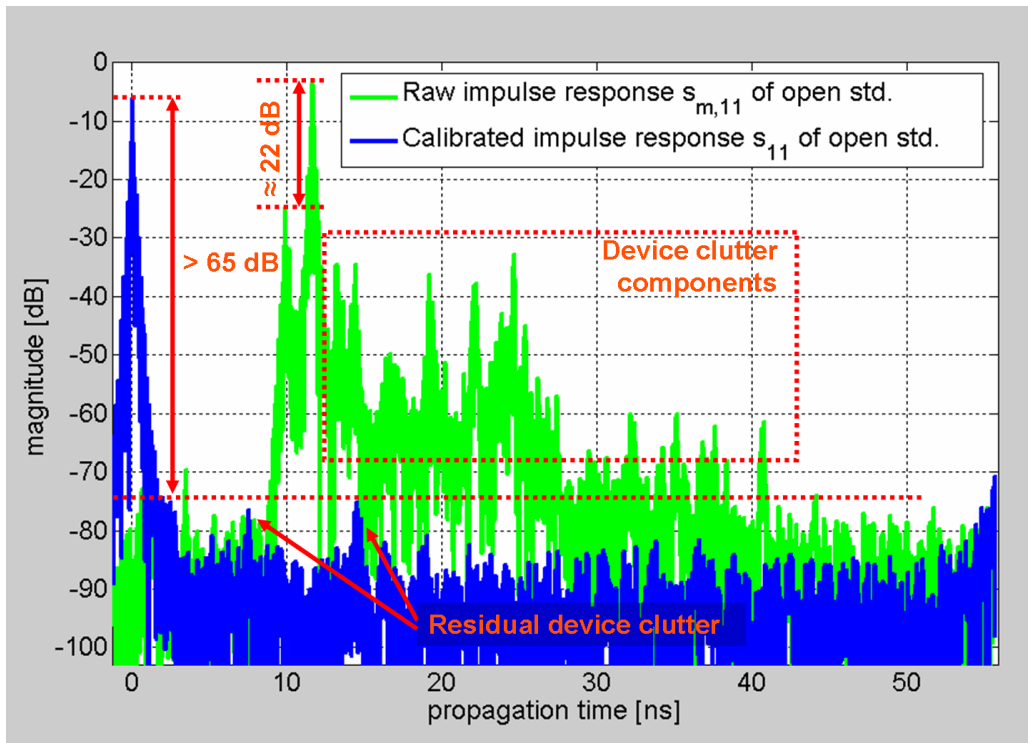
Fig. 5.15.: Raw and calibrated reflection measurement of an open by the M-Sequence device
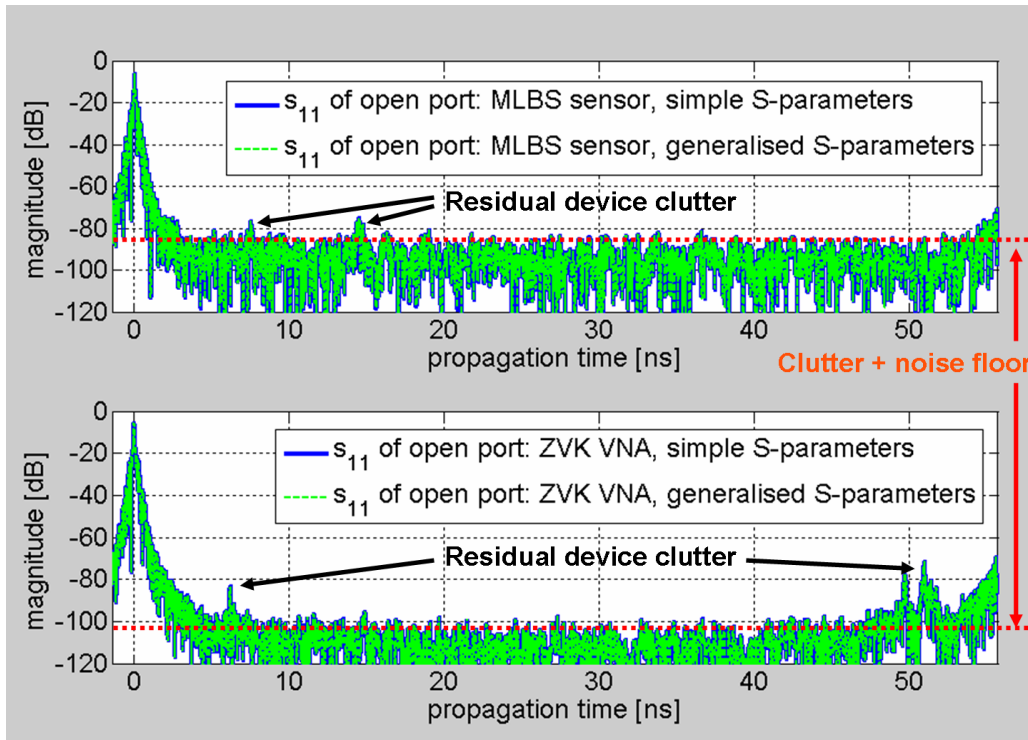
Fig. 5.16.: Comparison of calibrated reflections of an open port between M-Sequence and ZVK sensor

R. Herrmann
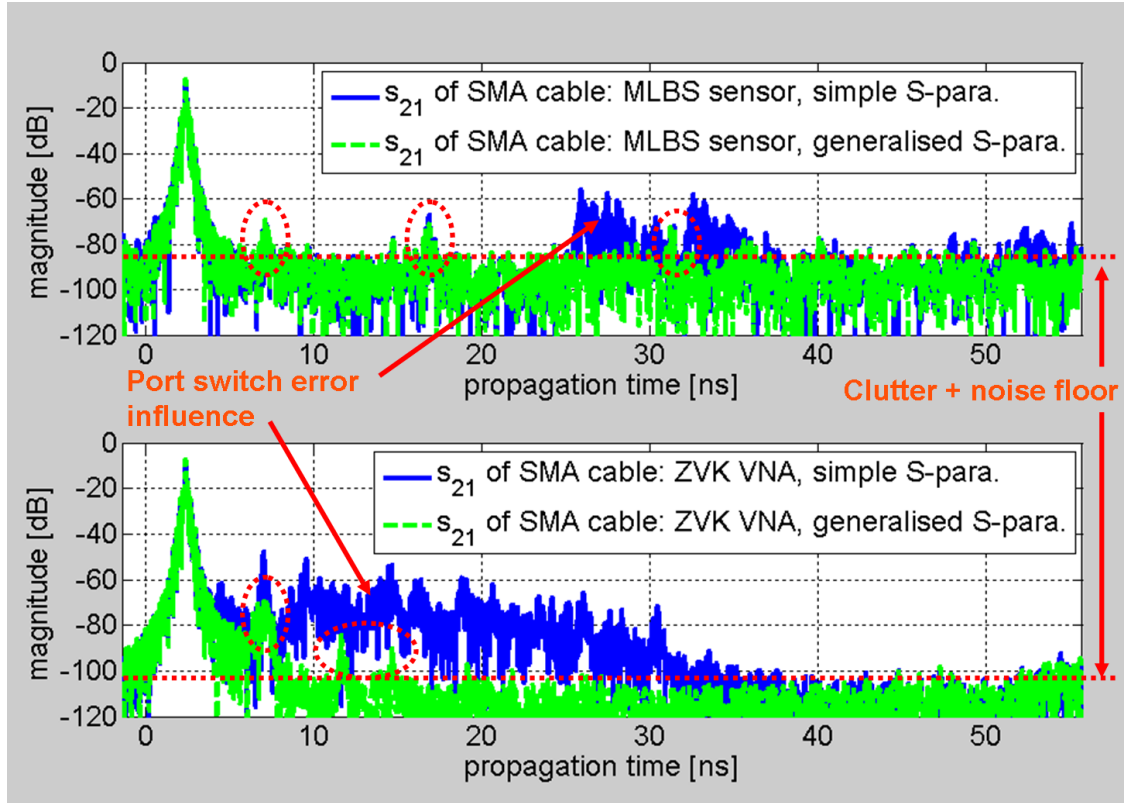
Fig. 5.17.: Comparison of calibrated transmission between M-Sequence and ZVK sensor

fore always recommended when applying 8-term calibration. The final results in the green curves are very similar to reflection measurements. The M-Sequence sensor has a higher clutter floor, but the strongest residual errors (also marked in the figure) are again comparable for both devices and a bit better than 60 dB below the actual main transmitted pulse.

So far, correction performance is similar and both sensors exhibit an excellent $SFDR_{td}$ beyond 60 dB. A complete overview with all values from the different test objects, different calibration kits, and different S-parameter modes are presented in table 5.3. ACU stands for the automatic calibration unit of the M-Sequence device. ZV-Z34 and ZV-Z59 relate to the respective commercial manual and automatic calibration kits.

Even for the high-quality commercial calibration kits and the use of manual calibration, achievable $SFDR_{td}$ does not improve significantly over the values obtained with the implemented automatic calibration unit. This means that remaining uncertainties, e.g. drift, reconnection errors, and inaccuracies in the knowledge of the calibration standards, must be comparable for all tested solutions. It can be assumed that the true S-parameters of commercial kits are more precisely known than the ones of the self-made unit. Drift is influenced by stability of power supply, environment, and the device itself. As discussed before, these parameters are comparable for both sensors and did not cause residual

Device, S-parameter mode	$SFDR_{td}$ [dB] reflection port 1			$SFDR_{td}$ [dB] reflection port 2			$SFDR_{td}$ [dB] transmission		
	ACU	ZV-Z34	ZV-Z59	ACU	ZV-Z34	ZV-Z59	ACU	ZV-Z34	ZV-Z59
M-Sequence sensor simple S-parameters	65.9	67.0	66.2	66.5	65.0	68.0	50.9	52.4	50.0
M-Sequence sensor general. S-parameters	65.9	67.0	66.2	66.5	65.0	68.0	64.8	66.9	68.2
ZVK, simple S-parameters	64.8	68.9	69.1	67.9	67.8	67.2	44.2	56.1	54.2
ZVK, general. S-parameters	64.8	68.9	69.1	67.9	67.8	67.2	60.1	63.2	not measured

Tab. 5.3.: $SFDR_{td}$ after calibration for different test cases

errors as high as in table 5.3. Consequently, the reconnection issue inherent to all tested cases defined the accuracy limits observed. Because of this, the potential of a lower clutter level in the case of the ZVK could not be exploited to achieve much better $SFDR_{td}$ values. However, the overall accuracy level is better than 60 dB, which is a very good result given the complexity of the compared devices and the simplicity of the 8-term method.

For both reflection and transmission measurements the clutter floor is higher for the M-Sequence device which deserves some explanation. The clutter floor is partly influenced by measurement noise. As pointed out before, measurement time was chosen to be sufficiently long to ensure a very high SNR for both systems. Moreover, calibration kits and the mathematical implementation of data correction have been the same and cannot explain the differences. There are two aspects providing some reasoning. First of all, despite the usage of switch error removal by generalised S-parameters, not all leakage paths could be incorporated into calibration for the M-Sequence device (see subsection 5.2.1). Moreover, the ZVK itself exhibited better port matching than the M-Sequence device[2]. The overall raw S-parameter performance of the ZVK is therefore slightly better and its device clutter lower than in the new M-Sequence sensor making calibration easier.

The second conceivable culprit could be the limited accuracy of sampling time calibration as explained in chapter 4. Residual non-uniformity in sampling times will lead to amplitude inaccuracies in all measured wave quantities, which are of non-linear nature. Thus the chosen calibration approach cannot remove these errors and consequently they

---

[2]For example, according to table 5.3, the type of calibration kit influences transmission measurements when simple S-parameters are used. The ZVK performs better than the M-Sequence sensor in this mode when calibrated with the commercial kits but not with the ACU. The errors of cable connections and the RF switches within the ACU are added to the raw ZVK port mismatch explaining the poorer results.

contribute to the increased clutter floor. Please note that a VNA also could suffer from non-uniformity, if its stimulus source does not exactly settle at the intended equidistant frequency steps. However, instantaneous measurement bandwidth of a stepped VNA is zero and out-of-band energy contained in harmonics is effectively filtered out. Moreover, non-uniform sampling would take place in spectrum and not in time domain, i.e. the spectral content to which calibration equations are applied is clean by design. For the considered test objects, there are no steep edges or large variations in their frequency response and thus slightly misplaced frequencies will still give sufficient S-parameter values for correction.

In conclusion, the results are very promising so far and show that the developed UWB sensor is competitive to VNAs at least for the discussed task in salt mines. It should be noted that similar comparisons have also been made with different more recent VNAs from Agilent and the conclusion was always the same. As it turns out, the ZVK even delivered best $SFDR_{td}$ performance for transmission measurements among all tested analysers. The achieved correction accuracy of the new M-Sequence sensor creates high confidence in its applicability for the inspection of the disaggregation zone in salt mines.

5.4. Summary of coaxial calibration for the new M-Sequence system

The ability to correct reproducible device errors (e.g. device clutter) is an important feature usually expanding the field of applications for a sensor. The same is true for the new M-Sequence system and theoretical analysis of the salt mine task has shown that calibration will be mandatory in this case. The M-Sequence principle provides the necessary stability and its system design was tailored to enable full two-port S-parameter measurements. Calibration can be done at different levels, e.g. including or excluding the antennas. As an intermediate step of development, correction at the coaxial level has been implemented. Given the environmental and working conditions in salt mines, an automatic calibration unit was chosen over a manual process.

The vast majority of established coaxial calibration methods are defined in frequency domain and consequently needed to be adopted for the M-Sequence sensor. Furthermore, a quick way of checking calibration success on-site should be provided to the operator in order to detect device damages which can sometimes occur in harsh environments. The basic idea behind the calibration methods is an abstract description of device clutter by decomposition of the real sensor into an ideal one connected to the test objects via a virtual error network. The process of calibration aims at determining the

S- or T-parameters of this error network through measurement of standards with known behaviour. In principle, a two-port sensor will have a four-port error network with at most 15 linearly independent coefficients. In some calibration methods, not all of these terms are obtained and some are assumed to be negligible. Especially when measurement port isolation is very good or crosstalk errors as well as switch mismatch can be removed otherwise, the number of necessary coefficients can be reduced to eight (only seven of which are linearly independent).

Characterisation of the new M-Sequence sensor revealed that port isolation is in the order of 60 dB and that main sources of cross talk are the port switch and the receiver chain. The first problem can be circumvented by calculating the measured S-parameters using a generalised formulation. Receiver leakage can be mitigated by clever assignment of track & hold channels to the directional couplers. In conclusion, calibration using 8-term methods was found feasible for the sensor. Since the M-Sequence device acquires data in time domain, additional steps need to be taken. Measured data must be transformed into frequency domain prior to calibration and after correction the results must be transferred back into time domain. The latter step needs additional care, since the calibration problem is ill-conditioned for frequency regions with low stimulus power. Such areas must be suppressed by some noise shaping filter before the inverse Fourier transform, which can be a simple window function or filter. The impulse response of the window has influence on the time-domain shape of corrected data.

Among the different varieties of 8-term correction, the method using an unknown through or line standard is especially attractive. There are two main reasons for this. First of all, the only real two-port standard needed is a simple coaxial line (RF cable) which only needs to be reciprocal and passive. No other information about the standard is used. The remaining test objects are simple one-port standards such as an open end, a short circuit, or a matched load. The other reason is that this method easily provides performance figures for checking success of calibration at almost no cost. Such an easy way to indicate device damage or other major errors is especially valuable outside the laboratory where other possibilities of checking are infeasible or difficult to apply. The calibration itself is essentially divided into two separate 3-term corrections, each one performed separately for the respective device port. In a final step, the remaining transmission error term is retrieved exploiting the reciprocity requirement of the line standard. During 3-term correction, a calibration matrix is inverted and the condition of this matrix provides a measure of success. Larger deviations of the conditions from a laboratory reference indicate a problem or even damage. Assessment of transmission calibration can be done by comparing the real phase shift of the line standard as measured in the lab to the values obtained during calibration. Should the phase shift differ too much, device and setup should be checked for errors, too.

The whole calibration process has been automated and takes only about two minutes. Drift of the sensor and calibration repeatability were investigated to derive recommendations for a validity interval and basic accuracy limits. Provided a stable environment and power supply, drifting could be observed but was very low. Throughout the runtime of one hour, average amplitude errors due to drifting stayed 70 dB below the maximum reflection or transmission amplitude. The results of reconnection repeatability of the RF switches in the automatic calibration unit turned out to be a bit worse. The average amplitude error throughout 100 reconnections was about 55 dB below the signal amplitude. Analysis of these results showed that the poor performance can be attributed to spurious low-quality reconnections of the used mechanical switches. Usual repeatability is expected to be better. Considering all investigated limitations for calibration accuracy - residual errors of sampling timing, limited port isolation, drifting, and RF switch repeatability — remaining device clutter can be expected to be about 60 dB below full scale.

In a further attempt to assess calibration performance, corrected datasets of simple coaxial test objects, such as an additional open standard or a short RF cable, have been compared between the new M-Sequence sensor and a Rohde & Schwarz ZVK network analyser. Implementation of 8-term correction was the same for both devices and three different calibration kits have been used — manual calibration using the ZV-Z34 kit from Rohde & Schwarz , the automatic calibration unit developed for the M-Sequence sensor, and another commercial automatic calibration unit Rohde & Schwarz ZV-Z59 with solid state switches. Measured S-parameters have been obtained in two different ways. A simple as well as a generalised formulation detailed in appendix B.1 were included in the performance comparison. Accuracy was assessed as an $SFDR_{td}$, relating the peak amplitude of the reflection or transmission to the peak residual device clutter contained in the impulse responses. This measure of dynamic range is an important indicator of performance for the detection of disaggregation because it basically represents the ability to recognise weak scatterers in the presence of a strong scatterer.

Results turned out to be very interesting. While the ZVK seems to have advantages in terms of remaining device clutter floor, maximum residual errors and consequently maximum $SFDR_{td}$ values were not much better than those obtained for the new M-Sequence sensor. Correction of reflection as well as transmission measurements reached a dynamic range in excess of 60 dB regardless of the device or calibration kit used. In some cases, the ZVK wins, in other cases it falls short — but always only by a small margin. The higher clutter floor of the M-Sequence sensor compared to the VNA can be attributed to limited accuracy of sampling timing (see chapter 4) and limited knowledge about the real behaviour of the standards because residual clutter appears to be stable across different calibration kits.

In conclusion, calibration performance of the M-Sequence system is excellent despite some potential for improvement. It is now time to look at some real-world measurements in salt mines to check if the system design translates into useful results for the intended application.

6. Selected salt mine measurement results

Throughout the previous chapters, the design and implementation of a new 12 GHz bandwidth UWB sensor based on the M-Sequence principle have been motivated and described. The following sections present two major on-site measurement results obtained with the sensor. The first example shows an investigation of the disaggregation zone in a very old and inoperative tunnel section representative of many existing transportation facilities in a salt mine. If you recall chapter 1, the motivation for development of the sensor was to assess the disaggregation of near-surface salt rock to find a suitable place for sealing constructions. The second example deals with the opposite situation. We had the opportunity to measure the development of disaggregation in a new tunnel section right after it had been cut. These results were important for verification, that the sensor is actually able to show small defects in salt rock since the real situation in the older tunnels is generally not known in detail (careful excavation of near-surface layers would be a possibility but could not be done during the project).

Before presenting the results in sections 6.3 and 6.4, the measurement setup including antennas and scanner will be introduced in section 6.1. In section 6.2 an overview of additional data processing will be given. Finally, a short comparison with processed data from an ultra-sound sensor is presented in section 6.5.

6.1. Measurement setup in salt mines

Doing measurement campaigns in real salt mines requires to consider a number of issues. The first problem is the selection of suitable test sites. Age and shape of tunnels can be very different and as pointed out before the actual structure of the disaggregation zone is unknown a-priori most of the time. Since the prospected aim of sensor development was to create a tool for fast inspection of extended tunnel sections, also test measurements should contain scans of larger surface areas. In order to keep the effort of scanning limited, investigation was done mostly in old inoperative tunnels with a cylindrical shape. Nominal diameter was 3 m. Such tunnels were traditionally equipped with rails and used

for transportation by mining trains. There were a number of advantages for testing the new M-Sequence sensor. First of all, scanning along the surface could be accomplished by a simple rotational scanner. Movement along the tunnel could be guided by the rails (e.g. using a lorry with motorised movement) or the scanner could be mounted on a trolley for manual movement. Figure 6.1 shows the concept used in this investigation. Another advantage is the fact, that the considered tunnels have been cut in a single run and therefore provide a rather smooth surface. The last point is the usage pattern involving a lot of vibrations induced by the trains running through the tunnels for many years and contributing to the formation of distortions near the surface.
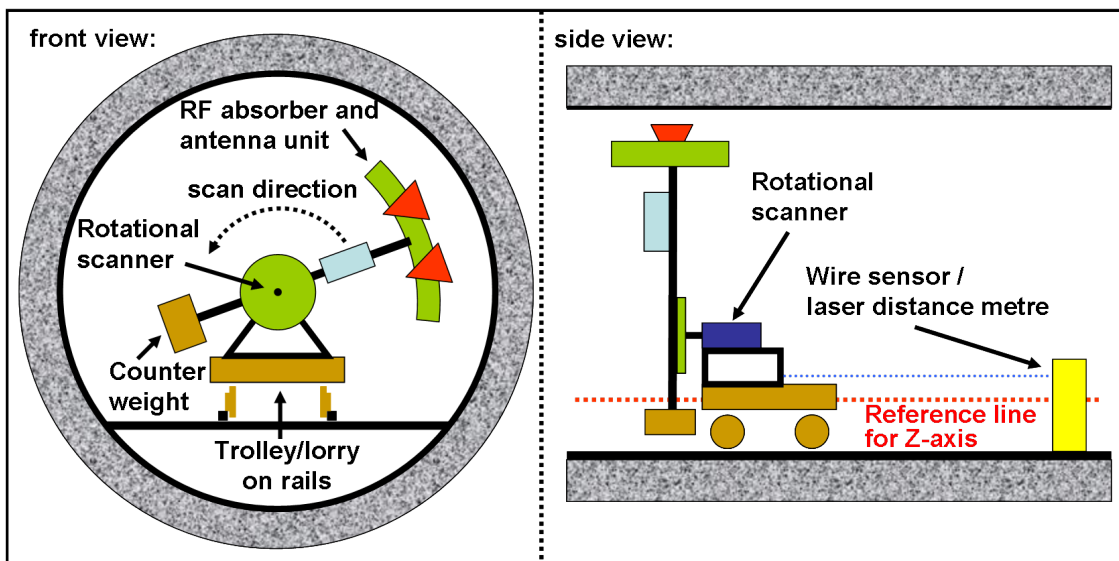
Fig. 6.1.: Scanner concept for salt mine measurements

A circular scanner has been implemented with an adjustable antenna arm and mount points for the antennas and the UWB sensor itself. This scanner was used in different cylindrical tunnels throughout mines in Germany. An additional linear scanner has been build to enable scans along ceiling tracks. The actual setup was realised depending on the conditions in the mines. More detailed information will be presented in the following sections 6.3 and 6.4.

Another aspect in salt mines or underground mines in general is the harsh working environment. While parameters such as temperature or humidity are often very stable and well-controlled, their absolute value can be problematic — especially temperature can be very high depending on the depth of the mine and other factors. Furthermore, the scanner, sensor, and antennas needed to be quite rugged to survive transportation and handling. A special aspect in salt mines is the very fine, ubiquitous salt dust present in the air. It could potentially harm electronic circuits. The new M-Sequence sensor was therefore build into a sealed case just like the scanner controller and the PC used for

data acquisition. Proper air ventilation inside the cases and cooling (for the PC) were the main challenges besides mechanical stability. Power supply in a mine can also be rather unstable and the devices have been protected by an uninterruptible power supply unit. It was working in a permanent battery-based mode providing excellent filtering of supply distortions.

The last part of the measurement setup consists of the actual applicators of the electromagnetic waves — the antennas. Obviously, their properties and how the antennas are placed will have a big influence on the results. Even though a lot of different antenna types are well-known and understood for the narrowband case, a consistent and generalised description of the three-dimensional behaviour for our UWB spectrum cannot be found to date[1]. Choices regarding antennas have therefore been made on an empirical basis.

6.1.1. Antenna type and arrangement

A basic pre-selection of suitable antennas can be made based on simple considerations. First of all, the operational frequency band from 1 GHz to 13 GHz should be covered by the radiators. This requirement already reduces the number of suitable antenna types. Furthermore, the use of directional antennas is preferable for two reasons. Directional antennas concentrate the stimulus power towards the salt rock resulting in a larger fraction of the total transmitted power interacting with the disaggregation zone. Assuming a given amount of transmit power and measurement time, this enables better SNR values — or put in another way: measurement speed can be increased while achieving a feasible SNR through directivity. Another very important advantage is the reduction of clutter reflections from the scanner construction. Antennas — even directional ones — also transmit partly towards the back. Since the scanner and trolley contain many metallic parts, strong responses would result in the same delay range as the disaggregation zone. This effect is also lowered with increased directivity. Additional shielding of the back side by means of RF absorbing material was used to further suppress reflections from the scanner. It should be noted that highly directive UWB antennas are usually three-dimensional structures (as opposed to long or flat antenna types) and that directivity is frequency dependent. This fact causes the time shape of the antenna's impulse response to depend on the direction of free-space waves making it difficult to correct their influence.

Another property to be considered is polarisation. As mentioned in subsection 2.3.3 of chapter 2, the polarimetric scattering behaviour of the disaggregation zone is unknown and hard to predict. Since the new sensor provides two ports, all polarisation combi-

---

[1]For some simple antenna types like dipoles, at least theoretical field simulations (for example using FEM) could be done, but such an approach becomes very difficult for complex antenna types and incorporating the results into data processing deserves dedicated research not in the scope of this thesis.

nations can be measured by using antennas of different polarisation preference and will be represented by their respective S-parameters. For example, linearly polarised antennas can be used in two alignments. Unfortunately, dual-polarised antennas for the selected frequency range with reasonable physical dimensions could not be found and two separate antennas needed to be used instead. The importance of antenna size will be explained shortly.

The final decision was based on numerous test measurements conducted at the beginning of the research project. Different types of UWB antennas — for example horn antennas, Vivaldi antennas, and bow-tie antennas among others — have been compared by measurements of the same track in a salt mine. At this occasion, antenna placement and orientation with respect to the salt rock surface were investigated, too. Derived conclusions will only be summarised here.

A main finding of the measurements was that antennas should be placed as close to the salt rock surface as possible. Otherwise, the received signals from disaggregation or even small discrete cracks became too weak. This is not surprising when recalling the analysis in sections 2.2 and 2.4 and that receive power depends on the distance to the target. Putting the antennas close to the surface also keeps the volume of interaction small as illustrated by figure 6.2. Since distortions in the disaggregation zone might well be distributed randomly in some cases, their responses within the interaction volume will superimpose and could potentially cancel out in the received data. The smaller the interaction volume, the lower the risk of this undesirable situation. A high antenna directivity is also beneficial in this case. The requirement of close proximity is, however, restricting a large antenna directivity. The directivity of a physical antenna is inversely related to its aperture [67, 77] — a highly directing antenna would be unfeasibly large for frequencies in the lower microwave range. The compromise of using physically small antennas and bringing them to within a few cm close to the surface delivered best results.

Such a setup has influence on other aspects as well. First of all, separation of the two antennas should be small, too. For reflection measurements (with the same antenna as transmitter and receiver) close proximity to the surface is not a problem. But transmission measurements between the two ports require that the reflections excited by one antenna must reach the second antenna as directly as possible. A large separation would mean that responses from disaggregation not far behind the salt rock surface would not reach the receiving antenna at all or only in a direction far from its main radiation lobe.

Placing antennas close to the surface and also close to each other has some further consequences. Measurements will be done in the near field of the radiators. Distance variations to a reflector will therefore have significant impact on received amplitudes. Moreover, antenna crosstalk and surface reflection are expected to be very strong components of the received signal which should not saturate the receiver. The main challenge
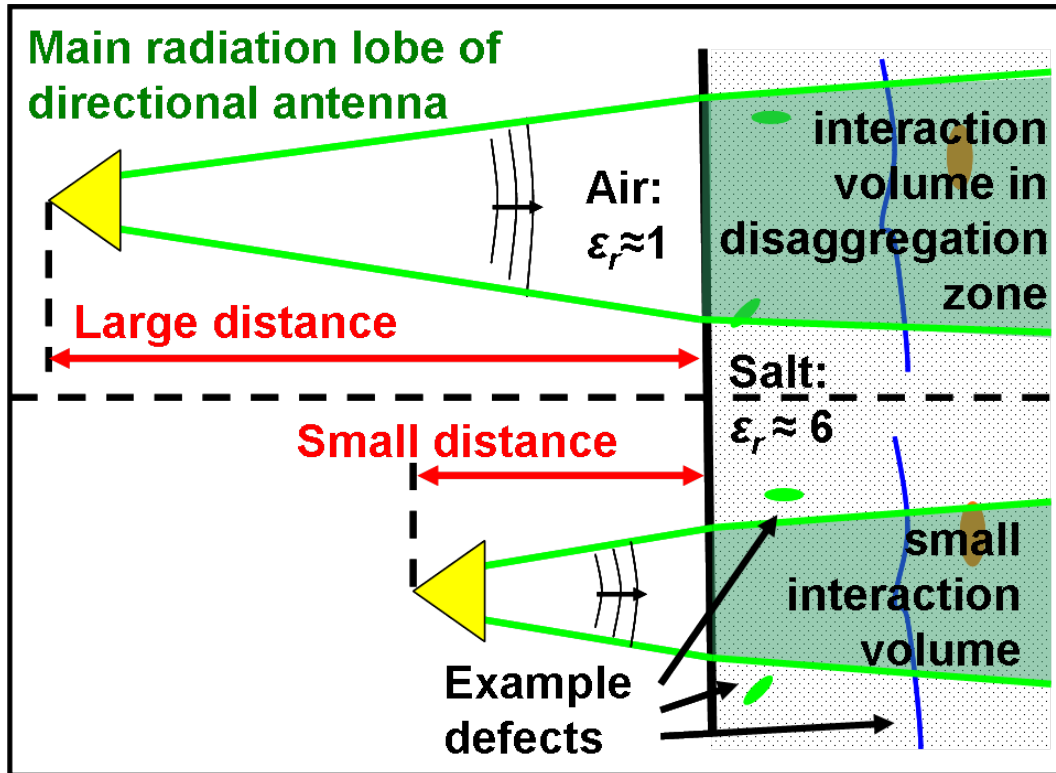
Fig. 6.2.: Illustration of interaction volume and antenna distance

of data processing will be to suppress these unwanted parts sufficiently to unveil the scattering from disaggregation (see also discussion in the next section). Some aid can be achieved by proper design of an antenna unit. Antenna crosstalk is a property of the antennas and how they are placed, but does usually not depend on the measured scenario. Integrating both antennas into an array with fixed separation was the easiest way to ensure reproducible crosstalk and enable its measurement outside the mine in a laboratory. The externally acquired crosstalk could then be used during data processing.

Another major outcome of test measurements was that a slight inclination of the antennas with respect to the surface normal effectively reduced the surface reflection while the responses from edges of small discrete cracks were even enhanced in some cases. The idea behind antenna inclination is shown in figure 6.3. Due to the non-zero size of real antennas, inclination is practically limited when placing them near the surface. Inclinations of $10° \leq \alpha \leq 30°$ out from the surface normal worked well (depending on the specific antenna type). Finally, two double ridged horn antennas of type RF-Spin DRH20 [128] specified in the frequency range from about 1.7 GHz to 20 GHz were selected. These antennas are of small size (104 mm x 122 mm x 78 mm) and have been mounted into a fixed array depicted in the left part of figure 6.4. Separation is 5 mm and the array housing provides additional RF absorber shielding towards the back and the sides.
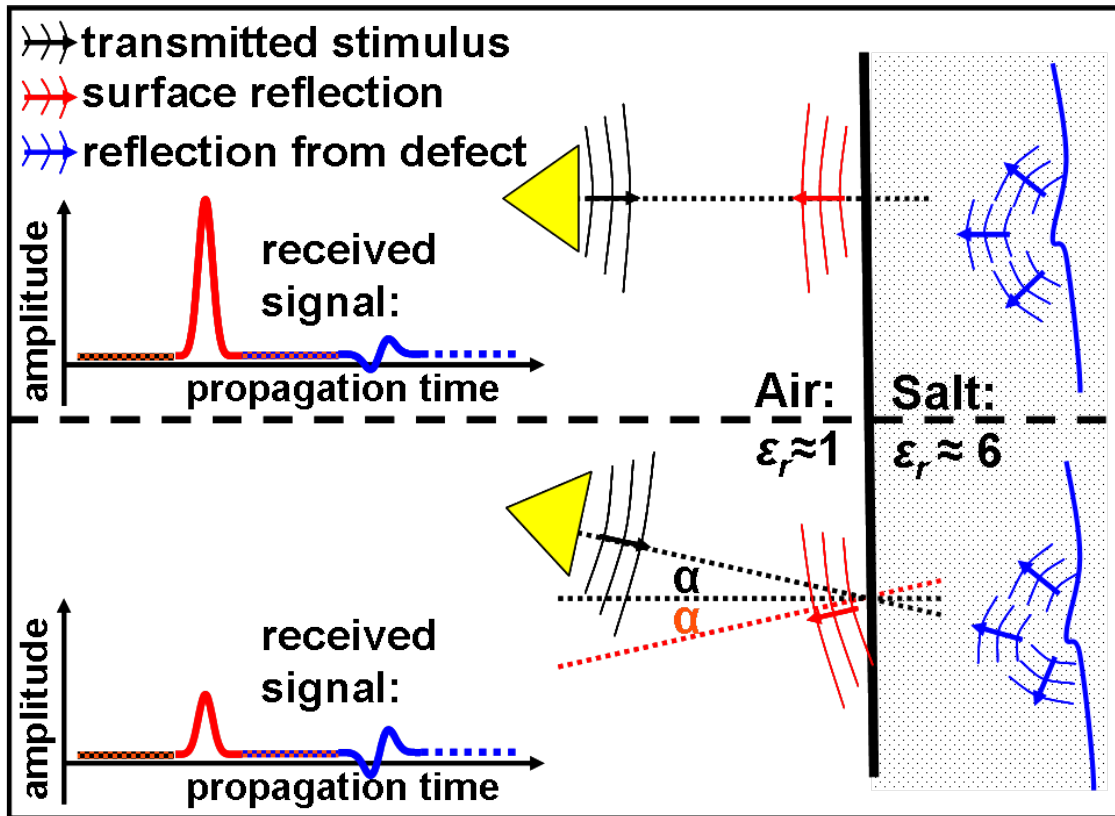
Fig. 6.3.: Influence of antenna inclination on surface reflection
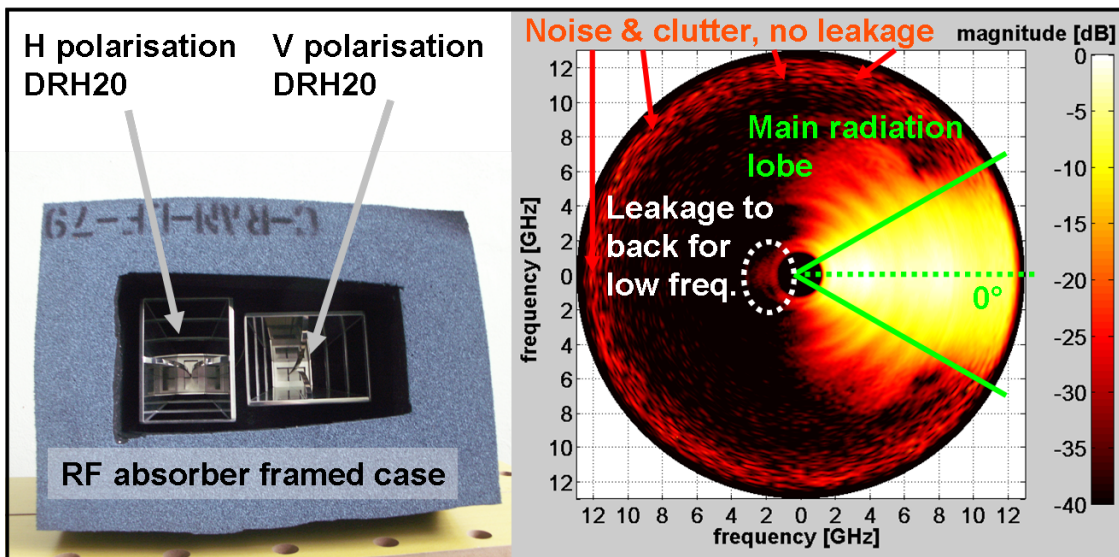
Fig. 6.4.: Implemented antenna array and resulting radiation pattern

All objects placed very close to the antennas influence their radiation pattern. To assess effectiveness and effect of the array case, a simple characterisation measurement was done. The power of the direct wave between an antenna in the array and a reference antenna of same type was acquired for all frequencies of interest. The array was rotated in front of the fixed reference using a turntable scanner. The right side of figure 6.4 shows the result in a circular diagram. The diametre corresponds to frequency with DC in the centre. The angle is given relative to the main radiation lobe of the antennas which is at 0°. The colour of the plot corresponds to relative power level in dB. As can be seen, most of the energy is transmitted and received in a narrow beam between -30° and 30°. Except for the frequencies below 2GHz, suppression of backward transmission and reception is very good. A further reduction of clutter from the scanner construction is possible by a high-pass filter if needed. The data also demonstrates the already mentioned frequency dependence of directivity and angle of propagation — which makes the description of UWB antennas generally very difficult. The introduced antenna unit completes the salt mine measurement setup. The following section discusses data processing for the mine data.

6.2. Data processing for detection of disaggregation zone

The aim of data processing is to remove or suppress all unwanted signal components in such a way, that the weak responses from defects inside the disaggregation zone become visible to the operator. Traditionally, the different steps are divided in a common pre-processing stage, an application-dependent main stage, and a visualisation stage. Pre-processing involves S-parameter calculation and removal of device clutter according to chapter 5. As a result, for each scanner position three time domain impulse responses are obtained, representing the scattering behaviour of the three polarisation combinations VV, HH, and VH. Please note that the antenna behaviour is not compensated unlike in many other radar processing schemes. The main reasons to omit this step are the near field operation (making it difficult to find correct reference functions) and the compact reproduction of impulses by the employed antennas (i.e. they feature a short impulse response).

The processing of the main stage is done in time domain individually for each polarisation combination. Some major issues have already been mentioned in the previous section. For each scanner position, the received signals contain strong clutter components — namely antenna crosstalk and surface reflection — as well as a superposition of the responses from all distortions within the volume of interaction. Since individual targets can be of mm or even sub-mm size, they are much smaller than the antennas needed to radiate and receive the used microwave frequencies and the interaction volume. How-

ever, as long as the responses do not vanish in the noise floor of the sensor, the statistical behaviour of the impulse responses and individual reflections from larger distortions will be different between scanner positions. The clutter components must be suppressed in order to make such signal features visible. Antenna crosstalk and surface reflection are two different matters and need to be treated according to their nature. It is important to understand that suppression of these components must be done as good as possible. Simple background removal techniques such as high-pass filtering along the slow- (i.e. measurement-) time dimension leave undesirable residual clutter strong enough to mask out target responses.

6.2.1. Removal of antenna crosstalk

Antenna crosstalk is the direct wave between transmitting and receiving antenna which does not pass through any part of the actual test object[2]. It therefore only depends on antenna placement relative to each other and objects very close to the antennas influencing their radiation pattern. Due to integration of the two antennas into a fixed array and shielded housing, the crosstalk is reproducible and can be measured in the lab or an anechoic chamber before going to a mine. Additionally, it does not change with scanner position and remains as a stationary component in all measured impulse responses. The easiest way to remove crosstalk is to subtract the measured reference. However, the cables connecting the antennas to the calibrated ports will typically show very small deviations of signal delay caused by cable bending and also temperature differences. To remove crosstalk as good as possible, the reference function $xtalk_{\mathrm{ref}}(t)$ must be shifted appropriately before subtraction. The correct amount of shifting τ is not known but it can be found by means of an optimisation. To do so, a signal to be compared to the crosstalk reference must be calculated. Since the crosstalk does not change with scanner position, the mean of all impulse responses provides a good starting point. If $x_k(t)$ is the impulse response measured at the kth scanner position and N is the total number of positions, the estimate of crosstalk during measurement $xtalk_{\mathrm{meas}}(t)$ can be calculated like in equation 6.1. The cost function $c(\tau)$ to be minimised is then given by equation 6.2.

$$xtalk_{\mathrm{meas}}(t) = \frac{1}{N} \sum_{N}^{k=1} x_k(t) \tag{6.1}$$

$$c(\tau) = |xtalk_{\mathrm{meas}}(t) - xtalk_{\mathrm{ref}}(t - \tau)|_p \tag{6.2}$$

---

[2]In the case of reflection measurements using only one antenna, impedance mismatch causes a part of the wave sent to the antenna to be reflected back directly. It also does not interact with the test object and can therefore be treated as crosstalk, too.

In this case, the 2-norm is used ($p = 2$) to find the best fitting between the two functions in a root-mean-squares' sense. It is not a good idea to incorporate the whole impulse response into $c(\tau)$ since the estimated crosstalk has other significant components such as the mean surface reflection, which depends on the actual test site and can heavily mislead the optimisation search. Instead, the 2-norm should only be calculated for a time interval containing the main energy of antenna crosstalk, i.e. only for $t_{\mathrm{start}} \leq t \leq t_{\mathrm{stop}}$. Due to the UWB nature of the sensor and the unavoidable remaining distance between antennas and the salt rock surface, crosstalk and surface reflection are somewhat separated in propagation time. Figure 6.5 shows an example for both $xtalk_{\mathrm{meas}}(t)$ and $xtalk_{\mathrm{ref}}(t)$ obtained in a real measurement and illustrates a reasonable choice for t_{start} and t_{stop}.
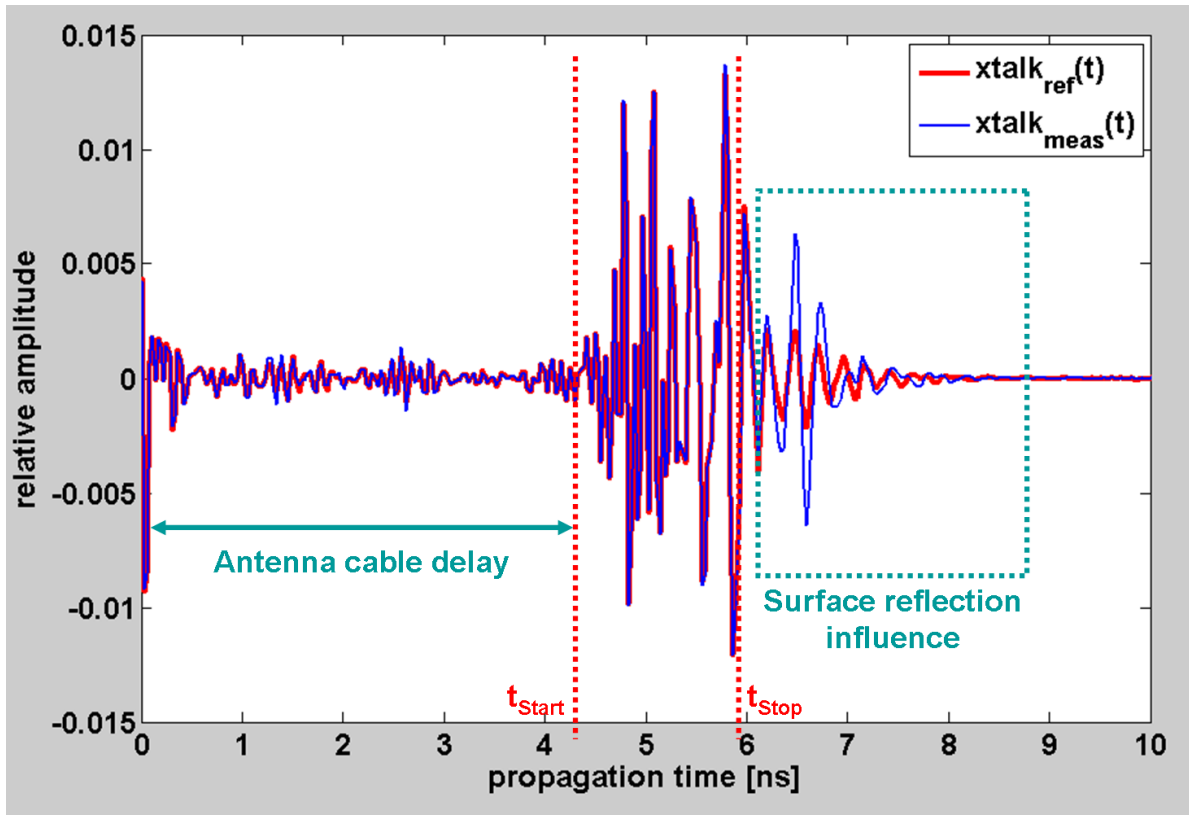
Fig. 6.5.: Comparison of crosstalk reference for HH polarisation and crosstalk estimate from mine data

Under ideal circumstances, τ_{opt} would be zero but during measurement campaigns, delay differences in the order of a few ps have occurred compared to data from the lab. It therefore makes sense to restrict optimisation for τ to be close to zero. The actual search was implemented using the MatLab function `fminsearch(...)`. It is based on the Nelder-Mead simplex search described in [117] and does not require an explicit formulation of the cost function. Once the optimal shift τ_{opt} is found, removal of antenna crosstalk is done for all N impulse responses according to equation 6.3. Figure 6.6 shows an example dataset from a one-dimensional scan along half the circumference of a tunnel with and without

antenna crosstalk. It is evident that crosstalk removal was efficient and the remaining data is now dominated by the second major clutter component — the surface reflection.

$$y_k(t) = x_k(t) - xtalk_{\mathrm{ref}}(t - \tau_{\mathrm{opt}}) \forall k \tag{6.3}$$
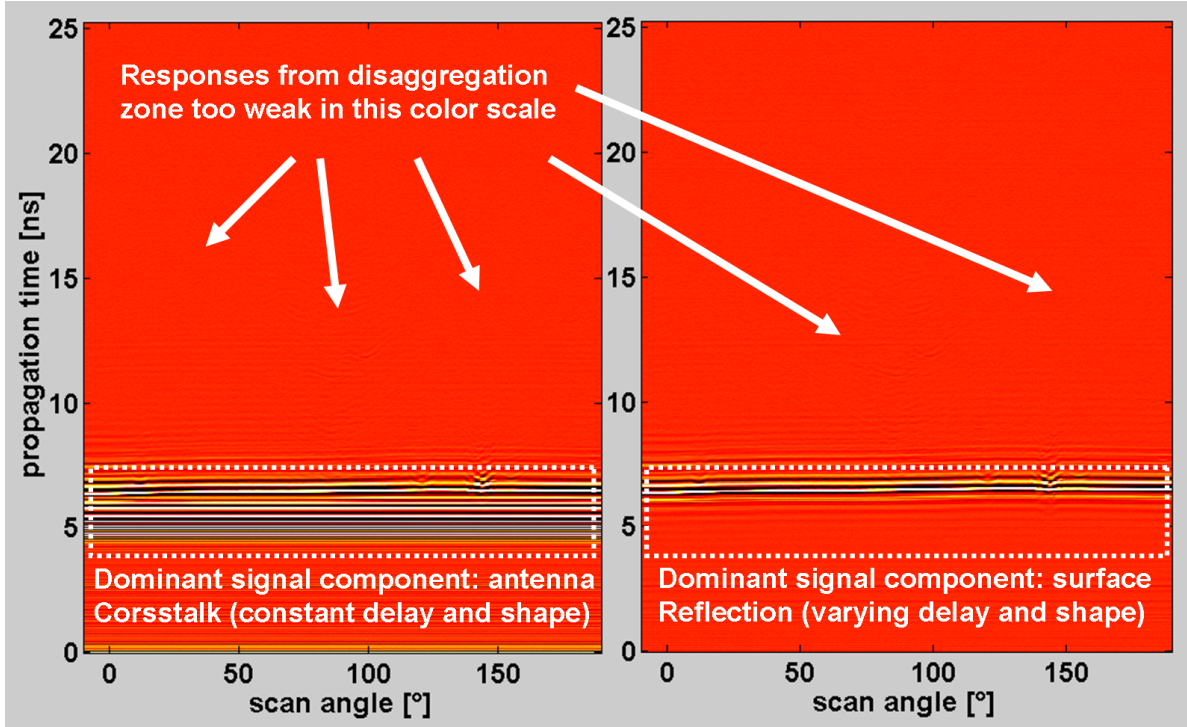
Fig. 6.6.: Example: HH polarised data before and after antenna crosstalk removal

6.2.2. Suppression of surface reflection

Removing the surface reflection is a much more critical task than antenna crosstalk removal. According to common experience, disaggregation is strongest close to the surface and should be detected by the sensor. Despite the high measurement bandwidth, the strong surface pulse takes a few ns to decay to the noise floor (also compare simulated results in section 2.4). If it is not removed properly, the first few cm behind the surface cannot be reliably visualised. Again, simple background removal techniques did not work at all leaving a lot of artefacts behind. The main reason is evident from figure 6.6. The distance between antennas and surface was not constant throughout scanning. Moreover, despite the rather smooth surface in cylindrical tunnels, its reflection behaviour will usually not be exactly the same for every antenna position.

It is important to understand that the overall precision of antenna placement achievable with the simple scanner concept was very limited. While the actual angle of the antenna

arm could be adjusted rather exactly (to less than a tenth of a degree), on-site tests have shown that movement along the tunnel could not be realised with high resolution and that keeping the whole scanner in the centre was not always possible. For example, the rails guiding the lorry in one mine were usually not in the middle of the tunnel and their distance to the ceiling changed to within a few 10 cm. In this particular case, the length of the antenna arm needed to be adjusted from time to time while scanning a tunnel section. However, in each scan along the circumference, antenna distance variations of at least a few cm still remained and must be accounted for by proper data processing. If the aim was to keep surface distance exactly constant to be able to remove the reflection from measured data in a similar way like crosstalk, precision requirements would be tremendous. Propagation time change to the surface and back should not be larger than a ps. Otherwise, using a removal similar to equation 6.3 would leave artefacts strong enough to be mistaken for disaggregation responses. That means the scanner would need to guarantee the distance to the surface to within fractions of a mm. Even if a more capable and flexible scanner concept would have been available during research, a practical scanner in a production system would certainly not provide enough precision to control surface distance for a maximum deviation in the sub-mm range. Moreover, small changes in surface roughness along a scan could not be accounted for anyway.

For these reasons, the approach used for crosstalk removal has been further extended to fit the task of removing a strong reflection which does not occur at the same propagation delay and may slightly change its shape throughout a scan. Matching a reference signal to a current impulse response by means of an optimisation search proved to deliver satisfactory results for crosstalk removal. This time, however, the reference function cannot be measured in the lab and it cannot stay constant for processing a whole scan. The density of scanning along the circumference was chosen rather high, i.e. the usual scan spanning $180°$ was done in approximately 900 steps (or one impulse response was taken every $0.2°$). Under such conditions it can be assumed, that the time shape of the surface reflection does not change very much between neighbouring snapshots. Instead, the reflection in impulse response $y_{k+1}(t)$ can be modelled as a slightly scaled and shifted version of the one in $y_k(t)$ with high confidence. To consider both — shifting and scaling — is necessary, because the surface is in the near field of the antennas and even small distance variations have significant amplitude influence. If one was able to find a good initial guess $surf_1(t)$ of the time shape for the surface reflection in the first impulse response $y_1(t)$, data from all scanner positions could be treated subsequently. An additional modification is necessary to account for changes in the time shape due to antenna near field and salt rock surface properties. It can be assumed that these changes are of gradual nature along a scan and consequently a slow adoption of the shape of the reference function will improve the overall surface suppression. The adoption was implemented using exponential filtering along antenna position using a low forgetting factor α between 1%

and 5%. The best choice for α depends on actual surface roughness and the amount of surface distance variation in the current scan. For the measurement examples presented later, it was fixed on an empirical basis, but automatic evaluation of a suitable value seems possible. However, this is a topic for future development and manual selection of α does not harm the evaluation of sensor feasibility for detection of near-surface disaggregation. The following equations describe the main steps taken for surface removal in all of the N impulse responses per scan.

$$surf_1(t) = \frac{1}{n} \sum_{n}^{k=1} y_k(t) \tag{6.4}$$

$$c_k(\tau, a) = \left| y_k(t) - a \cdot surf_k(t)(t - \tau) \right|_p \tag{6.5}$$

$$z_k(t) = y_k(t) - a_{\mathrm{opt,k}} \cdot surf_k(t - \tau_{\mathrm{opt,k}}) \tag{6.6}$$

$$surf_{k+1}(t) = (1 - \alpha) \cdot a_{\mathrm{opt,k}} \cdot surf_k(t - \tau_{\mathrm{opt,k}}) + \alpha \cdot y_k(t) \tag{6.7}$$

Equation 6.4 shows the calculation of the initial guess for the time shape of the surface reflection. The mean of the first n impulse responses serves this purpose with $n << N$. Calculation is done for the whole propagation time of the data, i.e. for all t. That implies responses from near-surface disaggregation of the first few scanner positions will be contained in $surf_1(t)$. However, averaging over several impulse responses not only lowers the noise level in the initial guess, it also suppresses the weak disaggregation responses. It should be noted that for this approach to work properly, there should not be strong scatterers (like large discrete cracks) from inside the salt rock for the n considered impulse responses. If the beginning of the scan contains disturbances, initial guess data could be obtained from any point within the scan and surface removal would start from this point towards the beginning and the end of the current dataset. In general, if strong distortions or cracks were present all over the current scan profile, they could be identified much easier than small disaggregation defects. If a tunnel section was distorted that much it would certainly be deemed leaky without further analysis.

For each subsequent impulse response, the current surface reflection reference $surf_k(t)$ is matched in terms of scaling a and shifting τ using a similar optimisation as in crosstalk removal. Equation 6.5 defines the cost function $c_k(\tau, a)$ for determining the values $a_{\mathrm{opt,k}}$ and $\tau_{\mathrm{opt,k}}$. The same limitations introduced for crosstalk removal in the previous subsection 6.2.1 apply here as well. The cost function only uses the propagation time interval where most of the energy of the surface reflection is concentrated. Moreover, the optimal value for τ is supposed to be found near zero and a should be close to one. Since the optimisation search must be repeated for every impulse response, significant computational burden results. On the other hand the whole process is iterative and can run through the equations every time a new impulse response arrives from the sensor. A typical modern

PC is able to do the surface removal in nearly real time while scanning despite the use of MatLab, which is not optimised for calculation speed.

The correction of measured data is done according to equation 6.6. The current surface reference is scaled and shifted with the optimal parameters obtained earlier and ideally $z_k(t)$ should now only contain responses from distortions and disaggregation. The last equation 6.7 shows the slow time shape adoption of the surface reference using exponential filtering. Just like the initial guess, the calculation is done for the whole impulse response meaning a small portion of $z_k(t)$ contributes to the new reference. The forgetting factor α of this adoption was set rather small but large enough to avoid smearing of responses from disaggregation into neighbouring impulse responses. Figure 6.7 shows the same scan as in figure 6.6 after surface reflection removal. It clearly shows the effectiveness of the proposed algorithm and that responses near the surface are enhanced very well.
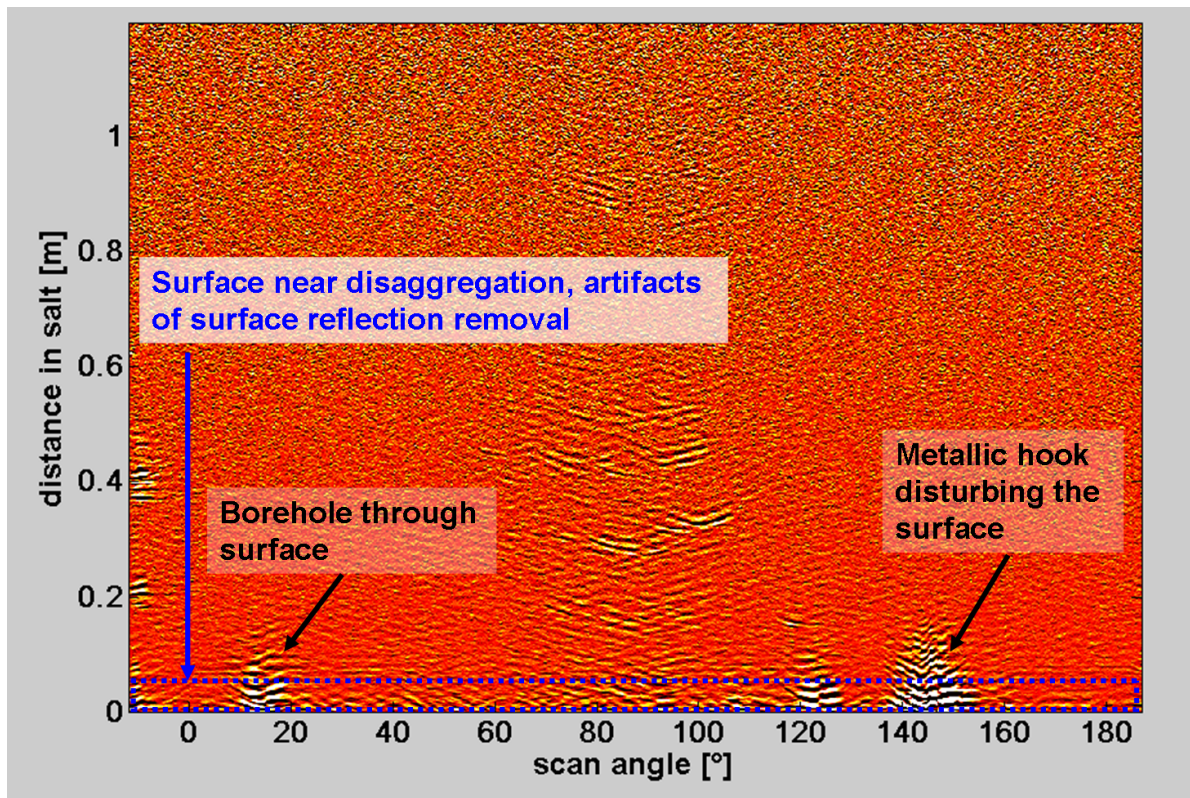
Fig. 6.7.: Data from a scan in HH polarisation after surface reflection removal

There are still some remaining surface artefacts, of course, but they are not present in the whole dataset and generally very low in amplitude. It should be noted that this surface removal tends to distribute reflections from a distorted surface a little bit to subsequent data vectors. However, in the case a discrete crack or borehole defect is visible at the tunnel's surface, it is clear that the surroundings are not compact and it is more interest-

ing to know how deep the crack is extending into the near-surface layers. Furthermore, the surface reflection decays within a few ns to the noise level. That means if one is concerned that the algorithm may cause problems for backscattered events far away from the surface (the disaggregation zone usually extends 50 cm up to 1 m inside the salt rock), equation 6.6 could be omitted for larger propagation delays t. For the measurements conducted throughout this research project the described algorithm delivered satisfactory surface suppression results. If other tunnel shapes than cylindrical tunnels with higher surface roughness were measured, further modifications and improvements may become necessary. Again, this is a task for future research. The obtained impulse responses $z_k(t)$ are directly used for visualisation described in the following subsection.

6.2.3. Visualisation of disaggregation zone

A very simple kind of visualisation has already been used for figures 6.6 and 6.7. In such a two-dimensional view, all impulse responses of one scan of the tunnel's circumference at a fixed position along the tunnel can be shown. The corresponding $z_k(t)$ are arranged in a matrix with k representing the angle of the antenna arm in the horizontal dimension and t representing propagation time in vertical dimension. The colour in the picture encodes the amplitude in a linear scale. Even though this kind of view is good for judging the local disaggregation zone and to check for artefacts remaining after removal of surface reflection, it is bothersome to look at several 10 or 100 such scans obtained from scanning a tunnel section and trying to get an impression about the distribution of defects and disaggregation. Another shortcoming of this simple view is the fact that the actual scanning geometry of the circular scan is not reproduced in the plot.

For these reasons, a 3D visualisation of the data from a whole tunnel section was developed as well. As mentioned before, scanning along the angle was possible in very fine steps, but precision of moving along tunnel axis was rather bad. Since the position error of the trolley or lorry was in the order of 1 cm, scanning slices were usually taken in steps of about 5 cm. This ensured about 50% of overlapping of the interaction volumes between scans (please also compare the size of antennas given in subsection 6.1.1). The engineering tool MatLab provides several interesting options to view a three-dimensional function. Finally, the function `isosurface(..)` has been used. It takes the X-, Y-, and Z-coordinates of a point in space as well as the corresponding function value. Furthermore, an amplitude threshold value must be specified. The function then constructs 3D volume objects enclosing those space regions, where the function value exceeds the threshold. These volume objects are shown in a 3D plot. Examples of how this looks like shall be postponed to the following section. Additional preparation of the processed data is necessary to get good visualisation results.

An appropriate coordinate system must be defined. By definition, the centre of the rotational scanner was set to $X = 0$ and $Y = 0$. The position along tunnel axis (i.e. position of the trolley or lorry) is directly used as Z-coordinate. Obviously, every single scan is taken in polar coordinates (k as angle and t as delay or distance). The amplitudes in all $z_k(t)$ need to be assigned to Cartesian X- and Y-coordinates. Transformation from polar coordinates (k, t) to Cartesian coordinates is not straight forward. The first few ns of each impulse response belong to propagation in air while the remaining data comes from inside the salt rock where a different wave velocity must be used to calculate distance. Fortunately, the delay to the surface reflection is known from the surface removal algorithm described earlier. It can be used to align each individual impulse responses to the salt rock surface and to calculate the distance between antennas and surface. This offset is added to the length of the antenna arm to get the correct distance between the coordinate system's origin and the salt rock surface. All data from behind the surface is treated with the mean wave velocity of salt rock as derived in section 2.1. The velocity is not precisely known and can slightly differ from tunnel to tunnel. However, since the aim of coordinate transformation is only visualisation and not radar imaging, the approximation using an estimated and constant ϵ_r is feasible.

With this preparation, each amplitude sample in the dataset from a tunnel section has valid coordinates in 3D space and the isosurface can be calculated. However, the threshold value must still be chosen and heavily influences the resulting view. On one hand, if a high threshold is used (for example 50% of the maximum amplitude of the whole dataset), only very strong scatterers like boreholes or large discrete cracks will be visible. On the other hand, if the threshold was too low, noise would dominate the resulting picture (evident as small enclosed volumes all over the displayed space). The range of thresholds giving meaningful results also depends on the actual content of the disaggregation zone. For a practical software implementation, it is best to give the operator the freedom to choose the threshold as a fraction of the maximum amplitude in the dataset. He can then decide to look at strong reflections only or to look at the smaller responses as well.

Since the threshold is fixed for the whole dataset to be displayed, the amplitudes in all impulse responses should at least be corrected according to the distance between antennas and surface. As mentioned in section 2.4, the received amplitudes depend on this parameter. For thin gaps, the amplitude of backscattering is approximately inversely proportional to two times the distance. For small volume scatterers, the amplitude even decreases with the square of distance. For the visualisation this would mean that the threshold needed to be lowered considerably to see disaggregation responses far away from the surface. This effect can be partly compensated by applying a propagation time dependent gain before feeding the data to the visualisation function. Trying to correct amplitudes according to the $1/r$ or even $1/r^2$ dependency did not give useful results. The reason for that is the low SNR for higher propagation times. Responses from weak and

far away targets tend to vanish in the noise floor of the sensor. Applying a high gain to these signal regions will merely amplify noise. It is clear that the sensitivity of the new M-Sequence sensor for responses from disaggregation is limited and that a reliable detection of small distortions is no longer possible from a certain distance on. Nevertheless, visualisation results could be improved using a linearly increasing moderate gain $tdg(t)$ as shown in figure 6.8. Equation 6.9 shows how the propagation time dependent gain has been applied to each impulse response to get the visualisation amplitudes $z_{\mathrm{vis},k}(t)$. Please note that the gain applies only after the salt rock surface for $t \geq t_{\mathrm{surf}}$ as defined by equation 6.8. The delay to the surface t_{surf} is obtained from the surface removal algorithm. The gain slope factor Δg was empirically set to 0.16 $\frac{1}{ns}$. This is another degree of freedom which could be provided to the operator in a production system. The whole processing flow is summarised in the following subsection.

$$tdg(t) = \begin{cases} 1.0, & t < t_{\mathrm{surf}} \\ 1.0 + \Delta g(t - t_{\mathrm{surf}}), & t_{\mathrm{surf}} \leq t \leq t_{\mathrm{surf}} + 25 \ ns \\ g_{\mathrm{max}}, & t > t_{\mathrm{surf}} + 25 \ ns \end{cases} \tag{6.8}$$

$$z_{\mathrm{vis},k}(t) = z_k(t) \cdot tdg(t) \tag{6.9}$$
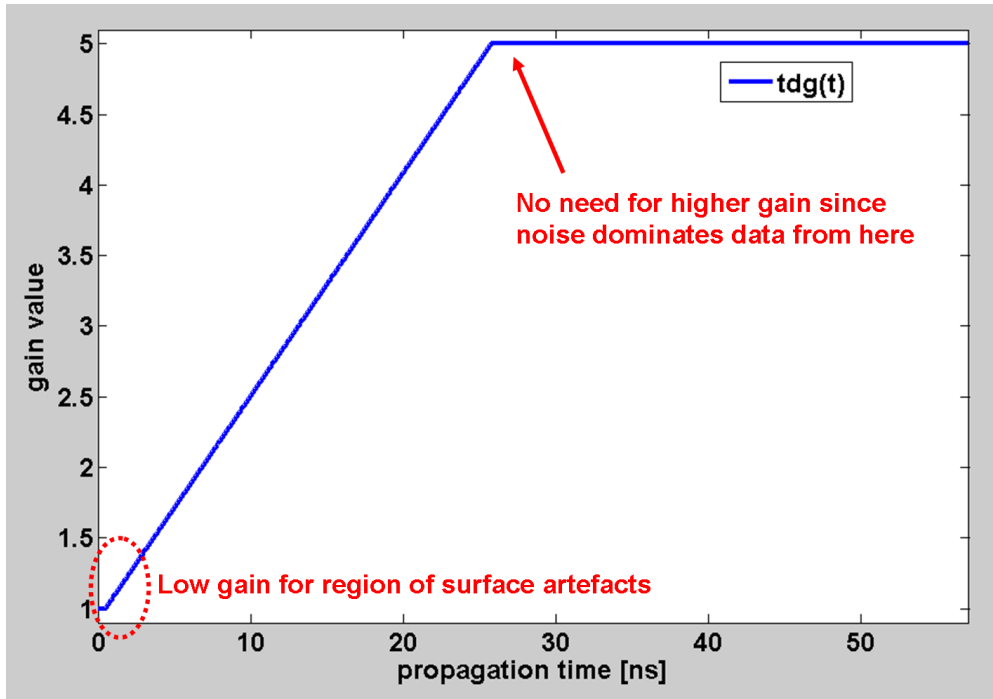
Fig. 6.8.: Time dependent gain function used for visualisation

6.2.4. Typical data processing flow for disaggregation in salt rock

The typical processing flow for salt mine measurements is shown in figure 6.9. The raw data coming from the sensor are the acquired wave quantities from all receivers combined with the current position of the antenna arm (angle ϕ) and the relative position of the trolley or lorry along the tunnel axis (Z-coordinate). Processing is divided into three stages — pre-processing, main processing for the disaggregation zone, and data conditioning for visualisation. Besides the actual measurement data, calibration measurements of the standards in the automatic calibration unit were taken after device warm up. Additional reference data comes from antenna crosstalk characterisation in the lab. It is assumed, that calibration of the sampling timing as described in chapter 4 has been done successfully before any other measurements. Please also note that pre-processing and visualisation use the complete dataset for a tunnel section, while main stage processing applies separately for each individual cylindrical scan, i.e. for a fixed Z-coordinate. A typical measurement and visualisation result is presented in the following section 6.3.
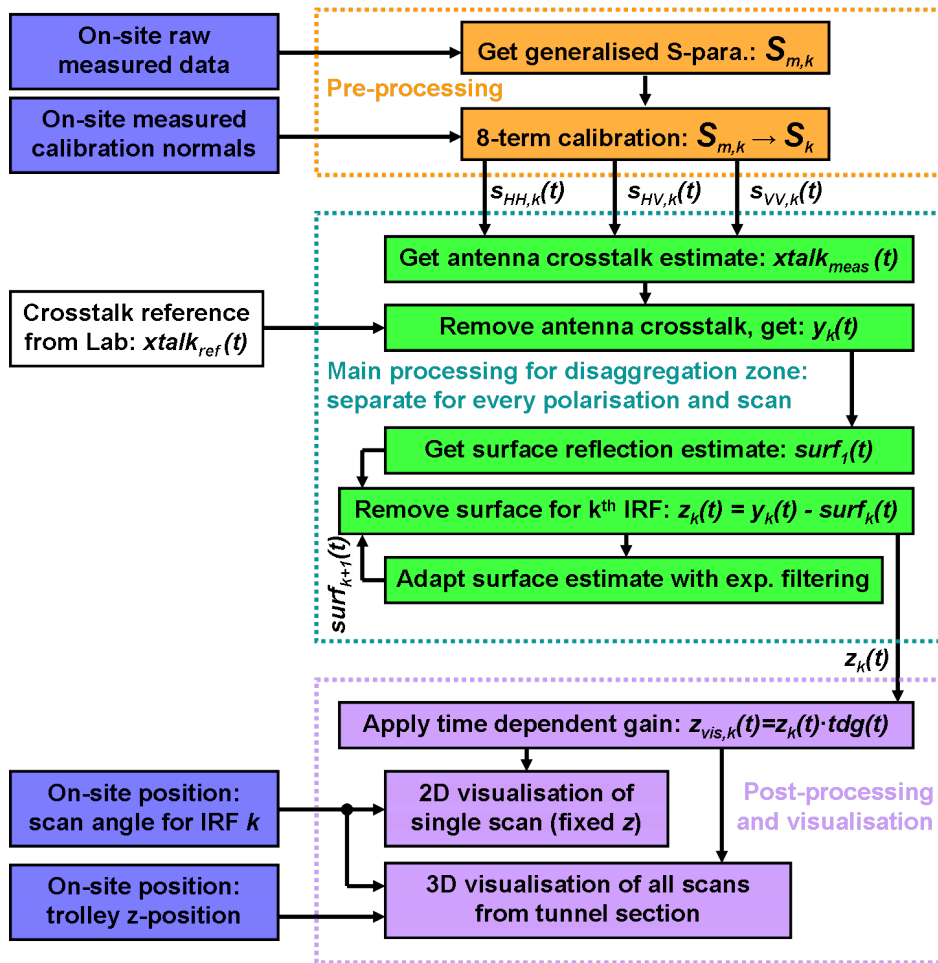
Fig. 6.9.: Typical data processing flow for salt mine measurements of tunnel sections

6.3. Measurement results for an old cylindrical tunnel

Development of the new M-Sequence sensor, its antenna unit, and the scanner have been accompanied by various measurement campaigns in salt mines to evaluate the devices under real conditions. The last two tests were dedicated to get final results and to look into the disaggregation zone of tunnel sections. Results from an old cylindrical tunnel in the mine of Bernburg (Germany) shall be presented here. Mining activities started in the early 20th century and the tunnels are about 500 m below ground. The investigated tunnel was cut in the 1960s and used for transportation by a mining train. It has not been active in years. Figure 6.10 shows a picture of the test site including the coordinate system used for scanning. The tunnel has a very common diametre of 3 m and used to have rails on the bottom. As can be seen in the figure, the rails have been removed and the lower part of the tunnel has been carved out. The former completely cylindrical shape having a rather homogeneous force distribution along the circumference has been destroyed. At the sides, where the cylindrical shape ends and transitions into the carved lower section, cracks and distortion of the salt rock are even visible at the surface. Measurements took place in two sections near old boreholes — BL1 and BL2 — which had been used for gas-permeability tests before. Each measured section was 1 m long. Along with the rails, also supply cables usually found at the sides or on the ceiling of tunnels had been removed. In some cases, metallic hooks or stubs looking through the surface remained.
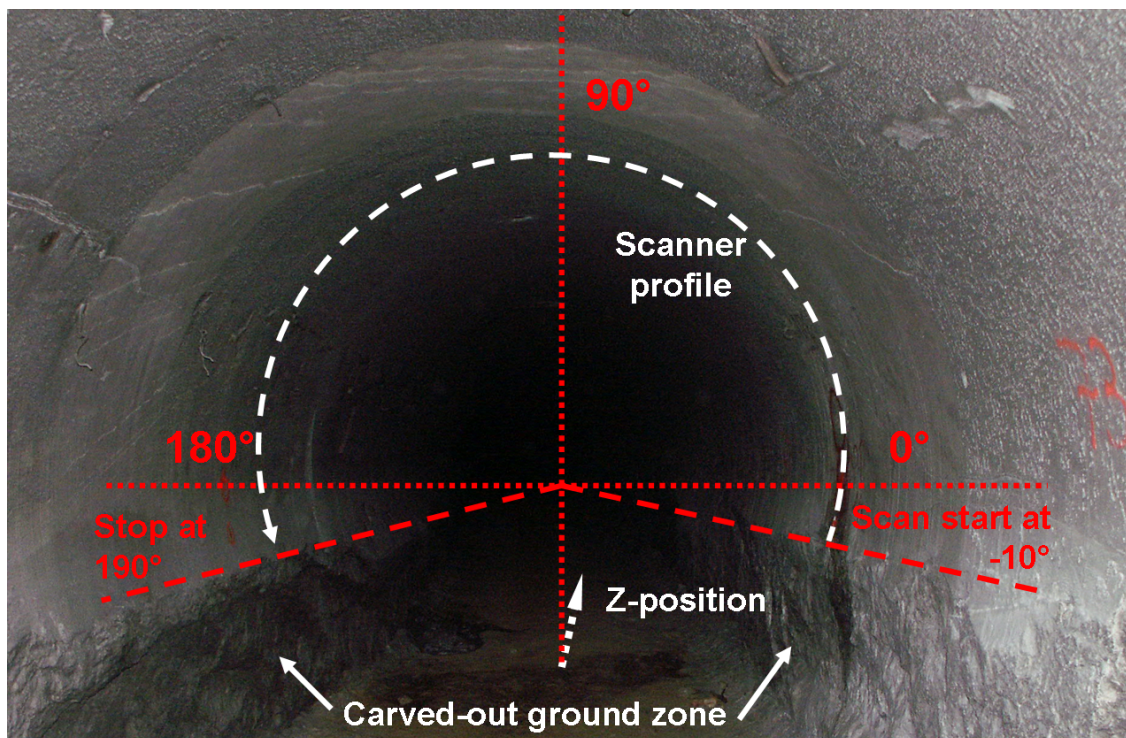
Fig. 6.10.: Test site in the mine of Bernburg
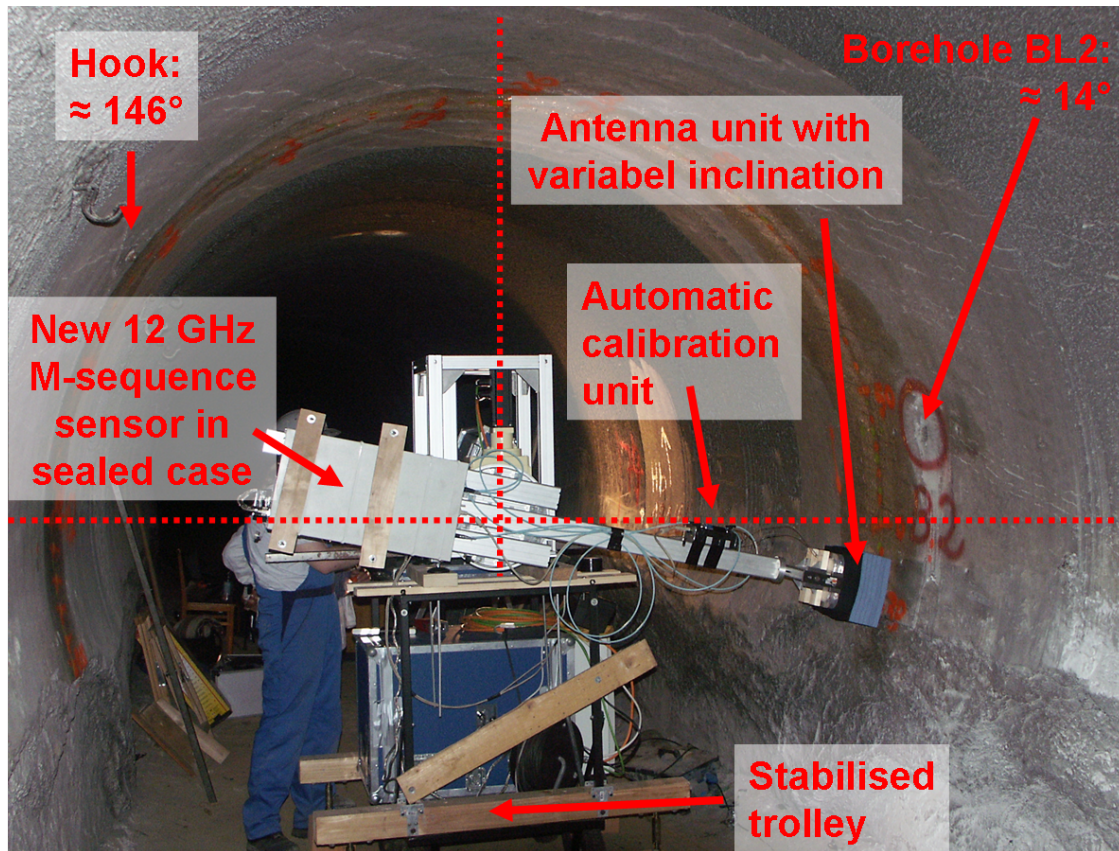
Fig. 6.11.: Measurement setup in Bernburg

6.3.1. Measurement setup for Bernburg

Due to the lack of rails and the larger distance between bottom and ceiling (about 3.5 m), the rotational scanner with the sensor and antenna arm needed to be mounted on a trolley movable by hand. Figure 6.11 shows the complete construction. The coordinate system for scanning is depicted in figure 6.10. By definition, the angle of 0° was exactly horizontal at the beginning of the investigated tunnel section. Since the rotation centre of the scanner was about 2.0 m above ground, the trolley was stabilised at its sides during scanning. In between scans, the trolley was moved along the tunnel Z-axis in about 5 cm steps. Care was taken to place it approximately in the middle of the tunnel to ensure a low variation of the surface distance while scanning. The distance from antennas to the surface was kept between 5 cm to 10 cm. The antenna array was slightly inclined by 15° towards the tunnel axis. Each profile was scanned through a continuous movement with low speed and a complete scan took about 3 minutes. The range from -10° to 190° has been measured to include the transition regions from the cylindrical shape to the ground section.
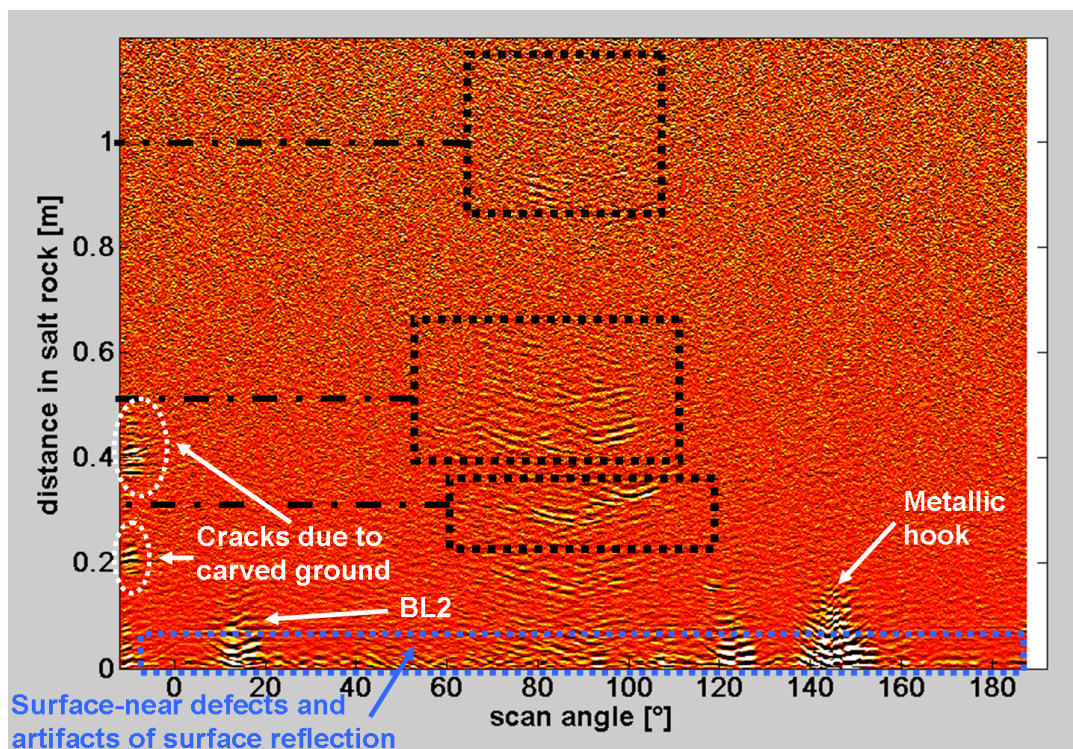
Fig. 6.12.: Example scan tunnel Bernburg, BL2, polarisation HH
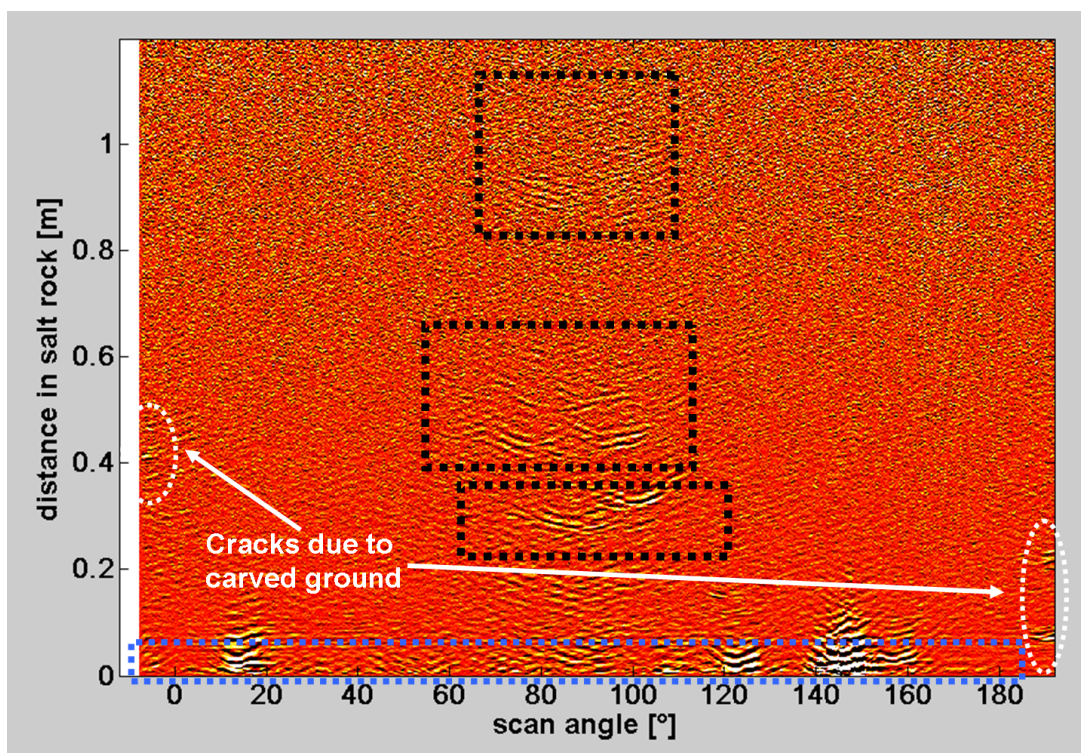
Fig. 6.13.: Example scan tunnel Bernburg, BL2, polarisation VV
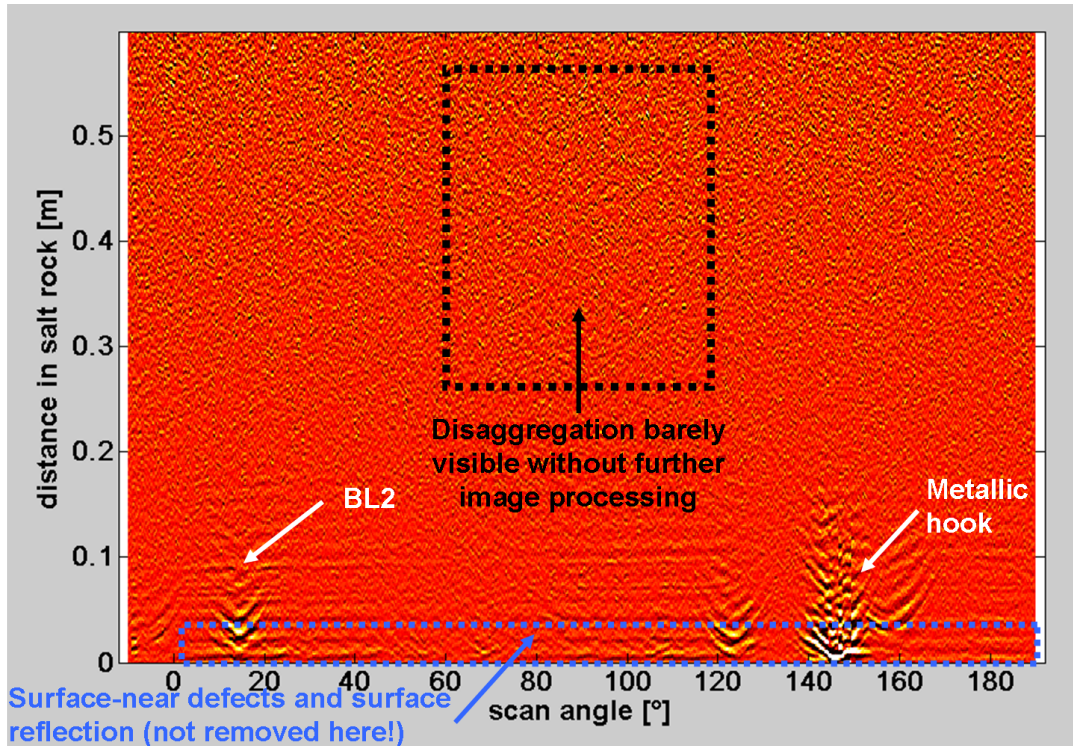
Fig. 6.14.: Example scan tunnel Bernburg, BL2, polarisation HV

6.3.2. Selected scans in 2D visualisation

The simple 2D view of single scans is ideal to compare different polarisation combinations. The following figures 6.12 through 6.14 show a scan taken directly at borehole BL2 for all acquired polarisations. Due to alignment of the antenna array, slightly different angle ranges have been covered by the scan — from -10° to 185° for HH, -5° to 190° for VV, and -7.5° to 187.5° for the HV case. The X-axis shows the angle of the antenna arm while the Y-axis denotes distance inside the salt rock. The datasets are aligned to the surface reflection, i.e. data from propagation in air has been removed. A mean relative permittivity of $\varepsilon_r = 6.0$ has been used to calculate distances from propagation times.

As marked in the three figures, the strongest scattering events originate from the borehole itself and a metallic hook also contained in this profile. Furthermore, a number of weaker distortions can be identified near the surface all over the circumference. This is at least true for co-polarisations in figures 6.12 and 6.13. Moreover, in the ceiling region there are a number of evident reflections from about 30 cm, 50 cm, and even further around 1 m. These events look like being caused by connected distortions rather than by single defects. Please keep in mind, that data has been acquired in polar coordinates but is presented in a rectangular grid. At least the reflections closer than 1 m are still slightly above the noise floor and could be enhanced through further image processing.

Looking at the start (i.e. angles below 0°) and the end (angles above 180°) of the scan, additional stronger reflections reaching deeper into the salt rock are visible. These responses have been expected since they originate form the transition region between the upper cylindrical part and the lower carved-out part of the tunnel. Due to destruction of the original round shape, the force distribution inside the rock changed and led to larger cracks and disaggregation. It is not only visible at the surface, but obviously also extending into the disaggregation zone. This situation is clearly detected by the new M-Sequence sensor.

Most responses discussed so far are not clearly visible in the cross-polarised dataset of figure 6.14. It is interesting to note, that surface reflection removal could be omitted for the HV dataset. For a simple dielectric medium like salt rock with a smooth reflection surface, almost no response for cross-polarisation is expected theoretically. The boundary conditions at the surface do not lead to a change in polarisation and the results indeed correspond to that. In general, the amplitudes of cross-polarised measurements are lower than those of co-polarisations for most targets in GPR. Cross-polarised responses usually emerge from multiple reflections within the test object [53, 78, 129]. For the disaggregation zone, chances are that some distributed distortions may lead to a change of wave polarisation and it is therefore necessary to acquire cross-polarisation as well. However, due to the overall weakness of disaggregation responses those going through multiple reflections tend to vanish in the noise floor. Despite that, the first few cm directly behind the surface are represented much better in the HV dataset since there are no artefacts from surface removal. If the noise floor of the sensor could be lowered (for example by scanning with a slower speed and increasing the number of averages), HV information would be even more valuable. This is another topic for future investigation and improvements.

In conclusion, the examples prove the effectiveness of data processing for co-polarised datasets and that the disaggregation zone in the investigated tunnel section indeed has some distortions as can be expected for such an old tunnel. It is also evident that the noise floor starts to dominate beyond 70 cm from the surface. This is not too much of a problem since the disaggregation zone often only extends about half a metre inside the salt rock. Moreover, larger discrete defects (starting from sizes in the cm range) will still be visible deeper inside the salt rock. Let us move on to the 3D visualisation of the data which provides an even better insight into the structure of the disaggregation zone at the test site.

6.3.3. 3D visualisation of a tunnel section

All scans taken at borehole BL2 have been combined into an isosurface view. This was done for the two co-polarisations HH and VV, respectively. As explained in subsection
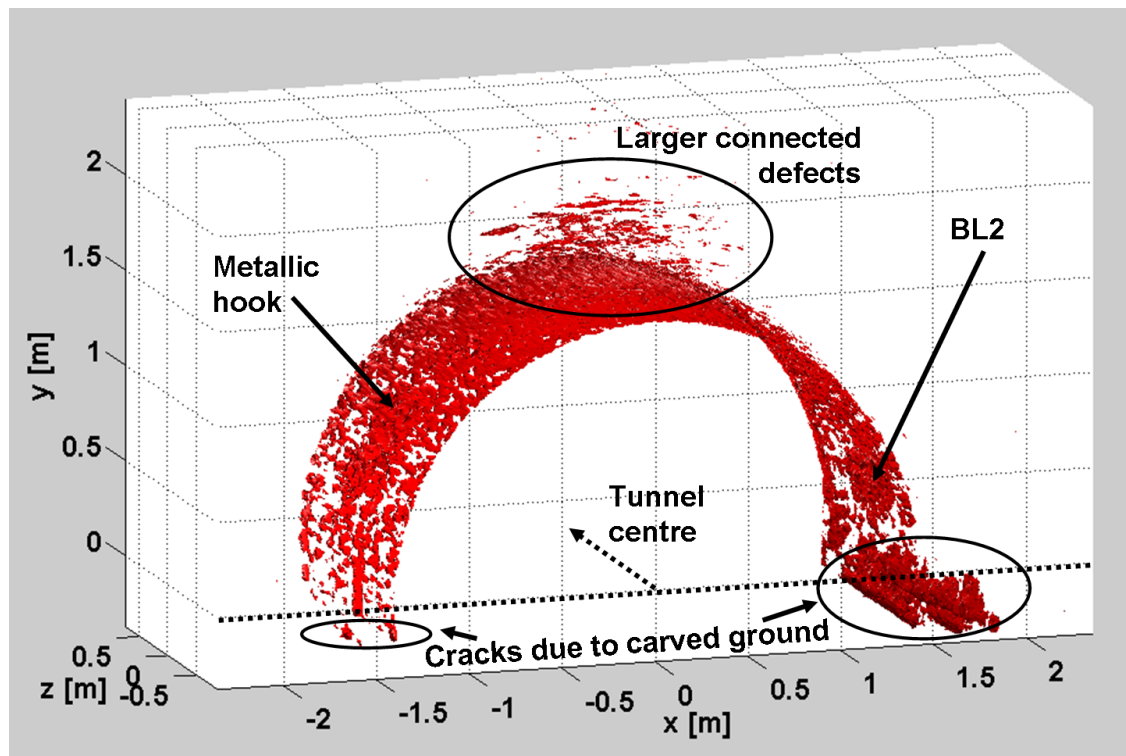
Fig. 6.15.: Disaggregation zone of a tunnel section around BL2, pol. HH, isothreshold 50%
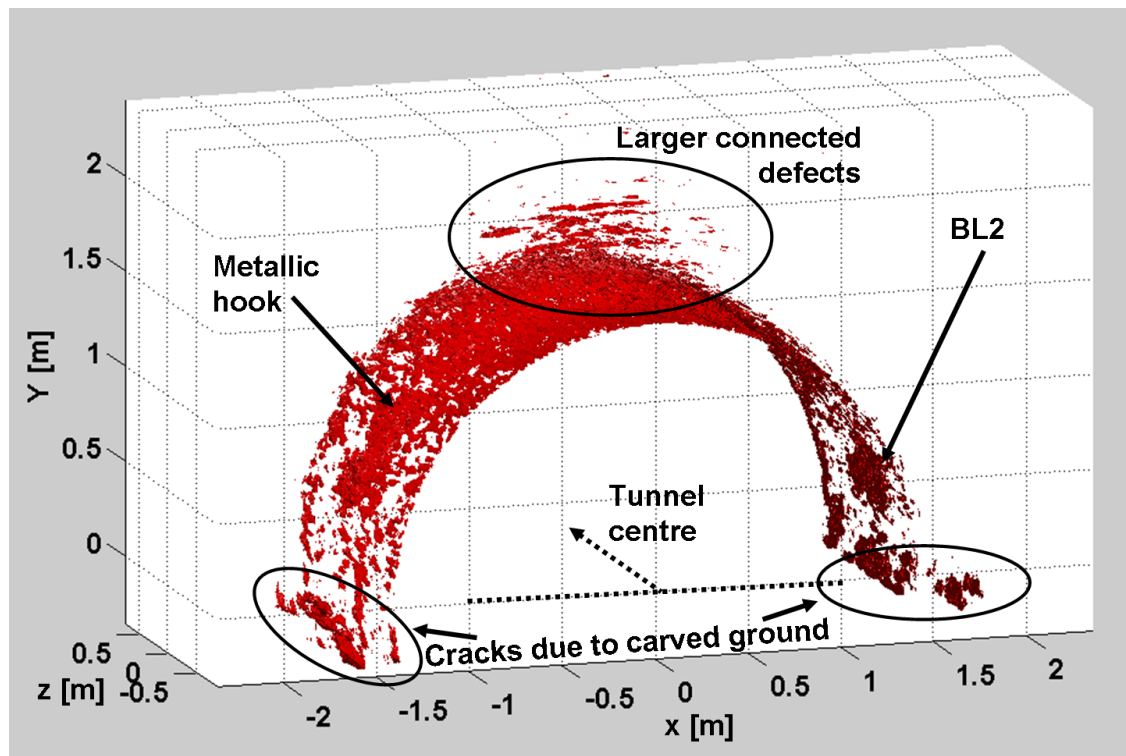
Fig. 6.16.: Disaggregation zone of a tunnel section around BL2, polarisation VV, isothreshold 50%

R. Herrmann

6.2.3, the threshold value is a degree of freedom and can be varied to get different impressions of the disaggregation zone. The first results presented in figures 6.15 and 6.16 were obtained with a threshold value of 50% of the maximum amplitude in the dataset. Some interesting aspects can be observed at this level. As indicated by the 2D results shown before, the first few cm behind the surface show responses from distortions along the whole section. Furthermore, disaggregation seems to increase towards the ceiling (around 90°). The 2D view already gave the impression, that these responses are not separated but rather belong together. The 3D visualisation confirms this fact and shows flat or even layered reflectors above the tunnel. Both results also show strong scattering from the sides of the tunnel where the salt rock was heavily destabilised. Scattering from the borehole BL2 and the metallic hook at the other side of the tunnel is clearly visible as well in both polarisations. Since such distortions disturb the otherwise smooth surface, the areas in their vicinity are not reliably imaged but rather dominated by artefacts of the surface removal algorithm. However, such objects represent distortions of the near-surface salt rock themselves. Furthermore, artefacts spread only locally a few degrees around the hook or borehole.

In the dataset presented here, not much difference between the polarisation combinations is evident. The HH case of figure 6.15 shows denser responses near the salt rock surface indicating a small sensitivity advantage. At least for the rather flat reflectors in the top region both polarisations worked equally well. Judging from only a single example that polarimetric measurements would not be necessary is certainly not an appropriate conclusion. Different geological conditions in other tunnels may lead to different alignments of cracks or layered disaggregation showing greater sensitivity to wave polarisation than in the case discussed here. As a last result from Bernburg, the 3D view of horizontal co-polarisation shall be repeated with a different threshold. Figure 6.17 shows the same data as figure 6.15 but the threshold was lowered to 37.5%. The result emphasises the strong inhomogeneities above the tunnel and that the reflections are somewhat connected in flat layers. Also the distortions in the bottom regions are enhanced significantly and it can be seen that they appear along the scanned tunnel section in a similar manner. Contrary to the other pictures using a threshold of 50%, noise starts to appear in figure 6.17 at greater distances from the surface. A further decrease of threshold level does not seem feasible in this case and would lower the clarity of the view. All in all, the presented results impressively show the potential of the developed M-Sequence sensor for measurement of the disaggregation zone. Despite the lack of complex image processing and conditioning a lot of information about the structure of near-surface salt rock layers could be obtained in Bernburg. The next section deals with another evaluation experiment where the formation of disaggregation for a new tunnel has been observed.
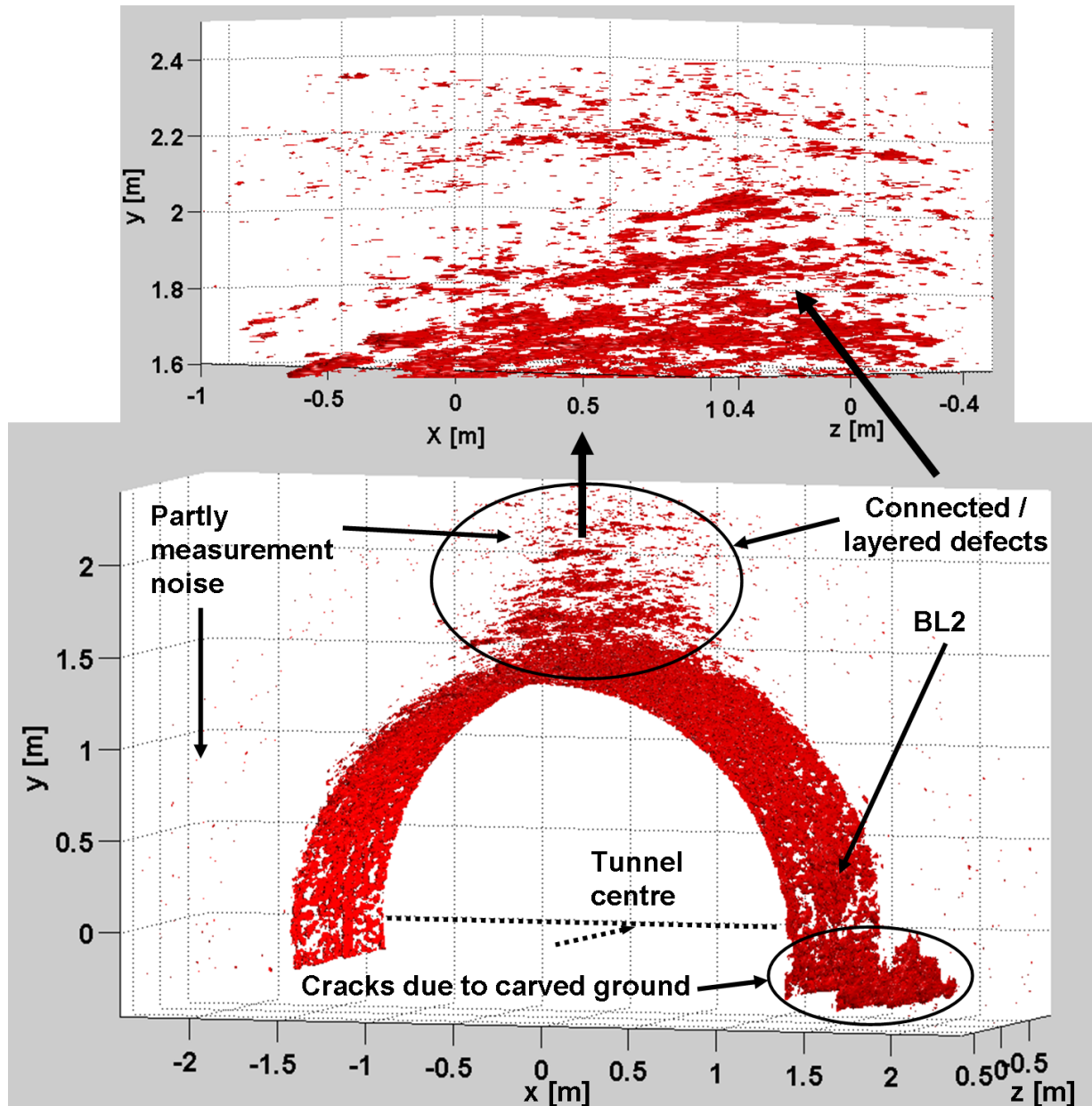
Fig. 6.17.: Disaggregation zone of a tunnel section around BL2, pol. HH, isothreshold 37.5%

6.4. Measurement results for a newly cut tunnel in Borth

It is a well-known fact, that a disaggregation zone is present around old tunnels. However, it is usually unknown how it looks and under which circumstances or how fast it develops. As demonstrated in the previous section, the new M-Sequence sensor can provide a valuable tool to measure the near-surface regions and probably even observe them over time. Then again, it would also be interesting to measure a site with known conditions and to see how radar data changes during observation. Under normal circumstances, this is

hardly possible since development of disaggregation is a slow process and research time was too limited for meaningful long-term observation. Fortunately, we had the chance to do a measurement campaign in the mine of Borth in Germany, which is about 900 m below ground. The salt rock in this mine is known to show significant subsidence even within the first hours after a tunnel has been cut. The mining company started to extend one tunnel in the northern area and invited us to observe formation of the disaggregation zone from a formerly undistorted state.

After a short stub with dimensions of 8 m x 3 m x 5 m had been cut by an AW4 miner, the machine left the tunnel and the already warmed-up measurement setup was carried inside. Figure 6.18 shows the AW4 miner in the upper part and the newly cut tunnel with the sensor and scanner in the lower part. The miner does not produce cylindrical tunnels and therefore a different scanner had to be used this time. The largest changes were expected above the middle of the ceiling because the tunnel shape is wider than high. Furthermore, the miner also produces a quite smooth surface at the top (even though not as smooth as in the old tunnel of Bernburg). Finally, a linear scanner for moving the antennas along a 2.7 m long track was chosen. The antenna unit was again placed close to the surface and was moved in discrete 2 cm steps. The scanner had a very high precision with a repeatability better than 0.1 mm to ensure comparable subsequent scans. In the interval of 6 h to 54 h after creation of the stub (earlier access was not possible due to technical reasons), one scan was taken per hour. Two main aspects of this experiment shall be discussed here. At first, the actual amount of subsidence along the scanned track will be calculated. Then differences in near-surface salt rock layers between scans from the beginning and the end of the experiment are shown.

6.4.1. Subsidence analysis of measurement results

The salt rock in Borth is known to show strong changes within the first hours after cutting a tunnel. Mining staff explained, that some times the AW4 miner even cannot easily move out of a new tunnel section because subsidence in the cm range could occur while the machine is working. This time, measurements began 6 h after creation of the stub and such strong changes could not be expected any more. However, it was interesting to find out if subsidence can be detected with the new M-Sequence sensor anyway.

For that purpose, scans taken at the beginning of the experiment have been compared to data from the end of the campaign. The time difference between the datasets amounts to 48 h. It should be noted that environmental conditions in the mine were challenging (e.g. an ambient temperature above 30 °C) but remained stable. Nevertheless, to be able to account for drifting of device electronics and environment, the automatic coaxial calibration has been repeated before every scan. Data pre-processing was almost the same
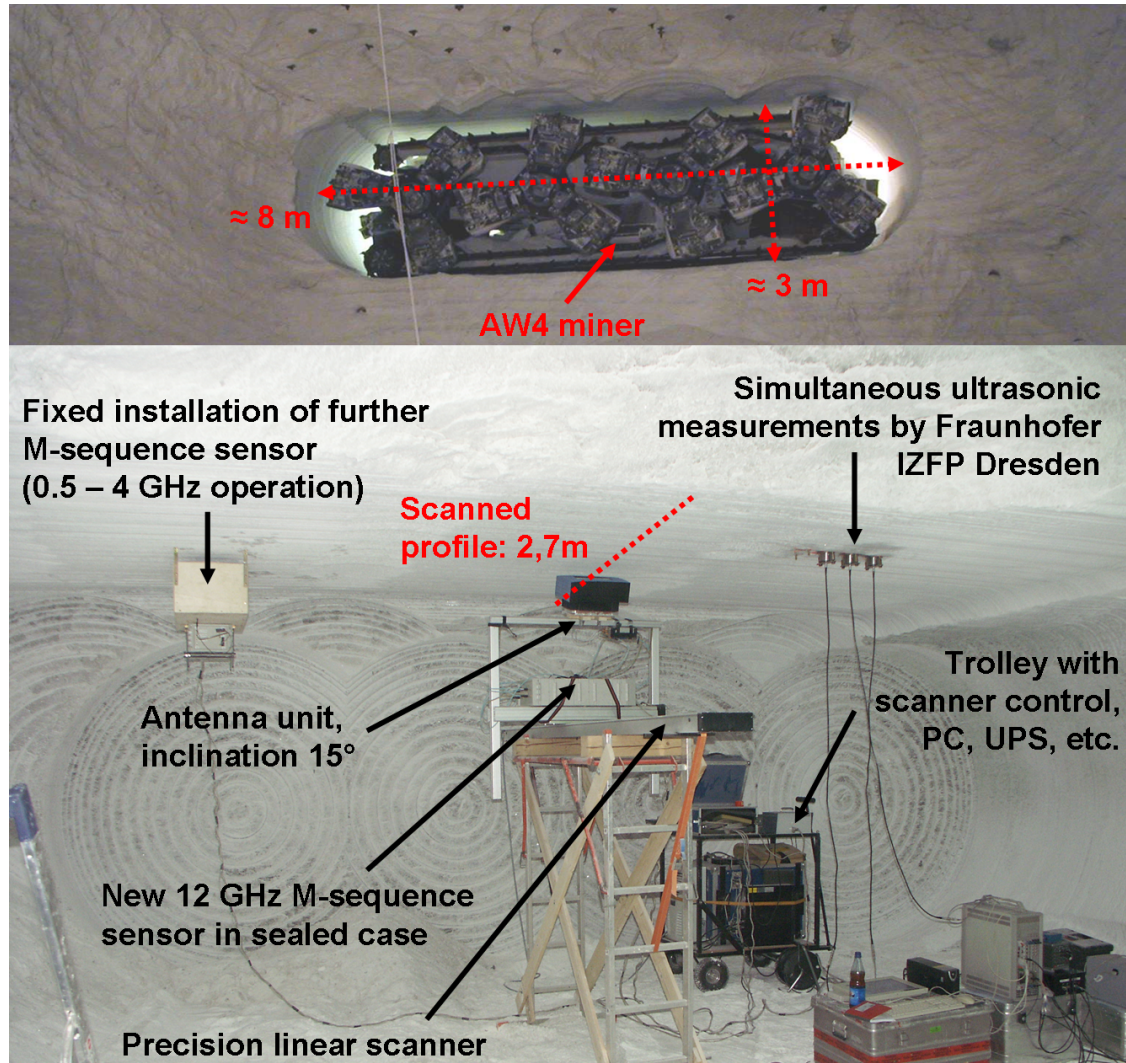
Fig. 6.18.: New tunnel stub and measurement setup in Borth

as described in section 6.2. The first step — removal of antenna crosstalk discussed in subsection 6.2.1 — was applied unaltered. Removal of the surface reflection was not necessary in this case. The idea of matching gain and delay shift between an actual surface response and a reference function by means of an optimisation process was adapted to find the amount of subsidence instead. Because of the high position-reproducibility of the scanner, the surface reflection found in data from the first scans could be used as references and compared to the impulse responses from later scans. In total $N = 136$ discrete positions along the 2.7 m track have been measured and the optimisation was done for all of them separately. Equation 6.10 gives the modified cost function $c_{\text{subs}}(\tau, a)$ using a similar notation as in the surface removal algorithm described in subsection 6.2.2. The impulse responses $y_{\text{start},k}(t)$ and $y_{\text{end},k}(t)$ refer to data from the beginning and the end of observation, respectively. The index k represents the discrete scanner positions.

Once more, the 2-norm ($p = 2$) was used during optimisation and the cost value was only evaluated for the propagation time interval containing most of the surface reflection energy.

$$c_{\mathrm{subs},k}(\tau, a) = \left| y_{\mathrm{end},k}(t) - a \cdot y_{\mathrm{start},k}(t)(t - \tau) \right|_p \tag{6.10}$$

When the cost function is minimised, the two compared impulse responses are matched to each other. For subsidence analysis, the optimal delay shift τ_{opt} is of major interest. It shows how much the distance between antennas and salt rock surface changed during the 2 days time. It can be directly converted from delay time into distance using the wave velocity in air. Figure 6.19 shows the results obtained for both co-polarisations. The information obtained from HH and VV coincide very well as expected for the scattering from a rather flat surface. Actual subsidence varies between 4.6 mm and 4.9 mm along the track. Because the scanner was standing inside the newly cut tunnel, it is not possible to distinguish between the ceiling coming down and the ground being pushed upwards. It can be assumed that both effects occur at the same time leading to the roughly 5 mm decrease in tunnel height. It is interesting to note the obvious trend in subsidence as well. The beginning of the track (position 0 m) was near the end of the stub, i.e. this part was cut last before the miner moved out. The scan ended near the entrance to the new tunnel stub, which had been cut a few hours earlier. The slightly smaller values around 2.7 m indicate that the speed of subsidence was already lower for those parts which had been cut first. Even though the differences are small, such behaviour coincides well with the experience of mining staff — biggest changes occur immediately after cutting and thereafter the situation stabilises fast. The variations of subsidence data along the profile position observed in figure 6.19 is in the order of 0.1 mm. This can be accounted to uncertainties in the scanner repeatability as well as the influence of measurement noise on the results of the cost function in equation 6.10. It can be concluded that subsidence effects could be detected with good precision building up confidence in the new UWB sensor and the developed data processing. Even though there are certainly easier methods of measuring subsidence, this example shows the potential for high precision measurements and also for long-term supervision tasks. Furthermore, stability of the employed optimisation process is demonstrated as well and the obtained scaling and delay shift values τ and a can be used for further analyses.

6.4.2. Development of the disaggregation zone in a new tunnel stub

Due to the detected subsidence it could be expected, that compactness of near-surface salt rock layers had changed in some way. Apart from the possible appearance of larger discrete cracks, distortions of very small size might have developed everywhere. To as-
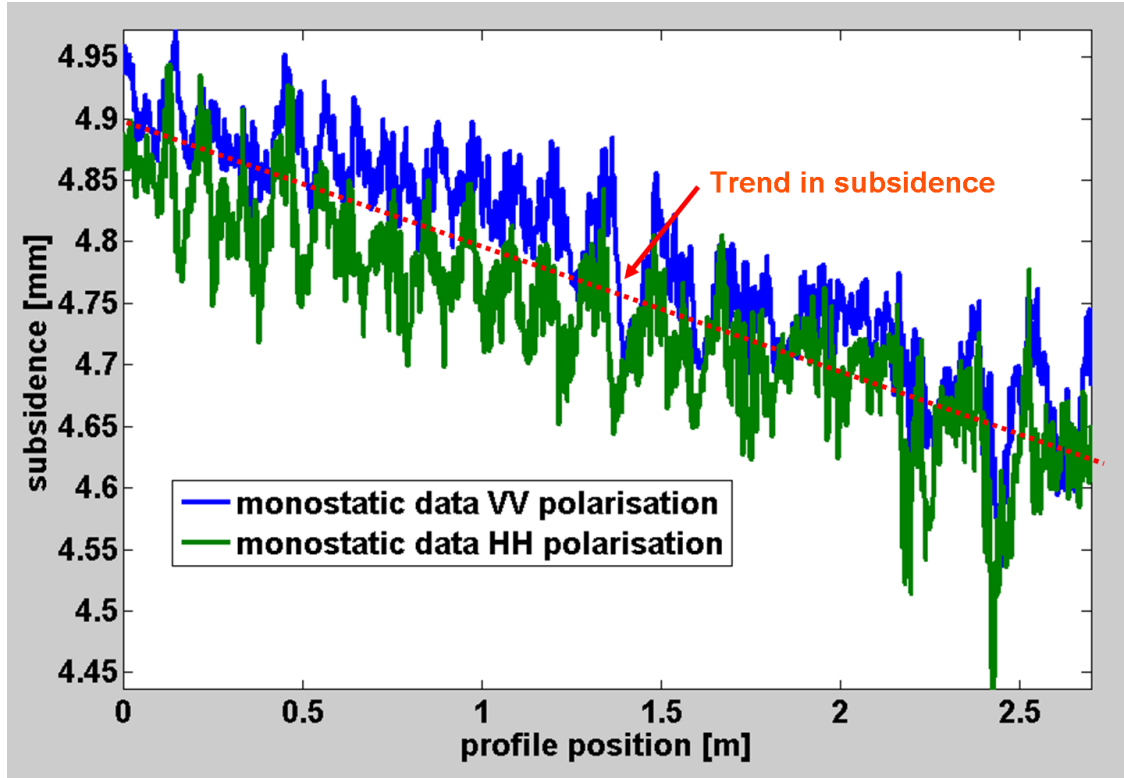
Fig. 6.19.: Amount of subsidence for new tunnel stub within 2 days after creation

sess the small changes, interferometric processing has been considered. For every scanner position, impulse responses from the start and the end of the experiment have been matched according to their surface reflection. The parameters $a_{\mathrm{opt},k}$ and $\tau_{\mathrm{opt},k}$ were obtained during this process. An interferometric result can now be obtained by applying equation 6.11.

$$d_k(t) = y_{\mathrm{end},k}(t) - a_{\mathrm{opt},k} \cdot y_{\mathrm{start},k}(t)(t - \tau_{\mathrm{opt},k}) \qquad (6.11)$$

If there were no changes in the disaggregation zone, $d_k(t)$ would contain merely noise (except for artefacts of the surface reflection caused by imperfect position reproducibility). The results proved quite the opposite. Figure 6.20 shows the interferometric datasets calculated for VV co-polarisation. Data from HH is not shown here since it provides no additional insight. First of all, a discrete crack can be found towards the entrance of the tunnel stub at a distance of about 50 cm from the surface which is marked in the figure. This crack was also visible in single datasets from the beginning and the end of measurements and its presence in the interferometric data means it also developed slightly over time and its distance to the surface changed. The near-surface regions up to about 20 cm are especially interesting. Due to higher surface roughness compared to the other tunnels measured, suppression of surface reflection left more evident artefacts despite the

optimised matching between subtracted datasets. Correspondence of waveforms from surface reflections is very good up to 10 cm. Still, there are changes in this area visible indicating an altered structure of the salt rock. Between 10 cm and 20 cm, strong differences exist between the datasets. They should not be mistaken as direct backscattering from distortions. The differences are caused by waveform deviations mainly in the trailing parts of surface reflection. Since they suddenly become stronger at a defined interface, it can be assumed that a small gap or similar layered distortion appeared there. Another factor leading to such interference patterns is a change in average relative permittivity. Permittivity and wave velocity change when vacuum or air-filled distortions form anywhere near the surface. The responses from inside the salt rock will be stretched or compressed along propagation time under such circumstances resulting in residual differences along the waveform. The results coincide very well with theoretical expectations. The disaggregation zone starts to develop near the surface and grows into the overlying rock. With the acquired data it would even be possible to show the history of changes throughout the 48 h period. This shall be a topic for further investigation with a more geological focus.

As a last result, figure 6.21 shows data from cross-polarisation acquired right before the end of the experiment (about 54 h after tunnel creation). The data has been processed including antenna crosstalk removal and 2D visualisation (compare subsections 6.2.1 and 6.2.3). Removal of surface reflection was omitted as usual. Again, there are significant responses which can be attributed to the surface. On the other hand there are many reflections evident within the interesting region up to about 20 cm behind the surface. Even the larger crack at 50 cm is partly visible above the noise floor. This time, HV mode proved to be valuable in imaging the disaggregation state and is therefore an advantage of the new M-Sequence sensor over common GPR equipment not taking care for such polarisation. Even though the number of measurement campaigns in the research project was quite limited and the presented data processing can certainly be extended and improved, the developed UWB system has shown its suitability for the task of disaggregation zone investigation. Moreover, it also proved to work under harsh handling and difficult environmental conditions in mines. The following section aims at a verification of the results by comparing the new radar sensor with an ultra-sonic device developed for the same task.
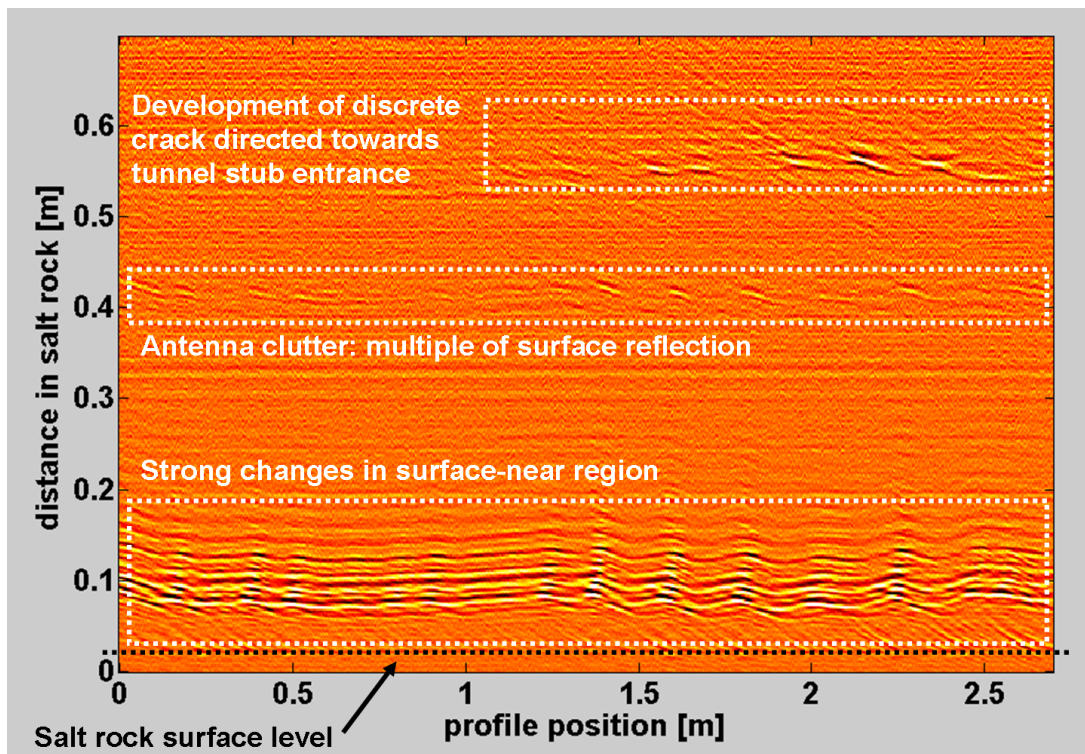
Fig. 6.20.: Interferometric comparison of datasets measured 48 h apart, pol. VV
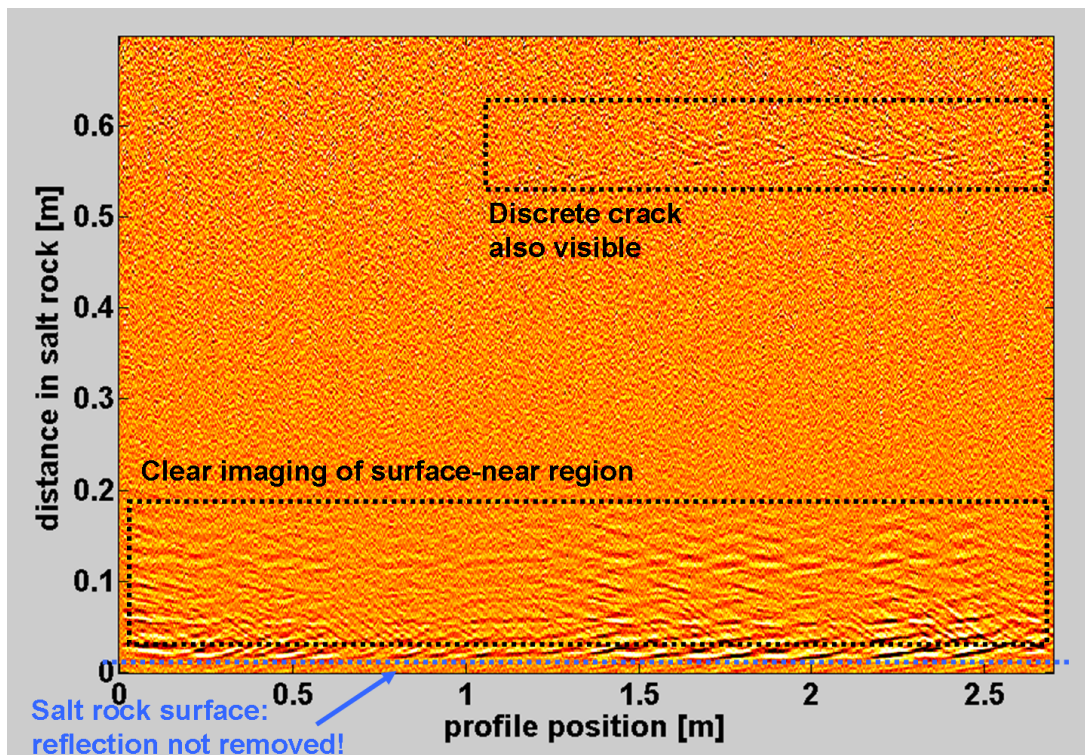
Fig. 6.21.: Fully processed dataset measured 54 h after tunnel creation, pol. HV

6.5. Comparison of UWB and ultrasonic sensor results

Despite the good agreement of the obtained radar results with geological expectations, especially for the old tunnel in Bernburg the actual state of disaggregation is not exactly known and a verification using ground truth was not possible. Increasing influence of noise evident in the data for larger distances inside the disaggregation zone show the sensitivity limits reached with the used setup and measurement speed. It is not easy to tell from radar data alone, whether most of the significant distortions could be detected or not. Comparison with measurement results using different approaches and sensors can be helpful in answering that question.

It has already been discussed in the introduction in chapter 1, that classical methods like gas-permeability measurements are not only destructive in their nature, but also do not provide such high-resolution information as obtained by the new M-Sequence sensor. Therefore, a comparison with another indirect wave based sensor solution shall be presented here to further judge the results. Parallel to the development of the UWB device, researchers at the Fraunhofer IZFP in Dresden developed an ultrasonic sensor for the same purpose in the framework of a partner project. Their sensor was also used to scan a profile near borehole BL2 in the old tunnel in Bernburg. Before doing a qualitative comparison of measurement results, some technical details and differences in the physical interaction with the disaggregation zone need to be mentioned.

6.5.1. Properties of ultrasonic prototype sensor for inspection of the disaggregation zone

The ultrasonic sensor is another technology for non-destructive testing and just like the radar approach employs an indirect measurement method based on wave propagation. It uses mechanical waves of high frequencies to excite the disaggregation zone and receives the backscattering from distortions inside the salt rock. The sensor developed at IZFP works in the broad frequency range from 50 kHz up to 400 kHz transmitting a directly synthesised pulse shaped Ricker-wavelet. Most of the stimulus energy is concentrated around 200 kHz. For sound frequencies that high, wave impedance of air and salt are so different, that almost all energy would be reflected at surface, i.e. the penetration of the sounding waves in the disaggregation zone would be insufficient. Coupling through the air interface is therefore not possible and the transmitter actuators as well as receivers must be pressed to the salt rock surface using a coupling material (usually gel pads) which seals the contacting areas against air gaps. This is also the first important difference to the UWB system. The ultrasonic sensor needs surface contact and scanning is therefore

much slower and more complicated. In fact, scanning one profile in Bernburg took several hours with the ultrasonic system rather than the 3 min for scanning with the radar sensor.

Mechanical wavelengths in salt rock range from about 45 mm (corresponding to 50 kHz) down to 6 mm (at 400 kHz). This is not very different from the M-Sequence sensor starting at about 120 mm (for 2 GHz lower cut-off according to the antennas) and going down to 9 mm (at 13 GHz). Resolution capability of both systems should therefore be similar with a small advantage for the ultrasonic device. More important than maximum spacial resolution is the fact, that for both sensors the wavelengths are much longer than the expected sizes of distortions in salt rock.

Nonetheless, physical conditions for wave scattering are very different. In the case of electromagnetic waves, scattering at a boundary between air/vacuum and salt rock depends on the rather low dielectric contrast. As explained in chapter 2, the reflection coefficient at a plane surface is only 42%. The contrast for sound waves at the same boundary is much higher. The ultrasonic waves are almost completely reflected and even thin air gaps of less than 1 mm cannot be passed by the stimulus. This has two main consequences. On one hand, sensitivity for air- or vacuum-filled distortions inside the salt rock is much higher for the ultrasonic sensor than for the radar device, i.e. backscattering at very small gaps or defects is stronger for the sound waves and can be easier detected. On the other hand, the ultrasonic system can hardly look even behind thin gaps since the waves do not penetrate through such a barrier. If there is a layered air-filled distortion, the sound waves might not be able to show further distortions behind that gap but the electromagnetic waves used by the M-Sequence sensor will do.

Looking at those principal differences, both sensors should show differences in the measurement results and should be used for suitable tasks matching their abilities. When starting both research projects, slightly different aims were already established and the two systems for non-destructive testing should finally complement each other. The biggest advantage of the radar sensor is its operation through the air interface enabling flexible and very fast scanning of long tunnel sections. It can also image thin gaps lying behind other gaps, etc. Due to limited sensitivity, it might not find all very small distortions and might underestimate the extension of the disaggregation zone. Consequently, the UWB system is perfectly suitable for pre-selection of tunnel sections where the distortions found by the sensor are minimal. The ultrasonic sensor on the contrary is suitable for a detailed analysis of selected tunnel sections. When radar data shows the absence of discrete or layered gaps or cracks, a few profiles can be measured by sound waves showing even smallest disaggregation due to the very high sensitivity. Using this two-stage approach, good areas for building sealing constructions can be found with acceptable effort and the extension of disaggregation can be measured with high confidence. Let us now take a look at data from both systems obtained in the old tunnel in Bernburg.

6.5.2. Ultrasonic and radar results for a reference profile in Bernburg

The scan along the circumference directly at borehole BL2 of the old tunnel in Bernburg was chosen to be a reference profile and measured by both sensor approaches. The Fraunhofer IZFP in Dresden voluntarily provided the result of figure 6.22. The measured and fully processed data from our new M-Sequence radar and the new ultrasonic sensor are superimposed using different colour schemes for reflectivity. White, blue, yellow, and red colours denote increasing reflection amplitudes of ultrasonic waves while green tones show radar responses. Please note that only strong radar amplitudes well above the noise floor have been plotted into the figure. The processing of sonar data from the ultrasonic sensor is described in [130] and radar processing was according to section 6.2. Visualisation was realised at the IZFP putting the data in the correct spacial coordinates according to the shape of the real tunnel.

Image courtesy E. Schulze of Fraunhofer IZFP Dresden
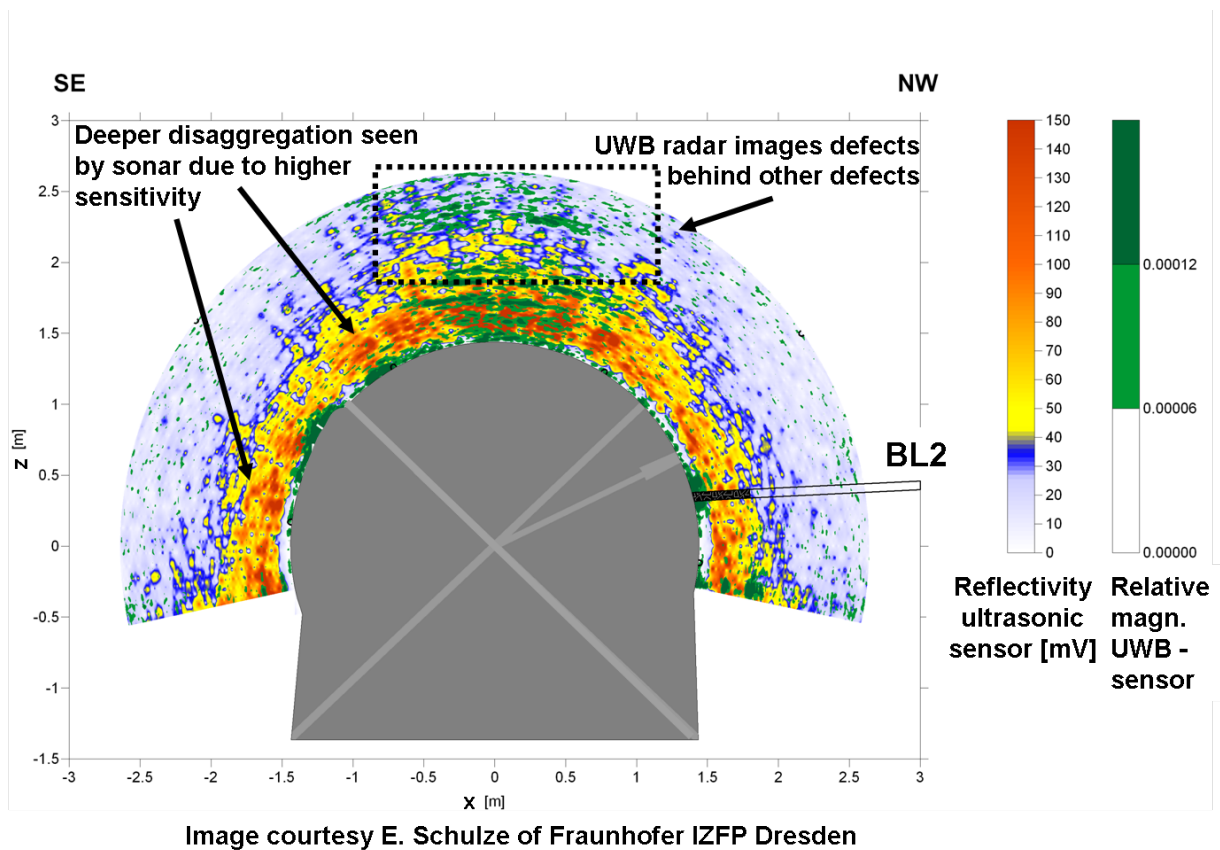
Fig. 6.22.: Comparison of fully processed radar and sonar data from the reference profile at BL2

At first glance, the results do not look very similar. If the technical and physical differences explained in subsection 6.5.1 are considered, good agreement with the theoretical expectations is evident. There are several important aspects to note. The first approximately 5 cm of salt rock cannot be reliably imaged by the ultrasonic sensor. The main

reason are strong surface waves travelling between transmitter and receiver along the salt rock surface. This clutter component is as problematic as the surface reflection for the radar sensor. With the current data processing, this region is a blind zone for the sonar sensor. Despite the artefacts remaining after surface reflection removal, better results are obtained by the radar sensor here.

Both sensors detect distortions all along the circumference and the concentration of defects is evident in the ceiling. Since only radar amplitudes well above the noise floor were included for clarity of the picture, green colour is concentrated in the first 20 cm behind the surface while the ultrasonic system could detect significant responses up to about 50 cm. Given the differences in sensitivity between both technologies, these results can be explained and the final extension of disaggregation in the sonar data agrees well with the geological situation.

Furthermore, both systems clearly show strong and deeper defects in the ground section caused by the shape distortion. Taking a closer look unveils that radar data suggests smaller but still discrete reflections around 1 m from the surface which are not visible in the sonar measurements. The explanation could be that larger cracks near the surface (evident with both sensors) somewhat block the ultrasonic stimulus from reaching behind them. The electromagnetic waves used by the new M-Sequence radar do not suffer from such effects and the sensor is able to image those defects behind other distortions. The situation is even more pronounced in the ceiling region. Data from both systems show strong and partly layered reflectors up to 50 cm, but only the radar sensor detected reliably further responses from layered structures around 1 m inside the rock. Again, the mechanical waves seemed to have difficulties reaching through the first distortions here.

These results emphasise the predicted strengths and weaknesses for both non-destructive testing methods and increase the confidence in the measurements, data processing, and finally data interpretation. The sensors have proven to be well suited for their respective tasks — tunnel pre-selection and detection of larger cracks behind other defects for the UWB radar on one side and a more detailed view into the extension of very small disaggregation provided by the ultrasonic system on the other side.

6.6. Summary of real-world measurements in salt mines

The new M-Sequence sensor has been used in several measurement campaigns in real salt mines for evaluation and prove of concept. To be able to do fast investigation of whole tunnel sections, test sites have been limited to cylindrical tunnels with a standard diametre of 3 m and a rather smooth surface. For these measurements, additional parts completing the setup needed to be implemented. These parts included a high resolution rotational

scanner, an antenna unit holding linearly polarised horn antennas RFSpin DRH20 in a fixed environment, and a carriage to move the whole system along the tunnel and to hold the control PC. All components were constructed according to the harsh conditions in salt mines.

Final measurement conditions influenced the development of a suitable data processing. The antennas were small enough to bring them close to the surface while scanning. However, placement of the rotational centre in the exact middle of the tunnels could not be guaranteed — the distance between antennas and salt rock surface varied by a few cm along a scan. The typical gap was between 5 cm and 10 cm. A slight inclination of 15° between the antennas and the surface helped to reduce the surface reflection. The antenna unit enabled fully polarimetric measurements. Antenna crosstalk and the surface reflection turned out to be major clutter components. The corresponding data processing is divided into three stages. The first pre-processing stage covers S-parameter calculation and coaxial calibration to remove systematic device clutter. The second stage aims at removal of the mentioned main clutter components. Antenna crosstalk is constant due to construction of the array. The reference waveforms were obtained at the lab in an anechoic chamber and can be subtracted from measured data when delay variations caused by the antennas cables are accounted for. To find the small delay differences between lab and mine, an algorithm for matching measured crosstalk with the reference functions has been developed. The algorithm uses an optimisation search based on the Nelder-Mead simplex method. The cost function for optimisation judges the amplitude differences between measured and reference data. The method has proven to obtain very good results in suppressing crosstalk. Surface reflection removal is a more complicated task but can be accomplished by a similar optimisation approach. The reference waveform must be calculated from measured data and slowly adopted while iterating over the impulse responses from a scan. Amplitude and delay are matched by means of the optimisation while shape variations are accounted for by exponential filtering with a low forgetting factor (usually 1% to 5%). The surface suppression achieved was satisfactory and remaining artefacts were small enough to not mask out most distortions very close to the surface.

The last processing stage is preparation of data and visualisation. To compensate the amplitude dependency of the received signals from target distance, a gain proportional to propagation time is applied to every impulse response. The gain is a degree of freedom which can be set by the operator to find a compromise between enhancing far responses and noise amplification. Finally, data can be shown in two different views. A 2D view for displaying single scan profiles with amplitudes in a colour code The second view is able to combine data from each profile acquired in a tunnel section. It uses 3D isosurfaces enclosing all regions with significant backscattering amplitudes. Measured data is associated with their real spacial coordinates (i.e. a polar coordinate system) to show where the responses approximately came from at the measurement site. The amplitude

threshold used to create the isosurfaces is another parameter which can be chosen by the operator. Values of 50% of the maximum emphasised mainly stronger scatterers near the surface and also discrete defects in the salt rock. Lowering the threshold unveiled weaker responses from disaggregation but also lead to stronger noise. Further image processing to enhance signal features such as variations of statistical properties has not yet been developed.

For evaluation of the developed UWB sensor, two main measurement campaigns have been conducted. One test site was an old inoperative tunnel in the mine of Bernburg. Because of its age and the former usage as a transportation facility, significant disaggregation was expected. The rails formerly present on the ground of the tunnel had been removed and the bottom section was additionally carved out disturbing the formerly round shape. Two sections of about 1 m length near two old boreholes have been measured in 5 cm steps. The processed results validated the functioning of the sensor and data processing - especially calibration and the new surface reflection removal technique proved to be effective. Along the whole circumference, responses from distortions were registered in the first 20 cm. Deeper defects have been detected in the bottom region at the boundary to the disturbed surface as expected. Especially the ceiling areas above the tunnel showed further reflections. They partly belonged to layered distortions appearing at different levels ranging from 30 cm to beyond 1 m behind the surface. The layered nature of these structures became very clear in the 3D visualisation of the disaggregation zone. This kind of view provides valuable insight into how the distortions are organised and connected. Doing fully polarimetric measurements did prove useful, too, but differences between the two co-polarisations HH and VV were not very large. A surface reflection removal was not necessary in the case of HV cross-polarisation, but overall backscattering amplitudes were very low. At the resulting SNR level, mainly the first 10 cm behind the surface showed HV responses. Nevertheless, potential to provide additional information was evident for cross-polarisation.

The reference profile at borehole BL2 has also been measured by researchers from the Fraunhofer IZFP in Dresden. They developed an alternative non-destructive testing sensor based on ultrasonic mechanical waves. Results from both sensors — radar and ultrasonic sonar — could be compared for verification purposes. Good qualitative agreement of the datasets was found. Both principles detected disaggregation all along the profile and a concentration of deeper responses in the ceiling and bottom region. However, there are some quantitative differences which fit very well with theoretical expectations. The sonar is surface-coupled (and thus slow) and much more sensitive due to material properties for sound waves. Despite a similar resolution capability of both sensors, responses from disaggregation are shown up to about 50 cm from the surface in sonar data. In the case of radar measurements most reflections are concentrated in the first 20 cm. Nevertheless, UWB radar data provides a better and clearer picture for the

first 5 cm behind the surface and it registered discrete reflectors from deeper inside the disaggregation zone especially in the ceiling and the ground regions. The new sensors consequently complement each other and should be used for different tasks — UWB for fast, non-contact scanning to enable pre-selection of tunnel sections and ultrasonic sonar for a better quantitative analysis of the extension of disaggregation zone.

The second main measurement campaign for verification of the new M-Sequence sensor has been conducted in the mine of Borth which is 900 m below ground. The salt rock there is known to show significant subsidence within the first hours after a new tunnel is cut. The mining company created a new 5 m deep tunnel stub and allowed to measure the formation of the disaggregation zone in this formerly undistorted mountain. Measurements took place from 6 h to 54 h after cutting of the stub. This time, a linear antenna scanner was used to scan a single 2.7 m track along the ceiling of the new tunnel. Measurements were taken every 2 cm and scanning of the track was repeated every hour. Data obtained at the beginning and the end of the measurements could be directly compared. The surface removal algorithm was modified in order to match surface reflections from different datasets. Analysis of the optimal shifting between the datasets resulted in a calculated subsidence of about 5 mm which took place during the two day observation period. Further interferometric analysis showed significant changes within the first 20 cm and the formation of a larger discrete crack about 50 cm away from the salt rock surface towards the entrance of the newly cut tunnel stub. Higher artefact levels after surface removal has been observed for the scans and was attributed to higher surface roughness in Borth compared to the old tunnel in Bernburg. The cross-polarised datasets without surface reflection removal showed good insight into the distortions forming in the near-surface region.

Overall, the new M-Sequence sensor delivered very good performance and worked well in the harsh environment of salt mines. Results coincided with theoretical expectations and the device has proven to be useful for fast inspection of tunnel sections. Despite the still unused potential of further data analysis, the implemented processing scheme provided interesting insight in the structure of disaggregation zones. It is now time to sum up development and application of the presented 12 GHz bandwidth M-Sequence sensor and to discuss possible aspects for future work.

7. Summary and outlook

After the extensive discussion of a complex research topic in the previous chapters, it is time to sum up the main achievements. At both the technical level and the application level the results only represent an intermediate stage and call for further development. Some ideas for future work will be listed and the thesis will be concluded with a general vision for M-Sequence sensors.

7.1. Summary of UWB sensor development for salt rock inspection

Using non-destructive testing methodologies is becoming more and more important and usual these days. The progress is driven by new sensor technologies and economical reasons in a large number of civil applications. Most of the time, avoiding damage to the test objects is a major advantage which saves cost and time. However, non-destructive testing is often based on indirect measurements and the quality of sensor output is often heavily influenced by data processing solving the inherent inverse problems. This gives rise to extensive scientific and engineering research in that area.

A typical example for NDTCE is the inspection of existing constructions of various kinds. One of the current problems many countries in Europe have to face is the long-term disposal of toxic waste, such as the one produced by nuclear power plants. Salt mines have been considered a good possibility to store problematic waste, since the salt rock has special properties helping to ensure long-term stability. A lot of empty space is available in salt mines throughout Germany, but when it is filled, also transportation facilities must be sealed with high reliability. This is where an interesting task for NDTCE emerges — inspection of the disaggregation zone in salt rock in order to detect possible leakage paths before a tunnel is closed.

The disaggregation zone is known to be comprised of small discrete defects in the salt crystals or distributed volume defects and usually extends up to about 0.5 m into the rock. Typical distortion sizes are in the mm and sub-mm range. Larger, discrete cracks may also exist near the surface, of course. Non-destructive sensors can help to assess the state of near-surface layers and finally select a suitable place to build sealing con-

structions. Among the different sensor principles, wave-based methods such as radar or sonar are prime candidates. The development of a sensor using very wideband electromagnetic waves has been introduced in this thesis. Requirements onto different sensor properties have been derived from test measurements, theoretical considerations, and side conditions associated with the task.

Investigation of electromagnetic wave propagation in salt rock has shown, that microwave frequencies up to 40 GHz can penetrate the material with moderate attenuation. It turned out that the band from near DC to 20 GHz should be preferred because it shows almost no attenuation in salt and allows easier hardware implementation. The relative permittivity of salt rock was found to be $\varepsilon_r \approx 6.0$ on average for the lower microwave frequencies and shows very low dispersion. Fresnel reflection and transmission coefficients for perpendicular incidence amount to $\Gamma \approx 0.42$ and $T \approx 0.91$, respectively.

Theoretical analyses of typical targets such as thin air-filled gaps or spherical volume defects showed that their backscattering favours high frequencies and steep signal slopes (requiring a large bandwidth). Thin gaps basically take the first derivative of the sounding wave form and the response is proportional to gap thickness. Individual small spherical defects reflect the second derivative of the stimulus and scale amplitude with their volume. This calls for an UWB sensor covering as much of the feasible frequency band below 20 GHz as possible.

Furthermore, the sensor needs to apply the stimulus via the air interface using antennas to enable fast scanning. This leads to another major challenge of sensor design: it must be able to detect weak responses from disaggregation despite the presence of the very strong surface reflection. For assessment of sensor performance in such a situation, the definition of a dynamic range applicable for UWB time domain signals has been introduced. $SFDR_{td}$ relates the amplitude of a strong signal event (such as the pulse of a surface reflection) to the maximum amplitude of any clutter present in the signal. Calculations for the measurement of thin gaps located 50 cm behind the surface showed, that $SFDR_{td} > 50 \, dB$ was needed to detect gaps of sub-mm thickness. Device imperfections are a major source of clutter for UWB sensors since the hardware cannot be build with even near-ideal behaviour for large bandwidths. Consequently, device calibration to suppress device clutter below 50 dB was another requirement defined for the new sensor.

The envisioned task defines further device properties. First of all, the device must be able to handle the harsh working environment in mines. It must be sealed to avoid ingress of the inevitable salt dust and must function precisely under very different environmental conditions. Furthermore, mining personell can not be expected to be experts in handling RF equipment, i.e. manual calibration and difficult device setup should be avoided. Thus, established laboratory equipment could not be used for the task. The last requirement is a fast scanning speed. The radar sensor was aimed for inspection of long tunnel sections to

allow pre-selection of suitable places where detailed analysis of the disaggregation zone may follow. This requirement again called for using antennas and non-contact scanning.

Among the known technical approaches for UWB sensors, only two principles provided the necessary stability and repeatability for successful calibration — vector network analysers and M-Sequence sensors. VNAs can be very precise, but are optimised for laboratory environments, very expensive, bulky, and their acquisition speed is slow due to sequential measurement of frequencies. Available M-Sequence sensors did not have sufficient bandwidth and calibration capabilities at the beginning of the development. However, they provided a good starting point due to their superior jitter performance and simple device construction.

For the salt mine task, a new M-Sequence sensor has been implemented. The stimulus bandwidth of the basic sensor only extended from DC to 4 GHz. It was shifted and broadened to finally reach coverage of 12 GHz bandwidth from 1 GHz to 13 GHz while still being fully synchronised to a single master clock $f_c = 9\,GHz$.

M-Sequence sensors use sub-sampling as most UWB devices do. Equivalent sampling rate of the principle is also f_c — not enough for capturing of the new stimulus. A mechanism for dense sub-sampling has been developed to increase the equivalent sampling rate by a factor of $r = 4$ to 36 GHz. The mechanism widely keeps the extremely stable regime of the original approach and introduces displacements of sample times smaller than the system clock period by means of a steerable phase shifter. It is controlled by a digital-to-analogue converter and does not provide completely uniform sampling out of the box. Data is gathered in a periodic non-uniform manner, but the phase shifter control can be calibrated to reach approximately uniform sampling. Analysis of required sampling time precision showed extreme demands for sampling of the system's UWB stimulus. For example, to ensure an $SFDR_{td}$ of 60 dB (i.e. the maximum amplitude error due to false sampling times stays below 60 dB with respect to full scale), sample times need to be precise to within about 20 fs. A calibration algorithm for sampling times has been invented to find correct phase shifter control values under different environmental conditions. It was estimated that the implemented solution is accurate enough to reach $SFDR_{td} = 60\,dB$ such that sampling can be assumed to be uniform with high confidence after phase shifter calibration.

To allow the use of efficient calibration algorithms for device clutter reduction, the sensor has been equipped with an S-parameter frontend providing two measurement ports and using four receivers to capture incoming and outgoing waves at both ports. The full matrix of S-parameters for a two-port — $\mathbf{S}_m$ — can be acquired allowing for fully polarimetric measurements when each port is connected to an antenna with different polarisation. A feasible level for calibration was the coaxial plane of the measurement ports. Since manual calibration is a sensitive task requiring special care by the operator, an automatic

calibration unit using mechanical RF switches was implemented instead. It connects the sensor to a number of calibration standards or the antennas, respectively.

A full two-port calibration using an 8-term method with unknown line standard has been selected as the most suitable algorithm for the new M-Sequence sensor. The S-parameter frontend allows using a generalised formulation for S-parameter measurement which removes major errors of the port switch. This enables the use of 8-term correction, which disregards some of the 16 error terms contained in the full calibration model. The neglected terms relate to switch errors and port crosstalk. The latter error could be reduced to more than 60 dB below full scale by device design. The calibration algorithm applies reflection correction using the 3-term method with OSL standards to either measurement port. It finally employs an unknown line standard to correct transmission. The only requirements on the line standard are reciprocity and an approximate knowledge of phase shift for frequencies of interest. This is very advantageous since the requirements can be easily fulfilled even under very different environmental conditions.

Another advantage of the selected 8-term algorithm is that it provides performance figures to assess the achieved quality at almost no additional cost. In a mine, device damage or accuracy problems can arise for various reasons and the operator can use these figures to check calibration before continuing with measurements. For every frequency of interest, 3-term correction needs inversion of a calibration matrix whose condition can be used as a performance indicator. If the conditions on-site differ too much from a lab reference, this could be a hint on device damage or other problems. Since the ports are treated separately, the operator might even get to know where the error source is located. Assessment of transmission correction is also possible. The transmission phase shift caused by the line standard is approximately known from lab characterisation. It is also calculated on-site during calibration and the actual values can be compared against the lab reference.

The achievable accuracy after calibration has been investigated, too. Drift of device characteristics (such as gain or signal delay) has been measured to be very low indeed. Within one hour, amplitude errors due to drifting turned out to be lower than 70 dB with respect to full scale. An hourly or even less frequent repetition of calibration therefore seems easily possible. The quality of the automatic calibration unit is influenced by the repeatability of its RF switches. The measurements also showed average deviations below 60 dB with occasional outliers of about 50 dB when the switches had been put under stress. Finally, a performance comparison regarding the $SFDR_{td}$ after calibration has been done between the new M-Sequence sensor and a Rohde & Schwarz ZVK network analyser. Both devices used the same 8-term correction, same methods for S-parameter calculation, and three different calibration kits. The basic values for $SFDR_{td}$ (judging strongest residual device clutter components), were comparable throughout all configurations for both reflection and transmission measurements, respectively. The implemented

calibration unit performed equally well like the two commercial counterparts — the manual Rohde & Schwarz ZV-Z34 kit and the automatic unit Rohde & Schwarz ZV-Z59. The VNA showed higher potential for further improvement due to a substantially lower clutter floor, but could not outperform the M-Sequence sensor with respect to strongest residual device clutter. The increased clutter floor in the M-Sequence device is partially caused by limited accuracy of sampling times in the dense sub-sampling scheme. Overall, both sensors reached an $SFDR_{td}$ in excess of 60 dB which is an excellent result given the ultra-wide bandwidth, device complexity, and simplicity of the 8-term method.

7.2. Summary of salt rock disaggregation measurement results

The M-Sequence sensor proved its laboratory performance to be effective in salt mines, too. On-site tests showed, that the antennas should be mounted in a fixed array shielded against reflections from the back and sides. This is to avoid clutter from the scanner construction and to be able to record an antenna crosstalk reference in the lab which can be used to process data collected in a mine. It also turned out, that the antennas should be placed as close to the surface as possible and that a slight inclination helps to reduce the surface response significantly without impacting backscattering from disaggregation behind it.

Major challenges of data processing are the removal of antenna crosstalk and surface reflection, which comprise the strongest signal components. Antenna crosstalk can be subtracted from every impulse response after calibration using a lab reference. To achieve good clutter suppression, the reference needs to be optimally shifted to match the measured data from the mine. This is ensured by a newly developed optimisation approach. The same approach forms the basis for effective removal of the surface reflection. It cannot be guaranteed that the distance between antennas and surface stays constant throughout a scan. However, similarity between neighbouring snapshots can be exploited by matching them with respect to delay and amplitude of the surface response. The shape of the reflection also varies slightly along a scan due to near-field conditions for the antennas. This is accounted for by a slow exponential adoption of the surface reference waveform while processing a scan. The proposed algorithm showed very good suppression of the main clutter components for different measurements in various mines. Two main measurement results are particularly noteworthy.

An old cylindrical tunnel in the mine of Bernburg has been measured using a rotational scanner with high angular resolution. The rails formerly present in that tunnel had been removed and the ground carved out. Due to this shape disturbance, strong disaggrega-

tion was expected for the lower part of the tunnel sides. Two 1 m long sections near old boreholes were scanned and fully processed to obtain 3D visualisations of the disaggregation zone behind the surface. The results showed interesting features and coincided very well with theoretical expectations. Distortion of the salt rock could be detected within the first 20 cm behind the surface along the whole circumference of the tunnel. Stronger responses appeared near the boreholes, in the lower areas where the tunnel was carved out, and in the ceiling region up to a distance of about 1 m from the surface. As evident especially from the processed 3D results, the responses from the ceiling belong to connected and layered distortions. All in all, the results gave interesting insight in the near-surface structure of the salt rock not accessible with traditional mine radars.

The second interesting result was obtained for a newly cut tunnel stub in the mine of Borth. It is about 900 m below ground. Ambient temperature in the mine was more than 30 °C which is very different from a laboratory and provided challenging environmental conditions. The salt rock in the mine is known to show strong subsidence right after a tunnel is cut. We were allowed to measure development of the disaggregation zone in the time interval between 6 h to 54 h after a new stub was cut by an AW4 miner. A linear scanner for acquisition of a 2.7 m long track along the ceiling of the stub was used for continuous observation. The algorithm for surface removal used for data from the old tunnel in Bernburg has been modified to estimate subsidence and to assess differences in the salt rock developing during the 48 h observation window. It could be calculated, that the distance between floor and ceiling decreased by about 4.8 mm during measurements and that the part of the stub which was cut last showed slightly more subsidence than the area where the miner started its work. Furthermore, significant changes in the first 20 cm behind the surface were demonstrated between datasets from the beginning and the end of measurements. A discrete crack farther away from the surface extending towards the entrance of the stub also changed its reflection behaviour. This strongly indicated a fast formation of a disaggregation zone and that the new M-Sequence sensor is able to detect such small differences.

In the datasets obtained from the older tunnel, co-polarisations HH and VV showed best results while the cross-polarised HV mode was dominated by noise after a few cm behind the surface. In the case of the new tunnel stub, HV data contained much more useful information and proved valuable to image the near-surface region without the need for any surface removal technique. Even the discrete crack at a distance of 50 cm could be identified in cross-polarisation.

To verify results from the M-Sequence sensor, a reference profile of the tunnel was compared to data from an ultrasonic sensor developed in a parallel research project by the Fraunhofer IZFP in Dresden. Their sensor is also wave-based, but uses mechanical instead of electromagnetic waves. There are significant differences in the interaction with disaggregation. Most notably, the ultrasonic wave sees a much higher contrast between

salt rock and air (or vacuum). In fact, such a boundary almost leads to total reflection and the sound wave barely penetrates gaps. I was therefore expected, that the sonar is much more sensitive to small volume defects than the radar sensor but might not be able to image defects behind other defects such as thin gaps. Comparison of data from both sensors showed very good agreement with these expectations. The sonar data showed near-surface responses deeper than the M-Sequence sensor. However, especially in the ceiling region it could not image the further away layered structures very well. The UWB sensor showed its advantage because it can easily overcome near-surface gaps and collect responses from behind them. Furthermore, the sonar requires air-sealed contact between its applicators and the salt rock surface, i.e. scanning is much slower than with the radar. A single scan by the M-Sequence device took only about 3 min, while the sonar needed several hours for the same task. In the end, both sensor conceptions proved to be valuable and to complement each other. The radar is perfect for fast pre-selection of tunnel sections. If a place was found where it cannot detect severe disaggregation, the ultrasonic sensor can be used to verify compactness of the near-surface salt rock layers.

In conclusion, the development of a 12 GHz bandwidth M-Sequence sensor with advanced calibration capabilities and a flexible antenna interface can be considered very successful. The implemented prototype showed excellent performance in the lab as well as in salt mines. It could be shown, that the measurement principle can be used to assess the disaggregation zone in salt rock and that the UWB sensor is able to deliver information in much greater detail than seen before. Still, the described research and its results can be seen as an extensive feasibility study calling for further development in many areas. The achieved state can be regarded as a promising starting point for future improvements. The following sections 7.4 and 7.5 name a few examples.

7.3. Contributions to the state of the art

The contributions of this work to the state of the art shall be mentioned here briefly. There are two main areas — ultra-wideband sensor design and development on one hand and investigation of salt rock disaggregation on the other hand.

In ultra-wideband sensor design, different extensions of the existing M-Sequence principle have been investigated, implemented and tested. Through the development of a transmitter module, the stimulus bandwidth has been increased form 4 GHz in the basic concept to 12 GHz by using the baseband and an up-converted band together. The M-Sequence transmitter has been combined with a new receiver concept using software-defined 4x dense sub-sampling to allow direct acquisition of the whole stimulus bandwidth. The dense sub-sampling realises an increase in equivalent sampling rate and does a-priori not ensure equidistant sampling times. A novel calibration method to correct

sampling times by means of an optimisation and test measurements has been developed. Two optimisation algorithms have been implemented and tested - a modified Nelder/Mead simplex search as well as optimisation by iterative approximation which is an own development. Furthermore, an S-parameter frontend for ultra-wideband time domain measurements has been designed. This frontend allows the use of the new M-Sequence sensor like a two-port time domain network analyser. For example, the measurement ports allow acquisition of fully polarimetric datasets. As an important contribution, full one-port (3-term) and two-port (8-term) coaxial calibration techniques have been adopted and applied to the new sensor. Calibration was automated with a calibration unit containing all necessary standards. Calibration effectiveness has been shown in a comparison with a network analyser. To allow fast and on-site assessment of calibration success, quality measures for reflection (condition of calibration matrix) and transmission calibration (phase deviation of line standard) have been introduced and it has been shown, how they can be used and interpreted. To allow judgement of calibrated results for ultra-wideband impulse responses as opposed to frequency domain data, the new figure of merit $SFDR_{td}$ has been derived. It describes the ratio of a full scale pulse amplitude to the amplitude of the strongest unwanted pulse event (e.g. caused by residual device clutter).

Radar sensors in salt mines are not new in general, but in this work ultra-wideband sensors with more than 10 GHz bandwidth have been used for the first time. The new M-Sequence sensor was prepared to work under harsh mining conditions and was combined with an antenna scanner. Also for the first time, an ultra-wideband sensor has been used to assess the state of the disaggregation zone in salt rock. This has not been possible before due to the limited bandwidth of classical salt mine radars. The new sensor enables fully polarimetric measurements and was used together with a horn antenna array covering horizontal and vertical linear polarisations. Sections of cylindrical tunnels have been scanned and the acquired data has been processed to image the inside of the disaggregation zone. A corresponding data processing flow tailored to the application has been developed. To be able to image the layers very close to the surface, a special algorithm for surface reflection removal was designed and implemented. This algorithm is based on optimisation and tries to match surface reflection waveforms between neighbouring scan positions. Its effectiveness for the acquired datasets has been shown. For the first time a detailed and high resolution look into disaggregation zone of an old tunnel in the mien of Bernburg could be obtained showing thin layers and small distortions. A modified version of the surface removal algorithm was further developed to analyse data form a fresh tunnel stub in the mine of Borth just after its creation. Formation of a new disaggregation zone in Borth could be demonstrated as well as the subsidence during the first two days after cutting the stub. Finally, ultra-wideband results from Bernburg have been compared with data from ultra-sound measurements and the distinct advantages and disadvantages of both sensor types have been emphasised.

7.4. Aspects of further technical development

Potential and flexibility of the basic M-Sequence principle could be demonstrated by the development of the new 12 GHz bandwidth UWB sensor. The design of this prototype was driven by the demands of the intended application, but the concepts used to extend the original M-Sequence scheme are of a more general nature.

Despite the large bandwidth, the sensor does not cover a good portion of the frequency range below 20 GHz. On-waver characterisation of the employed RF chipset already showed potential for even more bandwidth. For example, the track&hold circuits in the sensor have a 3 dB input bandwidth up to 15 GHz and a recent generation [101,131,132] can capture signals well beyond that. Using higher master clock rates and integration of the mixer component for bandwidth extension with the M-Sequence generator have already been realised in new designs. This not only enables a broader bandwidth, but also promotes savings in cost, space, and energy consumption. A re-design of the device concept using these new-generation ICs will also enable production of the system in commercial numbers.

A very important result of the research was the increase in equivalent sampling rate. It largely keeps the superior stability of the original M-Sequence sampling scheme, but the actual equivalent sampling rate can now be software-defined (by adapting phase shifter control) as multiples of the master clock rate. The calibration procedure to ensure uniform sampling is readily applied to cases where $r \neq 4$. This allows great flexibility for specialised or prototype systems. Another aspect of future developments could be to incorporate dedicated digital hardware for dense sub-sampling into the core chipset. For small r, the synchronisation unit could be extended to switch between different delays making a sampling time calibration obsolete altogether.

Apart from the RF chipset itself, improvements of the supporting hardware would also promote better device performance. For example, the real sampling rate of the sensor is currently limited by the digital backend. If the rate was increased, measurement speed or alternatively SNR would improve. Quality of the S-parameter frontend is mainly defined by the port switch and the directional couplers, which could be replaced with more recent, better components or might even be integrated into the transmitter or receiver ICs, respectively. The automatic calibration unit is another major candidate for development. At least for devices employed in stable (and predictable) environmental conditions, using solid state switches to connect the calibration standards would be beneficial. These switches are smaller, require less power and do not age. With modern MEMS-based [133] micro-switches, calibration standards could even be realised on-chip.

The system concept using chained receivers basically depending only on one single master clock also enables the design of sensors with more than two measurement ports.

The 8-term calibration method can be extended to more than two ports in a straightforward manner as well.

Another interesting aspect would be to shift the calibration level towards the antennas. For directional antennas such as the double-ridged horns used in this case, a compact and consistent 3D description of their behaviour is unknown to the author to date. Alongside such a description, suitable and predictable standards need to be developed as well.

In conclusion it can be said, that the concepts demonstrated in the prototype call for further device integration. This would not only enable improvement of device properties (such as bandwidth, energy consumption, etc.), but also promote mass production and affordable price points. A high level of integration is a major factor for the commercial success of a sensor technology and the M-Sequence principle is ideally suited for this aspect [131, 134]. Like any other sensor using indirect measurements, the usability of the device and the quality of results not only depends on hardware — data processing is another major aspect. It will usually be application-specific and enable the use of one UWB sensor for many different tasks.

7.5. Outlook for UWB sensor application in salt mines

Despite the excellent results obtained in salt mines with the prototype system, the current state of development can only be seen as a prove-of-concept. Specialised data processing has been developed coping with suppression of strongest clutter components — antenna crosstalk and surface reflection. Especially the latter one is a complex issue. Current results were achieved with the antennas very close to a smooth surface — something that may not always be feasible for other types of salt mine tunnels. Surface suppression worked unexpectedly well but further investigation must be done to make sure it also works for other surface roughnesses. It can be expected that adoption to different surface conditions will be necessary. Another unresolved issue is the influence of infrastructure present in the disaggregation zone, e.g. supply cables, metallic fixtures, or stabilising anchors. For such investigations, numerous measurements in different mines with different tunnels seem inevitable. Such additional measurement campaigns could also be used to provide directions for additional data processing steps.

Currently, the data is shown just after surface reflection removal. The results already show evidence of disaggregation and even small defects could be detected near the surface. Gaps and layered defects were visible even quite far away at a distance of up to 1 m. However, results also show that noise starts to dominate quickly as the distance from the surface increases. It is not clear from the results, if distributed volume defects are really visible in the datasets. This becomes especially noticeable when comparing the

UWB results to measurements with the ultrasonic sensor from Fraunhofer IZFP Dresden. Due to wave propagation properties, their sensor has a big sensitivity advantage and consequently shows responses from deeper inside the disaggregation zone were the UWB sensor does not show noticeable events. It fairly possible that these areas have many very small defects which cannot be individually identified in the radar data. However, if the backscattering from such regions does not only contain noise it should be possible to visualise disaggregation in statistical properties of the recorded data. This idea is a good starting point for further development of data processing also using data from additional measurement campaigns.

Verification of sensor data has also been addressed in this thesis. Data from two different sensor types — sonar and radar — has been compared against each other and also against theoretical expectations. Even though very good agreement could be observed, both sensors are new technologies which need to be challenged against ground truth. This would mean to excavate the disaggregation zone at a test site where prior measurements have been done. Further comparison would be possible against classical methods such as gas-permeability measurements even though they may not give a high-resolution image of the disaggregation zone.

In a further attempt to verify the sensors, measurement of the newly cut tunnel was an important step. It is clear that in this case disaggregation must have developed in formerly compact salt rock. Indeed, differences between the beginning and the end of observation were evident in the data. An important question still remains — the investigation did not lead to quantitative sensitivity results, i.e. how small distortion can become before they are no longer detectable. Due to the different scattering nature of various types of defects, the relation between response amplitudes and size of the defect should be done separately. For example, it would be interesting to know if certain types of disaggregation leave characteristic signatures in the data. A detailed analysis of real-world results of known targets could be done to derive rules for quantitative assessment.

It is clear that there are a lot of aspects worth investigating with the new M-Sequence sensor in salt mines. Finally, such developments require the continued support of the mine companies which helped making the presented results possible. Since these companies are also prospective customers of the UWB sensor technology, it would also be interesting to discuss their needs and ideas. Radar is already an established security technology in mines nowadays. However, current systems are not suitable for inspection of the disaggregation zone. Nevertheless, it can be expected that the full potential of UWB technology can only be explored in a dialogue with mining staff using their experience with mine radar.

Last but not least it should be possible to transfer the experience gained in salt mines to the assessment of other building constructions as well. Modifications of the hardware

and data processing will for sure be necessary, if different materials are to be measured. But the developed M-Sequence sensor shows a great degree of flexibility which opens up many innovative applications.

7.6. A near-future vision: a new family of UWB sensors for your favourite application

The development presented in this thesis is centred around the inspection of disaggregation in salt mines. Still, the implemented sensor can easily be applied for other tasks. It can serve as a VNA replacement in a lab, it can be used as a time domain reflectometre, or can be deployed as a short range radar even under harsh environment conditions in the field. There are many possible civil applications currently investigated by the EMR Lab:

- impedance spectroscopy [56, 58, 135]
- medical sensors [1, 136, 137]
- person detection [136, 138, 139]
- detection of insects in old wood [131, 140, 141]
- inspection of sewage infrastructure [142, 143]
- stability observation of dykes [134]
- agricultural supervision [124, 125]
- etc.

A main goal of current developments is to pursue component integration to enable even smaller, cheaper, faster, and more accurate M-Sequence devices than currently available. The concepts demonstrated in the 12 GHz bandwidth prototype all have potential to make it into a compact and affordable sensor as outlined in section 7.4. A whole new family of UWB sensors could result — all based on the same core technology but with modules or options specific to their application.

In many activities using electromagnetic sensors, researchers either use established but non-optimised laboratory equipment or sometimes develop new sensor devices for their application. This is not always effective, since measurement setup (applicators, etc.) as well as data processing are of major concern for the applicability of a sensor principle to a given task. Quick prove-of-concept in a short project runtime are often not possible. Once sensor hardware is available in flexible integrated configurations at affordable prices, engineers and researchers can just use the established and mature technology and simply focus on their application. This kind of development can partly be observed

with network analysers. They are used for their flexibility and precision. However, besides the high costs these devices are rarely employed outside the laboratory — not to mention for repeated or even continuous on-site observation tasks. UWB sensors based on M-Sequences have the potential to cover the range from high precision laboratory equipment down to cheap throw-away-or-bury sensors for mass-deployment in the field. Even hand-held devices are possible when component integration further evolves. It may just be the right sensor for *your* application.

A. Algorithms for calibration of equivalent time uniform sampling

The new M-Sequence sensor uses sub-sampling to acquire all UWB signals. The equivalent sampling rate achievable by the timing mechanism of the basic M-Sequence concept equals the master clock rate f_c. While f_c is only 9 GHz in the new sensor, the covered bandwidth extends from 1 GHz to 13 GHz requiring an equivalent sampling rate of at least 26 GHz for alias-free digitising. The sampling timing has been extended to enable dense sub-sampling with a final rate of $f_{s,\mathrm{equiv}} = 36\ GHz$. This is achieved by introducing a steerable phase shifter for adjusting the sample time instants in fractions of the master clock period $T_0 = 1/f_C$. In total $r = 4$ different phase states need to be applied in order to achieve the intended 36 GHz rate. To ensure that the digital data is sampled in a uniform manner, incremental phase shift between all four cycles must be exactly 90° corresponding to a relative delay of $T_0/4$. Theoretical analysis has shown, that the precision of sampling times needs to be extremely high in order to keep amplitude errors at a negligible level. It is therefore not possible to do a phase shifter control calibration in the laboratory and use the results at test sites with different environmental conditions. On-site calibration after device warm-up is mandatory to achieve best accuracy. For practical reasons, the process should take at most a few minutes.

A calibration procedure for correct phase shifter control has been implemented by means of an optimisation search using a test signal and a corresponding cost function. Phase shifter control values obtained at the lab can serve as a good initial guess and the optimum combination is assumed to be found in the vicinity of these starting values. Out of the four necessary control values, r_1 is always fixed and represents the reference phase shift while the other values r_2, r_3, and r_4 are to be found during optimisation. The optimisation problem is consequently defined in a three-dimensional parameter space. Furthermore, the parameter space is discrete and limited since the phase shifter control voltage is obtained from a digital-to-analogue converter. The full 360° shift with respect to the master clock rate is covered with integer numbers from one to 8192.

During optimisation, a test signal is subsequently measured with the current control value combination. Quality of sampling timing is judged by means of a cost value derived from that data. In order to ensure sufficient SNR conditions, each test measurement

takes about 2 seconds, i.e. limiting the number of test measurements to 150 if 5 minutes is the maximum objective duration of the process. The following subsections describe the employed cost function as well as two investigated search algorithms not requiring a closed cost formulation.

A.1. Definition of cost function

The cost function is used to judge how uniform the sampling of a test signal is done with the current combination of phase shifter control values r_1 through r_4. The complete UWB stimulus generated by the transmitter module is used as a test signal and it is permanently connected to one of the receivers during the optimisation process. Figure A.1 shows the relative magnitude spectrum of the signal measured by a spectrum analyser. As indicated in the figure, the analogue signal does not contain much energy in frequencies above 14 GHz. With the intended equivalent sampling rate of 36 GHz, theoretically an alias-free spectrum up to 18 GHz can be captured. Under the assumption of uniform sampling, sampled data should mostly contain noise in the interval from 14 GHz to 18 GHz.
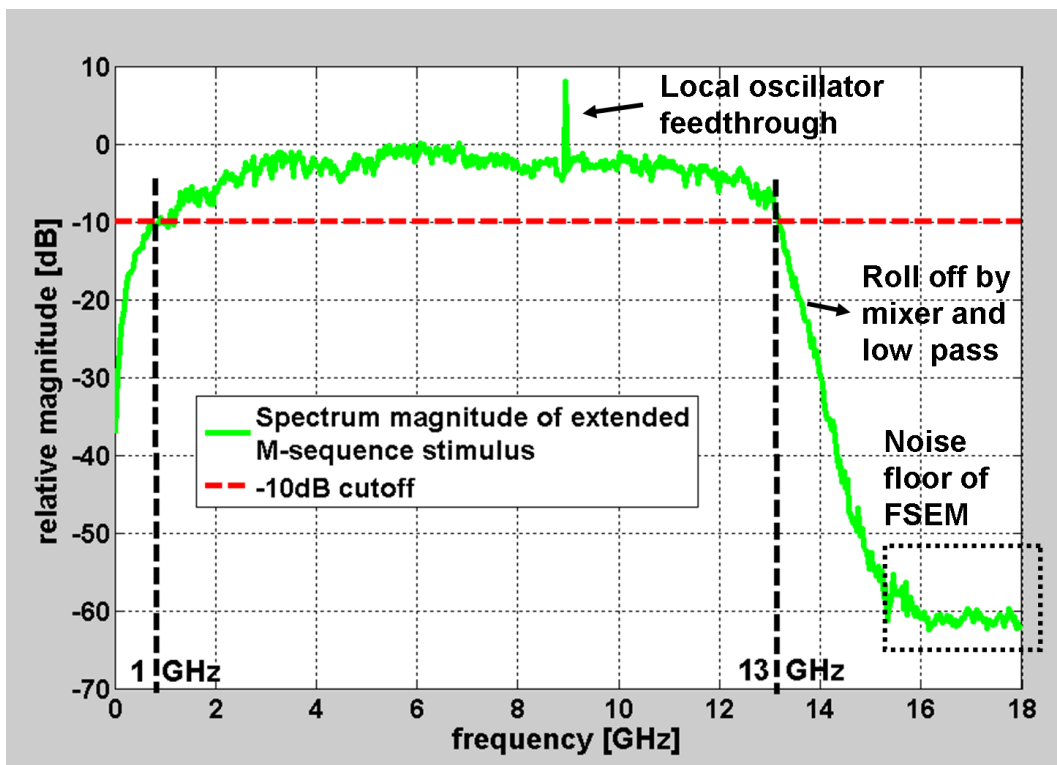

Fig. A.1.: Power spectrum of the test signal (extended M-Sequence stimulus)

If sampling timing was not correct, i.e. the phase shifter control values did not lead to equidistant time instants, images of the analogue spectrum would appear around all

harmonics of the master clock rate in digital domain [112, 113]. In such a case the digitised signal representation will have significant energy above 14 GHz even though there should be none. This behaviour is used for calculating a cost value for every measured test signal. The cost function could not be implemented as a closed-form equation, but rather as an algorithm using the discrete phase shifter control values. The algorithm is composed of three steps:

1. Apply phase shifter control values r_1, r_2, r_3, r_4 to the device

2. Measure the UWB test signal $t_{\mathrm{UWB}}(t)$ with current setup

3. Calculate the cost value $C_{\mathrm{UWB}}(r_1, r_2, r_3, r_4)$ from measured data

The first two steps are straight forward, but the last step holds some degree of freedom. Obviously, one must separate the frequency content between 14 GHz and 18 GHz in digital domain. This can be done by filtering or by application of a spectral window function after Fourier transform. However, there are different options to quantify, how much of the original spectrum has been leaked into the upper frequencies by non-ideal sampling times. When the phase shifter control values approach the optimal combination, even digitised data would be dominated by noise in the upper frequency range. Under such circumstances it is usually difficult to find a robust figure of merit from spectral power alone. To improve SNR conditions for the cost function calculation, the similarity between the unwanted signal image and the idealised sensor stimulus $uwb(t)$ as given in chapter 4 can be exploited. Once the frequency content below 14 GHz has been stripped from the data, correlation with the ideal signal is applied to suppress noise. The resulting image spectrum is transformed back into time domain and its envelope is analysed to finally obtain the cost value. Equations A.1 through A.5 describe the implementation. Figure A.2 shows how the correlated time domain shape of the false spectral image $c(t)$ looks like before and after optimisation.

$$uwb(t) = mlbs9(t) \cdot sin(2\pi f_c t) \tag{A.1}$$

$$\mathrm{UWB}(f) = \mathcal{F}\left\{uwb(t)\right\}^* \tag{A.2}$$

$$W(f) = \begin{cases} 1.0, & 14.0 \le f \le 18.0 \\ 0.0, & \text{otherwise} \end{cases} \tag{A.3}$$

$$c(t) = \mathcal{F}^{-1}\left\{\mathcal{F}\left\{t_{\mathrm{UWB}}(t)\right\} \cdot \mathrm{UWB}(f) \cdot W(f)\right\} \tag{A.4}$$

$$C_{\mathrm{UWB}}(r_1, r_2, r_3, r_4) = \left.|c(t)|\right|_p \tag{A.5}$$

In the equations, $\mathcal{F}$ and $\mathcal{F}^{-1}$ denote Fourier transform and inverse Fourier transform, respectively. Complex conjugate is written as * and $W(f)$ is a simple rectangular spectral window used to suppress all spectrum except the range from 14 GHz to 18 GHz. As can
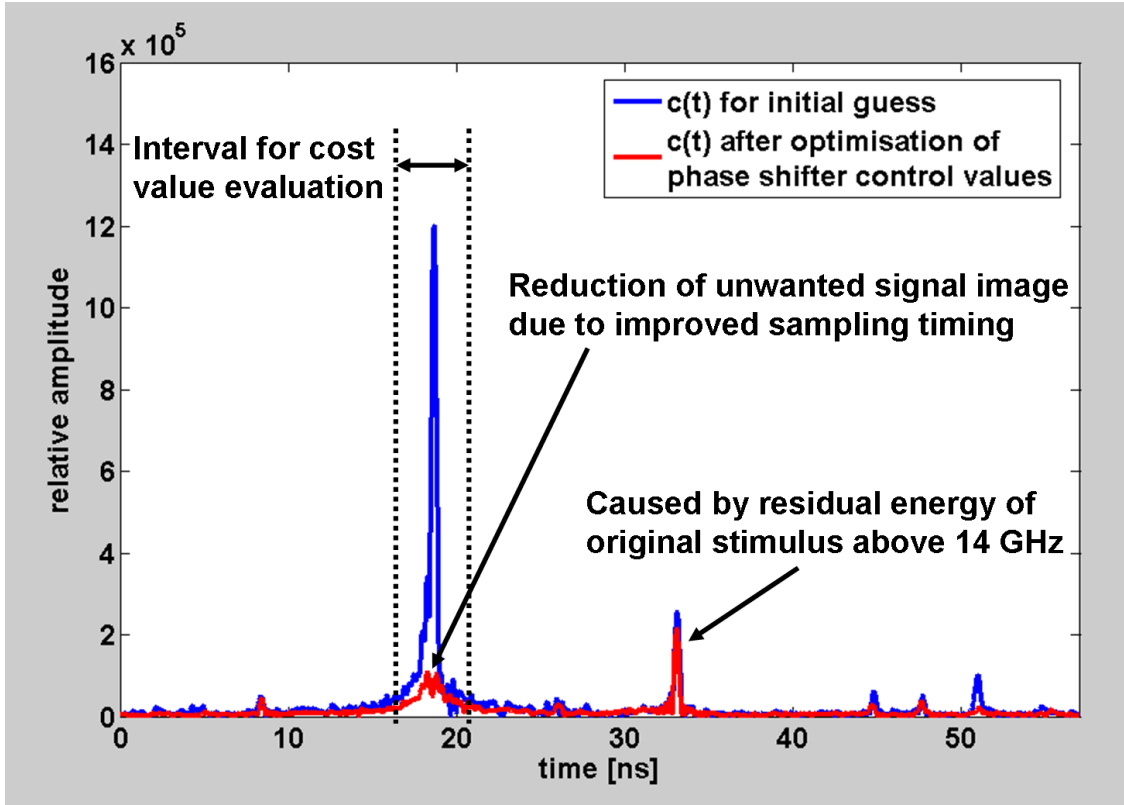
Fig. A.2.: Time domain shape of unwanted spectral image $c(t)$ used for cost analysis

be seen from figure A.2, $c(t)$ indeed shows a strong peak in the case of non-ideal control values and that this peak is greatly suppressed when using the optimal combination. Furthermore, there are additional peaks which do not change much when altering sampling timing. The second peak can be attributed to residual stimulus power in the analogue test signal above 14 GHz. Despite the fact, that no signal power is evident above 14 GHz in figure A.1, correlation with the idealised stimulus $uwb(t)$ unveils the presence of a small amount of stimulus in the noise.

In principal, every p-norm could be used to calculate the final cost value using equation A.5. In the actual sensor, the cost value equals the maximum amplitude within this interval, i.e. $p \rightarrow \infty$. Since only one of the peaks found in $c(t)$ is really sensitive to changes of control values r_i, it makes sense to restrict calculation of the norm to an interval around this main peak. Otherwise, the maximum value would fall to the second peak at some point and mislead the optimisation.

A.2. Nelder-Mead based optimum search

The first search algorithm considered was the Nelder-Mead simplex method fully described in [117]. It has some desirable features making it a good candidate for the problem of sample time calibration. Most notably, it is designed for N-dimensional optimisation and does not require a closed formulation of the cost function. It also uses no gradient information and is therefore suited for cost values derived by such algorithms as described in section A.1. Furthermore, investigation of its convergence behaviour in [118,119] showed, that it can deal with some amount of unsteadiness in the cost function and that it can also overcome local minima and find the global optimum. The algorithm describes a set of rules applied to a number of N-dimensional parameter vectors (called simplex) to approach the minimum cost value in a successive manner. The search is usually aborted, when the cost values for all current simplex are similar to within a user-defined threshold.

The original method is defined over a continuous and unbound parameter space. This is not the case here — all phase shifter control values r_i must be integer numbers between one and 8192. The algorithm has been modified to account for the discrete definition of optimisation parameters and also for a maximum search margin. As pointed out before, the optimal control value combination is expected in the vicinity of the initial guess where the cost function is well-behaved. To speed up the search (and lower the number of necessary cost function calls), each value r_2, r_3, and r_4 is only allowed to deviate within a margin of ± 32. Experimentation under different environmental conditions showed that this margin is large enough to find the optimum. These modifications have been realised in the cost function implementation by introduction of two additional preparation steps:

1.a Round input phase shifter control values r_1, r_2, r_3, r_4 to nearest integer: $\tilde{r}_1, \tilde{r}_2, \tilde{r}_3, \tilde{r}_4$

1.b Check if any value $\tilde{r}_i$ is outside the current margin; if so return a very high cost value which increases with distance from the margin

1.c Apply rounded phase shifter control values $\tilde{r}_1, \tilde{r}_2, \tilde{r}_3, \tilde{r}_4$ to the device

The other steps of the cost function calculation are done as described in section A.1. Step **1.b** ensures that the search procedure does not attempt to leave the allowed margin by delivering higher cost values as the parameters drift away from the intended interval.

The last modification is the use of an additional abort criterion for the search (besides the condition of similar cost values for all current simplex). If any two simplex are apart by 1 at most, i.e. $|\tilde{r}_{i,j} - \tilde{r}_{i,k}| \le 1 \forall i, j \ne k$, it means that the search has narrowed its scope to directly neighbouring combinations and the procedure can be aborted.

The modified Nelder-Mead simplex search has shown good convergence behaviour during laboratory tests with different (but high-quality) initial guess combinations. In a typical run, between 80 and 140 cost function calls were required to finish the procedure.

Even though each call requires a measurement of the test signal, the process could be finished in less than 5 minutes. However, there was no guarantee that this would hold for all conditions under which the sensor might be used, e.g. under extreme temperature differences to the lab. Further tests and analysis would have been necessary to fast-enough ensure convergence. Instead, a second search algorithm with a fixed number of test signal measurements has been developed.

A.3. Successive approximation search

To get an idea about the complexity of the cost function, an experiment has been done by evaluating the cost function for over 270,000 control value combinations around an initial guess. This experiment covered the usual interval $r_{i,\text{init}} - 32 \le r_i \le r_{i,\text{init}} + 32$ for all three control values r_2, r_3, and r_4 in a brute-force manner. Results have already been given in chapter 4 and will be repeated here for convenience. Figure A.3 shows a two-dimensional excerpt of the cost values obtained according to equation A.6.

$$\mathbf{C}_{2D}(r_3, r_4) = \min_{r_2} \mathbf{C}_{\text{full}}(r_2, r_3, r_4) \tag{A.6}$$
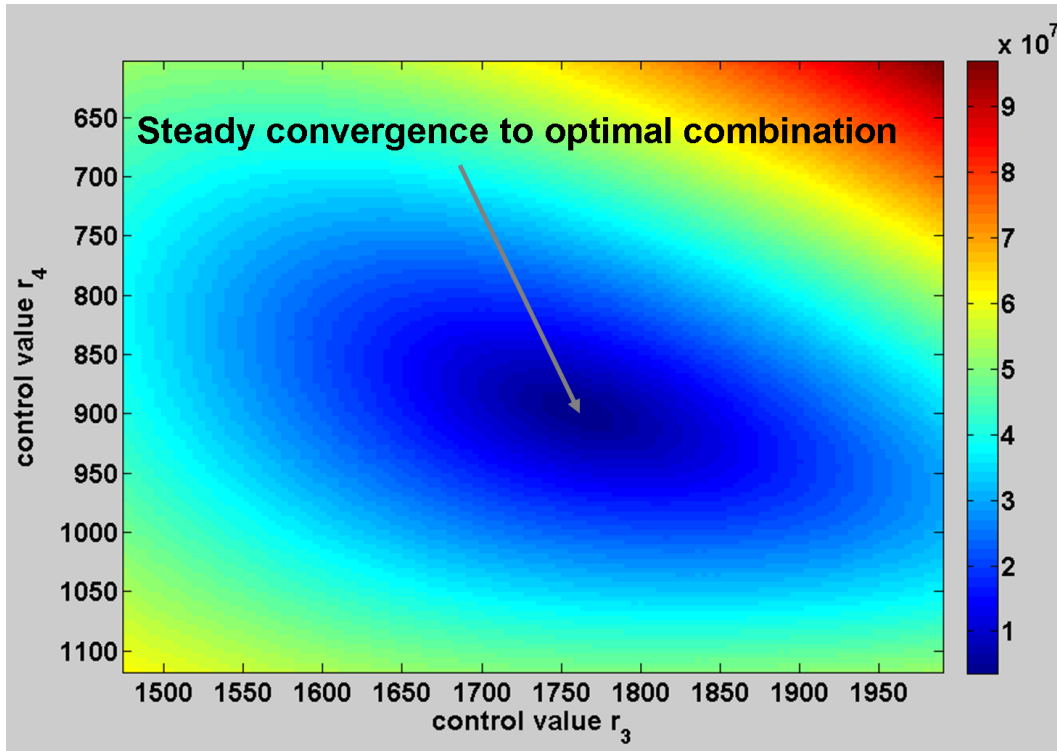

Fig. A.3.: Cost function value excerpt for variation of r_3 and r_4

Similar results were gained from minimising $\mathbf{C}_{\text{full}}(r_2, r_3, r_4)$ with respect to r_3 or r_4. The figure shows that no pronounced local minima exist near the optimal combination and the function appears to be monolithically decreasing when approaching the best cost value (this may not be true in the direct neighbourhood of the optimum, where noise influence on the cost value increases). For such a cost function behaviour, a search algorithm may approach the optimum in a successive manner by narrowing the search scope in iterative steps without getting trapped in a local minimum (provided the optimum falls within the expected intervals). This idea has been implemented for the new M-Sequence sensor.

A.3.1. Implementation and parameters of approximation search

For each iteration of the search, a current guess $r_{i,\text{cur}}$ and search margin m_{cur} must be provided. For every input parameter, only the three values $r_{i,\text{cur}} - m_{\text{cur}}$, $r_{i,\text{cur}}$, and $r_{i,\text{cur}} + m_{\text{cur}}$ need to be considered. Consequently, in one cycle $(3^{r-1} - 1)$ permutations of control values must be checked (assuming that the cost value for the current guess is known). The combination with the least cost value becomes the new current guess for the following iteration and the margin is narrowed. A sensitive choice for adjusting the margin is to use binary scaling, i.e. $m_{\text{cur},k+1} = m_{\text{cur},k}/2$. This ensures that the optimal combination can be any permutation within the initial margin regardless of how fast the cost function decays around the optimum, i.e. the search cannot accidentally jump over the optimum. Since the initial margin is $m_{\text{init}} = 32$, in total $S = ld(m_{\text{init}}) + 1 = 6$ iterations are required until the search process can be finished. The total number of cost function evaluations amounts to 157 according to equation A.7 with $r = 4$ and $S = 6$. The flow chart of the complete algorithm is given in figure A.4, which is derived from the common algorithm of figure 4.12 in chapter 4.

$$N_{cost} = S \cdot (3^{r-1} - 1) + 1 = (ld(m_{\text{init}}) + 1) \cdot (3^{r-1} - 1) + 1 \tag{A.7}$$

A.3.2. Reduction of number of test signal measurements

The total number of cost function evaluations is fixed for the introduced algorithm but doing them slightly exceeds the time limit of 5 minutes. However, the way dense sub-sampling is implemented in the sensor enables a significant reduction of necessary measurements. Each test vector is comprised of $r = 4$ sets of 511 samples interleaved to reconstruct the correct order of sampling times within the signal's period. There is no further mixing of data from different phase shifter control values in the samples that come out of the device. It is therefore possible to store the 511 samples associated with each single phase shifter control value in memory after the particular value first appeared. The data vector can be
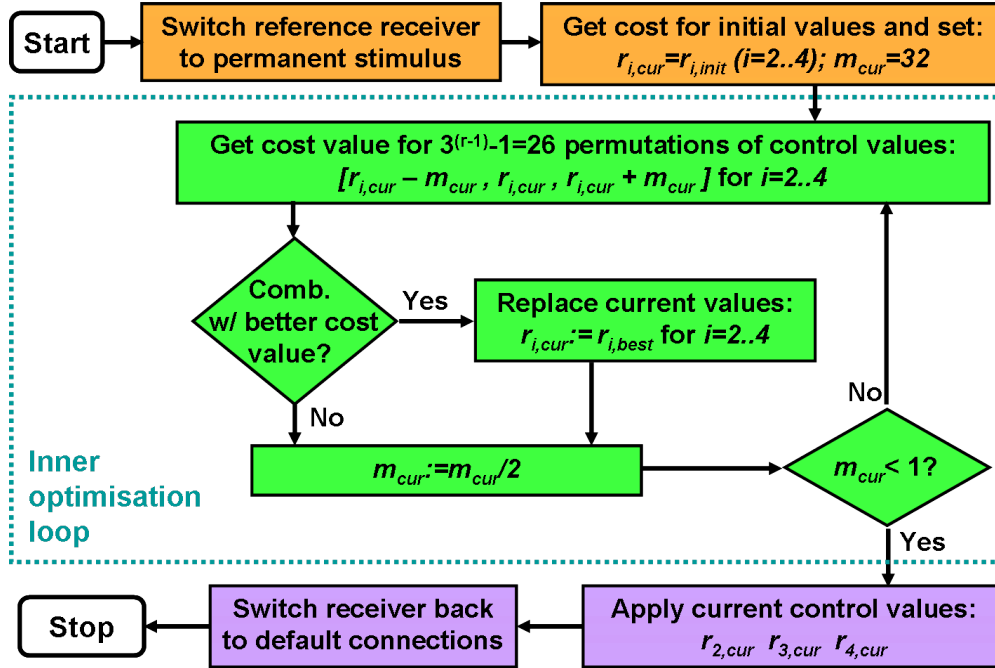
Fig. A.4.: Flow chart for optimisation of phase shifter control by successive approximation

reused for calculation of the cost function any time a phase control combination contains this value.

When the optimisation search is started, the cost function is evaluated for the initial guess. This delivers data vectors for the values $r_{i,\text{init}}; i = 1..4$ with one single measurement. In each iteration step of the inner optimisation loop, data for $r_{i,\text{cur}} \pm m_{\text{cur}}$ need to be acquired for $i = 2..4$ (since $r_1 = r_{1,\text{init}}$ stays fixed). After doing so, all $(3^{r-1} - 1)$ combinations can be calculated without any additional real measurement. Consequently, the number of necessary measurements reduces to equation A.8 (the number of cost function calls stays the same as in equation A.7). With an initial margin of $m_{\text{init}} = 32$ and $r = 4$, only 37 instead of 157 measurements are needed. The entire process is finished in a bit more than 1 minute with the optimised implementation.

$$N_{meas} = S \cdot 2(r - 1) + 1 = (ld(m_{\text{init}}) + 1)2(r - 1) + 1 \tag{A.8}$$

B. Summary of full two-port coaxial calibration for S-parameters

All UWB sensors spanning several GHz of bandwidth in the lower microwave range cannot be realised with ideal components regardless of their working principle. Common problems include frequency response of signal sources and amplifiers, limited directivity of directional couplers, and mismatch of wave impedance at component junctions (e.g. between coaxial RF cables). The system's impulse response functions (or equivalently frequency response functions) therefore contain systematic errors caused by these imperfections. Systematic errors are also called device clutter and can lead to false interpretation of measurement data. However, systematic means that they are repeatable, occur in a predictable manner, and can therefore be corrected or suppressed. The following sections summarise a basic calibration method developed for two-port S-parameter measurements and were mainly collected from [84], [96], and [123]. Some content is repeated here for convenience of the reader but also some additional explanatory notes will be provided.

Such calibration procedures are historically formulated in frequency domain, i.e. the algorithm needs to be applied for every frequency of interest separately. This does not limit the application to sensors working in frequency domain as long as Fourier transform and inverse Fourier transform can be used to switch between domains. Besides alias-free sampling, linearity of the receivers is an important requirement for the introduced method. Only systematic errors of linear nature can be corrected because superposition of different signal components is inherently assumed. Another requirement is an extremely stable device (e.g. low drift, low sampling time jitter, stable stimulus waveform) to ensure reproducibility of device clutter.

Under these conditions, the physical cause for individual errors does not need to be considered. All linear systematic errors of the real device can be summarised into a virtual passive error network, whose S-parameters contain all imperfections. In this sense, the real sensor is treated as a black box and is decomposed into an ideal measurement device (i.e. not producing any device clutter) and the virtual error network connecting the measurement ports of the ideal device with the ports of the real device. Figure B.1 shows the abstract system block diagram assumed for the two-port calibration method including

the decomposition. The test object (or device under test, DUT) is represented by its S-parameter matrix $\mathbf{S}$, which holds the wanted information. The device itself measures the (complex) wave quantities $\vec{a}_0$, $\vec{b}_0$, $\vec{a}_3$, and $\vec{b}_3$ representing the waves travelling out of and into the respective measurement ports of the ideal device. The aim of calibration is to obtain the S-parameters matrix $\mathbf{E}$ of the error network. Being a four-port network, $\mathbf{E}$ has 16 coefficients. Since the network is assumed to be passive, only 15 of them are linearly independent and the remaining coefficient can be used for normalisation. The 15 error terms are obtained through measurement of different DUTs with known behaviour (the calibration stamdards) and solving an inverse problem.
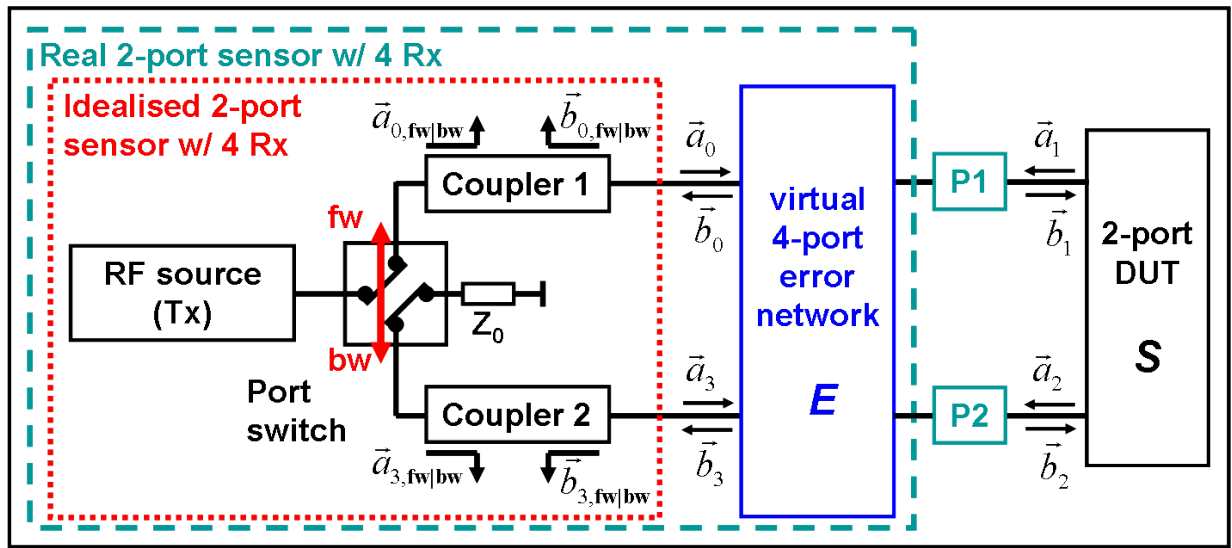
Fig. B.1.: Abstract system model for two-port calibration

As can be seen in figure B.1, the RF stimulus can only excite one of the measurement ports at a time. When the port switch is in so-called forward mode, it is directed to port P1 and the receivers acquire $\vec{a}_{0,\mathrm{fw}}$, $\vec{b}_{0,\mathrm{fw}}$, $\vec{a}_{3,\mathrm{fw}}$, and $\vec{b}_{3,\mathrm{fw}}$. In backward mode, the stimulus is switched to port P2 and $\vec{a}_{0,\mathrm{bw}}$, $\vec{b}_{0,\mathrm{bw}}$, $\vec{a}_{3,\mathrm{bw}}$, as well as $\vec{b}_{3,\mathrm{bw}}$ are gathered. With these two subsequent sets of measurement data, the sensor is able to calculate measured S-parameters $\mathbf{S}_m$ of the current DUT. These S-parameters are needed during the calibration process and later when correcting data from unknown test objects. There are two different ways of obtaining measured S-parameters which are discussed in the following section B.1. However, equation B.1 shows the principal relationship assuming all wave quantities are known. Equations B.2 and B.3 furthermore show the definition of S-parameters for the DUT and the virtual error network, respectively.

$$\begin{pmatrix} \vec{b}_0 \\ \vec{b}_3 \end{pmatrix} = \mathbf{S}_m \begin{pmatrix} \vec{a}_0 \\ \vec{a}_3 \end{pmatrix} = \begin{bmatrix} \underline{s}_{m,11} & \underline{s}_{m,12} \\ \underline{s}_{m,21} & \underline{s}_{m,22} \end{bmatrix} \begin{pmatrix} \vec{a}_0 \\ \vec{a}_3 \end{pmatrix} \tag{B.1}$$

$$\begin{pmatrix} \vec{a}_1 \\ \vec{a}_2 \end{pmatrix} = \mathbf{S} \begin{pmatrix} \vec{b}_1 \\ \vec{b}_2 \end{pmatrix} = \begin{bmatrix} \underline{s}_{11} & \underline{s}_{12} \\ \underline{s}_{21} & \underline{s}_{22} \end{bmatrix} \begin{pmatrix} \vec{b}_1 \\ \vec{b}_2 \end{pmatrix} \tag{B.2}$$

$$\begin{pmatrix} \vec{b}_0 \\ \vec{b}_3 \\ \vec{b}_1 \\ \vec{b}_2 \end{pmatrix} = \mathbf{E} \begin{pmatrix} \vec{a}_0 \\ \vec{a}_3 \\ \vec{a}_1 \\ \vec{a}_2 \end{pmatrix} = \begin{bmatrix} \mathbf{E}_1 & \mathbf{E}_2 \\ \hline \mathbf{E}_3 & \mathbf{E}_4 \end{bmatrix} \begin{pmatrix} \vec{a}_0 \\ \vec{a}_3 \\ \vec{a}_1 \\ \vec{a}_2 \end{pmatrix} = \begin{bmatrix} \underline{e}_{00} & \underline{e}_{03} & \underline{e}_{01} & \underline{e}_{02} \\ \underline{e}_{30} & \underline{e}_{33} & \underline{e}_{31} & \underline{e}_{32} \\ \hline \underline{e}_{10} & \underline{e}_{13} & \underline{e}_{11} & \underline{e}_{12} \\ \underline{e}_{20} & \underline{e}_{23} & \underline{e}_{21} & \underline{e}_{22} \end{bmatrix} \begin{pmatrix} \vec{a}_0 \\ \vec{a}_3 \\ \vec{a}_1 \\ \vec{a}_2 \end{pmatrix} \tag{B.3}$$

B.1. Calculation of measured S-parameters

Despite the compact definition of measured S-parameters in equation B.1, $\mathbf{S}_m$ cannot be acquired in a single step using the same stimulus. If both ports P1 and P2 were excited by the RF source at the same time, some of the measured waves (e.g. $\vec{a}_3$ and $\vec{b}_0$) would superimpose and could not be distinguished. This could be circumvented by using uncorrelated sources for both ports which is often impractical. As pointed out before, the port switch takes care of avoiding such situations and directs the stimulus to only one port at a time. With two subsequent measurements — one in forward mode and the other one in backward mode — $\mathbf{S}_m$ can be obtained. In the ideal case, $\vec{a}_3$ is zero in forward and $\vec{a}_0$ is zero in backward direction. It is then straight forward to calculate $\mathbf{S}_m$ as in equation B.4.

$$\mathbf{S}_m = \begin{bmatrix} \underline{s}_{m,11} & \underline{s}_{m,12} \\ \underline{s}_{m,21} & \underline{s}_{m,22} \end{bmatrix} = \begin{bmatrix} \dfrac{\vec{b}_{0,\mathbf{fw}}}{\vec{a}_{0,\mathbf{fw}}} & \dfrac{\vec{b}_{0,\mathbf{bw}}}{\vec{a}_{3,\mathbf{bw}}} \\[2ex] \dfrac{\vec{b}_{3,\mathbf{fw}}}{\vec{a}_{0,\mathbf{fw}}} & \dfrac{\vec{b}_{3,\mathbf{bw}}}{\vec{a}_{3,\mathbf{bw}}} \end{bmatrix} \tag{B.4}$$

In this case, the quantities $\vec{a}_{3,\mathbf{fw}}$ and $\vec{a}_{0,\mathbf{bw}}$ are measured but not used. Unfortunately, real port switches do not behave ideally. They have limited port isolation and termination of the unused port is not perfectly matched to the reference wave impedance Z_0. If a calibration for the full error network $\mathbf{E}$ with its 15 linearly independent error terms is applied, the switch errors are absorbed into the virtual error network and do not need to be treated separately. On the contrary, there are a number of calibration methods using only a subset of the error terms. They might neglect some of the coefficients in $\mathbf{E}$ partly carrying switch imperfections. One example is the 8-term method introduced in chapter 5. For these algorithms, switch errors need to be physically very low or must be removed otherwise to ensure good calibration quality.

If the sensor device has four dedicated receivers on the switch side as shown in figure B.1, there is a different way to calculate measured S-parameters [84] incorporating the otherwise unattended waves $\vec{a}_{3,\text{fw}}$ and $\vec{a}_{0,\text{bw}}$. They mostly contain leakage of the stimulus into the unexcited port as well as reflections at the switch due to imperfect impedance matching. Measuring S-parameters can be generalised by considering forward and backward mode of the switch separately. Equations B.5 and B.6 show the general relationships between wave quantities and S-parameters in the respective modes. Since the test object stays the same regardless of switch state, $\mathbf{S}_m$ is also the same in both equations. When summarising the two equations as in B.7, the different formulation of B.8 for $\mathbf{S}_m$ can be found. Some devices (such as vector network analysers) are better capable of ratio measurements than directly acquiring the wave quantities. In this case, one should use the equivalent equation B.9 instead. Please note that the inversion of matrix $\mathbf{A}$ requires non-singularity, which is usually achieved in real measurements. However, noise influence could make the inversion unstable and lead to unreliable values for $\mathbf{S}_m$. In fact, if port isolation of the switch was zero (i.e. both ports are excited at the same time with the same stimulus), $\mathbf{A}$ would come close to singularity expect for the measurement noise. Consequently, the outcome would be merely random. This is another reason why only one port should be stimulated at a time.

$$
\begin{pmatrix} \vec{b}_{0,\text{fw}} \\ \vec{b}_{3,\text{fw}} \end{pmatrix} = \mathbf{S}_m \begin{pmatrix} \vec{a}_{0,\text{fw}} \\ \vec{a}_{3,\text{fw}} \end{pmatrix} = \begin{bmatrix} \underline{s}_{m,11} & \underline{s}_{m,12} \\ \underline{s}_{m,21} & \underline{s}_{m,22} \end{bmatrix} \begin{pmatrix} \vec{a}_{0,\text{fw}} \\ \vec{a}_{3,\text{fw}} \end{pmatrix} \tag{B.5}
$$

$$
\begin{pmatrix} \vec{b}_{0,\text{bw}} \\ \vec{b}_{3,\text{bw}} \end{pmatrix} = \mathbf{S}_m \begin{pmatrix} \vec{a}_{0,\text{bw}} \\ \vec{a}_{3,\text{bw}} \end{pmatrix} \tag{B.6}
$$

$$
\begin{bmatrix} \vec{b}_{0,\text{fw}} & \vec{b}_{0,\text{bw}} \\ \vec{b}_{3,\text{fw}} & \vec{b}_{3,\text{bw}} \end{bmatrix} = \mathbf{B} = \mathbf{S}_m \begin{bmatrix} \vec{a}_{0,\text{fw}} & \vec{a}_{0,\text{bw}} \\ \vec{a}_{3,\text{fw}} & \vec{a}_{3,\text{bw}} \end{bmatrix} = \mathbf{S}_m \mathbf{A} \tag{B.7}
$$

$$
\begin{aligned}
\mathbf{S}_m = \mathbf{B}\mathbf{A}^{-1} &= \begin{bmatrix} \vec{b}_{0,\text{fw}} & \vec{b}_{0,\text{bw}} \\ \vec{b}_{3,\text{fw}} & \vec{b}_{3,\text{bw}} \end{bmatrix} \begin{bmatrix} \vec{a}_{0,\text{fw}} & \vec{a}_{0,\text{bw}} \\ \vec{a}_{3,\text{fw}} & \vec{a}_{3,\text{bw}} \end{bmatrix}^{-1} \\
&= \frac{1}{\vec{a}_{0,\text{fw}}\vec{a}_{3,\text{bw}} - \vec{a}_{0,\text{bw}}\vec{a}_{3,\text{fw}}} \begin{bmatrix} \vec{b}_{0,\text{fw}}\vec{a}_{3,\text{bw}} - \vec{b}_{0,\text{bw}}\vec{a}_{3,\text{fw}} & \vec{b}_{0,\text{bw}}\vec{a}_{0,\text{fw}} - \vec{b}_{0,\text{fw}}\vec{a}_{0,\text{bw}} \\ \vec{b}_{3,\text{fw}}\vec{a}_{3,\text{bw}} - \vec{b}_{3,\text{bw}}\vec{a}_{3,\text{fw}} & \vec{b}_{3,\text{bw}}\vec{a}_{0,\text{fw}} - \vec{b}_{3,\text{fw}}\vec{a}_{0,\text{bw}} \end{bmatrix}
\end{aligned} \tag{B.8}
$$

$$
\mathbf{S}_m = \frac{1}{1 - \frac{\vec{a}_{3,\text{fw}}}{\vec{a}_{0,\text{fw}}}\frac{\vec{a}_{0,\text{bw}}}{\vec{a}_{3,\text{bw}}}} \begin{bmatrix} \frac{\vec{b}_{0,\text{fw}}}{\vec{a}_{0,\text{fw}}} - \frac{\vec{b}_{0,\text{bw}}}{\vec{a}_{3,\text{bw}}}\frac{\vec{a}_{3,\text{fw}}}{\vec{a}_{0,\text{fw}}} & \frac{\vec{b}_{0,\text{bw}}}{\vec{a}_{3,\text{bw}}} - \frac{\vec{b}_{0,\text{fw}}}{\vec{a}_{0,\text{fw}}}\frac{\vec{a}_{0,\text{bw}}}{\vec{a}_{3,\text{bw}}} \\ \frac{\vec{b}_{3,\text{fw}}}{\vec{a}_{0,\text{fw}}} - \frac{\vec{b}_{3,\text{bw}}}{\vec{a}_{3,\text{bw}}}\frac{\vec{a}_{3,\text{fw}}}{\vec{a}_{0,\text{fw}}} & \frac{\vec{b}_{3,\text{bw}}}{\vec{a}_{3,\text{bw}}} - \frac{\vec{b}_{3,\text{fw}}}{\vec{a}_{0,\text{fw}}}\frac{\vec{a}_{0,\text{bw}}}{\vec{a}_{3,\text{bw}}} \end{bmatrix} \tag{B.9}
$$

B.2. Two-port calibration using all 16 error terms

In the most general case, all coefficients of the error network $\mathbf{E}$ must be obtained during calibration. Since the network is assumed to be passive, only 15 error terms are linearly independent and the 16th term can be used for normalisation, i.e. it can be set to 1.0. While theoretically any of the coefficients can be used for that purpose, it makes sense to chose one that will be close to 1.0 anyway to avoid numerical instabilities and noise amplification. The basic procedure of obtaining error terms is to measure a number of calibration standards with known $\mathbf{S}$, develop a relationship between $\mathbf{S}_m$, $\mathbf{S}$, and $\mathbf{E}$ from equations B.1 through B.3, and finally solve for the coefficients $\underline{e}_{xy}$ by using the resulting system of independent equations.

Unfortunately, when using S-parameters to describe the error network, the system of equations turns out to be non-linear with respect to the $\underline{e}_{xy}$. However, the behaviour of the network can also be described be using T-parameters as in equation B.10. The error matrix $\mathbf{T}_{err}$ has 16 coefficients and can be divided into four submatrices $\mathbf{T}_1$ to $\mathbf{T}_4$ just like it was done for S-parameters in equation B.3 above. There is a mutual relationship between S- and T-parameters since both are equivalent descriptions of linear network behaviour. Equation B.11 shows the calculation of $\mathbf{T}_{err}$ from $\mathbf{E}$ as an example.

$$
\begin{pmatrix} \vec{b}_0 \\ \vec{b}_3 \\ \vec{a}_0 \\ \vec{a}_3 \end{pmatrix} = \mathbf{T}_{err} \begin{pmatrix} \vec{a}_1 \\ \vec{a}_2 \\ \vec{b}_1 \\ \vec{b}_2 \end{pmatrix} = \left[\begin{array}{c|c} \mathbf{T}_1 & \mathbf{T}_2 \\ \hline \mathbf{T}_3 & \mathbf{T}_4 \end{array} \right] \begin{pmatrix} \vec{a}_1 \\ \vec{a}_2 \\ \vec{b}_1 \\ \vec{b}_2 \end{pmatrix} = \left[\begin{array}{cc|cc} \underline{t}_0 & \underline{t}_1 & \underline{t}_4 & \underline{t}_5 \\ \underline{t}_2 & \underline{t}_3 & \underline{t}_6 & \underline{t}_6 \\ \hline \underline{t}_8 & \underline{t}_9 & \underline{t}_{12} & \underline{t}_{13} \\ \underline{t}_{10} & \underline{t}_{11} & \underline{t}_{14} & \underline{t}_{15} \end{array} \right] \begin{pmatrix} \vec{a}_1 \\ \vec{a}_2 \\ \vec{b}_1 \\ \vec{b}_2 \end{pmatrix} \quad \text{(B.10)}
$$

$$
\mathbf{T}_{err} = \left[\begin{array}{c|c} \mathbf{T}_1 & \mathbf{T}_2 \\ \hline \mathbf{T}_3 & \mathbf{T}_4 \end{array} \right] = \left[\begin{array}{c|c} \mathbf{E}_2 - \mathbf{E}_1 \mathbf{E}_3^{-1} \mathbf{E}_4 & \mathbf{E}_1 \mathbf{E}_3^{-1} \\ \hline -\mathbf{E}_3^{-1} \mathbf{E}_4 & \mathbf{E}_3^{-1} \end{array} \right] \quad \text{(B.11)}
$$

Splitting equation B.10 vertically and inserting equation B.2 leads to B.12 and B.13. Putting both together and using equation B.1 results in B.14, which can also be written as B.15 or B.16.

$$\begin{pmatrix} \vec{b}_0 \\ \vec{b}_3 \end{pmatrix} = \mathbf{T}_1 \begin{pmatrix} \vec{a}_1 \\ \vec{a}_2 \end{pmatrix} + \mathbf{T}_2 \begin{pmatrix} \vec{b}_1 \\ \vec{b}_2 \end{pmatrix} = (\mathbf{T}_1 \mathbf{S} + \mathbf{T}_2) \begin{pmatrix} \vec{b}_1 \\ \vec{b}_2 \end{pmatrix} \tag{B.12}$$

$$\begin{pmatrix} \vec{a}_0 \\ \vec{a}_3 \end{pmatrix} = \mathbf{T}_3 \begin{pmatrix} \vec{a}_1 \\ \vec{a}_2 \end{pmatrix} + \mathbf{T}_4 \begin{pmatrix} \vec{b}_1 \\ \vec{b}_2 \end{pmatrix} = (\mathbf{T}_3 \mathbf{S} + \mathbf{T}_4) \begin{pmatrix} \vec{b}_1 \\ \vec{b}_2 \end{pmatrix} \tag{B.13}$$

$$\mathbf{S}_m = (\mathbf{T}_1 \mathbf{S} + \mathbf{T}_2)(\mathbf{T}_3 \mathbf{S} + \mathbf{T}_4)^{-1} \tag{B.14}$$

$$\mathbf{S} = (\mathbf{T}_1 - \mathbf{S}_m \mathbf{T}_3)^{-1}(\mathbf{S}_m \mathbf{T}_4 - \mathbf{T}_2) \tag{B.15}$$

$$[\mathbf{0}] = (\mathbf{T}_1 \mathbf{S} + \mathbf{T}_2) - (\mathbf{S}_m \mathbf{T}_3 \mathbf{S} + \mathbf{S}_m \mathbf{T}_4) \tag{B.16}$$

During calibration, equation B.16 is of special importance. It represents a set of four equations, which are linear with respect to the error terms and only contain known entries from $\mathbf{S}$ as well as $\mathbf{S}_m$. Each of the four single equations holds information for 9 of the 16 coefficients. Expanding yields B.17. Again, one coefficient is used for normalisation and set to 1.0 (this is done for a term whose true value can be expected to be close to one, e.g. $\underline{t}_{12}$). The relation B.17 only provides four equations not sufficient to solve for all 15 remaining error terms. However, it can be reused for every calibration standard employed during the process. By using different standards, i.e. with different $\mathbf{S}$, enough independent equations can be obtained. A thorough discussion on possible combinations of one-port and two-port standards can be found in [96].

An interesting conclusion of [96] is that at least five different standards are needed to fully solve for all 15 error terms, i.e. each standard effectively only delivers three instead of four equations out of B.17 when putting all observations together. Moreover, the system B.17 can be solved by using SVD which allows to incorporate more than five standards. In such a case, the solution for the error terms is a least-squares fit to all test objects involved. Redundant observations may well lead to increased robustness of the results but in reality there are other issues than measurement noise which must be considered. In general, the knowledge of the ideal S-parameters of calibration standards in $\mathbf{S}$ has some degree of uncertainty. For narrowband calibrations, very precise determination of $\mathbf{S}$ may be possible for some types of standards (e.g. by modelling and simulation calculations), but accuracy usually degrades when a test object needs to be characterised over a large bandwidth. Another problem are environmental conditions. The electrical and mechanical length of a line standard depends on ambient temperature, for example, which should be reflected in its $\underline{s}_{21}$ coefficient for maximum accuracy. In conclusion it can be said, that standards with higher uncertainty regarding their true S-parameters should be avoided if possible. The other way round it might be beneficial in special cases to neglect some of the error terms in $\mathbf{T}_{err}$ and decrease the number of necessary standards. This is the idea of 8-term methods which are discussed in chapter 5 and the following section B.3.

$$
\mathbf{C} \begin{pmatrix} \underline{t}_0 \\ \underline{t}_1 \\ \underline{t}_2 \\ \underline{t}_3 \\ \underline{t}_4 \\ \underline{t}_5 \\ \underline{t}_6 \\ \underline{t}_7 \\ \underline{t}_8 \\ \underline{t}_9 \\ \underline{t}_{10} \\ \underline{t}_{11} \\ \underline{t}_{12} \\ \underline{t}_{13} \\ \underline{t}_{14} \\ \underline{t}_{15} \end{pmatrix} = \begin{bmatrix} \underline{s}_{11} & \underline{s}_{12} & 0 & 0 \\ \underline{s}_{21} & \underline{s}_{22} & 0 & 0 \\ 0 & 0 & \underline{s}_{11} & \underline{s}_{12} \\ 0 & 0 & \underline{s}_{21} & \underline{s}_{22} \\ 1 & 0 & 0 & 0 \\ 0 & 1 & 0 & 0 \\ 0 & 0 & 1 & 0 \\ 0 & 0 & 0 & 1 \\ -\underline{s}_{m,11}\underline{s}_{11} & -\underline{s}_{m,11}\underline{s}_{12} & -\underline{s}_{m,21}\underline{s}_{11} & -\underline{s}_{m,21}\underline{s}_{12} \\ -\underline{s}_{m,11}\underline{s}_{21} & -\underline{s}_{m,11}\underline{s}_{22} & -\underline{s}_{m,21}\underline{s}_{21} & -\underline{s}_{m,21}\underline{s}_{22} \\ -\underline{s}_{m,12}\underline{s}_{11} & -\underline{s}_{m,12}\underline{s}_{12} & -\underline{s}_{m,22}\underline{s}_{11} & -\underline{s}_{m,22}\underline{s}_{12} \\ -\underline{s}_{m,12}\underline{s}_{21} & -\underline{s}_{m,12}\underline{s}_{22} & -\underline{s}_{m,22}\underline{s}_{21} & -\underline{s}_{m,22}\underline{s}_{22} \\ -\underline{s}_{m,11} & 0 & -\underline{s}_{m,21} & 0 \\ 0 & -\underline{s}_{m,11} & 0 & -\underline{s}_{m,21} \\ -\underline{s}_{m,12} & 0 & -\underline{s}_{m,22} & 0 \\ 0 & -\underline{s}_{m,12} & 0 & -\underline{s}_{m,22} \end{bmatrix}^T \begin{pmatrix} \underline{t}_0 \\ \underline{t}_1 \\ \underline{t}_2 \\ \underline{t}_3 \\ \underline{t}_4 \\ \underline{t}_5 \\ \underline{t}_6 \\ \underline{t}_7 \\ \underline{t}_8 \\ \underline{t}_9 \\ \underline{t}_{10} \\ \underline{t}_{11} \\ \underline{t}_{12} \\ \underline{t}_{13} \\ \underline{t}_{14} \\ \underline{t}_{15} \end{pmatrix} = [\mathbf{0}] \qquad \text{(B.17)}
$$

Once all error terms are known, measured data from any subsequent test object can be corrected using equation B.15. It has already been mentioned in chapter 5, that sensors working in time domain need to take an extra step if one wishes to obtain calibrated impulse response functions. Correction is done in frequency domain and calculated for each frequency component of the covered bandwidth individually. Corrected S-parameters in $\mathbb{S}$ can be converted into time domain by using inverse Fourier transform. In contrast to sensors using a stepped or swept sine stimulus, most time domain systems do not provide the same amount of power for all frequencies. This is also true for the new M-Sequence sensor where the stimulus spectrum starts to decay below 2 GHz and above 12 GHz (compare figure 3.9 in section 3.3.1). Fewer stimulus power basically leads to worse SNR conditions for these frequencies and consequently obtaining error terms from SVD of equation B.17 as well as correcting measured data with equation B.15 become more and more dominated by noise. In order to obtain clean and usable impulse responses, one has to use noise shaping filters or windows prior to IDFT. These filters must suppress regions with low or no stimulus power. As described in [124] designing a suitable weighting function has some degree of freedom (namely in the phase of the complex weights) making it possible to optimise the time domain shape according to the needs of the application.

B.3. Reduction of the 16-term error model to 8 terms

For most modern UWB sensor devices, some a-priori assumptions about certain coefficients in $\mathbf{T}_{err}$ (or $\mathbf{E}$) can be made. For example, except for the port switch there are often no significant leakage paths between measurement ports. That means interaction between waves belonging to different ports is only caused by the test objects and do not occur inside the device. Errors associated with the switch can be removed before the actual calibration by using the technique introduced in section B.1. In [123] it is pointed out, that under high port isolation conditions observations of the corresponding error terms during calibration measurements suffer from very low SNR and are dominated by noise. In order to avoid noise amplification after data correction it is better to not correct for these coefficients. In fact, the magnitude of port crosstalk terms in $\mathbf{T}_{err}$ will be close to zero anyway. That is why one can safely set them to zero and thus reduce the number of unknown error terms. Figure B.2 shows diagrams illustrating the relationships expressed by equation B.10. The diagrams look similar to Mason graphs often used for S-parameters. However, they are different since the connections express energy transfer between wave quantities according to the associated T-parameters. The left side contains all 16 terms, which are used by the full algorithm of section B.2. The coefficients representing device-internal crosstalk are highlighted. If they are assumed to be zero, the model on the right side results forming the basis for all variants of 8-term correction. The error network is now represented by $\mathbf{T}_{8T}$ defined in equation B.18. Please note that the submatrices $\mathbf{T}_{i,8T}$ are now diagonal matrices which can be easily inverted. Just like in the 16-term case, $\underline{t}_{12}$ is commonly used for normalisation.

$$
\begin{pmatrix} \vec{b}_0 \\ \vec{b}_3 \\ \vec{a}_0 \\ \vec{a}_3 \end{pmatrix} = \mathbf{T}_{8T} \begin{pmatrix} \vec{a}_1 \\ \vec{a}_2 \\ \vec{b}_1 \\ \vec{b}_2 \end{pmatrix} = \left[\begin{array}{c|c} \mathbf{T}_{1,8T} & \mathbf{T}_{2,8T} \\ \hline \mathbf{T}_{3,8T} & \mathbf{T}_{4,8T} \end{array} \right] \begin{pmatrix} \vec{a}_1 \\ \vec{a}_2 \\ \vec{b}_1 \\ \vec{b}_2 \end{pmatrix} = \left[\begin{array}{cc|cc} \underline{t}_0 & 0 & \underline{t}_4 & 0 \\ 0 & \underline{t}_3 & 0 & \underline{t}_6 \\ \hline \underline{t}_8 & 0 & \underline{t}_{12} & 0 \\ 0 & \underline{t}_{11} & 0 & \underline{t}_{15} \end{array} \right] \begin{pmatrix} \vec{a}_1 \\ \vec{a}_2 \\ \vec{b}_1 \\ \vec{b}_2 \end{pmatrix} \quad \text{(B.18)}
$$

By neglecting the very small coefficients one not only avoids noise amplification during correction calculations but also reduces the number of unknowns to be obtained by measurement of standards. In principle, equation B.17 still holds and could be used to solve for $\mathbf{T}_{8T}$. However, this time less standards are needed and consequently there are less uncertainties in the ideal S-parameters as well. It is even possible to select calibration standards, which are not fully known. Numerous 8-term methods have been developed over recent years, for instance [84,95]. Each of them relies on different types of standards. Depending on the measurement task of the sensor and the intended frequency range of operation, the algorithms are tailored for test objects, which are either easy to manufacture or whose ideal S-parameters can be known with high confidence. In many cases, the
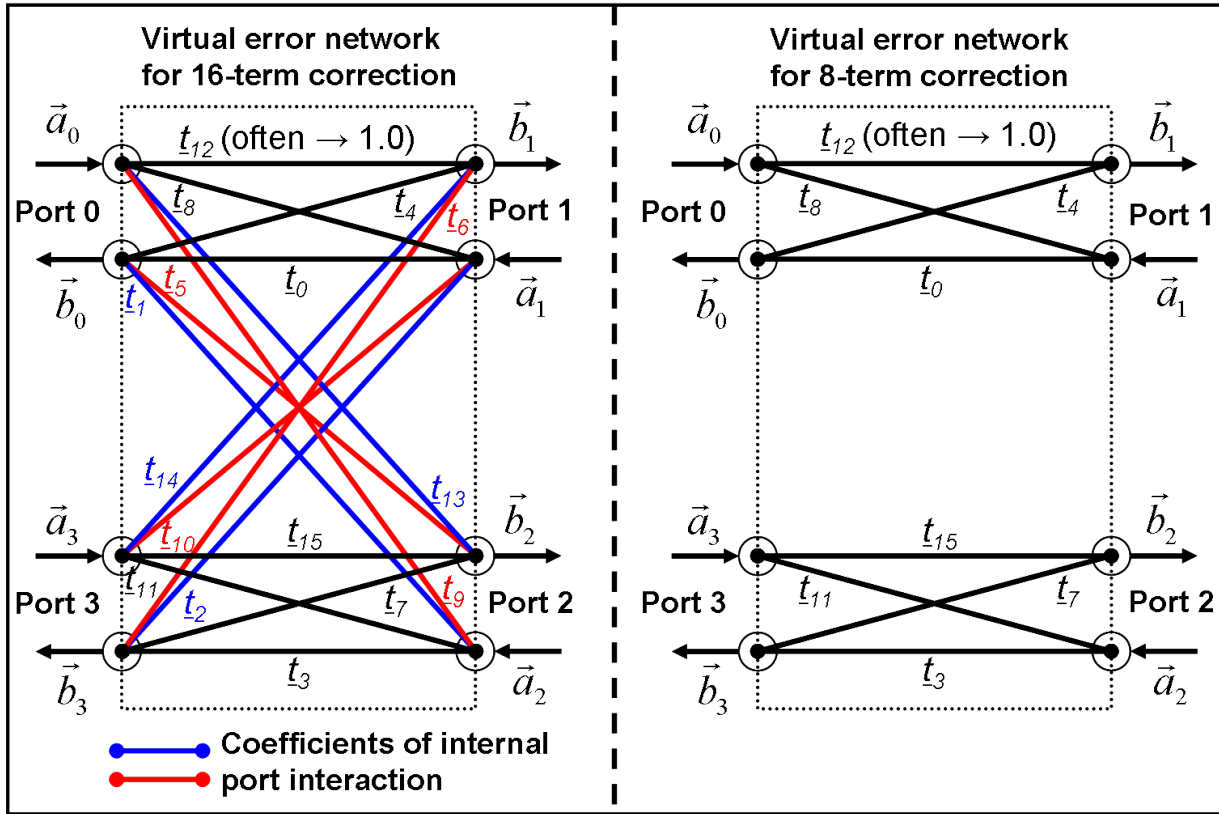
Fig. B.2.: Illustration of T-parameter error terms for 16-term and 8-term methods

error terms are not obtained by means of an SVD of equation B.17. Most 8-term methods use a stepwise approach solving for more and more coefficients each time an additional standard is measured. The adopted algorithm of the new M-Sequence sensor using an unknown transmission standard is no exception. It completes two separate 3-term corrections at each port and cares for transmission errors in a final step. The advantage of this implementation is that only reflection coefficients of one-port standards need to be exactly known. The transmission standard must simply be reciprocal — its S-parameters are not used during the process and can even be obtained during calibration.

Bibliography

[1]   HELBIG, M. ; HEIN, M.A. ; SCHWARZ, U. ; SACHS, J.: Preliminary Investigations of chest surface identification algorithms for breast cancer detection. In: *Proc. of International Conference on Ultra Wideband*, ICUWB, 2008 (Vol. 2), S. 195–198

[2]   BOND, E.J. ; XU, Li ; HAGNESS, S.C. ; VEEN, B.D. V.: Microwave imaging via space-time beamforming for early detection of breast cancer. In: *IEEE Transactions on Antennas and Propagation* 51, No. 8 (2003), Aug., S. 1690–1705

[3]   ALSHEHRI, S.A. ; KHATUN, S.: A confocal microwave imaging algorithm for breast cancer detection. In: *Progress In Electromagnetics Research C* 7 (2009), S. 79–93

[4]   RATCLIFFE, J.A. ; SACHS, J. ; CLOUDE, S. ; CRISP, G.N. ; SAHLI, H. ; PEYERL, P. ; PASQUALE, G. D.: Cost Effective Surface Penetrating Radar Device for Humanitarian Demining. In: *Proc. of EUROEM*, 2000

[5]   SAVELYEV, T.G. ; SATO, M.: UWB GPR target identification for landmine detection. In: *Proc. of Imaging Technology 7th International Symposium*, 2004 (Society of Exploration Geophysicists of Japan), S. 124–129

[6]   SAI, B. ; LIGTHART, L.: Improved GPR data preprocessing for detection of various land mines. In: *Proc. of 8th Conference on Ground Penetrating Radar*. Gold Coast Australia : GPR, May 2000

[7]   NAKASHIMA, Y. ; ZHOU, H. ; SATO, M.: Estimation of groundwater level by GPR in an area with multiple ambiguous reflections. In: *Journal of Applied Geophysics* 47 (2001), S. 241–249

[8]   LUALDI, M. ; ZANZI, L. ; SOSIO, G.: A 3D GPR Survey Methodology for Archaeological Applications. In: *Proc. of 11th International Conference on Ground Penetrating Radar*. Columbus Ohio, USA : GPR, 2006

[9]   PORSANI, J.L. ; SAUCK, W.A. ; JUNIOR, A.O.S.: GPR for mapping fractures and as a guide for the extraction of ornamental granite from a quarry: A case study from southern Brazil. In: *Journal of Applied Geophysics* 58 (2006), Nr. 3, S. 177–187

[10] SOLT, R.H.: Migration by fourier transform. In: *Geophysics* 43 (1978), S. 23–48

[11] GAZDAG, J.: Wave equation migration with the phase-shift method. In: *Geophysics* 43 (1978)

[12] HERRMANN, R. ; SATO, M.: Image Reconstruction by a Ground-Based SAR System. In: *Proc. of IGARSS*. Seoul, Korea : IGARSS, 2005

[13] SATO, M. ; FENG, X.: GPR migration algorithm for landmines buried in inhomogeneous soil. In: *Proc. of IEEE Antennas and Propagation Int. Symposium*. Washington D.C., USA : IAP, 2005, S. 206–209

[14] HEIN, A.: *Processing of SAR data : fundamentals, signal processing, interferometry*. Berlin, Germany : Springer Verlag Berlin, 2004. – ISBN 3–540–05043–4

[15] BISCHOFF, W. ; BRAMANN, H.: *Westfälische Berggewerkschaftskasse Bochum: Das kleine Bergbaulexikon*. Bd. 7. Essen, Germany : Verlag Glückauf GmbH, 1988. – ISBN 3–7739–0501–7

[16] K+S AG, Germany: *Kali und Salz: Standorte Deutschland*. Info page: `http://www.k-plus-s.com/de/presse/datenundfakten/standorte/deutschland.html`, 2010

[17] GSES GMBH, Germany: *Erlebnisbergwerk 'Glück auf´ Sondershausen*. Info page: `http://www.erlebnisbergwerk.com`, 2010

[18] SÜDWESTDEUTSCHE SALZWERKE AG, Germany: *Salzabbau in den Bergwerken Heilbronn, Berchtesgaden und Bad Reichenhall*. Info page: `http://www.salzwerke.de`, 2010

[19] BFS: ERAM - Endlager für radioaktive Abfälle Morsleben / Bundesamtes für Strahlenschutz. Version: Dec. 2009. `http://www.bfs.de/de/endlager/morsleben.html/morsleben_artikel.html`. 2009. – Online-Information

[20] BFS: Einführung zum Standort Gorleben / Bundesamtes für Strahlenschutz. Version: Jun. 2009. `http://www.bfs.de/de/endlager/gorleben/einfuehrung.html`. 2009. – Online-Information

[21] BFS: Endlager Asse: ein Überblick / Bundesamtes für Strahlenschutz. Version: Oct. 2009. `http://www.endlager-asse.de/cln_135/DE/5_AsseService/B_Publikationen/_node.html`. 2009. – Presse-Publikation

[22] BFS: Endlager Schacht Konrad: Einführung / Bundesamtes für Strahlenschutz. Version: Oct. 2009. `http://www.endlager-konrad.de`. 2009. – Online-Publikation

[23] KECKE, H.J.: Grundlagenuntersuchungen zum Dickstoffverfahren mit chem.-/tox. Abfällen, insbesondere MVA-Filteraschen, im Salinar, FKZ: 02C04867 / Otto-von-Guericke-Universität Magdeburg. 2004. – BMBF research report

[24] DÜSTERLOH, U.: Modellversuche an axial gelochten Steinsalz-Großbohrkernen im Hinblick auf die Überprüfung und Erweiterung theoretischer Prognosemodelle zum Sicherheitsnachweis von Untertagedeponien, FKZ: 02C00922 / Technische Universität Clausthal - Institut für Bergbau. 1996. – BMBF research report

[25] BAAR, C.A.: *Applied salt-rock mechanics 1: the in-situ behavior of salt rocks*. New York, NY, USA : Elsevier/North-Holland Inc., 1977

[26] BFS: Konzeptionelle und sicherheitstechnische Fragen der Endlagerung radioaktiver Abfälle. Wirtsgesteine im Vergleich. / Bundesamtes für Strahlenschutz. Version: Nov. 2005. `http://www.bfs.de/de/endlager/publika/Synthesebericht_Endfassung.pdf`. 2005. –

Synthesebericht

[27] BMU: Zwischenlager für Wärme entwickelnde radioaktive Abfälle und bestrahlte Brennelemente in Deutschland / Bundesministerium für Umwelt, Naturschutz und Reaktorsicherheit. Version: Aug. 2008. `http://www.bmu.de/atomenergie_ver_und_entsorgung/ zwischenlagerung/zwischenlager_waerme_entwickelnde_radioaktive_abfaelle/doc/ 40313.php`. 2008. – Online-Information

[28] BMU: Zwischenlager für radioaktive Abfälle mit vernachlässigbarer Wärmeentwicklung / Bundesministerium für Umwelt, Naturschutz und Reaktorsicherheit. Version: Aug. 2008. `http://www.bmu.de/atomenergie_ver_und_entsorgung/zwischenlagerung/ zwischenlager_waerme_entwickelnde_radioaktive_abfaelle/doc/40313.php`. 2008. – Online-Information

[29] BMU: BMU - 2003 - 618: Untersuchungen zur Sicherheit von Endlagern für radioaktive Abfälle nach ihrem Verschluss / Bundesministerium für Umwelt, Naturschutz und Reaktorsicherheit. Version: 2003. `http://www.bmu.de/files/pdfs/allgemein/application/ pdf/schriftenreihe_rs618.pdf`. 2003. – Schriftenreihe Reaktorsicherheit und Strahlenschutz

[30] MARTENS, P.N.: Gegenüberstellung und Vergleichende Bewertung unterschiedlicher Konzepte zur Untertägigen Deponierung Chemisch/Toxischer Abfälle, FKZ: 02C01832 / Rheinisch-Westfälische Technische Hochschule Aachen. 1996. – BMBF research report

[31] GERHARDT, H.: Systemanalyse über die Nutzung untertägiger Hohlräume des Steinkohlen-, Erz-, Salz- und Kalkbergbaus zur umweltverträglichen Verbringung von Abfällen, FKZ: 02C0011 / Technische Universität Bergakademie Freiberg. 1996. – BMBF research report

[32] SITZ, P.: Entwicklung eines Grundkonzepts für langzeitstabile Streckenverschlussbauwerke im Salinar - Bau und Test eines Versuchsverschlussbauwerkes unter realen Bedingungen, FKZ: 02C0547 / Technische Universität Bergakademie Freiberg. 2002. – BMBF research report

[33] KUDLA, W. ; GRUNER, M.: Streckenverschlüsse: Konzepte und Materialien. In: *Proc. of 7th annual review for BMBF/BMWi research projects on toxic waste disposal*. Karlsruhe, Germany : Projektträger Forschungszentrum Karlsruhe WTE, May 2006

[34] KÜHNICKE, H.: Entwicklung und In-situ-Test akustischer Verfahren zur zerstörungsfreien Beurteilung von Auflockerungszonen im Salinar, FKZ: 02C0537 / Fraunhofer-Institut für zerstörungsfreie Prüfverfahren Institutsteil Dresden. 2002. – BMBF research report

[35] HÄFNER, F.: In-situ-Ermittlung von Strömungskennwerten natürlicher Salzgesteine in Auflockerungszonen gegenüber Gas und Salzlösungen unter den gegebenen Spannungsbedingungen im Gebirge, FKZ: 02C0527 / Technische Universität Bergakademie Freiberg. 2001. – BMBF research report

[36] KÜHNICKE, H.: Inverse Methoden der Schallemissionsanalyse zur Quantitativen Bestimmung von Auflockerungszonen in Untertagedeponien, insbesondere der Lage, der Orientierung und der Größe von Rissen, FKZ: 02C01026 / Fraunhofer-Institut für zerstörungsfreie

Prüfverfahren Institutsteil Dresden. 1995. – BMBF research report

[37] UNTERBERGER, R.R.: Electromagnetic wave propagation in salt - probing into salt with radar. In: *Proc. of 4th International Salt Symposium*, 1974

[38] SATO, M. ; TAKESHITA, M. ; MIWA, T. ; NIITSUMA, H.: Polarimetric borehole radar applied to geological exploration. In: *Proc. 7th International Conference on Ground Penetrating Radar*. Lawrence, Kansas, USA : GPR, 1998, S. 7–12

[39] MALA GEOSCIENCE CORP., Sweden: *general information*. Company webpage: `http://www.malags.com`,

[40] GEOPHYSICAL SURVEY SYSTEMS INC., USA: *general information*. Company webpage: `http://www.geophysical.com`,

[41] PENETRADAR CORP., USA: *general information*. Company webpage: `http://www.geophysical.com`,

[42] GEOZONDAS LTD., Lithuania: *general information*. Company webpage: `http://www.geozondas.com`,

[43] UNTERBERGER, R.R.: Radar probing ahead of mining. In: *Proc. of 37th Meeting of the European Association of Exploration Geophysicists*. Bergen, Norway : EAEG, Jun. 1975

[44] BORATEC GMBH WEIMAR, Germany: *general information*. Company webpage: `http://www.boratec.net`,

[45] MALA GEOSCIENCE CORP., Sweden: *MALA Professional Explorer (ProEx) System*. Product page: `http://www.malags.com/Solutions/Products/Full-Range-Series/Professional-Explorer-ProEx-System.aspx`,

[46] SANDMEIER SCIENTIFC SOFTWARE, Germany: *REFLEXW - the GPR and seismic 2D processing and 2D/3D interpretation software*. Company webpage: `http://www.sandmeier-geo.de`,

[47] GEOPHYSICAL SURVEY SYSTEMS INC., USA: *Antennas for GSSI GPR sensors*. Product page: `http://www.geophysical.com/antennas.htm`,

[48] GEOPHYSICAL SURVEY SYSTEMS INC., USA: *Multi-channel GPR data acquisition unit SIR-20*. Product page: `http://www.geophysical.com/sir20.htm`,

[49] GEOZONDAZ LTD., Lithuania: *Pulse Generator Head GZ1117DN-25*. Product page: `http://www.geozondas.com/main_page.php?pusl=2`, Feb. 2009

[50] GEOZONDAZ LTD., Lithuania: *Precision Digital Sampling Converter SD203TM-18A*. Product page: `http://www.geozondas.com/main_page.php?pusl=3`, Feb. 2009

[51] NEZIROVIC, A.: *Trapped-Victim Detection in Post-Disaster Scenarios using Ultra-Wideband Radar*, Delft University of Technology: Faculty of Electrical Engineering, Mathematics and Computer Science, Diss., 2010

[52] TAKAHASHI, K.: *Detection and Localization of Subsurface Objects by Ground Penetrating Radar*, Tohoku University (Sendai, Japan): Center for Northeast Asian Studies, Diss., 2006

[53] ZHOU, Z.S. ; HAMASAKI, T. ; SATO, M.: Development of broadband ground-based polari-metric SAR systems for environment study. In: *Proc. of IEICE General conference*, 2003, S. SB–1–10

[54] SATO, M. ; ZENG, Z. ; FANG, G. ; FENG, X.: Stepped-frequency GPR system for Landmine detection. In: *Detection and remediation technologies for mines and minelike targets* VIII (2003), S. 179–184

[55] SATO, M. ; TAKAHASHI, K. ; FUJIWARA, J.: Development of the Hand held dual sensor ALIS and its evaluation. In: *Proc. of International Workshop on Advanced GPR*. Naples, Italy : IWAGPR, 2007

[56] SACHS, J. ; PEYERL, P. ; WÖCKEL, S. ; KMEC, M. ; HERRMANN, R. ; ZETIK, R.: Liquid and moisture sensing by ultra wideband pseudo-noise sequence signals. In: *Measurement Science and Technology* 14, 4th edition (2007), S. 1074–1087

[57] KMEC, M. ; SACHS, J. ; PEYERL, P. ; RAUSCHENBACH, P. ; THOMÄ, R. ; ZETIK, R.: A novel Ultra-Wideband real-time MIMO Channel Sounder Architecture. In: *XXVIIIth General Assembly of URSI*. New Delhi, India : URSI, Oct. 2005

[58] SACHS, J. ; KMEC, M. ; WOECKEL, S. ; PEYERL, P. ; ZETIK, R.: Combined Frequency and Time Domain Moisture Sensing by an Ultra Wideband IQ-M-Sequence Approach. In: *Proc. 6th conference on Electromagnetic Wave Interaction with Water and Moist Substances*. Weimar : ISEMA, 2005

[59] UNTERBERGER, R.R.: RADAR PROPAGATION IN ROCK SALT. In: *Geophysical Prospecting* 26, No. 2 (1978), S. 312–328

[60] STEWART, R.D. ; UNTERBERGER, R.R.: SEEING THROUGH ROCK SALT WITH RADAR. In: *Geophysics* 41, No. 1 (1976), S. 123–132

[61] AQIL, S. ; SCHMITT, D.R.: Dielectric permittivity of natural salt rock contaminated with clay. In: *SEG Technical Program Expanded Abstracts* 28, No. 1 (2009), S. 2175–2178

[62] PULLIAINEN, J. ; HEISKA, K. ; HYYPPA, J. ; HALLIKAINEN, M.: Backscattering properties of boreal forests at the C- and X-bands. In: *IEEE Transactions on Geoscience and Remote Sensing* 32, No. 5 (1998), S. 1041–1050

[63] INNOSENT GMBH, Germany: *general information*. Company webpage: `http://www.innosent.de/`, 2010

[64] OGAWA, H.: 24-GHz ultra-wideband short-range impulse radar for vehicular applications. In: *3rd IEEE Consumer Communications and Networking Conference* 2 (2006), Jan., S. 696–700

[65] RANVIER, S. ; KMEC, M. ; HERRMANN, R. ; KIVINEN, J. ; KOIVUNEN, J. ; THOMÄ, R.S. ; VAINIKAINEN, P.: mm-Wave wideband MiMo-Channel Sounding. In: *XXVIIIth General Assembly of URSI*. New Delhi, India : URSI, Oct. 2005

[66] BOSCH, R. (ed.): *Autoelektrik Autoelektronik*. Bd. 5. Wiesbaden, Germany : Vieweg & Sohn Verlag, 2007. – ISBN 978–3–528–23872–8

[67] ORFANIDIS, S.J.: *Electromagnetic Waves and Antennas*. Revised. 94 Brett Road, Piscataway, NJ 08854-8058, USA : ECE Department, Rutgers University, 2008 `http://www.ece.rutgers.edu/~orfanidi/ewa/`

[68] WALLMAN, H.: Transient response and the central limit theorem of probability. In: *Proc. of Symposia in Applied Mathematics*, 1950

[69] MIE, G.: *Beiträge zur Optik trüber Medien, speziell kolloidaler Metallösungen*. 330. Leipzig, Germany : Annalen der Physik, 1908. – 377–445 S.

[70] BOHREN, C.F. ; HUFFMAN, D.: *Absorption and scattering of light by small particles*. New York, USA : John Wiley, 1983

[71] V.D.HULST, H.C.: *Light scattering by small particles*. New York, USA : Dover, 1981

[72] BOWMAN, J.J. (ed.): *Electromagnetic and acoustic scattering by simple shapes*. Revised. Oxford, UK : Taylor & Francis Inc., 1988. – ISBN 978–0–891–16885–0

[73] GOUBAU, G.: Surface waves and their Application to Transmission Lines. In: *Journal of Applied Physics* 21 (1950), Nov.

[74] SOMMERFELD, A.: Propagation of waves in wireless telegraphy. In: *Ann. Physics* 81 (1926), S. 1153–1367

[75] THIO, T.: A Bright Future for Subwavelength Light Sources. In: *American Scientist* 94 (2006), S. 40–47

[76] THOMPSON, N.L. ; BURGHARDT, T.P. ; AXELROD, D.: Measuring surface dynamics of biomolecules by total internal reflection fluorescence with photobleaching recovery or correlation spectroscopy. In: *Biophysical Journal* 33, No. 3 (1981), S. 435–454

[77] BAUM, C.E.: General Properties of Antennas. In: *IEEE Transactions On Electromagnetic Compatibility* 44, No. 1 (2002), Feb., S. 18–24

[78] ZHOU, Z.S. ; BOERNER, W.M. ; SATO, M.: Development of a Ground-Based Polarimetric Broadband SAR System for Noninvasive Ground-Truth Validation in Vegetation Monitoring. In: *IEEE Transactions on Geoscience and Remote Sensing* 42, No. 9 (2004), Sep., S. 1803–1810

[79] SATO, M. ; ZHOU, Z.S. ; HAMASAKI, T. ; BOERNER, W.-M.: Development of a Ground-Based Synthetic Aperture Radar (GB-SAR) System and its Applications to Environment Monitoring and Disaster Prevention. In: *Proc. of the 2nd International Workshop POLINSAR*. ESRIN, Frascati, Italy : POLINSAR, Jan. 2005 (ESA SP-586), S. 61

[80] KESTER, W.: *The Data Conversion Handbook*. Burlington, MA 01803, USA : Newnes (Elsevier), 2004. – ISBN 0750678410

[81] KOSTYLEV, A.A. ; ASTANIN, L.Y.: *IEE Radar, Sonar, Navigation and Avionics*. Bd. 7: *Ultra-wideband radar measurements - analysis and processing*. 1997

[82] SACHS, J. ; KMEC, M. ; HERRMANN, R. ; PEYERL, P. ; RAUSCHENBACH, P.: An Ultra-Wideband Pseudo-Noise Radar Family integrated in SiGe:C. In: *Proc. International Radar*

Symposium IRS 2006, IRS, May 2006, S. 1 – 4

[83] ESKELINEN, P.: *Introduction to RF equipment and system design.* Boston, Mass., USA : Artech House, 2004. – ISBN 1–580–53665–4

[84] RYTTING, D.K.: Network analyzer error models and calibration methods. In: *ARFTG/NIST: RF & Microwave Measurements for Wireless Applications* (1996)

[85] KRESS, D. ; IRMER, R.: *Angewandte Systemtheorie - Kontinuierliche und zeitdiskrete Signalverarbeitung.* Verlag Technik, Berlin, 1989

[86] SAKAMOTO, T. ; SATO, T.: A target shape estimation algorithm for pulse radar systems based on boundary scattering transform. In: *IEICE Transactions on Communication* E87 B (2004), S. 1357–1365

[87] SACHS, J. ; HELBIG, M. ; HERRMANN, R. ; KMEC, M. ; SCHILLING, K.: On the Range Precision of UWB Radar Sensors. In: *Proc. of IRS2010.* Vilnius, Lithuania : IRS, Jun. 2010

[88] LJUNG, L.: *System Identification: Theory for the User.* Englewood Cliffs, N.J. : Prentice-Hall Inc., 1987

[89] SWORDS, S.S.: *Technical history of the beginnings of RADAR.* London, England : Peter Peregrinus Ltd, 1986

[90] DANIELS, D.J. (ed.): *IEE Radar, Sonar, Navigation and Avionics.* Bd. 15: *Ground Penetrating Radar.* 2nd edition. 2004. – ISBN 0–86341–360–9

[91] GÖBEL, J.: *Radartechnik : Grundlagen und Anwendungen.* Berlin, Germany : VDE Verlag, 2001. – ISBN 3–8007–2582–7

[92] STOVE, A.G.: Linear FMCW radar techniques. In: *IEE Proceedings F: Radar and Signal Processing* 139, No. 5 (1992), Oct., S. 343–350

[93] BARRICK, D.E.: FM/CW radar signals and digital processing / National Oceanic and Atmospheric Administration (Boulder, Colo, USA), Tech. Rep. ERL 283-WPL 26. 1973. – Forschungsbericht

[94] ROHDE & SCHWARZ GMBH & CO. KG, Germany: *R&S ZVA67 - A 67 GHz Vector Network Analyzer from Rohde & Schwarz.* Product page: `http://www2.rohde-schwarz.com/product/zva.html`, 2009

[95] SPECIALE, R.A.: A Generalization of the TSD Network-Analyzer Calibration Procedure, Covering n-Port Scattering-Parameter Measurements, Affected by Leakage Errors. In: *IEEE TRANSACTIONS ON MICROWAVE THEORY AND TECHNIQUES* MTT-25, No. 12 (1977), Dec., S. 1100–1115

[96] SILVONEN, K.J.: New five-standard calibration procedures for network analyzers and wafer probes / Helsinki University of Technology, Technical Report CT-19. Version: Mar. 1995. `http://www.ct.tkk.fi/publications/ct-19/main.html`. 1995. – Forschungsbericht

[97] ANRITSU CORP., Japan/USA: *Handheld Vector Network Analyzer - VNA Master.* Product page: `http://www.us.anritsu.com/products/Test-and-Measurement-Solutions/`

RF-and-Microwave-Solutions_ARPC1002ARPC.aspx, 2008

[98] AGILENT TECHNOLOGIES INC., USA: *App. Note 5965-7917E: Network Analyzer Basics*.
      PDF: http://cp.literature.agilent.com/litweb/pdf/5965-7917E.pdf, 2009

[99] SCHLEICHER, B. ; DEDERER, J. ; LEIB, M. ; NASR, I. ; TRASSER, A. ; MENZEL, W. ; SCHU-
      MACHER, H.: Highly Compact Impulse UWB Transmitter for High-Resolution Movement
      Detection. In: *Proc. of IEEE INTERNATIONAL CONFERENCE ON ULTRA-WIDEBAND
      Vol. 1*. Hannover, Germany : ICUWB, 2008

[100] AXELSSON, S.R.J.: Noise Radar using Random Phase and Frequency Modulation. In: *IEEE
      Transactions on Geoscience and Remote Sensing* 42, No. 11 (2004), Nov., S. 2370–2384

[101] SACHS, J. ; PEYERL, P. ; TKAC, F. ; KMEC, M.: Digital ultra-wideband-sensor electronics
      integrated in Si:Ge technology. In: *Proc. of EuMC 2002, Vol. II*. Milan, Italy : EuMC, Sep.
      2002, S. 539–542

[102] STRENG, B.: *Entwicklung und Implementierung eines Messplatzes zur Charakterisierung
      des HF-Teils von M-Sequenzmessköpfen in MATLAB*, TU Ilmenau, Fak. EI, FG EMT,
      diploma thesis, 2009

[103] KMEC, M. ; HERRMANN, R. ; SACHS, J. ; PEYERL, P. ; RAUSCHENBACH, P. ; TYO, J.S. (Hrsg.)
      ; BAUM, C.E. (Hrsg.) ; STONE, A.P. (Hrsg.): *Ultra-Wideband Short-Pulse Electromagnetics*.
      Bd. 8: *Extended Approaches for M-Sequence based UWB Systems*

[104] SACHS, J. ; PEYERL, P.: A New Principle for Sensor-Array-Application. In: *Proc. of 16th
      IEEE Instrumentation and Measurement Technology Conference*. Venice, Italy : IMTC, May
      1999, S. 1390–1395

[105] NEXYN CORP., USA: *Phase locked DRO - Phase Noise specification*. Product specification:
      http://www.nexyn.com/Specifications2006.htm, 2006

[106] HERRMANN, R.: *Charakterisierung des HF-Teils eines M-Sequenz Ultra-Breitband-
      Systems*, TU Ilmenau, Fak. EI, FG EMT, diploma thesis, 2004

[107] SCHILLING, K.: *Implementierung und Untersuchung eines Ultra-Breitband-M-
      Sequenzmesskopfes mit Überabtastung im Äquivalenzbereich*, TU Ilmenau, Fak. EI, FG
      EMT, diploma thesis, 2007

[108] UMC CORP., USA: *SR-U000-TS Pin Diode DPDT (Transfer Switches)*. Product specifica-
      tion: http://www.umcc111.com/DPDT.htm,

[109] RLC ELECTRONICS INC., USA: *SP-6T Standard Multi-Position Coaxial Switch*. Product
      specification: http://www.rlcelectronics.com/pdf_files/FINALRLC_18.pdf,

[110] LECROY CORP., USA: *4-channel 60 GS/s Serial Data Analyser SDA-18000*. Product spec-
      ification: http://www.lecroy.com/files/pdf/LeCroy_SDA18000_Datasheet.pdf, 2007

[111] TEKTRONIX INC., USA: *4-channel 50 GS/s Digital & Mixed Signal Real Time Oscillo-
      scope DPO/DSA72004B*. Product page: http://www.tek.com/products/oscilloscopes/
      dpo70000_dsa70000/, 2009

[112] MARKS II, R.J.: *Advanced Topics in Shannon Sampling and Interpolation Theory*. Berlin, Germany : Springer Verlag, 1992. – ISBN 3–540–97906–9

[113] SCOULAR, S.C. ; FITZGERALD, W.J.: Periodic nonuniform sampling of multiband signals. In: *Signal Processing* 22, No. 2 (1992), S. 195–200

[114] STROHMER, T. ; TANNER, J.: Fast reconstruction methods for bandlimited functions from periodic nonuniform sampling. In: *SIAM J. Numerical Analysis* 44, No. 3 (2006), S. 1073–1094

[115] THE MATHWORKS INC., USA: *MATLAB & SimuLink*. Product page: `http://www.mathworks.com/products/product_listing/index.html`, 2008

[116] HITTITE MICROWAVE CORP., USA: *SMA analog 6-15 GHz phase shifter HMC-C010*. Product page: `http://hittite.com/products/index.html/category/223`, 2010

[117] NELDER, J.A. ; MEAD, R.: A simplex method for function minimization. In: *Computer Journal* 7 (1965), S. 308–313

[118] MCKINNON, K.I.M.: Convergence of the Nelder-Mead simplex method to a non-stationary point. In: *SIAM Journal of Optimization* 9 (1999), S. 148–158

[119] LAGARIAS, J.C. ; REEDS, J.A. ; WRIGHT, M.H. ; WRIGHT, P.E.: Convergence Properties of the Nelder-Mead Simplex Method in Low Dimensions. In: *SIAM Journal of Optimization* 9 (1998), S. 112–147

[120] STREICH, R. ; V.D.KRUK, J.: An efficient vector-migration algorithm for imaging conventional 3-D GPR data. In: *Proc. 11th International Conference on Ground Penetrating Radar*. Columbus Ohio, USA : GPR, 2006

[121] MIWA, T. ; SATO, M. ; NIITSUMA, H.: Antenna compensation method using direct coupling wave in polarimetric borehole radar measurement. In: *Transactions of IEICE* J82-B, No.3 (1999), Mar., S. 442–451

[122] SAVELYEV, T.G. ; SATO, M.: Comparative analysis of UWB deconvolution and feature extraction algorithms for GPR landmine detection. In: *Proc. Detection and Remediation Technologies for Mines and Minelike Targets IX, SPIE Vol. 5415*, SPIE, 2004, S. 1008–1018

[123] FERRERO, A. ; PISANI, U.: Two-Port Network Analyzer Calibration Using an Unknown THRU. In: *IEEE Microwave and Guided Wave Letters* 2, No. 12 (1992), Dec., S. 505–507

[124] WÖCKEL, S. ; KONSTANTINOVIC, M. ; SACHS, J. ; LAMMERS, P.S. ; KMEC, M.: Application of ultra-wideband M-Sequence-Radar to detect sugar beets in agricultural soils. In: *Proc. 11th International Conference on Ground Penetrating Radar*. Columbus Ohio, USA : GPR, 2006

[125] KONSTANTINOVIC, M. ; WÖCKEL, S. ; LAMMERS, P.S. ; SACHS, J.: Yield mapping of sugar beet using ultra wide-band radar - Methodology and first research results. In: *Proc. of VDI Conference on Agricultural Engineering*. Hannover, Germany : VDI/VDE, 2005, S. 497–502

[126] RYTTING, D.K.: Appendix to: an analysis of vector measurement accuracy enhancement techniques / RF & Microwave Measurement Symposium and Exhibition, Hewlett Packard. Version: Mar. 1982. `http://www.hparchive.com/seminar_notes.htm`. 1982.

     – Forschungsbericht

[127] HAMME, H. V. ; BOSSCHE, M. V.: Flexible Vector Network Analyzer Calibration With Accuracy Bounds Using an 8-Term or a 16-Term Error Correction Model. In: *IEEE TRANSACTIONS ON MICROWAVE THEORY AND TECHNIQUES* 42., No. 6 (1994), Jun.

[128] RFSPIN S.R.O., Czech R.: *Double Ridged Waveguide Horn DRH20*. Product page: `http://www.rfspin.cz/en/antennas/drh20.php`, 2007

[129] FREEMAN, A. ; DURDEN, S.L.: A three-component scattering model for polarimetric SAR data. In: *IEEE Transactions on Geoscience and Remote Sensing* 36, No. 3 (1998), S. 963–973

[130] KÜHNICKE, H.: Entwicklung eines Messsystems zur hochauflösenden zerstörungsfreien Erkundung von Gesteinsnahbereichen mittels Sonar, FKZ 02C1184 / Fraunhofer-Institut für zerstörungsfreie Prüfverfahren Institutsteil Dresden. 2008. – research report

[131] SACHS, J. ; HERRMANN, R. ; KMEC, M. ; HELBIG, M. ; SCHILLING, K.: Recent Advances and Applications of M-Sequence based Ultra-Wideband Sensors. In: *Proc. IEEE International Conference on UWB*. Singapore : ICUWB, Sep. 2007

[132] KMEC, M. ; HELBIG, M. ; HERRMANN, R. ; RAUSCHENBACH, P. ; SACHS, J. ; SCHILLING, K.: M-Sequence Based Single Chip UWB-Radar Sensor. In: *Proc. Of AMEREM 2010*. Ottawa, USA : AMEREM, Jul. 2010

[133] RADANT TECHNOLOGIES INC., USA: *Radant MEMS Switch*. Product page: `http://www.radantmems.com/radantmems/switchoverview.html`, 2010

[134] SCHILLING, K. ; SACHS, J. ; KMEC, M. ; HERRMANN, R. ; HELBIG, M. ; BONITZ, F. ; RAUSCHENBACH, P.: System on Chip M-Sequence Sensor for Moisture Sensing and Impedance Spectroscopy. In: *Proc. Of Aquametry 2010*. Weimar, Germany, Oct. 2010

[135] SACHS, J. ; PEYERL, P.: Integrated Network Analyser Module for Microwave Moisture Sensors. In: *Proc. 4th conference on Electromagnetic Wave Interaction with Water and Moist Substances*. Weimar : ISEMA, May 2001, S. 165–172

[136] SACHS, J. ; BONITZ, F. ; KMEC, M. ; HELBIG, M. ; HERRMANN, R. ; SCHILLING, K. ; RAUSCHENBACH, P. ; ZAIKOV, E.: Ultra-Wideband Pseudo-Noise Sensors and their Application in Medical Engineering, Non-Destructive Testing and for Search and Rescue. In: *Proc. of 54th. Internationales Wissenschaftliches Kolloquium*. Ilmenau, Germany : Ilmenau University of Technology, Sep. 2009

[137] HELBIG, M. ; GEYER, C. ; HEIN, M. ; HERRMANN, R. ; HILGER, I. ; SCHWARZ, U. ; SACHS, J.: Improved Breast Surface Identification for UWB Microwave Imaging. In: *Proc. of World Congress of Medical Physics and Biomedical Engineering*. Munich, Germany : URSI, 2009

[138] SACHS, J. ; AFTANAS, M. ; CRABBE, S. ; DRUTAROVSKÝ, M. ; KLUKAS, R. ; KOCUR, D. ; NGUYEN, T.T. ; PEYERL, P. ; ROVNÁKOVÁ, J. ; ZAIKOV, E.: Detection and Tracking of Moving or Trapped People Hidden by Obstacles using Ultra-Wideband Pseudo-Noise Radar. In: *Proc. Of 5th European Radar Conference (EuRAD)*. Amsterdam, Netherlands : EuRAD,

Oct. 2008

[139] HERRMANN, R. ; SACHS, J. ; BONITZ, F.: On benefits and challenges of person localization using ultra-wideband sensors. In: *Proc. Of IPIN 2010*. Zurich, Switzerland : ETH Zurich, Sept. 2010

[140] SACHS, J. ; BADSTÜBNER, A. ; BONITZ, F. ; EIDNER, M. ; HELBIG, M. ; HERRMANN, R. ; KMEC, M. ; RAUSCHENBACH, P. ; SOLAS, H.: High Resolution Non-Destructive Testing in Civil Engineering by Ultra-Wideband Pseudo- Noise Approaches. In: *Proc. of ICUWB 2008*. Hannover, Germany : ICUWB, Sep. 2008

[141] SACHS, J. ; HELBIG, M. ; RENHAK, K.: Unsichtbares wird sichtbar - Mit Radar den Insekten auf der Spur: Neue Möglichkeiten zum Aufspüren von Insektenaktivitäten. In: *Proc. of HOBA 2008*. Duisburg, Germany : HOBA, Oct. 2008

[142] BONITZ, F. ; EIDNER, M. ; SACHS, J. ; HERRMANN, R. ; SOLAS, H.: UWB-Radar Sewer Tube Crawler. In: *Proc. 12th International Conference on Ground Penetrating Radar*. Birmingham, UK : GPR, Jun. 2008

[143] BONITZ, F. ; HERRMANN, R. ; EIDNER, M. ; SACHS, J. ; H.SOLAS: Application of Ultra Wideband Radar Sensors for Non-Destructive Testing of Pipe Systems and Salt Mine Tunnels. In: *Proc. of 54th. Internationales Wissenschaftliches Kolloquium*. Ilmenau, Germany : Ilmenau University of Technology, Sep. 2009

Publications with own contributions

[1] HERRMANN, R. ; SACHS, J. ; BONITZ, F.: On benefits and challenges of person localization using ultra-wideband sensors. In: *Proc. Of IPIN 2010*. Zurich, Switzerland : ETH Zurich, Sept. 2010

[2] HERRMANN, R. ; SACHS, J. ; SCHILLING, K. ; BONITZ, F.: New extended M-sequence ultra wideband radar and its application to the disaggregation zone in salt rock. In: *Proc. 12th International Conference on Ground Penetrating Radar*. Birmingham, UK : GPR, Jun. 2008

[3] HERRMANN, R. ; SACHS, J. ; PEYERL, P.: System evaluation of an M-sequence ultra wideband radar for crack detection in salt rock. In: *Proc. 11th International Conference on Ground Penetrating Radar*. Columbus Ohio, USA : GPR, 2006

[4] HERRMANN, R. ; T.HAMASAKI ; SATO, M.: 3D image reconstruction using square path SAR data. In: *Proc. of URSI Commision F Symposium on Microwave Remote Sensing of The Earth, Oceans, Ice, and Atmosphere*. Ispra Italy : URSI, Apr. 2005

[5] HERRMANN, R. ; SATO, M.: Image Reconstruction by a Ground-Based SAR System. In: *Proc. of IGARSS*. Seoul, Korea : IGARSS, 2005

[6] HERRMANN, R.: *Charakterisierung des HF-Teils eines M-Sequenz Ultra-Breitband-Systems*, TU Ilmenau, Fak. EI, FG EMT, diploma thesis, 2004

[7] KMEC, M. ; HERRMANN, R. ; SACHS, J. ; PEYERL, P. ; RAUSCHENBACH, P. ; TYO, J.S. (Hrsg.) ; BAUM, C.E. (Hrsg.) ; STONE, A.P. (Hrsg.): *Ultra-Wideband Short-Pulse Electromagnetics*. Bd. 8: *Extended Approaches for M-Sequence based UWB Systems*

[8] SACHS, J. ; HELBIG, M. ; HERRMANN, R. ; KMEC, M. ; RAUSCHENBACH, P. ; SCHILLING, K.: General Purpose High-Resolution Medical Sensor using Ultra-Wideband M-Sequences. In: *International Journal of Ultra Wideband Communications and Systems* Special issue on: 'Applications of Ultra Wideband Systems in Biomedicine´ (2009)

[9] SACHS, J. ; PEYERL, P. ; WÖCKEL, S. ; KMEC, M. ; HERRMANN, R. ; ZETIK, R.: Liquid and moisture sensing by ultra wideband pseudo-noise sequence signals. In: *Measurement Science and Technology* 14, 4th edition (2007), S. 1074–1087

[10] SCHILLING, K. ; SACHS, J. ; KMEC, M. ; HERRMANN, R. ; HELBIG, M. ; BONITZ, F. ; RAUSCHENBACH, P.: System on Chip M-Sequence Sensor for Moisture Sensing and Impedance Spectroscopy. In: *Proc. Of Aquametry 2010*. Weimar, Germany, Oct. 2010

[11] KMEC, M. ; HELBIG, M. ; HERRMANN, R. ; RAUSCHENBACH, P. ; SACHS, J. ; SCHILLING, K.: M-Sequence Based Single Chip UWB-Radar Sensor. In: *Proc. Of AMEREM 2010*. Ottawa,

USA : AMEREM, Jul. 2010

[12] SACHS, J. ; HELBIG, M. ; HERRMANN, R. ; KMEC, M. ; SCHILLING, K. ; RAUSCHENBACH, P.: Non-Destructive Testing and Super Resolution Imaging with Ultra Wideband M-Sequence Radar. In: *Proc. Of EUSAR 2010*. Aachen, Germany : EUSAR, Jun. 2010

[13] SACHS, J. ; HELBIG, M. ; HERRMANN, R. ; KMEC, M. ; SCHILLING, K.: On the Range Precision of UWB Radar Sensors. In: *Proc. of IRS2010*. Vilnius, Lithuania : IRS, Jun. 2010

[14] BONITZ, F. ; HERRMANN, R. ; EIDNER, M. ; SACHS, J. ; H.SOLAS: Application of Ultra Wideband Radar Sensors for Non-Destructive Testing of Pipe Systems and Salt Mine Tunnels. In: *Proc. of 54th. Internationales Wissenschaftliches Kolloquium*. Ilmenau, Germany : Ilmenau University of Technology, Sep. 2009

[15] SACHS, J. ; BONITZ, F. ; KMEC, M. ; HELBIG, M. ; HERRMANN, R. ; SCHILLING, K. ; RAUSCHENBACH, P. ; ZAIKOV, E.: Ultra-Wideband Pseudo-Noise Sensors and their Application in Medical Engineering, Non-Destructive Testing and for Search and Rescue. In: *Proc. of 54th. Internationales Wissenschaftliches Kolloquium*. Ilmenau, Germany : Ilmenau University of Technology, Sep. 2009

[16] HELBIG, M. ; GEYER, C. ; HEIN, M. ; HERRMANN, R. ; HILGER, I. ; SCHWARZ, U. ; SACHS, J.: Improved Breast Surface Identification for UWB Microwave Imaging. In: *Proc. of World Congress of Medical Physics and Biomedical Engineering*. Munich, Germany : URSI, 2009

[17] SACHS, J. ; KMEC, M. ; HERRMANN, R. ; SCHILLING, K. ; ZETIK, R. ; RAUSCHENBACH, P.: Ultra-Wideband Pseudo-Noise Radar: Principle of function, state of the art, applications. In: *NATO Specialist Meeting SET 120*. Toulouse, Franc : NATO, Oct. 2008

[18] BONITZ, F. ; SACHS, J. ; HERRMANN, R. ; EIDNER, M.: Radar Tube Crawler for Quality Assurance Measurements of Pipe Systems. In: *Proc. of EURAD 2008*. Amsterdam, The Netherlands : EURAD, Oct. 2008

[19] SACHS, J. ; BADSTÜBNER, A. ; BONITZ, F. ; EIDNER, M. ; HELBIG, M. ; HERRMANN, R. ; KMEC, M. ; RAUSCHENBACH, P. ; SOLAS, H.: High Resolution Non-Destructive Testing in Civil Engineering by Ultra-Wideband Pseudo- Noise Approaches. In: *Proc. of ICUWB 2008*. Hannover, Germany : ICUWB, Sep. 2008

[20] BONITZ, F. ; EIDNER, M. ; SACHS, J. ; HERRMANN, R. ; SOLAS, H.: UWB-Radar Sewer Tube Crawler. In: *Proc. 12th International Conference on Ground Penetrating Radar*. Birmingham, UK : GPR, Jun. 2008

[21] SACHS, J. ; HERRMANN, R. ; KMEC, M. ; SCHILLING, K. ; BONITZ, F. ; HELBIG, M.: M-Sequence Hardware for UWB-Imaging: Current state and future goals. In: *UKoLoS-Colloquium on Localisation and Imaging with UWB-sensor technology*. Georgenthal, Germany : DFG, Oct. 2007

[22] SACHS, J. ; HERRMANN, R. ; KMEC, M. ; HELBIG, M. ; SCHILLING, K.: Recent Advances and Applications of M-Sequence based Ultra-Wideband Sensors. In: *Proc. IEEE International Conference on UWB*. Singapore : ICUWB, Sep. 2007

[23] SACHS, J. ; HERRMANN, R. ; KMEC, M. ; PEYERL, P.: Modified M-Sequence UWB-Radar. In: *Proc. of German Microwave Frequency 2006*. Germany : GeMIC, 2006

[24] KMEC, M. ; HERRMANN, R. ; SACHS, J. ; PEYERL, P.: A familly of M-Sequence based UWB sensors. In: *Proc. of 51st Internationales Wissenschaftliches Kolloquium*. Ilmenau, Germany : Ilmenau University of Technology, Sep. 2006

[25] KMEC, M. ; HERRMANN, R. ; SACHS, J. ; PEYERL, P. ; RAUSCHENBACH, P.: Extended Approaches for M-Sequence based UWB Sensors. In: *Proc. of AMEREEM 2006*. USA : AMEREEM, Jul. 2006

[26] SACHS, J. ; KMEC, M. ; HERRMANN, R. ; PEYERL, P. ; RAUSCHENBACH, P.: An Ultra-Wideband Pseudo-Noise Radar Family integrated in SiGe:C. In: *Proc. International Radar Symposium IRS 2006*, IRS, May 2006, S. 1 – 4

[27] RANVIER, S. ; KMEC, M. ; HERRMANN, R. ; KIVINEN, J. ; KOIVUNEN, J. ; THOMÄ, R.S. ; VAINIKAINEN, P.: mm-Wave wideband MiMo-Channel Sounding. In: *XXVIIIth General Assembly of URSI*. New Delhi, India : URSI, Oct. 2005

Theses

1. Non-destructive testing in civil engineering is an emerging research field and UWB sensors are becoming interesting for many applications. Inspection of the disaggregation zone in salt rock is one example.

2. Electromagnetic waves up to 40 GHz can be used in salt rock. Frequencies below 20 GHz exhibit $\epsilon_r \approx 6$ and do not suffer significant attenuation.

3. Disaggregation can be modelled as thin gaps or spherical volume defects. Responses are proportional to their characteristic dimensions and derivatives of the stimulus. Polarimetric behaviour is not predictable due to unknown distribution and alignment.

4. The dynamic range definition $SFDR_{td}$ relating the largest wanted signal component to the maximum unwanted component in impulse responses can be used to asses measurement performance for the task.

5. Crucial sensor features are stability, repeatability, and high bandwidth B. Detection of sub-mm gaps behind the surface requires $B > 10\,GHz$ while $SFDR_{td} > 50\,dB$.

6. For device clutter levels below 50 dB, calibration is mandatory for UWB devices.

7. Among available technologies, M-Sequence sensors are best suited due to extremely good stability, fast measurement speed, high integration level, and low costs.

8. The basic M-Sequence concept can easily be extended to cover the frequency band from 1 GHz to 13 GHz by using a mixer and the master clock source as carrier.

9. Equivalent sampling rate of the M-Sequence principle can be increased by using a phase shifter for relative delays of fractions of the master clock period while keeping the stable sampling mechanism.

10. Phase control calibration is mandatory to ensure near-uniform sampling. For a maximum amplitude error of 60 dB below full scale, sampling must be accurate to within 20 fs for the stimulus, which can be reached by an developed optimisation search.

11. Despite the original formulation in frequency domain, established calibration procedures can be used for M-Sequence sensors as well. Receivers must be linear and ill-conditioned frequency bands must be suppressed when switching between domains.

12. 8-term correction using an unknown line is ideally suited for on-site calibration of the M-Sequence sensor. The sensor must provide an S-parameter frontend with four receivers to enable generalised calculation for measured S-parameters.

13. Conditions of calibration matrices from one-port corrections can be used to check reflection calibration on-site. An increase of more than 50% from lab reference indicates poor performance.

14. The phase shift caused by the line standard can be used to assess transmission calibration. Differences to the real shift should stay below 5°.

15. Validity of calibration is not limited by device drift when the procedure is repeated in an hourly schedule.

16. The new M-Sequence sensor and a Rohde & Schwarz ZVK network analyser perform similar with an $SFDR_{td} > 60\,dB$. The M-Sequence device has a higher clutter floor mainly due to inaccuracies of sampling timing.

17. Antenna crosstalk and salt rock surface reflection can be removed by an optimisation approach matching amplitude and delay of measured data to references. For surface suppression, similarity of neighbouring data must be ensured by dense spatial sampling.

18. Measurements require directional antennas at most a few cm away from the salt rock surface. Distance variations are tolerable. A slight antenna inclination of 15° suppresses surface without impairing responses from small gaps or cracks.

19. Disaggregation zone of an old cylindrical tunnel in Bernburg can be imaged by the new M-Sequence sensor. A 3D view of a 1 m long tunnel section shows distortions within the first 20 cm of salt. Connected and partly layered defects are detected in the ceiling up to 1 m distance and at the sides where the tunnel shape is disturbed.

20. Comparison of the UWB results with measurements by a novel ultrasonic sensor from Fraunhofer IZFP Dresden showed excellent agreement given the differences in wave interaction for salt rock.

21. UWB sensors and ultrasonic sensors complement each other. UWB is ideal for pre-inspection of long sections, while the latter one has higher sensitivity for detailed assessment.

22. The formation of a disaggregation zone was detected during a 48 h observation of a newly cut tunnel stub in Borth. A subsidence of 4.8 mm and development of defects within the first 20 cm behind the surface are evident in the data.

23. The developed UWB sensor is a prototype using advantages of the M-Sequence approach. It shows the potential for highly accurate, compact, and affordable UWB sensors. Flexible integrated configurations can be derived.

Thesen

1. Zerstörungsfreies Test ist ein aufstrebendes Forschungsgebiet und neue UWB Sensoren eignen sich für viele zugehörige Anwendungen. Messung der Auflockerungszone im Salzgestein ist ein Beispiel.

2. Elektromagnetische Wellen bis 40 GHz eignen sich für Salzgestein. Unter 20 GHz tritt kaum Dämpfung auf und $\epsilon_r \approx 6$ gilt.

3. Auflockerungen lassen sich als dünne Spalten bzw. kugelförmige Defekte modellieren. Ihre Rückstreuungen sind proportional zu charakteristischen Abmessungen sowie Ableitungen des Anregungssignals. Polarimetrische Eigenschaften sind aufgrund unbekannter Defektverteilung nicht vorhersagbar.

4. Um die Eignung eines Systems für die Messaufgabe zu beurteilen, ist die Zeitbereichsdynamik $SFDR_{td}$ geeignet, welche das Verhältnis von maximaler Nutzsignalamplitude zu Fehleramplitude angibt.

5. Wichtigste Sensoreigenschaften sind Stabilität, Wiederholbarkeit und hohe Bandbreite B. Detektion von Sub-mm Spalten setzt $B > 10\ GHz$ und $SFDR_{td} > 50\ dB$ voraus.

6. Zur Reduktion der Gerätefehler unter 50 dB ist eine Kalibrierung unumgänglich.

7. Von gängigen UWB-Technologien sind M-Sequenzsensoren aufgrund hoher Stabilität, Messgeschwindigkeit, Integrierbarkeit und geringer Kosten am besten geeignet.

8. Der M-Sequenzgenerator kann mittels Mischer und der Systemtaktrate als Träger erweitert werden, um das Frequenzband von 1 GHz bis 13 GHz abzudecken.

9. Die äquivalente Abtastrate des M-Sequenzprinzips kann mittels Phasenschieber unter Wahrung der Stabilität erhöht werden, welcher relative Verzögerungen kleiner als die Systemtaktperiode realisiert.

10. Kalibrierung der Phasenschieberzustände ist für äquidistante Abtastung notwendig. Für Amplitudenfehler 60 dB unter Vollaussteuerung, müssen die Abtastzeiten auf 20 fs genau sein. Dies wird über eine Optimumsuche erreicht.

11. Etablierte Frequenzbereichsmethoden zur Kalibrierung können für M-Sequenzsensoren adaptiert werden. Die Empfänger müssen linear arbeiten und Frequenzbereiche mit wenig Stimulusenergie müssen unterdrückt werden.

12. 8-Term Korrektur mit unbekanntem Transmissionsnormal eignet sich für Anwendung in Salzminen. Ein S-Parametermesskopf mit vier Empfängern ist notwendig.

13. Die Konditionen von Kalibriermatrizen der Eintorkorrekturen eignen sich zur Prüfung der Reflexionskalibierung. Eine Erhöhung um mehr als 50% gegenüber Laborreferenzen deutet auf schlechte Qualität hin.

14. Die Phasenlaufzeit des Transmissionsnormals eignet sich zur Prüfung der Übertragungskalibierung. Differenzen gegenüber dem wahren Verhalten des Normals sollten kleiner als 5° sein.

15. Die Kalibrierung bleibt trotz Gerätedrift bei stündlicher Wiederholung gültig.

16. Den neue M-Sequenzsensor und ein Rohde & Schwarz ZVK Netzwerkanalysator erreichen beide $SFDR_{td} > 60\,dB$. Das M-Sequenzgerät hat aufgrund der unperfekten Abtastzeiten ein höheres Restfehlerniveau.

17. Antennenübersprechen und Oberflächenreflex können in den Messdaten durch eine Optimumsuche unterdrückt werden, welche Amplitude und Laufzeit zu einer Referenz angleicht. Zur Oberflächenunterdrückung muss die Ähnlichkeit benachbarter Impulsantworten durch dichtes Scannen sichergestellt werden.

18. Die Messaufgabe setzt Richtantennen voraus, welche maximal einige cm von der Oberfläche entfernt sein dürfen. Abstandsvariationen sind erlaubt. Ein Anwinklung um 15° reduziert den Oberflächenreflex, nicht aber die Rückstreuung der Spalten.

19. Die Auflockerungszone eines alten kreisrunden Tunnels in Bernburg konnte mit dem M-Sequnezsensor abgebildet werden. Die entstandene 3D-Ansicht eines 1 m langen Abschnitts zeigt Auflockerungen innerhalb der ersten 20 cm. Zusammenhängende Defekte sind im Firstbereich bis zu 1 m im Salz nachgewiesen. Die Seitenbereiche sind wegen der aufgefahrenen Sole ebenfalls stark aufgelockert.

20. Vergleiche zwischen Messergebnissen des UWB Sensors und einem neuartigen Ultraschallgerät des Fraunhofer IZFP Dresden zeigt hervorragende Übereinstimmung unter Beachtung der Unterschiede der physischen Wirkprinzipien.

21. UWB- und Ultraschallsensoren ergänzen sich hervorragend. Radar ist ideal zur Vorauswahlmessung langer Abschnitte, während das Sonar aufgrund der hohen Sensitivität Detailuntersuchungen erlaubt.

22. Die Entstehung der Auflockerungszone konnte durch eine 48 h dauernde Messung eines frisch aufgefahrenen Tunnelstumpfes in Borth nachgewiesen werden. Eine Konvergenz von 4.8 mm sowie Veränderungen in den ersten 20 cm wurden ermittelt.

23. Der entwickelte UWB-Sensor demonstriert als Prototyp die Vorteile des M-Sequenzprinzips. Er zeigt Potential für hochgenaue, kompakte und bezahlbare UWB Sensoren. Flexible, hochintegrierte Konfigurationen können davon abgeleitet werden.

Erklärung / Statement of Origin

Ich versichere, dass ich die vorliegende Arbeit ohne unzulässige Hilfe Dritter und ohne Benutzung anderer als der angegebenen Hilfsmittel angefertigt habe. Die aus anderen Quellen direkt oder indirekt übernommenen Daten und Konzepte sind unter Angabe der Quelle gekennzeichnet.

Bei der Bearbeitung und Auswertung folgenden Materials haben mir die nachstehend aufgeführten Personen in der jeweils beschriebenen Weise unentgeltlich geholfen:

1. Dr.-Ing. J.Sachs, TU Ilmenau - allgemeine wissenschaftliche Betreuung und Beratung

2. Dipl.-Ing. K.Schilling, TU Ilmenau - Entwurf und Aufbau der HF-Gehäuse für M-Sequenzchipsatz; Grundsatzmessungen zur periodisch nicht-äquidistanten Abtastung

Weitere Personen waren an der inhaltlich-materiellen Erstellung der vorliegenden Arbeit nicht beteiligt. Insbesondere habe ich hierfür nicht die entgeltliche Hilfe von Vermittlungs bzw. Beratungsdiensten (Promotionsberater oder anderer Personen) in Anspruch genommen. Niemand hat von mir unmittelbar oder mittelbar geldwerte Leistungen für Arbeiten erhalten, die im Zusammenhang mit dem Inhalte der vorgelegten Dissertation stehen.

Die Arbeit wurde bisher weder im In- noch im Ausland in gleicher oder ähnlicher Form einer Prüfungsbehörde vorgelegt.

Ich bin darauf hingewiesen worden, dass die Unrichtigkeit der vorstehenden Erklärung als Täuschungsversuch angesehen wird und den erfolglosen Abbruch des Promotionsverfahrens zu Folge hat.

Dipl.-Ing. R.Herrmann
Ilmenau, July 6, 2011